Stimulus Responsive Functional Nano-assemblies of Short-peptides

A thesis submitted in partial fulfilment of the requirements for the degree of

DOCTOR OF PHILOSOPHY

by

JAHNU SAIKIA

Department of Biosciences and Bioengineering
Indian Institute of Technology Guwahati
Guwahati-781039, India

October 2021

Stimulus Responsive Functional Nano-assemblies of Short-peptides

A thesis submitted in partial fulfilment of the requirements for the degree of

DOCTOR OF PHILOSOPHY

by

JAHNU SAIKIA

Department of Biosciences and Bioengineering
Indian Institute of Technology Guwahati
Guwahati-781039, India

October 2021

Dedicated

To

My Family and My Teachers

Indian Institute of Technology Guwahati

Department of Biosciences and Bioengineering

DECLARATION

I do hereby declare that the research findings of this thesis are the result of research work carried out by me in the Department of Biosciences and Bioengineering, Indian Institute of Technology Guwahati, Guwahati, India, under the supervision of Prof. Vibin Ramakrishnan.

As per the general norms of reporting research findings, I take full responsibility for the data represented. Acknowledgments have been made wherever the research findings of other researchers have been cited in this thesis.

Date: 28.10.2021

Jahnu Saikia

Indian Institute of Technology Guwahati

Department of Biosciences and Bioengineering

CERTIFICATE

It is certified that the work described in this thesis entitled "**Stimulus Responsive Functional Nano-assemblies of Short-peptides**" by Mr. Jahnu Saikia for the award of the degree of Doctor of Philosophy is an authentic record of the results obtained from the research work carried out under my supervision in the Department of Biosciences and Bioengineering, Indian Institute of Technology Guwahati, India. To the best of my knowledge, no part of this work has been submitted elsewhere for the award of any degree.

Date: 28.10.2021

Place: Guwahati

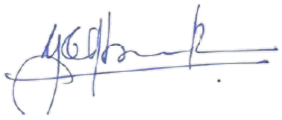

Prof. Vibin Ramakrishnan

(Thesis Supervisor)

Acknowledgments

When I first began my Ph.D., I don't think I anticipated how much my experiences during this time would change me. I want to thank everyone, past and present, who were a part of that change. I would like to express my heartfelt gratitude to those who have contributed throughout my Ph.D. journey and motivated me on the path to success.

At the onset, I would like to express my heartfelt gratitude to my Ph.D. thesis supervisor, Prof. Vibin Ramakrishnan, for his scholarly guidance, encouragement, and support throughout my Ph.D. program. He has helped me to enhance my knowledge on the subject and inspired me to make the right decisions at crucial moments. I am also thankful to him for giving me the freedom to pursue my interests in his lab, and I find privileged to have worked under his kind guidance.

I would like to thank my doctoral committee members, Dr. Nitin Chaudhary, Dr. Sachin Kumar, and Dr. Senthilkumar Sivaprakasam, for their valuable suggestions and pieces of advice during my doctoral studies.

I am grateful to University Grant Commission (UGC), India, for financial support as Junior Research Fellowship and Senior Research Fellowship during my research. I want to thank the Department of Biosciences and Bioengineering and the Central Instrument Facility, IIT Guwahati, for providing various facilities to carry out my experiments efficiently. I am grateful to the Centre of Nanotechnology, IIT Guwahati, for allowing me to operate the FESEM instrument as an authorized operator for three years.

I am immensely thankful to my collaborator Dr. T. Venugopal, Organic Synthesis and Catalysis Laboratory, SRM Research Institute, Chennai, for helping me with my catalysis experiments and correct the manuscripts. My profound gratitude goes to Dr. Vipin Agarwal, Assistant professor, and his student Dr. Lokeshwar Rao at TIFR-TCIS Hyderabad for helping me with the solid-state NMR studies and result analysis. I am thankful to Dr. R. Anandalakshmi, Associate professor, and her student Dr. K. Dharmalingam, Department of Chemical Engineering, for helping me with the rheological studies. My heartfelt thanks to Dr. Sachin Kumar, Associate professor, and his student Miss Ferrin Antony for helping me with

the cell culture experiments. Last but not the least, I am thankful to Dr. Kailash Chandra Bhattacharya, Head, Department of Biochemistry, Gauhati Medical College and Hospital, Guwahati, for gifting us fresh human cerebrospinal fluid samples for our experiments.

I would like to thank all my seniors (Dr. Prakash, Dr. Gaurav Jerath, Dr. Gaurav Pandey, Dr. Sajitha, Dr. Ruchika, Dr. Debika and, Dr. Karabi) my colleagues (Dr. Vinay, Anshuman, Vivek, Yvonne, Feba, and Kalpana) for their invaluable contributions throughout my research work. I would like to thank my best buddies at IIT Guwahati, Dr. Kishore Banik, Dr. Harsha Chaudhary, and Dr. Devibhasha Bordoloi, for making my life happier and giving me those countless memories. I am grateful to Nimisha Bania for her unconditional support in performing the catalysis experiments and for our friendship. I am thankful to Devipriya Gogoi and Nayan for helping me in performing few important experiments. My sincere thanks go to Manashi Das for her valuable scholarly inputs and immense support throughout the journey. My heartfelt thanks to my college friends Hemanta, Rishi, Jyoti, Ruksana, Poonam for believing in me and giving me those priceless memories.

Last but not the least; I would like to express my deepest appreciation and gratitude to my family. To my parents – my father who taught me the meaning of hard work and my mother, who is the strongest person I know – thank you for always telling me I could do anything I wanted. My heartfelt thanks to my grandmother for always pushing me to achieve my absolute best. Thank you for your endless patience and support throughout my life. I am especially grateful to my sister Dr. Subhalakshmi Saikia and my brother-in-law Dr. Devajit Nath for their unwavering support and motivation. This would not have been possible without your support.

--Jahnu Saikia

Table of Contents

List of Figures

fragments after treatment with trypsin exposed to 300 Vcm^{-1} (DC) for 24h. No noticeable difference in the band position of the BSA fragments among the three different experimental conditions is observed confirming the functional stability of trypsin in the presence of an external field.L7 and L8 show band position of standard trypsin and undigested BSA alone.

List of Tables

List of Abbreviations

AD	Alzheimer's Disease
AFM	Atomic Force Microscopy
BBB	Blood Brain Barrier
CD	Circular Dichroism
DAPI	4′,6-diamidino-2-phenylindole
DIPEA	N,N-Diisopropylethylamine
DMEM	Dulbecco's Modified Eagle's - Medium
DMF	N,N, Dimethylformamide
DLS	Dynamic Light Scattering
EDTA	Ethylenediaminetetraacetic acid
EF	Electric Field
FITC	Fluorescein isothiocyanate
Fmoc	Fluorenylmethyloxycarbonyl chloride
FESEM	Field Emission Scanning Electron Microscope
FETEM	Field Emission Transmission Electron Microscope
FTIR	Fourier-transform infrared spectroscopy
HBTU	*N,N,N′,N′*-Tetramethyl-*O*-(1*H*-benzotriazol-1-yl)uronium hexafluorophosphate
HCCA	α-Cyano-4-hydroxycinnamic acid
HFIP	Hexafluoroisopropanol
HOBt	1-Hydroxybenzotriazole Monohydrate

HPLC	High Performance Liquide Chromatography
KBr	Potassium bromide
MALDI-TOF	Matrix Assisted Laser Desorption Ionization-Time of Flight
MF	Magnetic Field
MTT	3-(4,5-Dimethyl-2-thiazolyl)-2,5-diphenyl-2H-tetrazolium bromide
NMR	Nuclear Magnetic Resonance
PB	Phosphate Buffer
PI	Propidium iodide
TFA	Trifluoroacetic acid
ThT	Thioflavin T
THF	Trihydrofuran
TFE	Trifluoroethanol
TLC	Thin Layer Chromatography

Abstract

The ability to direct peptide self-assembly opens up important avenues to construct a rich variety of molecular assemblies with novel functions. Besides, directing the folding and inhibiting aggregation may be an effective strategy in reducing amyloid elicited toxicity. In this thesis, we have explored and unveiled various physical and chemical modulators during peptide self-assembly for producing functional materials and developing non-invasive therapy against Alzheimer's disease. Central to our strategy is to rationally design peptide sequences with residues that respond to the applied stimulus and direct the self-assembly. We have designed, synthesized, and characterized a minimalistic peptide model that structurally mimics the active site of lytic polysaccharide monooxygenase at physiological pH. We have employed various spectroscopic techniques such as UV-Vis, CD, EPR, and NMR to characterize the structure of the complex. Using the knowledge of the Ramachandran plot, we have designed a series of 12 tri-peptides and tested their ability to form catalytic hydrogels for the C-C bond-forming Aldol reaction. We have examined the effect of external electric field on the structure-property relationship of the hydrogels in terms of their catalytic stereoselectivity. Further, we have extended our study to examine the effect of electric and magnetic field on the aggregation propensity of $A\beta_{1-42}$ peptide during the primary and secondary nucleation process. The efficacy of the applied fields was characterized using various biophysical techniques and cell viability assay on human neuroblastoma (SH-SY5Y and IMR-32) and human embryonic kidney cells (HEK-293). Overall, this thesis put forth the possibility of employing a physical perturbant like the electric field, in modulating chemical as well as biological effects, in fine-tuning their designed functions.

1.

Introduction, Research Design and Thesis Objectives

Originally described in 1993, self-assembling peptides have attracted interest in diverse fields, ranging from biomedicine, electronics, tissue culture, catalysis, and more. The process of peptide self-assembly has often been explained by assuming that the system rapidly equilibrates through reversible non-covalent interactions, thereby yielding the most stable structure in terms of free energy. However, controlling the hierarchical organization of self-assembling peptides into supramolecular nanostructures opens up the possibility of developing unprecedented supramolecular systems with unique properties. This chapter introduces a hybrid approach of employing various internal and external stimuli as modulators for self-assembling peptides.

INTRODUCTION

Self-assembly is a bottom-up process in which the components of a system spontaneously form ordered aggregates or patterns due to specific, non-covalent interactions without any external direction.[2] It is a common phenomenon found in nature. Some of the natural examples of functional self-assembled structures are phospholipid bilayer, viral capsid protein, and DNA-double helix. The dysfunctional assembly of proteins and peptides results in various amyloid pathologies such as Alzheimer's disease, Parkinson's disease, type II diabetes, and prion diseases.[3] These disorders are marked by the aberrant self-assembly of peptides into one-dimensional cross-β amyloid fibrils. Over the years, researchers have realized that the amyloid aggregates are not only related to diseased states, but can be exploited to form functional biomaterials. While designing synthetic peptide materials, protein aggregation may be viewed as a "feature" rather than a "bug". This recognition has inspired extensive efforts to develop novel peptide-based biomaterials and has found applications in biomedicine, energy storage, and catalysis.[4] The report of the first chemically synthesized peptide by Emil Fischer and E Fourneau (1901),[5] followed by the discovery of solid-state peptide synthesis (SSPS) by R.B. Merrifield (1963),[6] permits synthetic peptide chemistry to explore the chemical space beyond that available to natural molecular building blocks. Last few decades have seen increasing research efforts, focused on producing new peptide-based functional structures, either by mimicking nature or by using entirely new design paradigms with novel functionality.

The process of peptide self-assembly has often been explained by assuming that the system rapidly equilibrates through reversible non-covalent interactions, thereby yielding the most stable structure in terms of free energy. However, controlling the hierarchical organization of self-assembling peptides into supramolecular nanostructures opens up the possibility of developing unprecedented supramolecular systems with unique properties. Modulating the self-assembly process by effectively manipulating the environment alters the interaction pattern of the molecules in the system; a process commonly called 'directed self-assembly'. [7] The stimuli to direct the self-assembly can be introduced either externally, where the changes are felt throughout the system, or internally, in which the changes are felt only in the local environment. The underlying principle is that changing the native properties of the system can change the dynamic pathways of the assembly. External stimuli such as temperature, light,

ultrasound, pH, electric, and magnetic fields act on the macroscopic scale where it is easier to implement modulation but do not provide the control provided by chemical constitution such as amino acid composition and chirality.[8]

The growing demand for enantiopure products in pharmaceutical and agricultural applications is the driving factor for the ever-increasing market value of chiral products.[9] However, synthesizing enantiopure compounds is a challenge that is both fundamental and critical for chemists. One strategy is to take inspiration from nature's catalytic machinery by employing oligopeptides as chiral catalysts. The ultimate goal is to mimic the active site of an enzyme within a simpler framework. Besides, the incorporation of unnatural D-amino acids may tune the metal binding affinity of small peptides and hold great promise in designing ultra-short peptide motifs mimicking a metalloenzyme's active site. The diastereopeptides allow the manipulation of amino acid side chains' spatial orientation, altering the steric interactions of the metal binding pockets without modifying the side-chain chemistry. Peptide addresses the fundamentally challenging problem in asymmetric catalysis and is, in principle, ecofriendly.

Protein misfolding diseases like Alzheimer's disease (AD), Parkinson's disease, and type II diabetes are major unmet medical conditions because of their prevalence, severity, cost, and lack of mechanism-based treatments. AD alone constitutes 80% of all dementia cases and affects millions of people globally.[10] The current FDA-approved treatments include small molecules[11] and immunotherapy,[12] that can only provide symptomatic relief or are in the initial phases of development. The ability to modulate peptide self-assembly using external stimuli harbors the potential to be developed into non-invasive treatment strategies against such diseases. Promoting folding and inhibiting aggregation using non-invasive physical modulators such as ultrasound, light, electric, and magnetic field holds assurance as an alternative or complementary therapeutic adjuvant strategy to reduce amyloid elicited toxicity.

1.2. RESEARCH DESIGN

In this thesis, we have explored a hybrid approach of employing various internal and external stimuli to modulate the self-assembly of catalytic peptide nano-assemblies. We used the knowledge of Ramachandran map, aromatic π-π interactions, stereochemistry, and unnatural

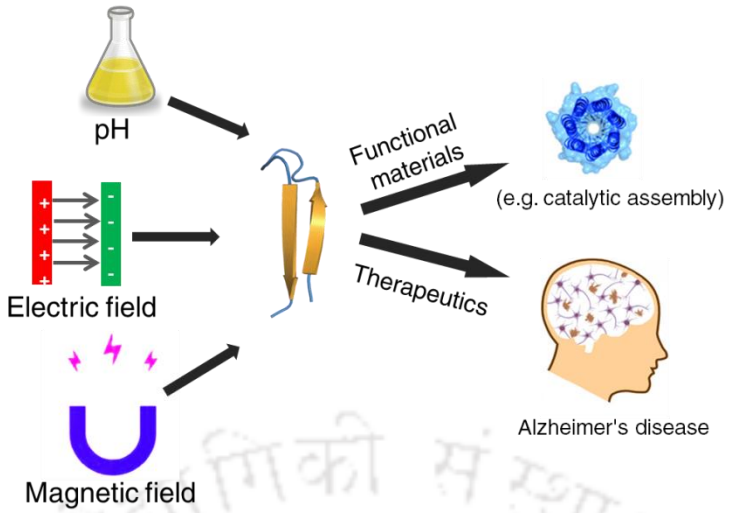

Figure 1.1. Schematic diagram representing the overall research approach, detailed in the thesis.

D-amino acids in the design of the biomimetic heterogeneous peptide catalysts. We further extended our study to test the effect of the electric and magnetic field on the aggregation propensity of the $A\beta_{1-42}$ peptide and its respective cytotoxicity, thus, paving the way for the development of a non-invasive treatment strategy against AD.

In chapter 3, we have designed a heterochiral self-assembling tripeptide catalyst by mimicking the 'histidine brace' active site of lytic polysaccharide monooxygenases (LPMO). At physiological pH, the complex has similar structural and functional features as in LPMO's active site. In chapter 4, we rationally designed a library of tri-peptides to understand the role of quadrupole interaction in peptide self-assembly. We studied the effect of a subtle change in the amino acid position and chirality on peptide's hydrogelation propensity and catalytic streoselectivity during C-C bond-forming Aldol reaction. Next, the modulatory effect of the electric field was tested during the self-assembly of the peptides in terms of the structure and function of the assemblies. Chapter 5 deals with investigating the role of external electric and magnetic fields on the aggregation kinetics of AD model peptide ($A\beta_{16-22}$) and its parent peptide $A\beta_{1-42}$. Also, cellular uptake and cytotoxicity assays were performed to verify any reduction in amyloid-elicited cell death by the electric field treated (EF) peptides.

In this thesis, efforts have been made to modulate the environment of the system during the peptide self-assembly process using various internal and external stimuli. From the translational perspective, it offers conceptual insights to design biomimetic peptide-based

functional materials that are responsive to an external stimulus such as electric field and pH. In addition to this, it postulates a scientific roadmap for futuristic non-invasive, therapeutic solutions for the treatment of Alzheimer's disease.

1.3. THESIS OBJECTIVES

The present study was designed to address the following objectives:

1. Verify the effect of peptide chain stereochemistry in modulating nano-assembly.

2. Design, synthesis and characterization of short peptide molecules and study their assembly at the nano-level.

3. Examine the modulatory effect of electric and magnetic fields on peptides, in the formation of functional nano-assemblies with an aim to catalyze C-C bond forming Aldol reaction.

4. Minimalistic design of lytic polysaccharide monooxygenases (LPMO).

5. Extend the effect of field response to therapeutically relevant peptide aggregates like $A\beta_{1-42}$ and KLVFFAE and their co-recognition motif, responsible for Alzheimer's disease.

2.

Stimulus Responsive Peptide Nano-assemblies

Self-assembling systems play an important role in physiological functions and are of great interest for applications in the field of biomedicine, energy, and catalysis. Over the years, peptides have immerged as a popular building block for synthesizing diverse self-assembled functional materials with unique properties. The process of peptide self-assembly is driven by thermodynamics; however, directing the self-assembly using various chemical and physical stimuli is a critical factor in structural modulation and function integration. This chapter is intended to provide an overview of peptide self-assembly and the influence of various external and internal modulators on their structure and functions.

2.1. INTRODUCTION

Self-assembly is a spontaneous bottom-up process.[13] It involves specific, local interactions among disordered pre-existing individual components to form a more organized structure or pattern. The bottom-up process starts with a stochastic and seminal step called nucleation that initiates the formation of ordered structures ranging from simple organic crystals to various macromolecules.[2] The process can be explained by a two-step nucleation model,[14] in which the first step is clustering of the solute and second step involves re-organization into ordered structures of nano or micro dimensions. The latter is the rate-limiting step as complex molecules in solution have a high degree of conformational freedom and need more time to arrange themselves into a regular crystalline lattice with minimum free energy.[15,16,17]

In the field of bio-nanotechnology, molecular self-assembly may lead to a diverse array of arrangements ranging from zero-dimensional lipid micelles and one-dimensional DNA double helices to two-dimensional lipid bilayers and three-dimensional complex protein structures.[18] Nucleic acids such as DNA, undergo self-assembly by a simple 'interaction with spatial periodicity' mechanism as seen in the DNA double helix to form functional supramolecular architectures, with great predictability and consistency.[19] Although DNA and lipid-based nanostructures are promising candidates in bio-nanotechnology, they lack the advantage of the functionality and higher-order complexity of 3D structures, offered by proteins or peptides.

Peptides are attractive building blocks in bioorganic and supramolecular chemistry due to the diversity of amino acid sequences and their predictable conformational properties. In 1901, Emil Fischer and Ernest Fourneau synthesized the first synthetic peptide glycylglycine, a dipeptide, that marked the beginning of peptide chemistry.[5]

Peptides are short-chained biologically active molecules of amino acid subunits linked together by peptide bonds. A peptide bond is formed by joining the carboxyl group of one amino acid to the amino group of the subsequent one through a condensation reaction, resulting in the release of a water molecule. The linear sequence of amino acids is termed as the primary structure of the peptide. The secondary structure of the peptide is determined by its most energetically favored chain conformation directed by the combination of torsion angle φ and ψ of the peptide backbone. The major secondary structures are α-helices and β-structures.[20]

2.2. SELF ASSEMBLY OF PEPTIDES

Zhang et al. in 1993 reported the first self-assembling peptide n-AEAEAKAKAEAEAKAK-c (EAK16) from a DNA binding yeast protein called 'zuotin' while trying to understand a left-handed Z-DNA structure.[21] Over the years, material scientists have used the design rules established by the peptide community to develop controlled molecules that can self-assemble into functional nanomaterials.[22, 23] Two general approaches have been used. Firstly, biomimicry of the natural motifs, where the designed peptide sequence is based on the understanding of the functional motifs available in nature. This approach allows researchers to overcome the difficulties in synthesizing protein-based complex biomolecules by developing bioinspired minimalistic designs, using short peptide sequences that self-assembles, through non-covalent interactions into hierarchical structures.[24] The second approach involves *de-novo* designs of nanostructures based on the understanding of the chemistry of the amino acid residues. The rich chemical diversity generates various interactions between the amino acid residues resulting in complex assemblies. Besides, peptide offers many attractive advantages, such as inherent biological origin, structural programmability, good biocompatibility, biodegradability, low immunogenicity, versatile functionality and cost-effectiveness.[25, 26] Self-assembling short peptides is guided by intermolecular interactions to generate well-defined nanostructures including nanospheres, nanosheets, nanotubes, and nanofibers.[26, 27] The interplay of various non-covalent interactions such as hydrogen bond, electrostatic interactions, van der Waals interactions, hydrophobic interaction, and π-π stacking pre-dominantly facilitates the molecular arrangements, wherein each type of interactions has its specific role.[2] These forces are weak individually, but in synergy, can generate stable and ordered assemblies (Figure 2.1f).

2.2.1. π-π interactions in peptide self–assembly. The π–π stacking interaction is mediated by the attraction between the electron-rich and electron-deficient π-surfaces of large π-conjugated systems.[28] The interactions of π–π stacking can drive the directional growth in water, because of the limited solubility of the participating aromatic groups. Infact, π–π stacking interaction is approximately 10X stronger in water compared to any organic solvent.[29] However, recent studies also reported π–π stacking as a distinct driving force in pure organic solvents, such as toluene.[30]

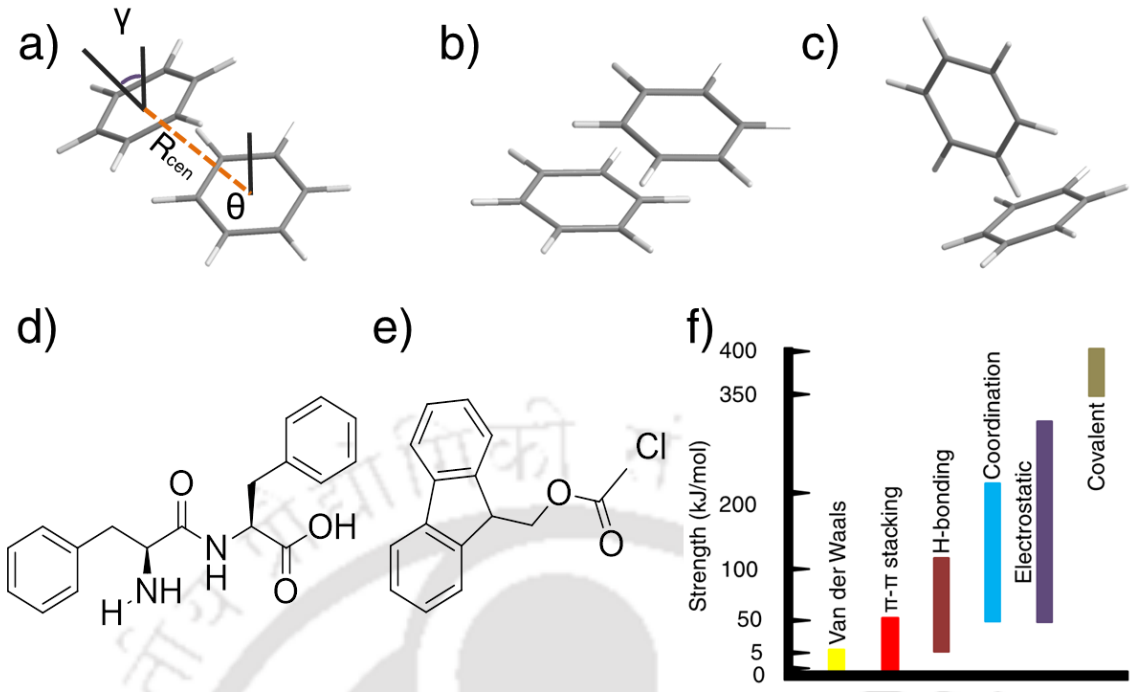

Figure 2.1. The geometry of the π-π interactions between aromatic systems. a) Two angles and a distance are defined; where the angle θ is between the plane normal of one ring and the inter-centroid vector R_{cen}, and γ being the angle between the plane normal. b) A representative favorable parallel displaced interaction classified by - 20◦< θ< 50◦, γ<30◦. c) T-shaped edge-to-face geometry classified by 60◦<θ and γ<90◦. Adapted from ref [1]d) Structure of the diphenylalanine motif e) Structure of the Fmoc- protecting group f)Non-covalent interactions governing peptide self-assembly with their respective strengths.

The two most preferred geometries of π–π interactions for stable conformations are the parallel displaced and T-shaped (Figure 2.1a-c). Both the geometries are isoenergetic and experimentally bound by 8–12 kJ/mol (2–3 kcal/mol) with a separation of 4.96 Å. Several studies have reported peptide self-assembly driven by π-π stacking interactions. Gazit's group has demonstrated the ability of the two residues long FF peptide to assemble into various nanostructures by π-stacking interactions(Figure 2.1d).[27, 31,32] They first identified this motif by employing a reductionist approach in the core of the Aβ peptide responsible for Alzheimer's disease.[32] The discovery of the "Phe-Phe motif" has revolutionized the field of short peptide-based nano-technology with research reports spanning from chemical and material research to biomedical applications.[33, 34] The incorporation of fluorenylmethoxycarbonyl (Fmoc) group further enhances the π-stacking interactions among themselves, thus playing a vital role in the self-assembly of otherwise non-aggregating peptides (Figure 2e).[33, 35, 36,37] Fmoc peptide gels

have been reported to have applications in different fields such as cell culture,[36] catalysis, and drug delivery.[38-41]

2.2.2. Peptide self-assembly in misfolding diseases. Recent studies suggest that several neurodegenerative diseases, such as Alzheimer's disease (AD), Parkinson's disease (PD), Huntington's disease (HD), amyotrophic lateral sclerosis (ALS), and prion diseases, have a similar molecular mechanism that involves protein aggregation.[42, 43] The aggregates usually contain fibers that are made up of truncated peptides with a β-sheet conformation called "amyloid."[42] Further studies of these amyloid fibrils revealed the role of aromatic residues in directing the self-assembly of the peptides into ordered fibrils.[27] The fibrillation process is characterized by a sigmoidal kinetics, consisting of a lag phase, a log phase, and a saturation phase (Figure 2.2).[44, 45] Nucleation starts in the lag phase and is also the rate-limiting stage of the process. This is followed by the log phase, which involves exponential addition of monomers to the growing protofibrils. The saturation phase corresponds to the addition of protofibrils to form a matured fibril. Under *in vitro* conditions, such peptides fibrillate at the

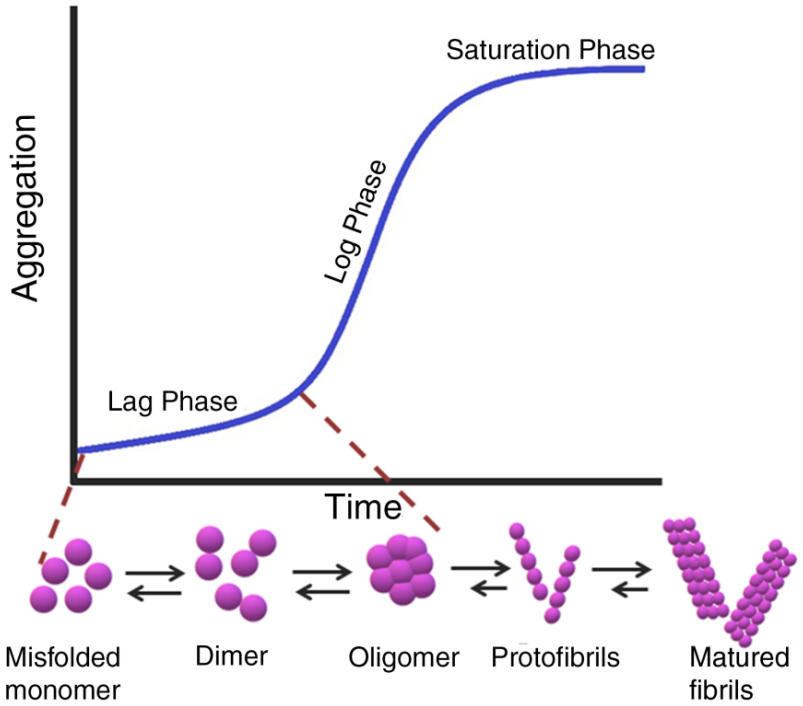

Figure 2.2: Schematic representation of the self-assembly during amyloid formation.[46]

Table 2.1. Some of the important self-assembling sequences and their parent proteins responsible for various protein aggregation diseases.

Aggregation prone motif	Parent peptide/protein	Disease	Ref
KLVFFA	β-amyloid	Alzheimer's Disease	47, 48
GAIIGL	β-amyloid		
MVGGVVIA	β-amyloid		
NKGAII	β-amyloid		
AIIGLM	β-amyloid		
GGVVIA	β-amyloid		
VQIVYK	Tau Protein		
GNNQQNY	Yeast prion sup-35	Prion diseases	47, 48
SNQNNF	Prion protein		
MMHFGN	Human Prion		
SNQNNF	Human prion		
GYMLGS	Human Prion		
NNQNTF	Elk Prion		
GAVVTGVTAVA	α-synuclein	Parkinson's disease	49,50
consensus KTKEGV repeats	α-synuclein		
SSTNVG	Islet amyloid polypeptide	Type II diabetes	47,48
LVEALYL	Insulin		
HSSNNF	Islet amyloid polypeptide		
VEALYL	Human insulin		

timescales of tens of minutes for islet amyloid polypeptide (IAPP) to days for Aβ and α-synuclein peptides. It is suggested that the amyloid state represents the thermodynamically most favorable state, even compared to native proteins.[51] The aggregation-prone stretches in the parent amyloidogenic peptide are listed in Table 2.1.

2.3. THERMODYNAMIC AND KINETIC CONTROL OF PEPTIDE SELF-ASSEMBLY

Peptide assembly is a spontaneous thermodynamically driven process.[17] The synergistic effect of different non-covalent interactions, including hydrogen-bonding, π–π stacking, electrostatic, hydrophobic, and van der Waals interactions, determine the thermodynamic stability of the nanostructures formed.[17] In general, the focus of a thermodynamic control is in two points: (a) forces governing or driving self-assembly; and (b) free energy of the assembly.[8, 16, 17] On the other hand, kinetic control is also a critical factor in structural modulation and functional integration.[52] The studies on the kinetics of self-assembly have two important aspects: (a) structural regulation by kinetics; and (b) kinetic nucleation and growth processes.[17] It can disrupt the fine-balance of the driving forces that were originally present in the system, thus, generating a kinetically trapped state, e.g., fibers or gels (Figure 2.3). Kinetic control may also affect the time scale of the rate-limiting nucleation steps during assembly. [17,18] The principle of entropy maximization suggests that fast nucleation induces an increase in the local concentration of the participating entities, which in turn determines the extent of modulation by an external stimulus.[53-55] This can be exploited in the case of fibrillating peptides such as amyloids and may have therapeutic implications.[56]

2.3.1. Factors affecting self-assembly kinetics. The use of stimuli to control bottom-up fabrication has long been considered a powerful means for tailoring the mechanical, optical, or electronic properties of the materials.[57] More recently, the potential application of a stimulus to direct peptide self-assembly has been explored to develop novel functional nanostructures (Figure 2.4). Stimuli may either be of chemical or physical origin. Amino acid sequence, chirality and pH belong to the class of chemical stimuli and temperature, ultrasound, electric and magnetic fields are physical stimuli that can potentially modulate self-assembly.

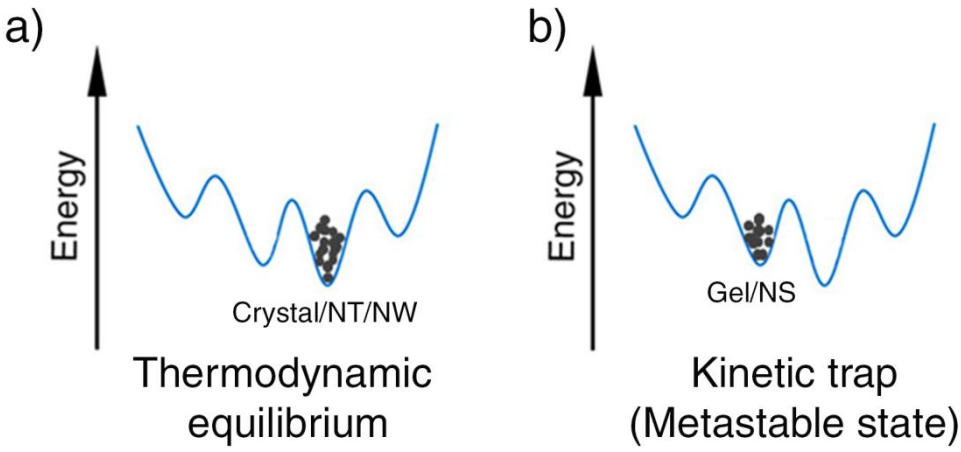

Figure 2.3: Schematic representation of the self-assembly pathways under thermodynamic and kinetic control. a) The thermodynamic control results in structures (e.g., crystal, nanotube(NT), and nanowire(NW)) that corresponds to a free energy minimum; b)The intervention of kinetic control such as temperature, pH, and external field that directs the structures to a metastable state (e.g., gels or nanosphere (NS)). Under certain kinetic control, these structures may inter-convert to the state of minimum free energy. Adapted from ref [58].

2.3.1.1. Amino acid sequence and chirality. The pattern of the amino acid sequences influence the self-assembling propensity and the morphology, even when the net hydrophobicity or charge of the related peptides are conserved.[59] Subtle molecular variations in the minimalistic building blocks may lead to macroscopic differences in the self-assembled system and its function. In general, amphipathic peptides containing alternating hydrophobic and hydrophilic amino acid residues have an increased propensity to self-assemble forming amyloid-like β-sheet fibrils.[60-62] For example, the β-sheet fibrils formed by alternating $(XZXZ)_n$ patterned peptides, where X is a nonpolar and Z is a polar residue, lead to the emergence of various interesting properties.[63] Other approaches include exploiting the aromatic π-π interaction or electrostatic interactions between positively and negatively charged groups in the sequence.[17, 64, 65]

The incorporation of D-amino acids in the sequence by carefully exploring the possibilities of Ramachandran plot may lead to a divergent path for assembly. [66-69] Heterochiral sequences generated by the combination of both D- and L- amino acids may be a promising strategy for building supramolecular architectures, especially when their homochiral analogs do not self-

assemble. Such sequences have proven to be more resistant to enzymatic hydrolysis.[67, 68,70] The first key observation on the structural role played by a single D-amino acid dates back to almost 20 years. The authors reported the stabilizing effect of a single D-proline in a heterochiral type II' turn which was absent in the homochiral analog.[71] Ghadiri and co-workers, in 1993, reported peptide nanotubes using D, L-α-peptides bearing 1, 4, 5, 8-naphthalene tetracarboxylic acid di-imide (NDI) side chains with charge transfer ability.[72] Previously, our lab has reported the role of peptide sequence stereochemistry in controlling peptide self-assembly[73] and designing therapeutic peptides that are immune to proteolytic cleavage.[74-78] D-amino acids have been found to promote β-sheet formation in dilute solutions of concentrations at which other peptides do not fold, suggesting a stabilizing effect played by the amino acid sequence bearing the D-residues.[79] Gracia et al. have reported a series of heterochiral hydrophobic tripeptides ^{L}Phe-^{D}Xaa-^{L}Phe, where ^{D}Xaa is an aliphatic D-amino acid, that could overcome the steric hindrance present in their homochiral analogs to form stable hydrogels.[68] Interestingly, heterochiral analogs bearing a D-amino acid at the *N*-terminus of the sequences Val-Phe-Phe, Phe-Phe-Val, and Leu-Phe-Phe show faster hydrogelation while the homochiral analogs do not form gel.[80, 81]All these studies suggest that peptide chirality is a versatile tool for directing peptide self-assembly into desired structures. Table A1.1. in Appendix 1 shows various amino acid abbreviation systems.

2.3.1.2. pH. The addition acid or base can rapidly lead to significant shift in the system's pH, and can drastically affect the self-assembly process. The pH-triggered self-assembling systems have found potential applications in drug delivery systems,[82] scaffold design,[83] tissue engineering,[84], and biosensing.[85] It strongly influences the intra- and inter-molecular hydrogen bonding interactions present in the system. A plethora of pH-responsive peptides have been reported to undergo structural transitions ranging from α-helix to β-sheet, at different pH levels.[57, 86, 87] By rationally positioning Glu or Orn side chains in an eleven residue peptide, Aggeli et al. could generate diverse reversible nano assemblies such as β-sheet tapes, ribbons, fibrils, and fibers with small changes in pH.[88] A pH-triggered self-assembly is largely dependent on the reversible protonation and deprotonation of the acidic and basic residues in the sequence. However, pH might also affect the intensity and strength of the hydrogen bonds between the sequence and the surrounding water molecules.[89]

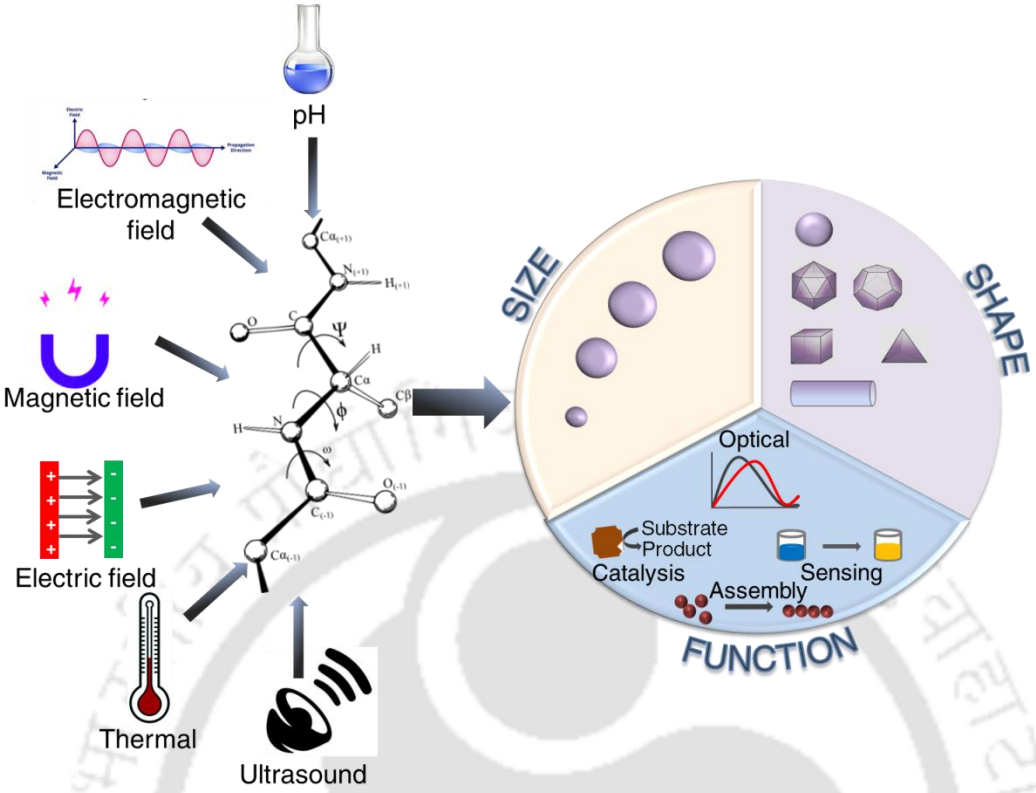

Figure 2.4. External stimuli dictating the size, shape, and function of peptide nano-assemblies.

2.3.1.3. Metal ions. Coordination between the metal ion and different functional groups can be exploited to introduce special reactivity or construct nanostructures in short peptides. The generation of peptidyl motifs designed to bind metal ions emphasize the importance of tuning the metal binding affinity of such constructs.[90] A pre-requisite for designing a metal peptide complex is to incorporate metal-binding residues in the sequence, specific to a metal ion. Usually, histidine, cysteine, tryptophan, and glutamic acid residues serve as metal-binding sites in peptides.[90, 91] The metal-binding sites of naturally occurring metalloproteins frequently possess these residues in multiple numbers to achieve the high selectivity to the metal ion. Understandably, incorporating more than one metal-ligating amino acid in the designed construct by placing the coordinating side-chain functionalities in close proximity could enhance its affinity and selectivity. Molecular modelling studies suggest that type II turn-forming short peptides with at least two metal-binding amino acids place the metal coordinating moieties in the same face of the motif and in close proximity.[92-95] Therefore, the

metal binding affinity of the peptide can be varied by changing the extent of structural pre-organization of the motif.

The metal-ligand coordination can be either intramolecular or intermolecular. In intermolecular coordination, the metal ions act as a linker between peptides[90, 96, 97] and conjugate through another binding motif to direct the molecular conformation and assembled structure.[98] For example, Lee et al. developed peptide nano-fibers from the GNNQQNY–NH_2 sequence in the presence of divalent metal ions that readily dissolve when a metal chelating agent like EDTA breaks the coordination.[99] In addition to the natural metal-binding ligands, chemists have developed a series of artificial variants such as nitrilotriacetic acid, pyridine, bipyridine, and terpyridine that are more robust and can promote structural changes in the peptide self-assembly.[100] Such metal ion triggered structures have found diverse utilities such as gas storage and separation,[101] sensors,[102] biomedical applications,[103, 104] and catalysis.[105]

2.3.1.4. Temperature. Temperature can alter the hydrogen bonding and hydrophobic interactions in the system.[17] Hydrogen bonding is a major force behind peptide folding; therefore, peptides are inherently sensitive to any change in temperature. This makes temperature a powerful external stimulus to trigger a change in the peptide conformation. Elevated temperature can be used as a tool to re-constitute hydrogen-bonding patterns, due to which α-Helix to β-sheet transitions are often temperature-triggered.[106] Working on this front, Chen et al. documented thermo-responsive PEGylated poly-L-glutamate showing tunable lower critical solution temperature (LCST) behavior.[107] Temperature has been reported to have a diverse response in both natural and synthetic peptides. Some of them include changing the peptide chirality,[108] control hydrogel formation,[109] trigger micelles formation[110], and induce molecular rearrangements in the peptide crystal structure.[111] In particular, thermo-responsive hydrogels capable of undergoing reversible sol-gel transition are widely considered useful for biomedical applications as an injectable hydrogel for drug delivery.[112-115] Ryu et al. used high temperature to grow vertically aligned nanowires in aniline vapor on a silica.[116] The progresses in research over the years have put temperature as one of the most potential modulators of peptide self-assembly.

2.3.1.5. Ultrasound. The use of ultrasound of varying frequency, provides substantial and largely unexplored opportunities to provide mechanical energy to direct transient

nanostructure formation.[117] The high-frequency oscillating pressure waves are long proven to overcome kinetic barriers associated with dissolution, assembly and gelation by disrupting the weak non-covalent interactions.[118, 119] Recent findings suggest that such high oscillating pressure waves can be exploited to temporarily modulate the interplay between hydrophobic or H-bonding interactions in peptides.[117, 120] The energy of ultrasonic vibrations (>1 MHz) leads to the generation of microscopic velocity gradient or radiation pressure in anisotropic macromolecules in solution, thus, directing them to align to the field, e.g., aligned peptide hydrogel.[121, 122] Ultrasound has also been reported as a promising stimulus to induce gelation of low molecular weight gelators (LMWGs). In 2005, independent works of two different research groups of Naota and Zhang, for the first time, demonstrated sonication-induced gelation in hydrogen-bonded gelators.[123,124] Aligned patterns of self-assembled peptide amphiphile nano-fibres were produced by sonication-assisted solution embossing.[125] Pappas et al. demonstrated sonication-induced assembly with an aligned tripeptide (FFD and FFI) that forms anisotropic organogels and hydrogels.[120] More recently, ultrasound has been reported to cause rheology switching and conformational changes in short peptides.[126, 127] Ultrasonic irradiation may cause reversible molecular rearrangement of supramolecular nanostructures by generating local high temperatures and high pressure. Fmoc-FF peptide derivatives have been shown to sequentially convert the nano-assembly from thin nano-sheets to long and thick nano-belts but revert to the original state when the source of ultrasound is switched off.[128] They attributed it to the altered balance between H-bonding and π-stacking among the sequences that changed the chiral organization of the peptide building blocks in the presence of the stimulus. Fmoc peptides are found to be more responsive to ultrasound-stimulus owing to their extensive π-π stacking.[128]

2.3.1.6. Magnetic field. There are research reports suggesting that high static magnetic fields can drastically affect DNA synthesis, orientation of microtubule as well as zygote division.[129, 130] Although the effects of high magnetic field strength have been repeatedly demonstrated on some biological samples, it has not been adopted in a device. This directly impedes our understanding of the effect of an external MF during self-assembly. Surprisingly, peptide microfibers exhibit strong diamagnetism.[131, 132] This can be attributed to the alignment of electrons in the peptide bonds between amino acids or to the aromatic electron currents. Additionally, theoretical studies suggest that a magnetic field can modulate the number of

hydrogen bonds between the peptide and surrounding water and promotes clustering.[133] In an interesting investigation, Yang and colleagues, measured the force exerted by peptide-containing liquids placed in a static magnetic field.[134] Using AYFFF peptide, with a high percentage of aromatic groups, they found that the samples allowed to assemble in the presence of a magnetic field had at least eleven times more diamagnetic susceptibility than the control. They concluded that the electron dynamics of the aromatic rings, rather than the peptide bonds, are responsible for strong diamagnetism in peptides. The external magnetic field could also induce the formation of aligned aromatic peptide nanotubes, regardless of the presence of a ferrofluid.[132] This mainly originates from the well-ordered stacking of aromatic rings in the peptide nanotube, given that the aromatic rings have a large diamagnetic anisotropy.[132, 135-137] Studies on the fiber-forming GANPNAAG peptide showed aligned structures in the presence of a strong magnetic field.[138]

2.3.1.7. Electromagnetic field. Polypeptides sensitive to electromagnetic fields have been proposed for various applications such as nano-electronics, biomedicine, and ecology.[139] Incorporation of photochromic molecules like azobenzene,[140, 141] 2-nitrobenzyl group[142], etc. in the peptide sequence makes them responsive to photons which in turn regulates the conformation of the peptide backbone to achieve programmed self-assembly. By incorporating a photo-responsive ruthenium (II) complex $\{[Ru(bpy)_3]^{2+}\}$, Son et al. showed dissociation of β-sheet-rich Aβ aggregate under illuminating white light-emitting diode light into small, nontoxic fragments.[143] In another study, photo-switchable sulfonic-azobenzene 4-[(4-ethoxy) phenylazo] benzenesulfonic acid (EPABS) resulted in the reversible structural transition of cationic diphenylalanine peptide H-Phe-Phe-NH_2·HCl molecules.[144] Photosensitive moieties such as 6-nitroveratryloxycarbonyl-diphenylalanine(Nvoc) in gelating peptide sequences have been reported to form light-responsive peptide hydrogels capable of controlled drug release.[145] Typically, the photochromatic chromophores undergo a photoreaction such as isomerization, dimerization, or cleavage, resulting in the dissociation of polymeric structure.[146] Alternatively, dimerization or polymerization can result in the robustness of the gel, thus altering the permeability behaviour.[147] While photo stimulus is a promising strategy in modulating peptide self-assembly, there are few drawbacks as well. Its low penetration due to scattering and UV light-induced damage to the peptide chain restricts its application significantly. Microwave, on the other hand, has a low oscillation frequency with a power of approximately 10 kW that can

reach deep inside the system. These physical features can cause remarkable structural changes to target peptide molecules.[148, 149] Some of the exciting reports on stimulus-responsive peptide-based materials are summarized in Table 2.2.

Table 2.2.: Effect of different external stimuli on peptide self-assembly.

Stimulus	Motif/Peptide sequence	Source	Transition	Ref
Temperature	ADADADADARARARAR	Designed	β-sheet → α-helix	150, 151
	SIRELEARIRELELRIG	Designed	α-helix → β-sheet	152
	YGCVAALETKIAALE TKKAALETKIAALC	Designed	α-helix→ β-sheet	153
	VPGXG	Elastin	Disordered → β -turn	154, 155
	H^DF^DF	Designed	β-sheet → α-helix	156
	VKVKVKTKVPPTKVKTKVKV	Designed	Disordered → β -hairpin	115
Electromagnetic field	MAX7CNB	Designed	Disordered → β -hairpin	142
	RGDS	Designed	Increased β-sheet structure	157
	Aβ peptides	Natural	Decrease in fibrillation	143
	Nvoc-FF	Designed	Disordered → β-sheet	145
	PNBL-b-PLL	Designed	Sol-Gel Transition	128
	Fmoc-Phe-pazoDbg	Designed	Sol-Gel Transition	158

Stimulus	Motif/Peptide sequence	Source	Transition	Ref
Ultrasound	TTR108–111	Designed	β-sheet→ Disordered	159
	Boc-L-Phe-L-Lys(Z)-OMe (Z=carbobenzyloxy)	Designed	Disordered→ α-helix	160
	Tripodal peptide	Designed	Disordered → β-sheet	161
	Fmoc-FL Fmoc-YL	Designed	β-sheet→ Disordered	117
	Fmoc-l-Lys(Fmoc)-OH, Fmoc-l-Lys(Boc)-OH, OMe-l-Glu(OMe)•HCl and OtBu-l-Glu-(OMe)•HCl	Designed	Disordered → β-sheet	128
Magnetic field	SNNFGAILSS (human amylin(20–29)	Natural	β-sheet→ Disordered	133
	FF	Designed	Alignment	132
	Lysozyme	Natural	Alignment	162
	BocNH-ACPC$_6$-OH	Designed	Alignment	131
	NapFF	Designed	Alignment	163

2.3.1.8. Electric field. Electric field can direct peptide self-assembly through induced interactions.[164, 165] It exploits the mismatched dielectric properties of the peptide molecule that are polarized in an electric field. As a result, a strong anisotropic dipole-dipole interaction is generated between the molecules. Such interactions can overcome the inherent Brownian motion and align to the applied field once they attain threshold strength. The asymmetrically charged molecules repel and attract like-charged and oppositely charged regions of a peptide

respectively, thus directing the molecules in a particular orientation.[164, 165] Although the mechanism of electric field effects is not completely understood, it is believed that fields of specific frequency and intensity can excite certain vibrational modes of a macromolecule, which alters its conformation. Martin et al. used variations in solution pH and electric field strength, to orient a designed peptide to develop a functionalized surface.[165] Peptide is reported to have an inherent piezoelectric property based on their chemical composition and crystal structure. Liquid crystalline diphenylalanine peptide nanowires were aligned in an electric field generated by two oppositely charged electrodes mounted on a glass slide.[166] Velichko et al. investigated the effect of electric fields during the dynamic self-assembly of a negatively charged polyelectrolyte and a positively charged amphiphilic peptide in forming an ordered membrane in water. They have observed a direct correlation between the membrane thickness and stiffness with the strength and orientation of the applied field.[167] A uniform electric field between two parallel aluminium plates resulted in an oriented growth of FF peptide micro-rod array, and was subsequently used for nanogenerator fabrication.[168] The effect of the external electric field has been demonstrated on the alignment of silk fibers that induce electric dipole along the nanofibers. The fibrils formed hierarchical anisotropic structures due to their electrostatic interactions.[169] In addition, electroporation is a promising technique that can deliver specifically designed therapeutic peptide molecules into cells through direct permeation.[170-172]

Various theoretical studies regarding the intermolecular interaction of π- systems governing the self-assembly of peptide nanomaterials have emerged in last two decades.[173,174] Interestingly, π-electrons are prone to polarization in the presence of external electric fields. Application of adequate field strength must change their electrostatic and dispersive contributions to the non-covalent interactions. This may lead to the generation of field-induced anisotropy on the system, which modulates the molecular conformation of the peptides.[175] Tan et al. have reported electric field mediated non-reversible transition from *β*-sheet to a mixture of *α*-helical and *β*-sheet conformations of two amphiphilic peptides in solutions.[176] Previously, Yu et al. demonstrated the structural transition from random coil to β-sheet in V_6K peptides in the presence of an electric field.[177] List of reports, both theoretical and experimental, on the modulatory effect of external electric field on the peptide self-assembly are compiled and presented in Table 2.3.

Table 2.3.: Effect of external electric field of peptide self-assembly.

	Motif/Peptide sequence	Source	Transition	Ref
Theoretical Studies	FF	Designed	Disordered → ordered	164
	Insulin	Natural	β-sheet→ Disordered	56
	Aβ(16–42)	Natural	β-sheet→ Disordered	178
	Bovine Serum Albumin (BSA) and Lysozyme	Natural	β-sheet→ Disordered	179
	Gliadin protein	Natural	N/A, reduced H-bonding	180
	Prions	Natural	β-sheet → α-helix	181
	Aβ (29-42)	Natural	β-sheet → α-helix	182
	$A\beta_{1-42}$	Natural	β-sheet → α-helix	183, 184
	$A\beta_{29-42}$	Natural	β-sheet → α-helix	185
	1BBL protein	Natural	α-helix → Disordered	186
Experimental observations	FF	Designed	β-sheet → Disordered	187
	FF	Designed	Alignment	188, 189
	Human islet amyloid polypeptides (hIAPP37)	Natural	β-sheet → α-helix	190
	PBLGSS	Designed	Disordered → α-helix	191
	Human Serum Albumin(HSA)	Natural	β-sheet → α-helix	192

	Motif/Peptide sequence	Source	Transition	Ref
Experimental observations	Ac-VQIVYK-am Ac-VQIINK-am	Natural	β-sheet → Disordered	[193]
	Elastin protein	Natural	β-sheet → α-helix	[194]

2.3.2. External stimuli as a therapeutic option in treating protein misfolding diseases. The ability to modulate the conformation of a large protein molecule using an external stimuli is one of the most fascinating developments in molecular self-assembly. It harbors the potential to modulate and treat different protein misfolding disorders and diseases such as Alzheimer's disease, Parkinson's disease among others. Such non-invasive stimuli can even alter the blood-brain barrier (BBB) and help to deliver drugs that are otherwise difficult to reach areas of the brain. The evolution of non-invasive stimuli is emerging as an alternative or complementary adjuvant therapeutic strategy for protein misfolding diseases.[195] Some of the effective stimuli are the following.

2.3.2.1. Ultrasound: Transcranial Focused Ultrasound (FUS) application has been reported to significantly reduce the amyloid plaque burden in the AD mouse model within days of treatment.[196-199] It promotes the delivery of therapeutic agents by temporarily increasing the BBB permeability. The acoustic pressures used to open BBB are magnitudes lower than those used for ablation studies.[200] The results of using ultrasound as a therapeutic tool are promising but need to be systematized for use in humans.

2.3.2.2. Light. Recent progress in optogenetics, a technology to control a specific neural activity in the brain circuit using light,[201] facilitates the delivery of light to the targeted areas in the brain. Martorell et al. reported a 50% decline in insoluble Aβ load in the cortex of an AD transgenic mouse model, after one-hour exposure to a 40 Hz non-invasive light stimulation each day for seven days. A similar study by Ismail et al. using 40 Hz light flicker stimulation showed reduced cortical Aβ load in model mice.[202] The photo treatment of Aβ aggregates tagged with xanthene dyes has suppressed the conformational transition of Aβ monomers into

β-sheet-rich structures by interfering with the early steps of aggregation.[203] Park et al. showed dissociation of ruthenium (II) complex, tagged β-sheet-rich Aβ aggregates into nontoxic short fragments using visible light.[143] With these recent advancements, light-based modulation of peptide aggregation holds promise as an effective and broad-spectrum therapeutic strategy for protein misfolding diseases.

2.3.2.3. Magnetic field. Transcranial Magnetic Stimulation (TMS) is a non-invasive procedure that uses strong magnetic fields that can stimulate nerve cells in the brain and improves the symptoms of dementia.[204] A pulsed magnetic field creates current flow in the brain that can temporarily excite or inhibit specific areas. In another study, Gustavo et al. used a vortex magnetic field against Aβ aggregation and reported an 86% reduction in aggregate formation within 24h of field treatment.[205] They propose that the use of a vortex magnetic field reduces the side-effects associated with parallel magnetic field stimulation.

2.3.2.4. Electric field. Electric fields are receiving increased attention as a non-invasive therapeutic tool for various protein misfolding diseases. Based on a plethora of theoretical investigations (Table 2.4.), a handful of research groups have experimentally studied the effects of an external electric field (EF) on amyloidogenic peptides. Sen and Dasgupta have reported that oscillation induced by the application of AC field can aid the disintegration of preformed human serum albumin (HSA) fibrils.[192] More recently, studies with $A\beta_{1-42}$ peptide were recently reported with low EF strengths generated by vertical nanowire electrode array that meets the high-field limit for biological function.[206] Pandey et al., in an extended study, found that both AC and DC electric fields have a defibrillation effect on different amyloidogenic segments of Tau proteins.[193] In another study with hIAPP37 peptide, responsible for type 2 diabetes, the samples exposed to EF have shown an impressive 57% increase in the α-helix percentage compared to the control.[190] Zheng et al. reported defibrillation of aptamer treated $A\beta_{40}$ in the presence of EF to form stable $A\beta_{40}$ oligomers.[207] The evolution of new, non-invasive approaches is substantially more safe and cost-effective compared to standard treatments. Some of these approaches, such as ultrasound and electric field, demonstrate promising findings and proof of concept. However, it requires more experimental findings to test its efficacy before adapting to clinical use.

Table 2.4. List of theoretical reports on the effect of external electric field.

Peptide/protein	Disease	Transition	Ref
Insulin	Type II diabetes	β sheet →α helix	56
$A\beta_{1-42}$	Alzheimer's disease	β sheet →α helix	178
$A\beta_{1-42}$	Alzheimer's disease	β sheet →α helix	183
Insulin β chain	Diabetes	β sheet →α helix	208
$A\beta_{1-42}$	Alzheimer's disease	β sheet →α helix	184
$A\beta_{1-42}$	Alzheimer's disease	β sheet →α helix	181
$A\beta_{1-42}$	Alzheimer's disease	α helix → β sheet	209

2.4. PEPTIDE BASED ORGANOCATALYSTS

The rate of a reaction is governed by multiple parameters, of which frequency of collision of the reactants is the most predominant one.[210] Product formation occurs when the collision between the reacting molecules is sufficient to overcome a certain threshold energy called the activation energy (Ea) (Figure 2.5(red)). However, the collision involves reactants with random orientations, and therefore, E_a is formally the average energy barrier that must be overcome for product formation. The lower the E_a threshold of a reaction, the greater will be the proportion of successful collisions and faster will be the rate of reaction. The rate of a chemical reaction is given by Arrhenius's equation,

$$k = Ae^{-Ea/RT}$$

where, k is rate constant, A is frequency factor, e is mathematical quantity, Ea is activation energy, T is temperature, and R is gas constant.

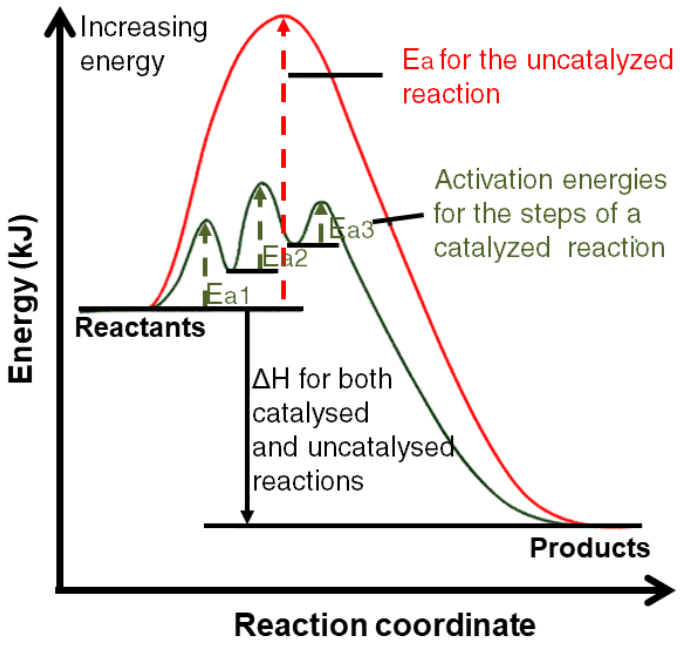

Figure 2.5. Comparison of the activation energies of a catalytic (E_a 1-3, olive) and non-catalytic (Ea, red) reactions. The energy *vs* reaction coordinate diagram showing a two-step enzyme-catalyzed reaction, having two catalytic intermediates and three transition states.

Catalysis is the process of increasing the reaction rate by adding a substance called a catalyst. A catalyst provides a new route to the chemical reaction with lower E_a without getting effectively consumed during the reaction (Figure 2.5(olive)). This is achieved by a) orienting the reacting particles to promote successful collision and b) by binding the reactant to form an intermediate complex with the lower activation energy. The intermediate complex is also referred to as the activated complex. The characteristics of a catalytic reaction are the turnover frequency (TOF) and the turnover number (TON). The TOF is the number of rotations of the catalytic cycle per unit time.[211] It is calculated as the number of molecules converted per active site with respect to time,[212] and is given by,

$$TOF = \frac{NAv}{S} \cdot \frac{dNi}{dt}$$

where, dNi/dt is the differential concentration change of i with time, NAv is Avogadro's number, and S is the number of active sites.

The TON is a measure of catalyst stability and is highly sensitive to the reaction time considered. It is calculated as the number of catalytic cycles a site can perform until it is completely deactivated.[212] The TON is expressed as a function of the TOF,

$$TON = \int_0^\infty TOF(t)dt$$

2.4.1. Types of catalysts. Catalysts are broadly divided into homogeneous and heterogeneous, depending on the reaction phase. Homogeneous catalysts and the substrate are present in one phase, most often the liquid phase. They contain well-defined, single-site centers that can be prepared using organic synthesis and offers high activity with remarkable selectivity.[213] In addition, they extend the scope for fine-tuning and optimization through functionalization or subtle structure variations. However, homogeneous catalysts are not suitable to perform continuous flow reactions due to the high cost of separation and recovery. Besides, they have limited thermal stability up to <100 °C.[214]

In contrast, a heterogeneous catalyst and the substrate are in distinct phases, typically solid-liquid or solid-gas, respectively. They offer ease of separation from the reaction mixture and, therefore, can be recycled and reused until loss of catalytic activity. This makes them the ideal catalyst to perform continuous flow reactions amid robust conditions. Numerous reports also suggest that such catalysts can be reactivated to perform like fresh materials.[215] Heterogeneous catalysis lacks the degree of knowledge of the transformation at the molecular level and demands further research to reach activity and selectivity values similar to homogeneous ones. According to the heterogeneous catalyst theory, the entire surface of the solid catalyst is not responsible for catalyzing the reaction. Only specified locations called the 'active site' on the catalyst surface will effectively take part in the reaction.[216] The active site may be generated due to unsaturated functional groups resulting from the surface irregularities or atoms with inherent chemical properties that enable the interaction with the adsorbed reactant at atomic or molecular scale. In the case of porous catalysts, such as gel, the steps 1, 2, 6 and 7 (Figure 2.6) involving the diffusion and mass transfer determines the reaction rate irrespective of the number of the active site in the catalyst.

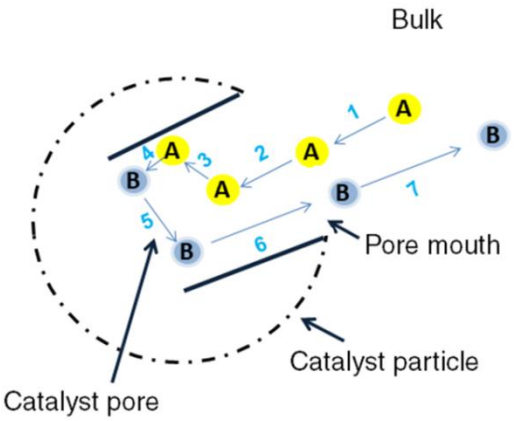

Figure2.6: Steps involved in a typical heterogeneous catalytic reaction. 1.Transportation of reactant (A) 2. Diffusion of the reactant (A) to the internal catalytic surface 3. Adsorption of reactant (A) on the catalytic surface 4. Surface reaction to produce (B) 5. Desorption of the product (B) from the catalytic surface 6. Diffusion of the product (B) to the pore mouth 7. Transfer of the product (B) to the bulk fluid. Steps 1,2,6, and 7 are the diffusion steps that determine the mass transfer, and step 3,4 and 5 are the adsorption and reaction steps in the reaction.[217]

However, in recent times, the frontiers between homogeneous and heterogeneous catalysis have been surpassed and becoming less defined. The development of various analytical techniques has allowed researchers to gain insight and characterize the catalytic sites of complex materials based on their composition, structure, and distribution of the catalytic sites. For example, it is now possible to synthesize heterogeneous catalysts with a single catalytic site that resembles a homogeneous catalyst.[218]

2.4.2. Enantioselectivity in catalytic reactions. Enantioselective catalysis is important for providing enantiomeric compounds to the pharmaceutical and agrochemical industries. Enantioselectivity in asymmetric reactions involves the preferential selection of one enantiomer over the other chiral product. Such reactions are mediated by chiral and non-racemic catalysts. The enantioselective C–H, C–C, C–O, and C–N bond formation have been extensively studied using asymmetric homogeneous catalysts.[219] However, they do not comply with the atom economy at the industrial level. On the other hand, stereochemical selectivity can be introduced in a heterogeneous catalyst to ensure that a chiral transition state is achieved.[220] The major disadvantage of heterogeneous catalysts, however, is the presence of an invariable range of active sites that makes it difficult to control the overall enantioselectivity.

2.4.3. Enzyme catalysis. Enzymes are enantiomerically pure, natural catalysts; responsible for conserving the chirality in living systems.[221] They catalyze the synthesis of a vast number of biomolecules and act as a model for energy-efficient, environmentally benign chemical agents. The enantioselectivity of an enzyme has been widely exploited in organic synthesis for synthesis of chiral products from achiral precursors. The industrial application of enzymes is restricted largely due to their instability in harsh conditions such as elevated temperature, pH, presence of organic solvents, and oxidative factors.[222] This has led to a new frontier in catalysis research called enzyme mimetics.

Enzyme mimics are artificial enzymes that have heralded much interest as a viable alternative to natural enzymes in terms of their functions. Besides, they offer additional advantages such as tunable structures, high stability, and lower cost of synthesis.[223] Enzyme mimics can be designed using two approaches; functional and structural. Functional mimics generally incorporates metal complexes with a similar activity of the natural enzyme, while structural mimics translate the enzyme's active site structure using functional moieties.[224] Till date, different types of enzyme mimics have been reported, ranging from nanoparticles to supramolecular structures.[223]

2.4.4. De-novo designs of supramolecular peptide catalysts. Supramolecular self-assembly of short peptides offers a minimalistic approach to mimic the functional properties of a multifaceted biocatalyst such as the active site or a hydrophobic pocket.[225] They have been utilized to assemble catalytic functional groups in a nano-environment that is adequate for efficient organic transformations. Micelles formed by amphiphilic peptides,[226] peptide-nanoparticle complexes,[227] and rigid-rod β-barrels,[228] are the most significant examples. Figure 2.7 shows different strategies used for designing supramolecular catalysts, using simple molecular building blocks.

The efficiency of their catalysis may be attributed to the combination of two factors; a) affinity to substrate binding and b) proximity effects of the catalytic moieties.[229] Recent studies also suggest catalytic efficiency in peptide-based nanotube and nanofiber structures.[230]

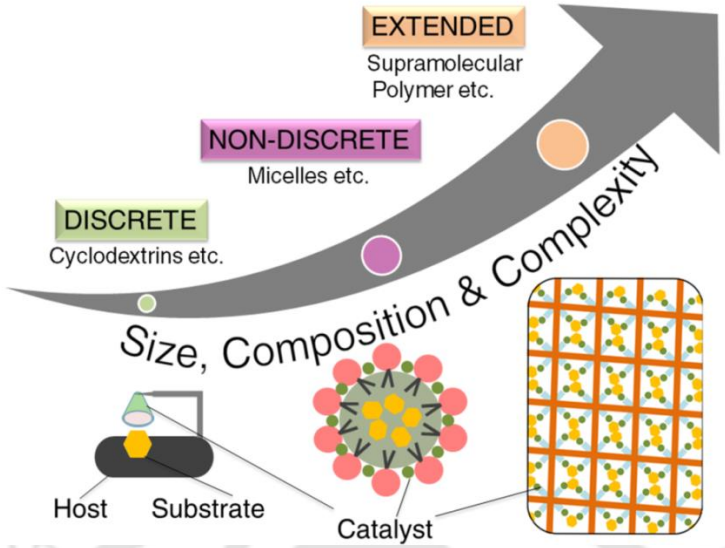

Figure 2.7. Different strategies for engineering a catalytic system using molecular building blocks through supramolecular chemistry and self-organization.

In the first report of supramolecular assembled peptide catalyst, Stupp et al., showed well-defined peptide-based catalytic nanostructures in aqueous media.[231] The ability to perform organic reactions in aqueous media motivated the designing of amphiphilic peptide molecules that formed hydrogels. Escuder and Miravet's groups have extensively studied the catalytic activity of L-proline-based supramolecular gelators in C-C bond forming reactions, such as Michael addition and aldol reactions.[232-234] Liu et al. have reported a Fmoc-tripeptide containing histidine as a catalytically active residue (Fmoc-FFH-$CONH_2$) that self-assembles at pH 7.5 to form nanotubes.[41] The nanotubes were able to catalyze the hydrolysis of *p*-nitrophenyl acetate (PNPA) in aqueous conditions.

While there are several reports on peptide-based supramolecular catalysts, the streoselectivity and efficiency of such systems is yet to match with that of an enzyme. The study of simple molecular systems, however, provides great insight into understanding the underlying catalytic mechanisms. Several parameters, such as temperature, solvent, and chirality, may affect the catalysis and must be considered in detail, with an aim to control the reaction performance by tuning the structure at the molecular or supramolecular level.

2.4.5. Biomimicry of the active site of a metalloenzyme. The active site of a metalloenzyme comprises of a metal complex where a transition metal monomer or dimer is coordinated by few amino acids.[235] Biomimicry of such active sites using designed peptides and metal ions is envisaged as a powerful strategy to create artificial catalysts. The complementary effect of a highly reactive metal ion and the peptide's structural and functional versatility can be translated into reactive and selective catalysts. Also, exploring this field provides information regarding the fundamental aspects of molecular recognition in catalysis, protein design, and protein folding.[236] The combination of peptides and metal catalysts has been used in several asymmetric transformations such as hydrosilylation,[237] allylic alkylation,[238] conjugate additions to enones,[239] and Strecker reaction.[240]

Artificial metalloenzymes (ArMs) are assembled using four design strategies (Figure 2.8).[241] The most common design of ArMs involves a scaffold peptide containing uniquely reactive nucleophilic residues (e.g., histidine) and a corresponding electrophilic reaction partner (e.g., Cu^{2+}, Fe^{2+}, Fe^{3+}). A reductionist approach has shown that ultra-short peptides (3-7 residues) can form a well-defined primary coordination sphere around the metal ion.[242]

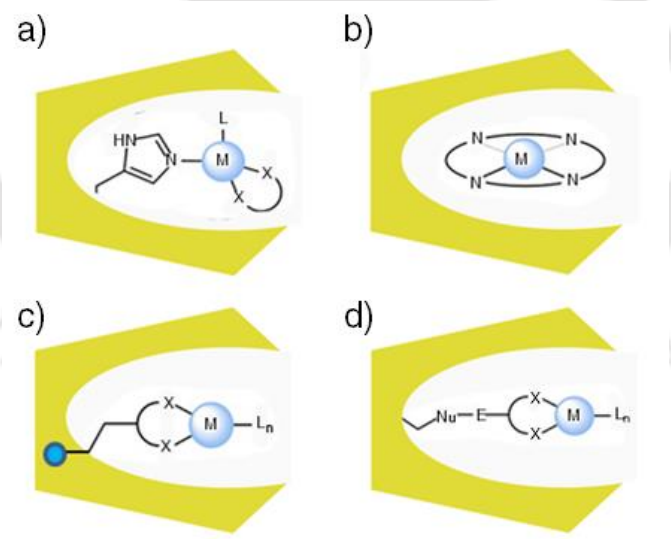

Figure 2.8. Four general approaches to artificial metalloenzyme assembly. (a) Nucleophilic residue positioned within a cavity may interact with the transition metal ion (b) Metal substitution approach, where another metal substitutes the metalloenzyme's native metal cofactor, thus conferring novel catalytic activity to the complex. (c) Supramolecular coordination through a high-affinity inhibitor embedded inside (d) Covalent immobilization due to reaction between the complementary functional groups present on the ligand and on the host peptide. Adapted from ref [243].

Kaiser's helichrome catalyst is among the earlier examples of synthetic metallo-peptide catalysts designed by covalently linking four 15-residue peptides to tetrahydroxysuccinamide esters through their N-terminus.[244] The design resulted in helix formation with a hydrophobic substrate-binding pocket. In another study, Dervan et al. reported a metallopeptide catalyst by rationally modifying a conserved fold with synthetic metal binding moiety.[245] The group also reported a Gly-Gly-His tripeptide based on the consensus sequence present in the copper-binding domain of serum albumin.[246] Sambasivan and Ball have convincingly demonstrated the potential application of the metallopeptides KADAALDAK for enantioselective catalysis upon binding to Rhodium (II).[247-249]

Few research groups have explored unnatural amino acids, including D-amino acids, to enable designs and functions beyond those accessible using natural amino acids.[250] Gilbertson et al.; demonstrated that it is even possible to design a non-helical secondary structure that specifically binds to the metal ion and performs catalysis. Using different turn-inducing motifs such as Pro-d-X, where d-X is a D- amino acid, they have constructed peptides containing Yyy-Pro-d-X-Zzz, where Yyy and Zzz are phosphoserine residues.[251, 252] The peptides showed excellent metal binding affinity and moderate catalytic efficiency. Pecoraro mimicked the active site of the carbonic anhydrase (CA) using three-helix bundles of TRI peptides with distinct metal binding sites for Hg(II) and Zn(II) that are facilitated by three histidine and three cysteine residues.[253]

While such developments are exciting, there is still room for improvement, particularly in the realm of chemical reactivity, where metallopeptides as catalysts are dwarfed by the sheer number of industrially important chemical reactions available to small-molecule catalysts.

3.

Minimalist *de novo* design of an artificial enzyme

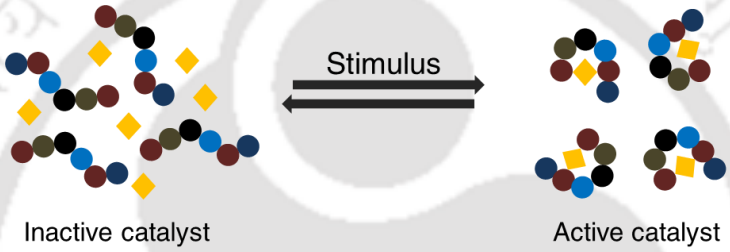

We employed a reductionist approach in designing the first heterochiral tripeptide that forms a robust heterogeneous short peptide catalyst similar to the 'histidine brace' active site of lytic polysaccharide monooxygenases. The histidine brace is a conserved divalent copper ion-binding motif that comprises two histidine side chains and an amino group to create the T-shaped 3N geometry at the reaction center. The geometry parameters, including a large twist angle (72°) between the two imidazole rings of the model complex are identical to those of native LPMOs (82°).The complex was synthesized and characterized as a structural and functional mimic of the histidine brace. UV-vis, vis-CD, Raman and EPR spectroscopic analysis suggests a distorted square pyramidal geometry with 3N coordination at pH 7. Solution and solid-state NMR results further confirm 3N coordination in the copper center of the complex. The complex is pH-dependent and could catalyze the oxidation of benzyl alcohol in water to benzaldehyde with yields up to 82% in 3h at pH 7 and above at 40°C. The catalyst achieved 100% selectivity for benzaldehyde compared to conventional copper catalysis. The design of such a minimalist building block for functional soft materials with a pH switch can be a stepping stone in addressing needs for a cleaner and sustainable future catalyst.

3.1. INTRODUCTION

Mimicry of the enzyme active site through supramolecular assembly has been of great interest for the design and synthesis of various novel catalysts.[254] Nature is a dominant source of inspiration in the area of supramolecular chemistry, and enzymes have served as natural prototypes for the design of supramolecular catalysts. In general, enzymes work by binding to their substrates and then use the action of two or more well-placed functional groups to achieve catalysis. Such an organization leads to substrate selectivity, reaction selectivity, and stereoselectivity. One way to achieve such natural enzyme-like-precision in catalysis is by mimicking the active site of an enzyme. Biomimetic modeling of enzymes involves the design of compounds containing similar functional groups mimicking a specific enzyme's active site.

Over the years, researchers have found that copper oxygenase enzymes possess His-Xaa-His chelating sequences at their active sites.[255, 256] In addition, they exhibit δN vs. εN tautomeric preferences in the imidazole group. Currently, efforts are directed towards trying to achieve a degree of control in the binding of transition metals in biologically common histidine-rich sites in a minimalistic construct. While histidine-containing linear peptides are reported as metalloenzyme mimetics with hydrolytic,[257, 258] and oxidative activities,[259-262] however, their metal ion environments are highly unstable. As a consequence, the metal-binding ability of such peptides is rather limited, which directly affects their catalytic efficiency. A survey of His imidazole group binding to copper proteins involved in redox chemistry, including O_2 reactivity, indicates that the His-Xaa-His (Xaa = amino acid) tripeptide motif is a frequently observed sequence. Some of the reported motifs include His-Thr-His in peptidylglycine α-hydroxylating monooxygenase (PHM)[263] and dopamine β-monooxygenase (DβM),[264] His-Val-His in superoxide dismutases 5,[265] and His-Gln-His in Amyloid-like protein 2.[266]

Over the last decade, the introduction of amino acids of both chirality in a peptide sequence has seen remarkable success in terms of novelty and creativity.[67, 267] Our laboratory, reported the advantages of using D-amino acid in the sequence, for the design of novel functional materials,[73] and enzymatically stable molecular constructs.[74, 76, 78] The ability to tune the metal binding affinity of small peptides through the incorporation of unnatural D- amino acids holds great promise in designing ultra-short peptide motifs resembling the active site of an enzyme. The peptides which are diastereomerically different offer the possibility of altering the spatial

orientation of amino acid side chains. This helps to modulate the local structure and interactions in the metal binding pockets, without altering the side-chain chemistry.

Lytic polysaccharide monooxygenases (LPMOs) are metalloenzymes that activate molecular oxygen and cleaves the C-H bond in polysaccharides.[268] They are attracting considerable attention due to their industrial applications.[269, 270] LPMOs utilize copper as their functional active site metal for oxidizing recalcitrant polysaccharides in nature. The LPMO domains usually comprise of 200–250 amino acids that drastically restrict their commercial application due to the excessive cost associated with their synthesis and stability at a range of temperature and pH. Interestingly, various spectroscopic and computational investigations have provided insights into the three-dimensional copper-containing active center featuring the 'histidine brace'.[268, 271 272 273] The histidine brace is conserved and comprised of a single divalent copper ion which is chelated with two nitrogen atoms of histidine at position 36 (one atom from the backbone and one from the side chain) and a nitrogen atom from a second histidine at position 135, forming an overall T-shaped 3N configuration.[268, 274] The main chain amino group of the N terminal histidine (His1) and imidazole side chain contributes two of its nitrogen while the second conserved histidine is the source of the third nitrogen.

Conventionally, the aerobic oxidation of C-H bonds is performed using reducing agents and radical initiators under severe conditions [6]. This study focuses on developing a peptide-based heterogeneous, environment-friendly, inexpensive molecular system with high catalytic efficiency. We have synthesized and characterized a *de-novo* designed heterochiral tripeptide redox enzyme system that mimics the structurally conserved histidine brace, found in LPMOs. The complex exhibits a very close chemical and structural resemblance to the active site geometry of the enzyme. It shows enhanced catalytic activity in the oxidation of benzyl alcohol in water. This heterochiral peptide design may be an example of a structurally and functionally optimized biomimetic model for LPMOs

3.2. EXPERIMENTAL SECTION

3.2.1. Materials. All reagents were of analytical grade and used without further purification. All the amino acids and resin were purchased from Novabiochem (Merck, Germany). Copper

chloride dihydrate ($CuCl_2.2H_2O$) was procured from Sigma Aldrich, India. All solutions were prepared in Milli-Q (18 MW) water.

3.2.2. Peptide synthesis. The peptide was synthesized manually by solid-phase peptide synthesis using Fmoc-chemistry on a Rink amide resin (0.74mmol/g, Novabiochem). The peptide was precipitated in cold ether and purified by reverse-phase HPLC (Make: Shimadzu Ltd, Japan), using an analytical C-18 column. The gradient elution of 100-10% acetonitrile in water with 0.1% TFA, at 0.5ml min^{-1} has been used. The HPLC chromatogram was recorded at 210nm for fraction collection. The molecular weight of the peptide was evaluated using HR-MS analysis. (Figure A2.1, Appendix 2)The peptide was stored at 4°C for further use.

3.2.3. Synthesis of Cu-HPh complex. Metal to ligand ratios was maintained at 0.9: 1(4.5mM $CuCl_2$:5mM HPh) to ensure total binding of Cu (II) to the peptide. The mixtures were stirred for 30 minutes at room temperature before UV–Vis absorption measurements. The precipitates were filtered through a 0.2-micron filter, washed several times with hexane to remove excess Cu (II), and dried in vacuum.

3.2.4. UV–vis. UV–vis absorption measurements in the range of pH 3–9 were performed. The Cu:HPh ratio was maintained at 0.9:1 for all the experiments. The spectra were recorded in the 400–800 nm spectral range using a dual-beam spectrometer (Agilent Cary 60) in a quartz cuvette with a one cm path length. pH titrations were carried out by adding drops of 1M NaOH directly to the samples. Solutions were allowed to saturate for at least 5 minutes before recording the spectra.

3.2.5. Circular Dichroism. Circular dichroism spectra were recorded on a JASCO J-1700 (JASCO) spectropolarimeter at room temperature. Measurements were performed in the 800–190 nm range with a 3mm path quartz cuvette with a final volume of 0.5µL. The CD experiments were performed at a low concentration, maintaining the 0.9:1 ratio of Cu and peptide (1.8 mM $CuCl_2$ and 2mM peptide). The pH titration was performed by adding 1 M NaOH.

3.2.6. Raman Spectroscopy. Raman spectroscopy was performed using a Laser micro-Raman system (Horiba Scientific, LabRam HR Evolution Raman Spectrometer) equipped with a CCD detector. A 532 nm laser (argon) was used to excite the sample (output power of

16.5 mW). The laser was focused using a 20× objective. Ten microliters of the sample were deposited on a Si window and air-dried before taking measurements. For each sample, 10 accumulations were averaged with an exposure time of 20 s. The spectral range for all Raman spectra is 1750−1200 cm^{-1}.

3.2.7. EPR analysis. Electron paramagnetic resonance (EPR) spectra of the sample were recorded at the X-band frequency (9.5GHz) by using a JEOL (Model JES FA200) spectrometer. The following parameters were used; modulation frequency: 100.00 kHz, modulation amplitude: 10.00 G, microwave power: 1.002 mW, time constant: 2.560 ms, receivers gain: 1.00 × 103. Ethylene glycol was added as a cryo-protectant to each sample (30% v/v). Samples were freeze-quenched in liquid nitrogen before carrying out the measurements at 77 K.

3.2.8. ^{1}H and ^{13}C solid-state NMR analysis. Solid-state NMR: ^{1}H and ^{13}C solid-state NMR spectra of HPh peptide and the complex were acquired at 60 kHz MAS frequency on a Bruker 700 MHz Avance-III spectrometer using 1.3 mm rotors and HXY triple resonance probe. For proton decoupling during acquisition, a rCW^{ApA} decoupling sequence with rf amplitude of 12 kHz was used.[275] One pulse proton spectrum was obtained with a pulse length of 2.7 μs. For the complex, ^{13}C spectra were obtained using one pulse (2.5 μs) with ^{1}H heteronuclear decoupling applied during acquisition. The proton spectrum of the complex was acquired with 32 transients and a recycle delay of 0.2s. For the ^{13}C spectrum of peptide, 20480 transients with a recycle delay of 0.1s were collected.

For peptide, ^{13}C spectra were acquired with one pulse and ^{1}H -^{13}C cross-polarization (CP) with 1ms contact time and heteronuclear decoupling of protons during the acquisition. The ^{1}H and ^{13}C spectra of the peptide were acquired with 8 transients, 2s recycle delay, and 12288 transients, 2s recycle delay, respectively. ^{1}H spectra were referenced with respect to H^{N}-Leu peak of MLF tripeptide at 9 ppm as an external reference. The ^{13}C spectra were calibrated with reference to the proton spectrum using the gyromagnetic ratio of proton to the carbon nuclei.

Longitudinal relaxation (T_1) values for protons of nascent peptide were measured using a saturation recovery experiment. In the saturation recovery experiment, the delay values used were 1ms 50ms, 100ms, 200ms, 300ms, 500ms, 800ms, 1s, 1.5s, 2s, 2.5s, 3s, 3.5s, 4s, 4.5s, 5s,

6s, 9s, 12s. Each experimental point is obtained with 8 transients. Initial saturation of the proton signal is achieved by a train of 50 pulses with length of 3.15 μs, and a inter pulse delay of 8 μs.

3.2.9. Solution state NMR. Solution state proton NMR spectra of the peptide and the complex have been acquired in 90% H_2O+10% D_2O solvent at pH 3 and 7 using a Bruker 300 Avance III spectrometer with 5mm H/X probe. Water suppression was carried out using the pre-saturation technique. All the spectra were calibrated with respect to the D_2O signal (4.79ppm). Pulse length for ^1H was 14μs.

3.2.10. Field Emission Scanning Electron Microscopy Analysis. The complex formed at pH 7 and 9 were directly loaded on a glass cover slide. Samples at pH below 7 were prepared by drop-casting on a clean coverslip followed by vaccum drying. Samples were sputtered with platinum in a JEOL JFC-1600 High-Resolution Sputter Coater at 30 mA for 120 sec. The surface of interest was examined with a JEOL JSM-7400F field-emission scanning electron microscopy system at an acceleration voltage of 15 kV. SEM-EDS mapping was performed at 2kV.

3.2.11. Field Emission Transmission Electron Microscopy Analysis. The complex was loaded on a carbon-coated copper mesh grid (300 mess) and were negatively stained using 2% (w/v) saturated uranyl acetate. After 30 s, excess stain was wicked away, and the grids were allowed to air-dry. Images were captured with a JEM-2100F (Make: Joel) field emission transmission electron microscope at 200 kV.

3.2.12. Catalysis. 0.5 mmol of benzyl alcohol was added along with different amounts of the peptide complex (10, 15 and 30 mol% respectively) to a round bottom flask, capped using an O_2 balloon and left to react at 40°C in water for 3h. The reaction was stirred continuously using a magnetic stirrer. Aliquots (25 μL) were collected at regular time intervals and filtered using a 0.2 micron filter. The filtrates were then analyzed for product formation using reverse-phase HPLC (Shimadzu Prominence, Make Shimadzu Ltd, Japan) with a C18 column at 283nm.

3.3. RESULTS

3.3.1. Characterization of the active site geometry. Histidine brace is a result of the spatial interaction between two histidine residues at the 36th and 135th positions in a typical lytic polysaccharide monooxygenase. To mimic the chemical and structural features of the

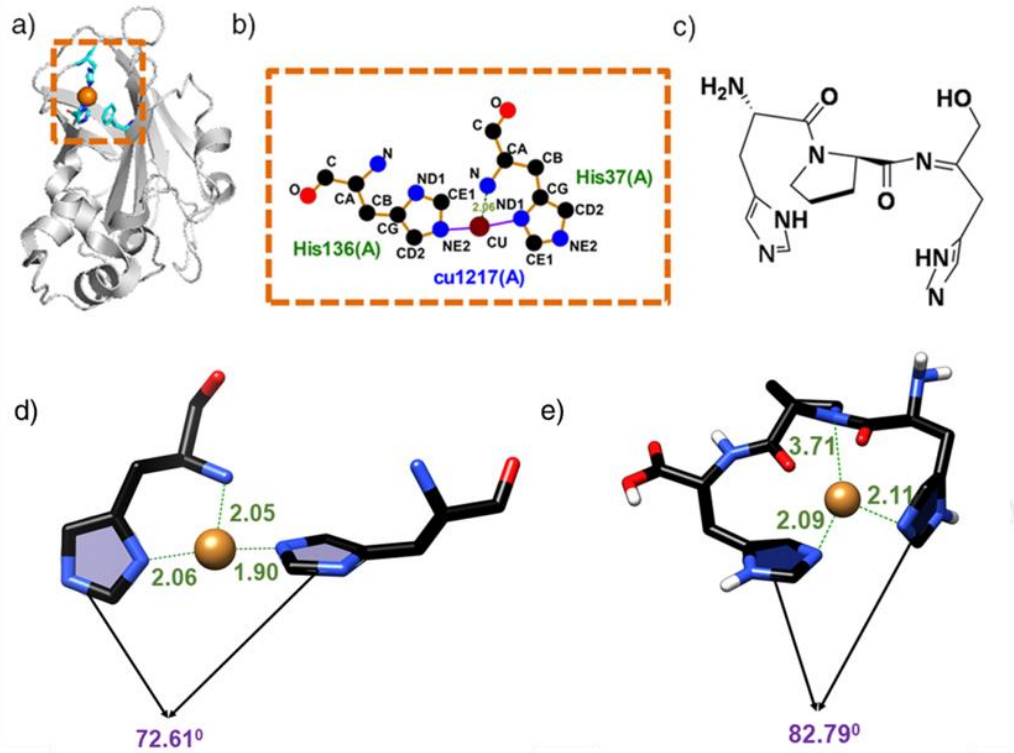

Figure 3.1: (a) The 3D structure of the lytic polysaccharide mono-oxygenase (PDB: 5FJQ) and active-site residues (cyan). (b) Ligplot showing the ligand interactions with the histidine residues in the LPMO active site (c) Chemical structure of the designed peptide mimicking the histidine brace. d) and e) Comparison between the structural parameters of the copper chelated modelled peptide and enzyme active site.

Table 3.1: Comparison of the observed parameters of the modelled complex with those of the reported crystal structure of the LPMO active site.

Parameters	Geometry parameters of LPMO active site	Geometry parameters of designed complex
Cu-His37ND1	2.06 Å	2.05 Å
Cu-HIS136NE2	1.97 Å	2.01 Å
Cu-HIS37N(amide)	1.97 Å	1.99 Å
Twist angle between two imidazole rings	72.61^0	82.79^0

LPMO active site, we have designed the peptide; His-Pro-^{D}His-NH_2 (HPh), bearing two imidazole groups. A proline residue connects the two histidines, creating T-shaped 3N geometry for copper coordination (Figure 1c). In our design, this spatial geometry was achieved by incorporating a D-Histidine residue in the C-terminus of the sequence.

The Cu-HPh complex was modelled using Avagadro 1.2.0.[276, 277] Interestingly, we have observed a large twist angle (83°) between the two imidazole groups (Figure 3.1 and Table 3.1.), which is in agreement with the reported LPMO (Protein data bank, 5FJQ.pdb). This endorses the observation that the Cu-HPh complex successfully mimics the structural motif of the Histidine brace. In the next phase, we have synthesized the peptide molecule and characterized the physiochemical properties of the complex using various spectroscopic techniques.

3.3.2. Cu Binding to HPh. The pH-dependent coordination of the Cu (II) with the designed peptide was verified in a wide range of pH values ranging from 3 to 9, using UV-Vis spectroscopy. A 0.9:1 Cu (II) to peptide stoichiometry is considered for the experiments, to ensure that there is no excess of copper, thus preventing a copper hydroxide precipitation in neutral and alkaline pH. At low pH, the λ_{max} of the *d–d* bands are around 800 nm, which correlates with a band for a Cu (II) aqueous ion (Figure 3.2a). With the increase in pH, a blue shift is observed. The absorption peak at 620 nm is reported to be specific to 3N-Cu coordination.[278] The position of these bands indicates a square pyramidal geometry around Cu (II) coordination sphere with the $d_{x^2-y^2}$ ground state[256, 279] and is close to the d-d transition seen in LPMO (655nm).[280] The absence of any absorption band at 520nm further confirms the 3N geometry.[281]

The circular dichroism (CD) data are in good agreement with the pH-dependent UV–vis spectra. Major changes in visible-CD spectra are observed at pH 7 and above, suggesting that at this pH, a change in the coordinating ligands around the copper ion occurs. At pH 7, two negative bands around 550 nm and 310 nm (Figure 3.2b and Figure A2.2, Appendix 2) are accompanied by a strong negative peak at 280nm, validating an N-imidazole-to-Cu (II)charge transfer.[282] At pH 9, however, the negative band at 550 nm broadens and, together with the strong negative band at 310 nm, indicates the presence of mixed species. This may be

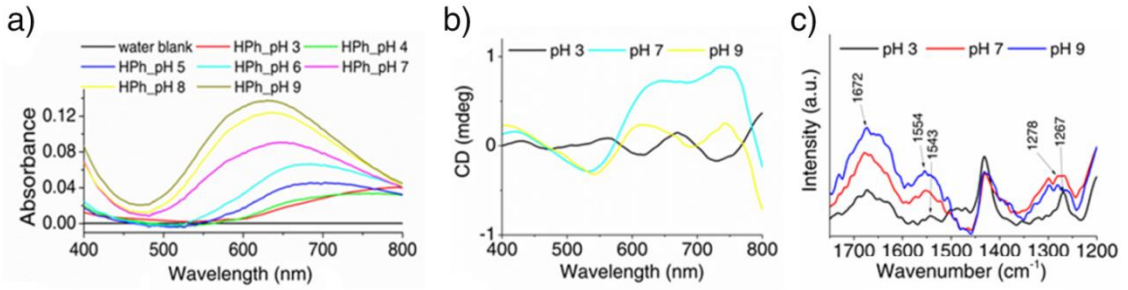

Figure 3.2: Analysis of the Cu/HPh complex formation: a) UV–vis b) circular dichroism c) Raman at different pH values. Experimental conditions: final concentrations of 5 mM HPh and 4.5 mM $CuCl_2$ were titrated with 1 µL aliquots of 1 M HCl or NaOH solution, and the reaction was left to equilibrate for 10 min after each addition.

attributed to the amide deprotonation of the peptide backbone.[283] In the UV-CD analysis, we have observed a negative maximum at 330 nm at pH 7 and above (Figure A2.3, Appendix 2). This typically suggests the presence of high β-turn content in proteins.[284] Besides, the electronic transition of the amide group is affected by the solvent environment. This may explain the observed increase in the negative intensity of the UV-CD spectrum at 230 nm at higher pH. Hydrogen bonding between the excited amide nitrogen and water due to the intramolecular charge transfer from the amide-nitrogen to the amide-oxygen atom leads to a much stronger π-π* transition and hence the strong absorbance.[285]

Further characterization of the Cu-HPh complex formation was obtained by measuring Raman spectra at pH 3, 7, and 9 (Figure 2c). The Raman signal at 1543cm^{-1} for pH 3 corresponds to the C=C stretching vibration. The shift to the higher frequency ($\Delta\vartheta$=11cm^{-1}) upon increasing the pH to 7 and above signifies the chelation of the anionic imidazole group. In addition, we have observed a shift of the peak at 1267cm^{-1} for pH 3 to 1278cm^{-1} at pH 7 and 9, confirming His binding to Cu (II) via N_{π}. It is due to the C-N stretching ring vibration of imidazole of N^{π} or N^{τ} Cu bound form while N^{τ} or N^{π} is protonated.[281] The increase in the pH resulted in the increased peak intensity at 1672cm^{-1}, ascribed to the C=N stretching vibration.

3.3.3. EPR characterization: The coordination of Cu-HPh complex was investigated at pH 3 and 7 using low-temperature EPR (100 K). The hyperfine features have been resolved into parallel ($g_{||}$) and perpendicular ($g_{\perp}$) regions (Figure 3.3a). The axial EPR spectra for pH 7 with $g_{||}$, 2.38 > $g_{\perp}$, 2.11 suggests the presence of $^1B_{2g}$ ground state with the unpaired electron in

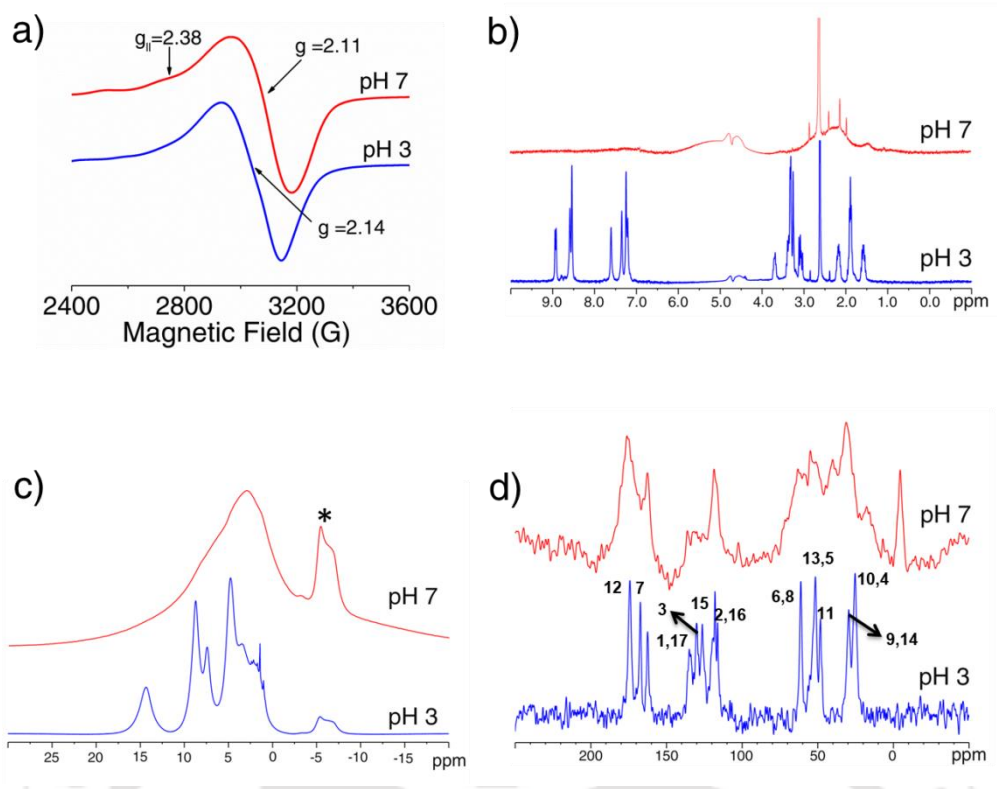

Figure 3.3: a) Frozen-solution EPR of Cu-HPh complex at pH 3 (blue) and pH 7(red) in 30% glycerol (v/v). b) Solution state ^{1}H NMR of Cu-HPh complex at pH 3 and pH 7. c) Solid state ^{1}H NMR of Cu-HPh complex at pH 3 and pH 7; * the peak at -5 ppm is due to the spectrometer artefact d) Solid state ^{1}H NMR of Cu-HPh complex at pH 3 and pH 7. The peaks in the ^{13}C spectra corresponds to the peptide backbone shown in Figure A.2.4 and Table A2.1, Appendix 2.

$d_{x^2-y^2}$ orbital.[286 287] The complex exhibit very similar EPR parameters to the LPMOs ($g_{||}$= 2.23-2.28; $g_{\perp}$= 2.06-2.09). Interestingly, no $g_{||}$ component was observed in the case of pH 3 ($g_{\perp}$= 2.14) suggesting isotropy in the applied field.[288]

In agreement with the UV–vis and CD spectra, the EPR fingerprints at pH 7 show the presence of the 3N geometry ($g_{||}$= 2.232, $g_{\perp}$ = 2.048).

3.3.4. NMR characterization. In order to further verify the 3N binding modes of the complex, we recorded the ^{1}H and ^{13}C NMR spectra of HPh and HPh in the presence of Cu (II) at pH 3 and 7. We have employed both solid-state and solution-state NMR for the analysis. The UV-vis spectrum shows no complex formation at pH 3 and therefore is considered as a reference here. The ^{1}H NMR spectrum in solution state at pH 3 further validates this observation (Figure 3.3b). Moreover, the solution state ^{1}H spectra of the sample at pH 7 show

broad featureless lines due to fast relaxation, indicating the Cu-HPh complex formation. In the solid-state, the ^{1}H and ^{13}C NMR spectra of the nascent peptide showed resolved resonances. In contrast, for the Cu (II) complex, ^{1}H and ^{13}C solid-state NMR spectra showed broadening of the resonances (Figure 3.3 c, d). The ^{1}H NMR spectrum of the complex shows a non-selective broadening of the signals over a spectral range of 20 ppm, due to the binding of the paramagnetic Cu (II). In the nascent peptide ^{1}H spectrum, a clear peak at 14.5 ppm can be attributed to the ring HN proton. In contrast, the proton resonance in the complex is either broadened out or shifted to a new position. Similar non-selective broadening of the peaks was also observed in the carbon spectrum of the Cu (II) complex and a new peak appears at 0-5 ppm (check the exact chemical shift). This peak broadening and change in shifts may be attributed to the paramagnetic center of Cu^{2+}, and is absent for the nascent peptide.

Longitudinal relaxation (T_1) values for protons of nascent peptide were estimated to be 600-700 ms by using a saturation recovery experiment. The proton signal of the peptide with complex was collected at 0.1s, 0.2s, and 1s. We observed that upon complex formation, the proton signal recovered to equilibrium magnetization with in less than 0.1s delay after saturation. We expect the actual T_1 values to be much less than 0.1s, which is an order of magnitude smaller in comparison to the nascent peptide (pH 3). The observed large difference in the T_1 values of the nascent peptide and the complex is a good indicator of a complex with a paramagnetic center. Overall, our NMR spectroscopic results are in good agreement with the theoretically observed 3N geometry of the complex.

3.3.5. Morphological and elemental characterization of the complex. Field emission scanning electron microscopy (FESEM) was employed to determine the morphology of the Cu-HPh complex. It shows flower-like structures that are formed by the agglomeration of uniform micro-flakes stacked in different orientations (Figure 3.4a). Transmission electron microscopy of the complex after negative staining confirms solid flake-like structures of around 214 nm (Figure 3.4b). The EDS line mapping of the structure was performed to confirm the presence of copper ions (Figure 3.4c). The intensity of Cu signals shown in the red line reveals its abundance. The signals from other elements like phosphorus may be attributed to the phosphate buffer used for the experiment.

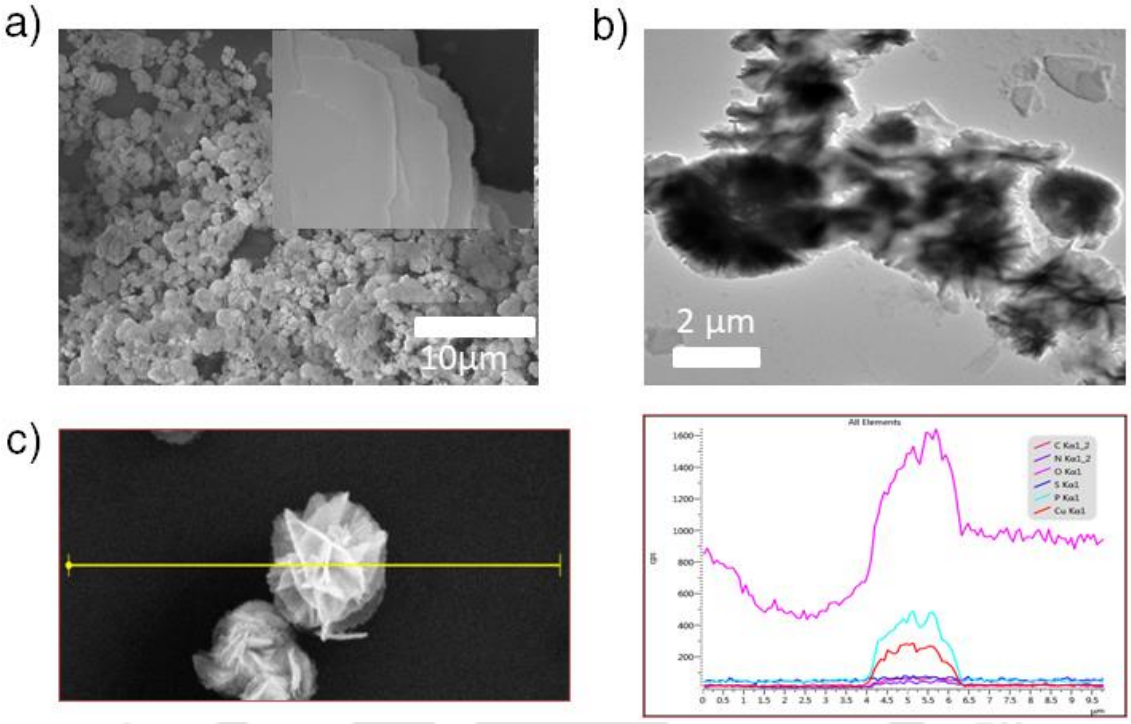

Figure 3.4: Morphology characterization of the complex. a) FESEM image showing flakes like morphology (inset) that are clustered to form a flower of around 214 nm in diameter (b) Negatively stained TEM image of the 'flower' c) Corresponding SEM-EDS line map spectrum of the complex showing Carbon (magenta), nitrogen (purple), Oxygen (pink), Sulphur (blue), Phosphorus (cyan) and Copper (red).

3.3.6. Catalytic efficiency of the designed tripeptide catalyst. We assessed the catalytic activity of the peptide complex for the selective aerobic oxidation of benzyl alcohol to its corresponding aldehyde. (Scheme 3.1)

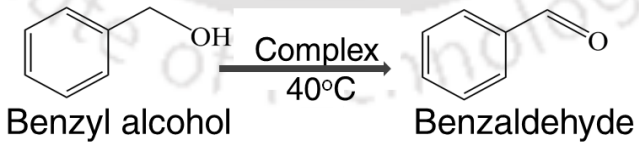

Scheme 3.1: Selective oxidation of benzyl alcohol to benzaldehyde in the presence of Cu-HPh complex at 40°C.

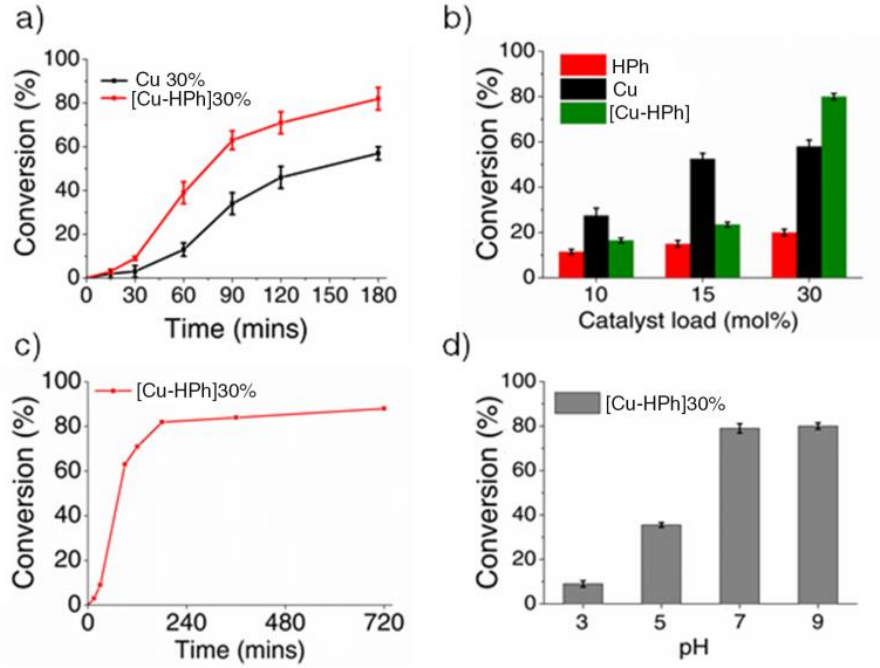

Figure 3.5: Conversion of benzyl alcohol into benzaldehyde in water: pH = 7 at 40 °C is the standard reaction conditions used except in the pH titration experiment. a) Conversion comparison between copper alone and the complex at 30% load as a function of time. b)Histogram comparing percentage conversion by nascent HPh (red), copper (black), and Cu-HPh complex (olive) after 3h. c) Conversion of benzyl alcohol into benzaldehyde at 40°C in 6 h under aerobic conditions. d) Histogram showing the catalytic efficiency of Cu-HPh complex at different pH (mean ±standard deviation, *n* = 3).

The oxidation of benzyl alcohol was carried out in a round bottom flask (25mL), fitted with an O_2 balloon atop a magnetic stirrer at 40°C. We screened different catalyst loading (10, 15, and 30 mol%) and monitored the rate of conversion of benzyl alcohol at different time intervals for 3h. At low catalytic loads (10 and 15 mol%), the percent conversion of benzaldehyde after 3h was also low at 10 and 27 %, respectively (Figure 3.6a and Figure A2.5, Appendix 2). In general, the trend suggests that by doubling the catalyst load from 15 to 30 mol%, we could achieve an impressive 300% increase in the catalytic efficiency. Next, we compared the catalytic efficiency of the catalyst and Cu(II) at 30 mol% catalyst load (Figure 3.5a). After 3h of the reaction we have observed 82% conversion of benzyl alcohol in the case of complex with 100% selectivity. For Cu (II) however, the conversion was significantly low (62%) and is comparable to previous reports that suggest a moderate conversion by Cu (II) alone (72–83 % conversion

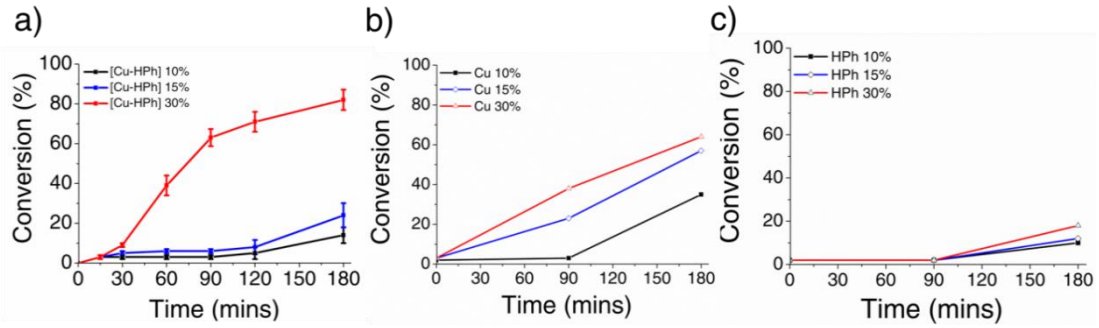

Figure 3.6: Catalytic efficiency of complex (a) copper (b)Cu and (c) HPh at different catalyst load, 10(black), 15(blue) and 30 (red) mol%.

after 24 h at 70°C).[49] Further, we have then compared the catalytic efficiency of the complex with an equimolar concentration of individual entities i.e., peptide and copper alone as control (Figure 3.6a-c). While HPh alone did not show any significant conversion at even 30 mol% load, we have observed an increased catalysis by Cu(II) after 90 mins of the reaction. We have considered 30 mol% catalyst load for all subsequent experiments unless mentioned otherwise.

Next, we explored the scope of achieving complete conversion of benzyl alcohol by extending the reaction time to 12h (Figure 3.5c). While no significant increase in the conversion (in percentage) was observed, the selectivity remained 100%, and no trace of benzoic acid was observed in the HPLC spectra. This may be attributed to the application of low temperature in the reaction, which prevents auto-oxidation of the aldehyde.

3.3.7. Dependency of pH in modulating catalysis. The measurement of reaction rate as a function of pH provides essential information about the underlying correlation between the protonation states of the imidazole nitrogen and catalysis. The protonation state affects the imidazole donor-acceptor capabilities, which are key determinants for redox properties and reactivity. In addition, metal-induced histidine deprotonation was also suggested for different metalloenzymes at varied pH.[289] Therefore, we have tested the catalytic efficiency of our complex across pH 6, the effective pK_a of histidine.

Extrapolation from Figure 3.5d suggests that the catalytic efficiency of the peptide increases with increase in pH. At pH 3, no product formation was detected in the HPLC spectra, but the conversion rate increased to 35% at pH 5. In the case of higher pH (above pH 6) however, the

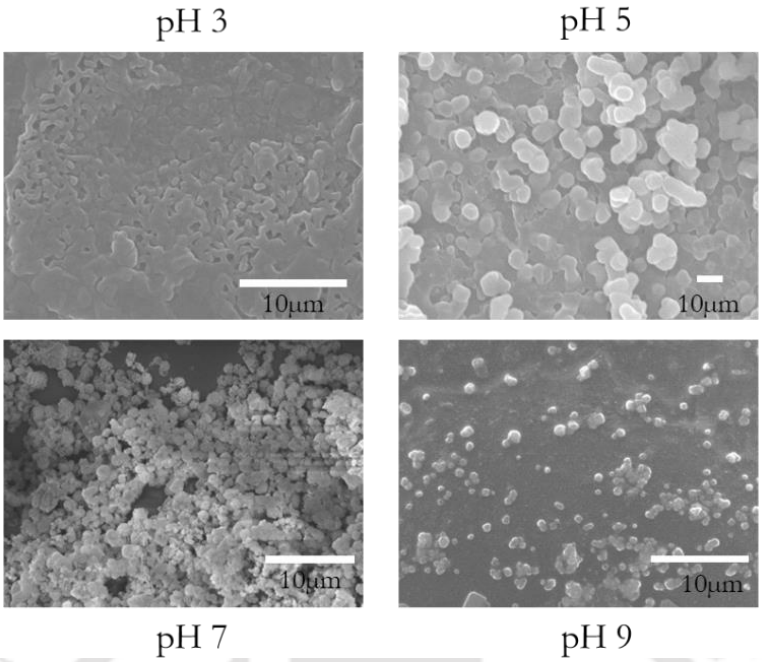

Figure 3.7:FESEM characterization of the assemblies formed by Cu-His complex at different pH. Scale 10μm.

conversion has reached 80% demonstrating the formation of a tailor-made catalytic active site at physiological pH. Morphological verification of the catalyst at different pH reveals the gradual transition from the disordered to the more ordered nano-assembly at higher pH (Figure 3.7).

3.4. DISCUSSION

Mimicking the active site of metalloenzymes in artificial systems is the key to understand the selectivity and efficiency of enzymatic reactions. Specifically, one must design structural sites where the metal can impart thermodynamic stability, direct the protein fold and overcome non-preferred metal-binding geometries. Recent advancements in metal–peptide supramolecular chemistry led to the development of artificial macromolecular structures that operate as a geometric template functioning as an electron reservoir.[290, 291] However, the designed metallopeptides show significant lack of catalytic efficiency relative to their natural counterparts.[292] Over the years, the advancements in understanding the balance between protein scaffold stability and metal ion coordination preferences, lead to exploring the un-

natural D-amino acids.[293] The ability to tune the metal binding affinity of small peptides by incorporating D-amino acids and the pre-organization of peptide structure holds great potential in designing ultra-short catalytic domains derived from the active site of a metalloenzyme.

In the present study, we have designed a tripeptide to mimic the histidine brace motif found in the active site of an industrially important enzyme lytic polysaccharide monooxegenase (LPMO). Our goal is to generate a structural mimic through a minimalistic design approach. The otherwise difficult mimicry of LPMO active site was achieved by incorporating D-histidine at the C-terminal. The modelling studies suggests that the copper coordinates with the peptide through 3N coordination, that results in a distorted square pyramidal geometry, similar to that observed in LPMO active sites.

Interestingly, one can modulate the protonation state of histidine across the physiological pH ($pK_a \approx 6–7$). The imidazole group of histidine ligands can bind to Cu ion through either the δN or εN site, and the tautomeric preference varies with pH. The spectroscopic characterization at various pH suggests that the complex formation occurs only at pH 7 or above. Increasing the pH from 3 to 9 resulted in an increase in the intensity of d–d transition band, in the UV and vis-CD spectra. A plausible explanation for this phenomenon is the participation of one amide nitrogen (N_{am}) atom and two imidazole nitrogen (N_{im}) atoms to form equatorial plane coordination, while the carboxylic oxygen (O_c) atom moves to the axial position. Relatively strong CD bands are often observed for d–d transitions of tetragonal complexes, involving backbone amide and histidine coordination through imidazole ring.[281] Additionally, it causes a distortion in the tetragonally elongated symmetry, causing large transition and hence the enhanced d-d transition with increasing pH. The spectral changes in UV-vis, vis-CD between pH range of 7 and 9 are relatively small suggesting the formation of a predominant species at pH 7.The coordination of N_{am} and N_{im} is also confirmed from the vibrational Raman spectra. The N_{im} coordination can be extracted from the drop in intensity of the Raman-active N-H deformation bands at 1440cm^{-1}. Furthermore, the signal corresponding to the Raman C=C or C=N stretching band (1543 cm^{-1}), observed at pH 3 also red-shifts to 1554 cm^{-1} at pH 7 and 9, suggesting formation of a complex with N^{τ} coordination.[281] The presence of N^{τ} coordination form is further evidenced by the small

bandwidth of the Raman-active ring-breathing vibration at 1278 cm^{-1}.[294 295 296] The EPR spectrum of the complex at pH 7 and 9 is typical for a Cu (II) complex with a distorted square pyramidal geometry.[297] Based on the NMR experiments we can conclude that the predominant species is in 3N form, as it is able to considerably accelerate the Cu (II) exchange (within ms). Overall, our model Cu-HPh complex can reproduce the physicochemical features of the active site of LPMOs.

Catalytic activity of our model complex was tested for the oxidation of benzyl alcohol in water. While His alone does have very low to no catalytic activity, it is the most important amino acid playing the role of a proton donor or acceptor in a catalytic reaction.[298] The results above clearly demonstrate that the binding of copper ion to the structure is through the creation of multivalancy of the histidine residues at pH 7. Based on previous reports,[299, 300] we postulate that the protonation of one of the imidazole near pH 7, facilitates H-atom transfer in the presence of oxygen. Stahl and co-workers have earlier demonstrated this to be the energetically most favorable route for oxidation of a Cu-alkoxide.[301]

3.5. CONCLUSIONS

A structurally well-defined Cu (II) complex of 3 N ligands using HPh peptide backbone have been synthesized as a model for the histidine brace active site of LPMO. The complex is characterized by various spectroscopic techniques and the catalytic function was tested for the model, benzyl alcohol oxidation. The molecular structure of the Cu-HPh complex adopts very similar distorted square-pyramidal coordination geometry, as seen in the LPMO active site. The position of d-d transitions as observed in UV-vis and CD spectroscopy and the EPR parameters support the existence of square-pyramidal geometry of the complex through 3N coordination at pH 7, identical to the histidine brace. The pH dependence is explained by the absence of any complex at pH below 7. The 3N coordination is further validated by the solid state NMR analysis that shows an accelerated Cu (II) exchange (ms or faster) at pH 7. The heterogeneous Cu-HPh complex showed a high yield of benzaldehyde, up to 82% through selective oxidation of benzyl alcohol in water, in the presence of molecular oxygen at 40°C. This study presents a minimalistic design strategy using D-amino acid for structural and functional mimicry of the LPMO active site, which can be a stepping stone for generating sustainable and environment-friendly, alternative catalytic solutions.

4.

Stimulus Responsive Hydrogel Nano-catalyst

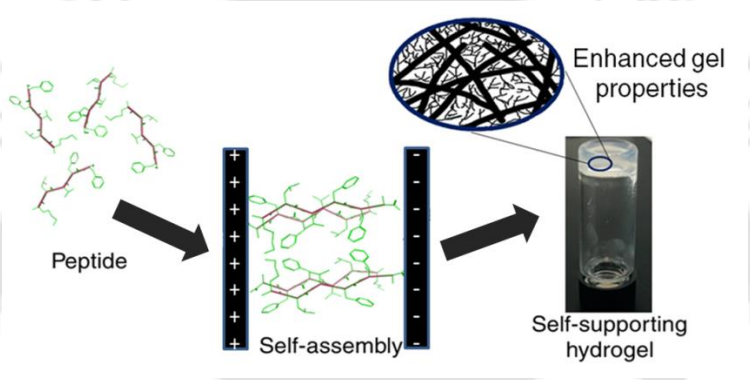

The ability to modulate self-assembly is the key to manufacture application-oriented materials. In this study, we investigated the effect of three independent variables that can modulate the catalytic activity of self-assembling peptides. The first two variables, amino acid sequence and its stereochemistry were examined for their specific roles in the epitaxial growth and hydrogelation properties of a series of catalytic tripeptides. We observed that the aromatic π-π interactions that direct the self-assembly of the designed peptides, and the catalytic properties of the hydrogels, are governed by the position and chirality of the proline residue. Subsequently, the influence of the third variable, an external electric field, was also tested to verify its catalytic efficiency for the asymmetric C-C bond-forming aldol reaction. The electric field treated pff and PFF gels, in particular, showed 10 and 36% higher stereoselectivity, compared to the control. Structure-property analysis using CD and FTIR indicates electric field-induced beta to non-beta conformational transition in the peptide secondary structure, which corroborates respectively with its reduced cross-link density and fibril width. Amplitude sweep rheology of the gels suggests a decrease in the storage modulus, with increased field strength. Results showed that the electric field of optimal strength can modulate the physical characteristics of the hydrogel, which in turn, is manifested in the observed difference in enantioselectivity.

4.1. INTRODUCTION

The emergence of short to ultra-short peptides as minimalistic building blocks has resulted in the discovery of new functional properties following their self-assembly. Such peptides can act as low-molecular-weight gelator (LMWG) that self-assemble to form supramolecular gels. Epitaxial growth of such LMWGs is primarily mediated through intermolecular non-covalent interactions, resulting in the formation of a supramolecular gel. Recently, there are reports of gels used for the development of new catalysts, because gels can potentially combine heterogeneous and homogeneous characteristics.[302] Solid like fibrous network of gels allow swift diffusion of reagents and products through the gel matrix and functional groups of a catalytic site can in principle be reproduced in such gel nanofibers. The ability to modulate the self-assembly of LMWG by an external stimulus, resulting in 'tunable' nanocatalysts, have not been demonstrated so far. In this report, we present twelve proline containing tri-peptides for their ability to form catalytic hydrogels by tuning their efficiency and stereo selectivity by systematically changing three variables; amino acid side-chain chemistry, sequence, and more importantly external electric field.

Hydrogels are self-supporting, water-swollen three dimensional cross-linked network that permits the diffusion and transient attachment of molecules.[37] Peptide hydrogels have wide-ranging potential applications, particularly in drug delivery, tissue culture, environmental remediation, and catalysis. Supramolecular peptide hydrogels have been shown to possess enhanced catalytic efficiency compared to the non-assembled peptides.[231, 303, 304]

Peptide self-assembly is governed by the relatively weak nature of the non-covalent interactions such as electrostatic interactions, hydrophobic effect, hydrogen bonding, Vander Waal's interactions, and π-π- stacking.[17] Among them, the aromatic π-π- stacking interaction is of particular interest for driving peptide self-assembly into functional supramolecular structures.[305, 306] The basic understanding of the π–π stacking suggests the role of quadrupolar interactions among delocalized π-electrons of aromatic rings.[28] Several research groups have exploited it to design ultra-short peptide hydrogelators based on π-π interlocking of aromatic moieties such as diphenylalanine[307] and *N*-fluorenylmethoxycarbonyl.[174, 308-311] Developing an effective way to modulate the pattern of interactions involved in the organization of the self-assembled structures is crucial for fabricating materials with novel properties. It can be

achieved by altering the chemical environment of the peptide by changing the pH, ionic strength, residue chirality, and addition of metal ions.[312] They act on the microenvironment and provide great control during assembly. External stimuli such as light,[142, 313] temperature,[17, 314] ultrasound,[17, 315] and electric[165, 187] and magnetic fields[187, 316] are non-invasive in nature and can be remotely controlled to modulate the self-assembly and structures. They are easier to implement and can effectively alter the possible hydrogen-bonding pattern. While there are several reports on the modulatory effect of ultrasound[118, 119, 124] and electromagnetic field[143-145] on peptide self-assembly, the potential of electric field (EF) has not been explored for tuning organocatalysts.

The π-electrons in an aromatic peptide system are prone to polarization in the presence of external EF.[188] Application of adequate field strength can potentially alter the individual contributions of electrostatic and dispersive interactions that direct supramolecular architecture. This may lead to the generation of field-induced anisotropy in the system, which modulates the molecular conformation of the peptides.[175] Nguyen et al. reported oriented growth of FF peptide micro-rod array in the presence of a uniform EF between two parallel aluminum plates.[168] In an earlier published report, our laboratory has experimentally demonstrated the modulatory effect of EF on the self-assembly of diphenylalanine in water without affecting its chemical composition.[187] We have further demonstrated the EFs ability to cause β to non-β conformational transition in aggregation-prone peptides responsible for various protein-misfolding diseases.[193, 206, 317] Another strategy is to exploit the mismatched dielectric properties of the peptide molecules that are polarized in an EF.[187, 190, 206, 317] Martin et al. has explored the variations in solution pH and EF strength to orient a designed peptide to develop a functionalized surface.[165] Velichko et al. investigated the effect of EFs during the self-assembly of a negatively charged polyelectrolyte and a positively charged amphiphilic peptide in forming an ordered membrane in water.[167] They have observed a direct correlation between the membrane thickness and stiffness with the strength and orientation of the applied field. Interestingly, no report on the effect of EF on peptides forming catalytic hydrogels and its manifestation in terms of catalytic efficiency has been demonstrated. The economic benefits of such an investigation are apparent, along with the scientific reasons for making decisive advancements in the field of catalysis.

Escuder, Miravet, and co-workers have demonstrated the ability of gel networks performing various catalytic processes, which includes amino acid-mediated aldol reactions.[233, 234, 318] The asymmetric aldol reaction is widely regarded as an important reaction for forming C-C bonds.[319] While there are several ways for achieving directed catalytic stereoselective aldol reactions in organic synthesis,[320] methods for catalyzing enantioselective aldol reactions in water are rare.[321] Proline have been reported to function as a micro-aldolase (Type-1), that catalyze aldol reactions through a six-membered enamine transition state.[322] It is noteworthy that owing to the cyclic structure, proline has a higher pK_a compared to other amino acids.[323] The presence of both acidic and basic functional groups makes proline an efficient bifunctional catalyst, and has been found to furnish racemic products in water.[324] One plausible explanation is that, the presence of water mediated hydrogen bonding, results in the distortion of the enamine transition states, which in turn lowers the enantioselectivity.[219] In such a case, incorporating proline residues in a peptide sequence prone to self-assembly may be the most logical way of designing catalytic organogels.

In this study we have screened a series of twelve proline containing tri-peptides for their ability to form catalytic hydrogels. We report the effect of three independent variables that can modulate the function of a self-assembling peptide. The first two variables are amino acid position and its stereochemistry, while the third variable is an external electric field (EF). We present the modulatory effect of EF on a series of rationally designed hydrogel-forming tripeptides, specifically focusing on their structure and catalytic efficiency. We further investigated the structural and morphological changes in the presence of the EF, in order to correlate with the observables that account for catalytic efficiency and enantiomeric excess.

4.2. EXPERIMENTAL SECTION

4.2.1. Peptide synthesis. All chemicals purchased (mostly from Sigma) were of analytical grade and used as received. Peptides were synthesized manually using the standard Fmoc-solid-phase peptide synthesis in HMPA-NovaGel™ resin. The purity of these peptides is verified by reverse-phase high-performance liquid chromatography (Shimadzu, LC 20 CE system) using a C-18 analytical column (10 to 100% acetonitrile gradient) at a flow rate

of 0.5 $mLmin^{-1}$. The collected fractions were then verified by mass spectrometry using MALDI TOF MS (Make: Bruker, Autoflex Speed)(Table A3.1, Appendix 3).

4.2.2. Preparation of catalytic hydrogels. For each peptide, 2% (w/v) stock solutions were prepared in DMSO: phosphate buffer (pH 7) in 1:10 ratio. The solutions were then heated to 95°C for 15 min until the solution turns transparent.[111] White opaque hydrogels were formed during cooling to ambient temperature (25°C) without any disturbance. After 12h of incubation, the hydrogel formation was confirmed using vial-inversion test.

4.2.3. Catalytic reaction. 6.04 mg (0.04 mmol) of 4-nitrobenzaldehyde were dissolved in 41 µL (0.4 mmol) of cyclohexanone, were dissolved in 0.5 mL of toluene, added on top of the hydrogel, and left to diffuse and react at room temperature. The reaction was monitored using C18 HPLC by taking aliquots of the upper toluene phase at regular time intervals.

4.2.4. Determination of enantiomeric excess%. Enantiomeric excess percentage (*ee%*) was determined by chiral liquid chromatography using a Chiral Art Amylose-SA (YMC Inc.; Japan). A gradient of hexane was prepared with an elution maximum at hexane/isopropanol (v/v: 75/25 and flow rate = 1 mL/min). The enantiomeric selectivity was estimated by the integration of individual peaks at 254 nm. The *ee%* is determined using the following formula:

$$ee\% = \frac{(\text{Area under peak A} - \text{Area under peak B})}{(\text{Area under peak A} + \text{Area under peak B})} \times 100\%$$

4.2.5. Electric field modulation experiments. As shown in Figure 2a, an electric field set up was built using two parallel plate aluminum electrodes separated by 1 cm to produce an adjustable horizontal DC electric field, with field strengths ranging from 0–375Vcm^{-1}. Experiments were performed by placing the vials containing 0.3 mL of 30 mM peptide solution (heated at 95°C) and allowing it to cool in the electric field for 12h.

4.2.6. CD spectroscopic measurements. Circular dichroism (CD) spectral measurements were recorded in a 1mm quartz cell (Hellma Analytics) using a Jasco J-1500 spectro-polarimeter with a slit width of 1 nm. Spectra were recorded immediately after taking them out from the EF, at soluble peptide concentrations, below the minimum gelation

concentration, in miliQ water. The 12h old EF treated and untreated peptide samples were diluted to obtain 30-50 μM in water using a molar absorption coefficient of 286 M^{-1} cm^{-1} at 254 nm. The CD data points were collected from 260 to 190 nm at room temperature with a spectral bandwidth of 1.0 nm and an averaging time of 3s. Each spectrum represents the average of three acquisitions to minimize the noise.

4.2.7. FTIR spectroscopic measurements. The peptides samples prepared in D_2O were loaded on a potassium bromide (KBr) pellet immediately after taking out from the field. FT-IR spectra were recorded on a Shimadzu IR Affinity 1S equipped with an MCT detector at 4 cm^{-1} spectral resolution, between 1400 cm^{-1} to 1800 cm^{-1} (amide 1 region). The 16 scan data are collected, and the spectral evaluation was carried out by inbuilt spectral manager software (Jasco Co.).

4.2.8. Field Emission Scanning Electron Microscopy (FESEM). Aliquots from incubated samples were loaded on a clean glass coverslip and dried. The dry samples were coated with platinum using a Polaron SC7640 Sputter Coater and scanned in a Joel JSM-7610F instrument at an acceleration voltage of 15kV.

4.2.9. Rheology. Viscoelasticity of the peptide hydrogels was measured using a Physica MCR 301 (Make: Anton Paar, Austria) rheometer, operating in oscillatory mode, with a 25 mm parallel plate geometry. The gap distance was maintained at 0.5 mm gap for all the analyses. 6The critical strain was determined by drawing two tangent; one to LVER and another to the nonlinear region and the intersection of both asserted the value of γ_c.[325] The error bars represent the standard errors of three independent observations.

4.2.10. Doxorubicin diffusivity experiment. Doxorubicin was trapped inside the peptide gels at 0.5 mg ml^{-1} concentration during the gelation process as reported elsewhere.[326] Briefly, 10 μl of 50 mM peptide stock solution in HFIP was added to a polystyrene cuvette. Subsequently, 40 μl of 0.55 mg ml^{-1} doxorubicin hydrochloride solution prepared in water was added and the cuvette was left undisturbed for 12 h in presence and absence of electric field, resulting in gel formation. Water (950 μl) was gently loaded on top of the drug-loaded gel and absorbance at 481 nm was monitored at 0, 1, 3, 5 and 48 hours of incubation. The concentration of doxorubicin in the solution was calculated using Beer–Lambert law (ε_{481} =

10,410 $L \cdot mol^{-1} \cdot cm^{-1}$)[327] and 0.5 mg ml^{-1} doxorubicin in water was used as the control. All the data are shown as the mean of three independent observations with the indicated standard deviation.

4.3. RESULTS

It is well known that proline does not catalyze in water.[328] Furthermore, methods for catalyzing enantioselective aldol reactions in water are rare. Precisely placed hydrophobic groups on proline could mediate specific hydrophobic interactions with substrates in water to create efficient organocatalysts with high diastereo- and enantioselectivity.[329-331] Proline-based self-assembled peptide hydrogels have also been reported to catalyze the C–C bond-forming asymmetric aldol reaction.[232, 233, 332] In most of the early examples of reactions catalyzed by these assemblies showed no diastereoselectivity and enantioselectivity,[232] however quantitative yield with 92:8 anti/syn ratio and 90% enantiomeric excess (*ee*%) was observed in few cases.[234, 318] Previous research have extensively reported the β-sheet forming propensity of di-phenylalanine during assembly.[333] If placed next to proline in sequence, phenylalanine can modulate catalysis, probably through secondary interactions at the transition state of the reaction.[334]

In this study, we have screened a series of twelve designed tri-peptides with phenylalanine (Phe, F) and proline (Pro, P) residues for their ability to form catalytic hydrogel (Figure 4.1).

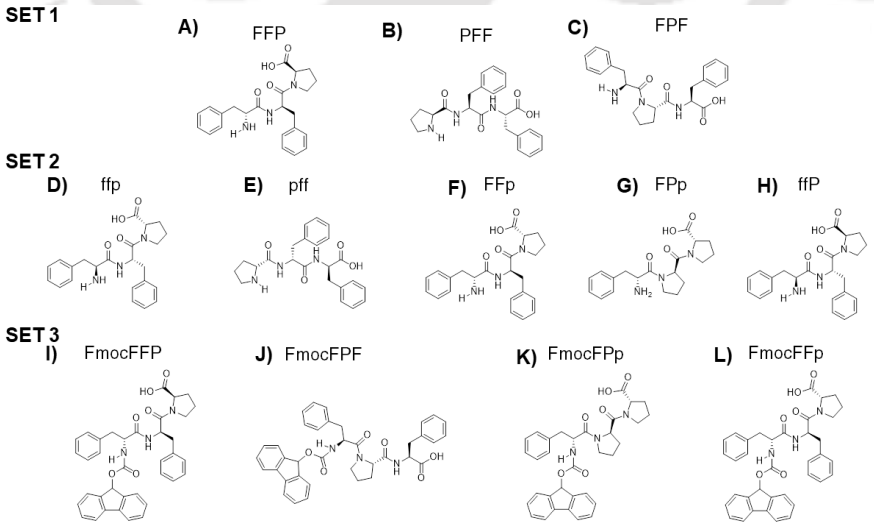

Figure 4.1: Molecular structures of the designed tri-peptides with Phenylalanine (F) and Proline (P) residues. L- and D-amino acids are written as upper and lower case characters, respectively.

We hypothesize that exploring the self-assembly of the tripeptides would provide flexibility in chemical design, and propensity for gelation, while offering scope for external modulation. The peptides were divided into three sets based on their sequence composition. The sequences in set 1, comprising all L-amino acids, were designed to study the effect of a subtle change in the amino acid position (Figure 4.1.A-C). The set 2 peptides comprised of the D-isomers of set 1 peptides and heterochiral sequences of Phe and Pro residues that enable the tripeptide to assume conformations that are otherwise not accessible to homochiral peptides. Based on previous reports, we expect preferential selection of opposite enantiomer from the D-proline-containing peptides[335] (Figure 4.1.D-H).

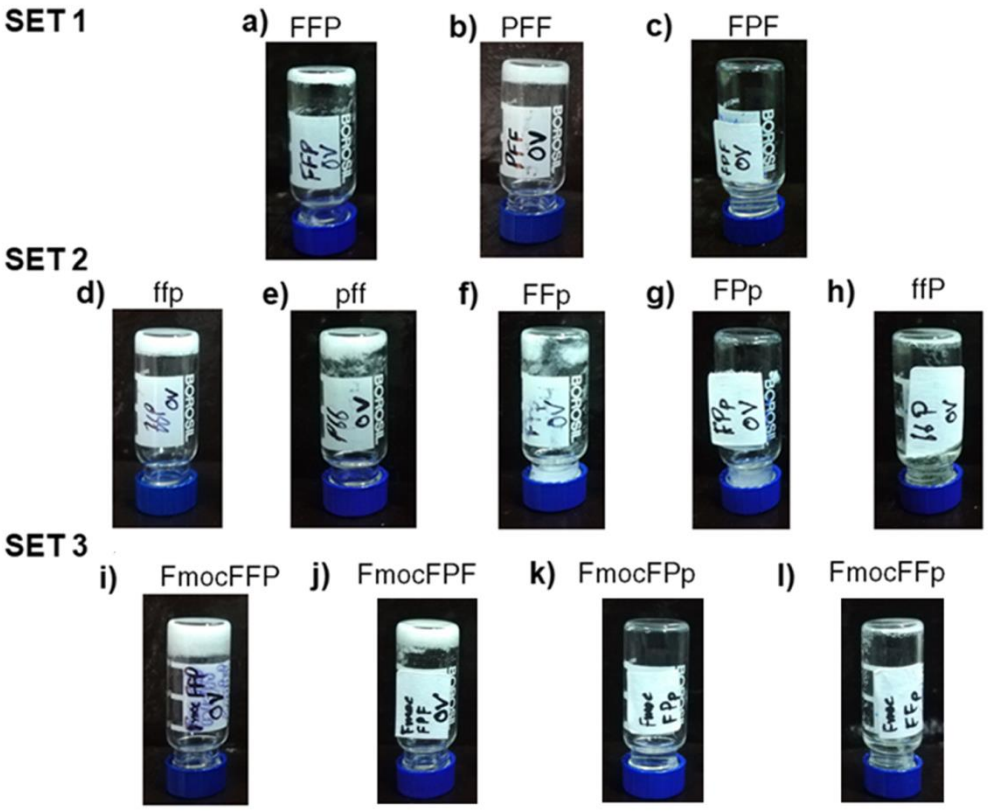

Figure 4.2. Vial inversion test confirming the hydrogel formation. A total of six peptides, FFP, PFF, ffp, pff, Fmoc-FFP, Fmoc-FFP, formed white, opaque self-supporting hydrogels in phosphate buffer following a temperature trigger.

Efficient hydrogelation of oligopeptides usually requires the presence of a large aromatic group on the oligopeptide N-terminal.[336] In set 3, we have introduced a bulky aromatic N-terminal protecting group fluorenylmethoxycarbonyl (Fmoc) to increase the aromaticity and

hydrophobic interaction of some selected set 2 peptides. (Figure 4.1.I-L). All the peptides were tested at 2% (w/v) for their ability to form a self-supporting hydrogel. The sol-to-gel transition was monitored visually and confirmed by a standard vial inverted test.62 (Figure 4.2). We have observed that six peptides, **FFP, PFF, ffp, pff, Fmoc-FFP,** and **Fmoc-FPF** formed self-supporting hydrogels in phosphate buffer following a temperature trigger.

4.3.1. Catalytic efficiency and stereo-selectivity of the peptide hydrogels.

Subsequently, the catalytic activity of the peptide was tested towards the aldol coupling of cyclohexanone and 4-nitro-benzaldehyde as a benchmark reaction (Scheme 4.1). This reaction has been previously studied, regarded as a standard test for the catalytic activity of hydrophobic aggregates in water.[337]

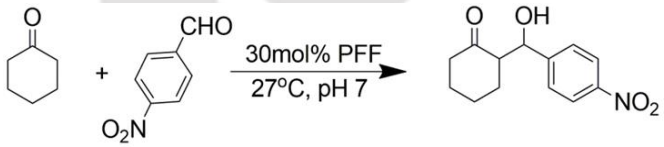

Scheme 4.1. Direct aldol reaction between cyclohexanone and 4-nitro benzaldehyde in the presence of 30mol% **PFF** catalyst.

The product of the aldol reaction between cyclohexanone and 4-nitrobenzyldehyde has two stereocenters. This leads to the generation of four isomers in pairs of two diastereomers; *syn* which has two enantiomers 2R,1'R and 2S,1'S and *anti* which has also two enantiomers 2S,1'R and 2R,1'S. [338] The products were separated by standard chromatographic techniques, and the enantiomeric excess (*ee*, a term we used synonymously for diastreomeric excess as well in this paper) was analyzed by chiral HPLC. Chiral HPLC traces (Figure A3.4-9, Appendix 3) shows the diastereomeric ratio (*d.r.*) of the product and the peaks are assigned based on literature.[338]

The catalysis results after 94h of the reaction at room temperature are presented in Table 4.1(0V). It can be noticed that all the gel-forming tripeptides showed quantitative conversion of the product, but their streoselectivity differed significantly. Among the set 1 peptides, the highest *ee* was observed for **FFP** hydrogel (97 *ee*%). On the other hand, the quantitative

conversion of the aldehyde was faster in **PFF** gel (48h) but resulted in a low *ee* value (53 *ee*%). It behaved similarly to other homogeneous phase catalysts derived from N-terminal L-proline described in the literature.[339, 340] The *ee*% of the set 2 peptides **ffp** and **pff** was 83 and 73 respectively. Interestingly, by changing the amino acid residues' chirality, we could alter the gels' streoselectivity. The conversion rate was low for set 3 peptides (70%) with 74 and 87 *ee*%. This low conversion rate may be attributed to a lack of substrate availability owing to the increase hydrophobicity of the peptides.[329] These results pointing to the spatial orientation of functional groups and morphology of the gel, prompted us to study the influence of the external electric field during the hydrogel formation and its implications in catalytic conversion and stereoselectivity.

4.3.2. Effect of low electric field in modifying the catalytic efficiency and stereo selectivity of peptide hydrogel. To study the modulatory effect of external electric field (EF) during gel formation, electric field (DC) strengths of 150 and 300 Vcm^{-1} were applied across two parallel plate electrodes. Figure. 4.3(a) shows the circuit diagram of the setup used to generate the desired EFs. The pre-heated peptide samples were allowed to cool in the presence of EFs at room temperature and incubated for 12 hours. The catalytic activity of the gels was tested by adding the reagents on top of the hydrogel placed outside the EF. The observables recorded for catalysis after 94h, are presented in Table 4.1 (150 and 300 Vcm^{-1}). The effect of the EF is more pronounced in the peptides with N-terminal proline. The **PFF** hydrogel formed in the presence of the 300 Vcm^{-1} field showed a 36% increase in the *ee* (89%) compared to the control (53%).

The *ee* of the 150 Vcm^{-1} treated **PFF** hydrogels is low (66%) and is comparable to the control. The observation is consistent with **pff** gels, in which the 300 Vcm^{-1} treated sample showed a 10% increase in *ee* compared to the control. The remaining peptide gels did not show any modulatory effect in the *ee*% upon field exposure

Table 4.1: Estimates of catalytic efficiency and stereo selectivity for the aldol reaction between cyclohexanone and 4-nitro benzaldehyde, using a hydrogel formed in the presence and absence of EF after 94h of incubation.

Sl No.	Catalyst	Conversion %[a,b]			*de%*[c]		
		0V	150V	300V	0V	150V	300V
1	FFP	92	87	88	97	98	97
2	PFF	94(48h)	93(48h)	93(48h)	53	66	89
3	ffp	>90	>90	>90	83	82	84
4	pff	>90	>90	>90	66	75	76
5	Fmoc-FFP	72	74	74	74	81	79
6	Fmoc-FPF	68	70	71	87	81	83

a Estimated by reverse phase HPLC, error ±10%.
b If quantitative conversion was reached earlier, time is given in brackets.
c Determined by chiral stationary phase HPLC.

All of these results point out the effect of applied EF in the reaction's outcome. To understand these results, we investigated the characteristics of the gels, formed in the presence of EF at the molecular and supramolecular level.

4.3.3. Modulation of hydrogel forming peptide secondary structure using electric field. CD and FTIR were employed to assess the peptide conformations in the presence and absence of electric field (red, Figure 4.3-4). The CD spectra of **Fmoc-FPF** control (0 Vcm^{-1}) peptide show random conformations. On the other hand, the aggregates of **PFF, pff**, and **ffp** showed typical β-sheet conformation with the two characteristic CD signals at around 195 and 218nm arising from the $\pi-\pi^*$ and $n-\pi^*$ transition respectively (red, Figure 4.3- 4) Interestingly for **ffp**, a third signal was observed at 252nm, suggesting a strong $\pi-\pi$ stacking interaction among the phenylalanine residues.[341] CD spectra of both **ffp** and **pff** peptides showed opposite handedness in their secondary structure.

Next, the modulatory effect of the EF on the peptide secondary conformation was assessed by recording the CD spectra after 12h of incubation in EF. Application of EF on **Fmoc-FPF** peptides show a gradual structural transition from the predominant random conformation as

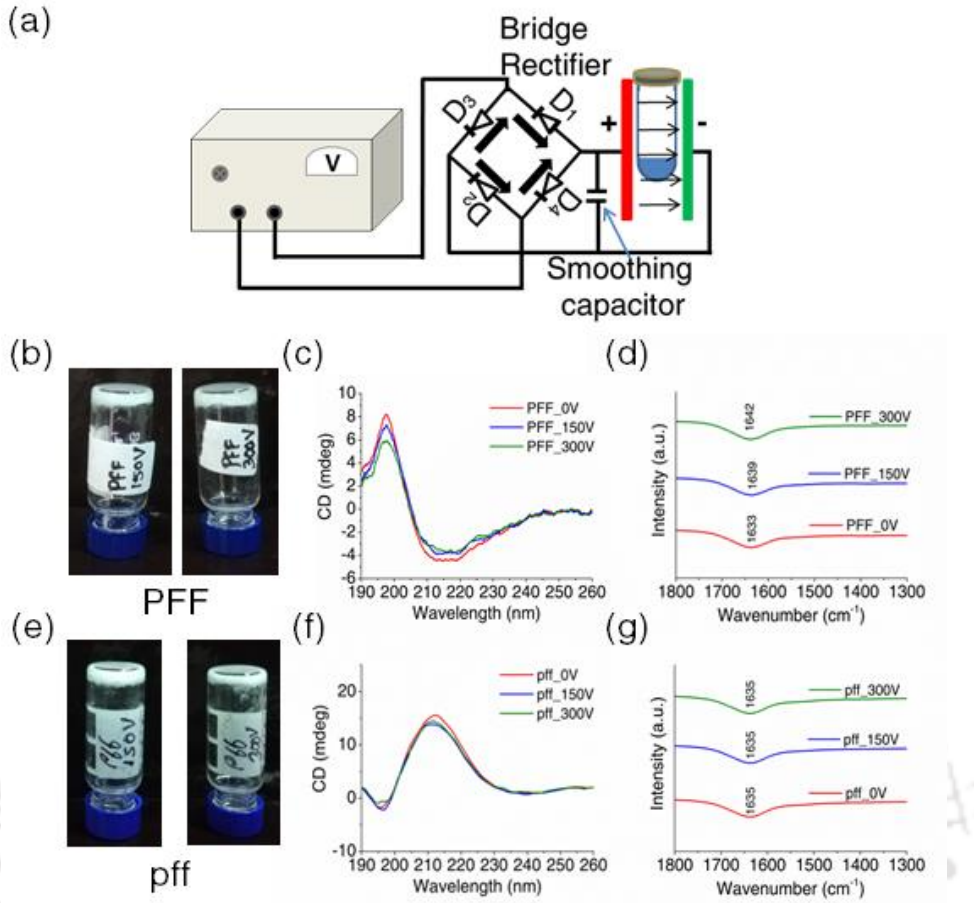

Figure 4.3. a) Schematic representation of the electric field set-up with adjustable field strengths from 0–375 Vcm^{-1} (b) Vial inversion test with 2% w/v **PFF** peptide, modulated by 150 and 300Vcm^{-1} electric field (c) CD spectra of **PFF** peptide in 0 (red),150 (blue) and 300 Vcm^{-1} (green) (d) FTIR spectra of the **PFF** peptide in three different field strengths; 0 Vcm^{-1} (red),150 Vcm^{-1} (blue) and 300 Vcm^{-1} (green) (e) Vial inversion test of EF modulated **pff** hydrogel, formed in 150 and 300 Vcm^{-1} (f) CD spectra of **pff** peptide 0 (red),150 (blue) and 300 Vcm^{-1} (green) (g) FTIR spectra of **pff** peptide in 0 (red),150 (blue) and 300 Vcm^{-1} (green). Uppercase letters and lower case letters in amino acid sequence indicating L- and D-chiral amino acids respectively.

seen in the control peptides 150 Vcm^{-1} is blue and 300 Vcm^{-1} is Olive, Figure 4.3 and 4. The effect was most prominent in the case of **FFP** and **Fmoc-FPF** peptides. The CD spectrum of **PFF, pff FFP** and **ffp** samples showed reduced peak intensity at 218nm and 190nm confirming a beta to non-beta transition. Interestingly, the peak at 252nm is absent in field-treated **Fmoc-FPF** samples, suggesting the aromatic stacking modulation by the applied EF.[342] This observation is in line with previous findings that suggests the modulatory effect of

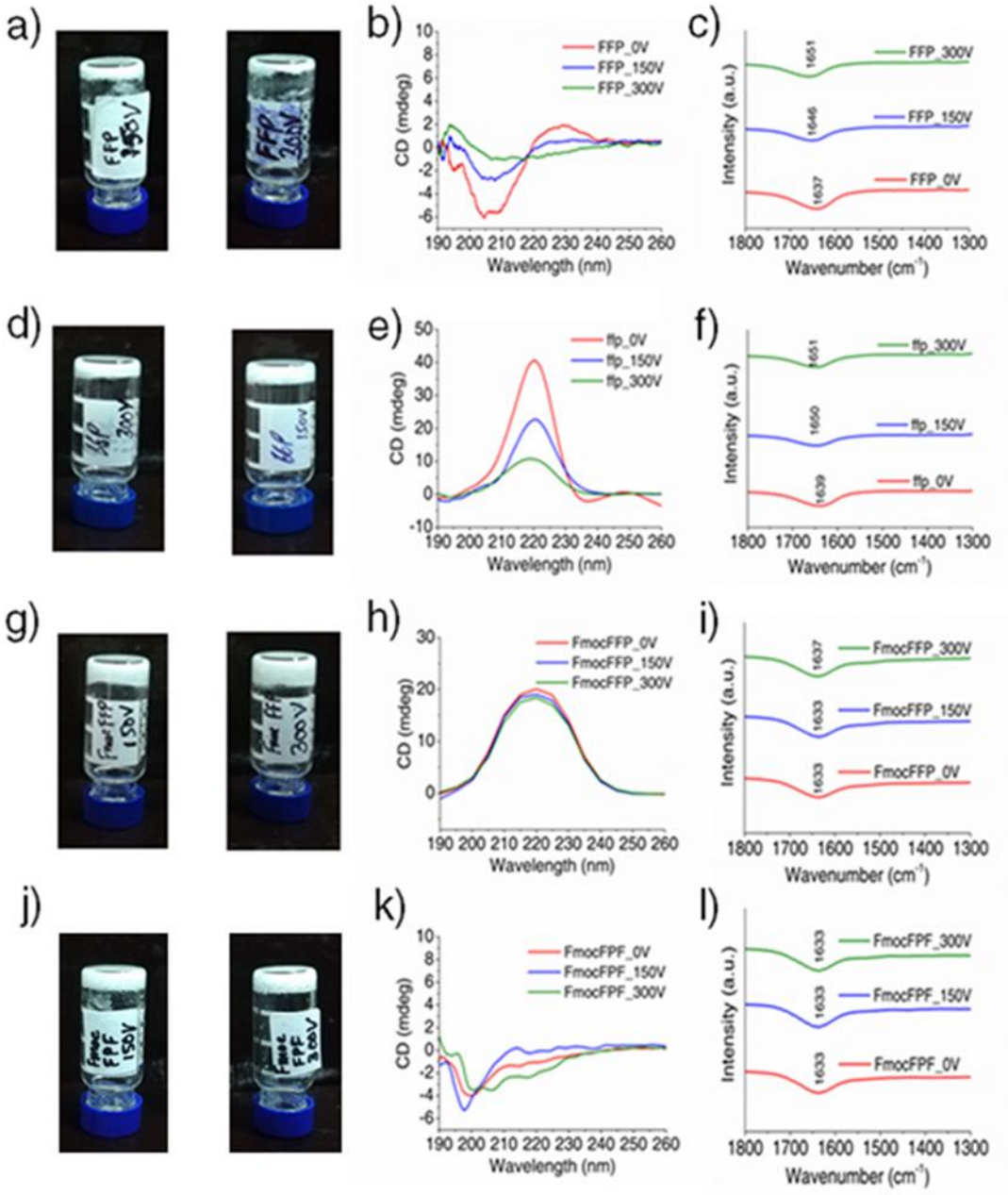

Figure 4.4. Characterization of the hydrogels. (a) Vial inversion test of FFP hydrogel formed in the presence of 150 and 300Vcm^{-1} (b) Superimposition of the CD spectra of FFP in 0 (red), 150(blue) and 300 Vcm^{-1} (green). (c) FTIR spectra of FFP peptide in 0 (red), 150(blue) and 300 Vcm^{-1} (green). (d) Vial inversion test of ffp hydrogel formed in the presence of 150 and 300 Vcm^{-1} (e) Superimposition of the CD spectra of ffp peptide in 0 (red), 150(blue) and 300Vcm^{-1} (green). (f) FTIR spectra of ffp peptide in 0 (red),150(blue) and 300 Vcm^{-1} (green).(g) Vial inversion test of Fmoc-FFP hydrogel formed in the presence of 150 and 300 Vcm^{-1} (h) Superimposition of the CD spectra of Fmoc-FFP peptide in 0 (red),150(blue) and 300 Vcm^{-1} (green). (i)FTIR spectra of Fmoc-FFP peptide in 0 (red), 150(blue) and 300 Vcm^{-1} (green). (j) Vial inversion test of Fmoc-FPF hydrogel formed in the presence of 150 and 300Vcm^{-1} (k) Superimposition of the CD spectra of Fmoc-FPF peptide in 0 (red), 150(blue) and 300Vcm^{-1} (green). (l) FTIR spectra of Fmoc-FPF peptide in 0 (red), 150 (blue) and 300 Vcm^{-1} (green).

external electric field on diphenylalanine moiety.[187, 317] The CD spectra of **Fmoc-FFP** peptide is eclipsed by the predominant cotton effect arising at 222nm. Samples were further verified using FTIR in the amide-I region. Among the control samples, **PFF**, **pff**, **Fmoc-FFP**, and **Fmoc FPF** showed a signal maximum centered around 1633cm^{-1}, suggesting a beta-conformation (red, Figure 4.3. and Figure 4.4.). The IR absorbance signal for the **FFP** and **ffp** samples is slightly red-shifted at around 1637cm^{-1}(Figure 4.4. (c) and (f)). Gels formed by **PFF**, **FFP**, **ffp** peptides in the presence of EF and 300Vcm^{-1} in particular show bands typical of non-β conformation (1642-1651cm^{-1}) (Figure 4.3(d); Figure 4.4(c) and (f)). The FTIR spectra of the **pff**, **Fmoc FFP**, and **Fmoc-FPF** peptides did not show a significant change in their band position even after 12h incubation in the EF and is comparable to the control blue for 150 Vcm^{-1} and 300 Vcm^{-1} Figure 4.3-4).

4.3.4. Modulation of peptide hydrogel morphology using electric field. Field emission scanning electron microscopy (FESEM) was used to analyze and contrast the nanostructures within the peptide hydrogels. As illustrated in (Figure 4.5-6), the fibrils of **FFP** are rigid without noticeable cross-linking. On the other hand, the **PFF** (Figure 4.5(a)), **Fmoc-FFP**, and **Fmoc-FPF** hydrogel (Figure 4.6(g) and (j)) show extensive cross-linking at physiological pH. The fibrils of **PFF**, in particular, appear thick with a diameter of approximately 1μm. In contrast, **pff** and **ffp** peptides show highly branched structures without any cross-linking (Figure 4.5-6). The application of EF during the self-assembly, in general, resulted in substantial alteration in the hydrogel morphology. **FFP** samples treated with 150 Vcm^{-1} showed a uniform and compact fibrillar network. The homogeneity in the fibril structure further increased in the 300 Vcm^{-1} treated samples. (Figure 4.6 (b and c)). At 300 Vcm^{-1}, the **PFF** gel showed highly cross-linked fibrils. The fibrils, however, appear thin in comparison to the control (Figure 4.5(band c)). No remarkable difference was observed in the FESEM micrograph of EF treated **pff** and **ffp** hydrogels and is similar to the control (Figure 4.5 (e and f), Figure 4.6 (e and f)). Among the set 3 peptides, the increase in the EF strength showed a gradual decrease in the cross-link density of the **Fmoc FFP** hydrogel, while **Fmoc FPF** gel showed extensively branched filaments, crossing over without cross-linking resulting in fibrillar entanglements (Figure 4.6(h, i and k, l).

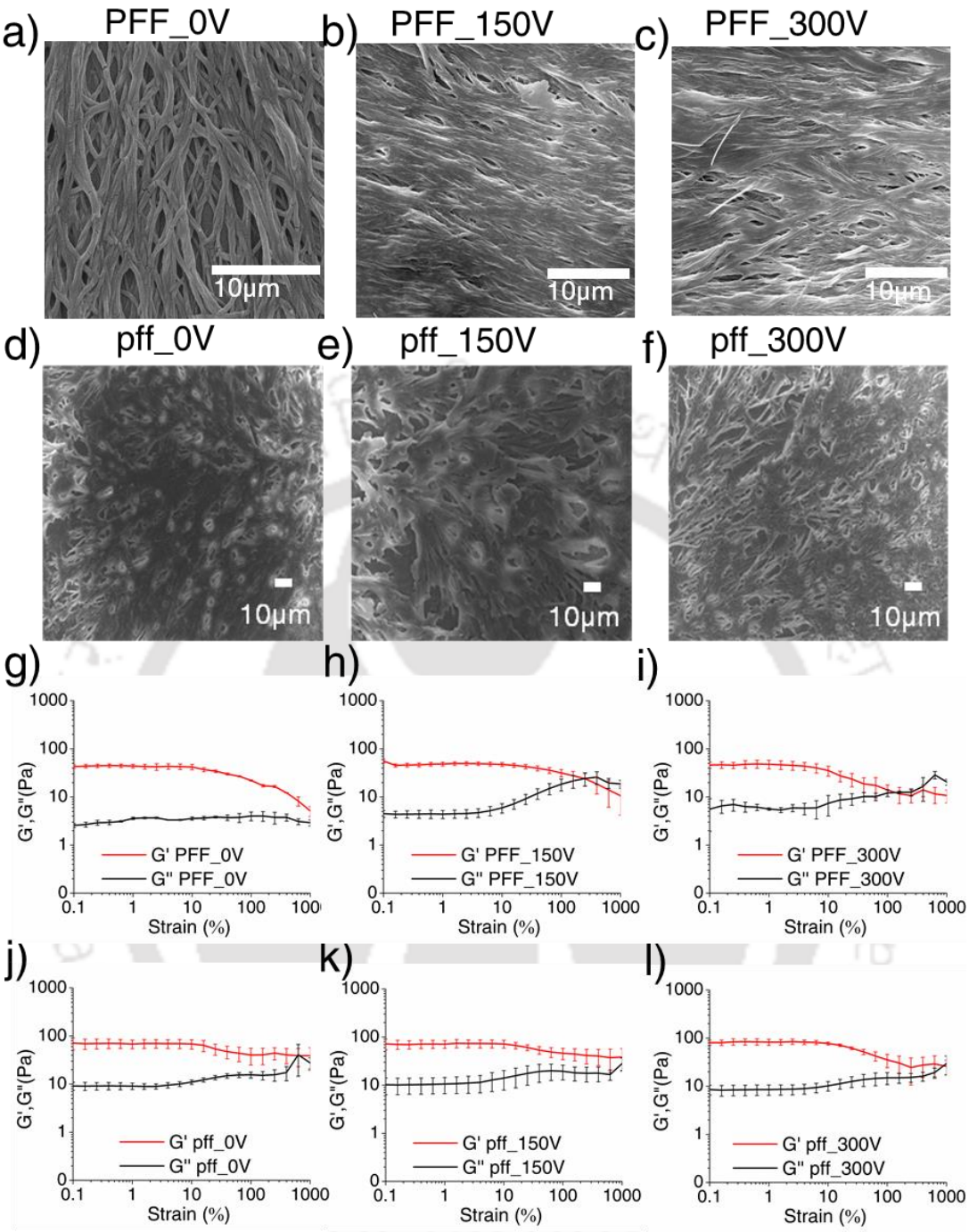

Figure 4.5. Morphological and viscoelastic characterization of the peptide hydrogel. Figures (a-f), showing FESEM images of **PFF** and **pff** hydrogels formed in 0, 150 and 300 Vcm^{-1}. Figures (g-l), showing amplitude sweep rheological measurements (storage modulus *G'* and loss modulus *G''*) of **PFF** and **pff** hydrogels performed at a gap of 0.5mm, in 0, 150 and 300 Vcm^{-1}. The error bars represent the standard errors of three independent observations.

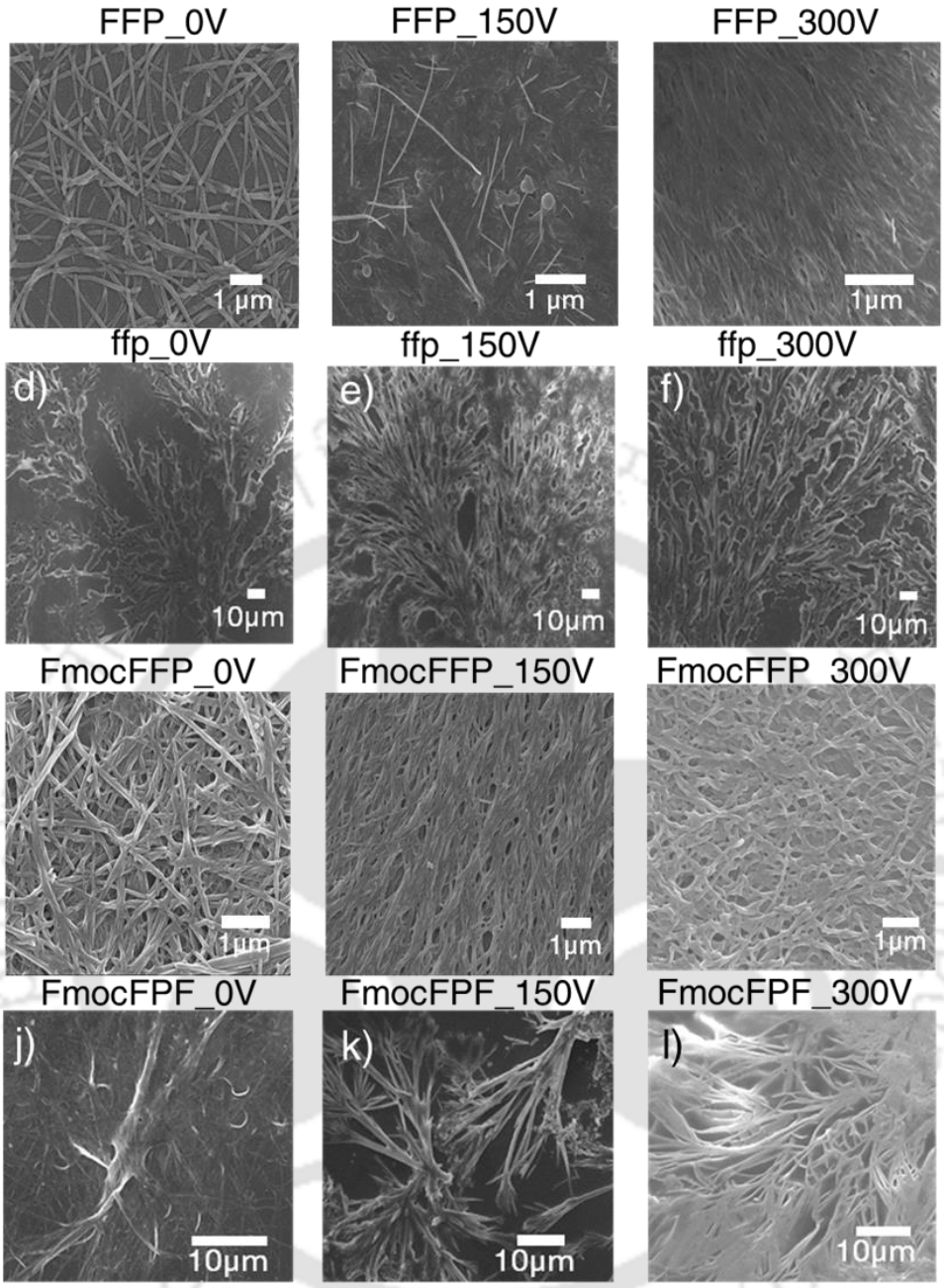

Figure 4.6. Morphological characterization of the gel forming peptide assemblies. FESEM images (a-c) of FFP hydrogel formed in 0, 150 and 300 Vcm^{-1}. The ffp hydrogel formed in 0, 150 and 300 Vcm^{-1} (d-f). Fmoc-FFP hydrogel formed in 0, 150 and 300 Vcm^{-1} (g-i) and Fmoc-FPF hydrogel formed in 0, 150 and 300 Vcm^{-1} after 12h of incubation under ambient conditions.

4.3.5. Modulation of visco-elastic properties by electric field. Next, the viscoelastic property of the hydrogels was assessed by amplitude sweep rheometry. For all the gels, storage moduli (G') were greater than loss moduli (G'') confirming the gel character of the resulting networks.

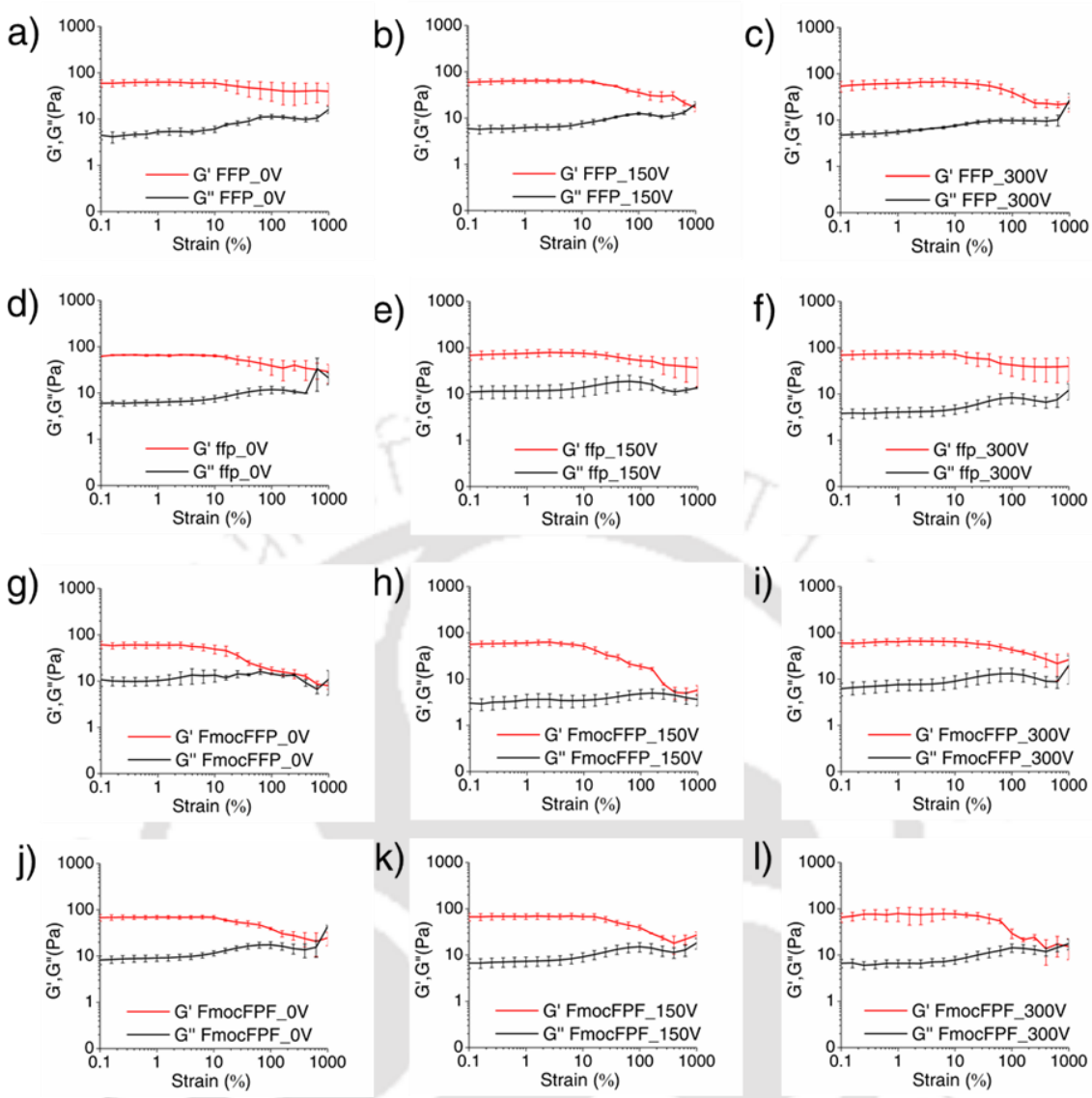

Figure 4.7. Amplitude sweep studies were carried out from 0.01 to 1000 % strain at a frequency of 10 rad s^{-1} at 25 °C. Storage *G'*(red) and loss *G''* (black) moduli of (a-c) FFP, (d-f) ffp (g-i)Fmoc-FFP and (j-l) Fmoc-FPF peptide hydrogels formed in the absence (0 Vcm^{-1}) and presence (150 and 300 Vcm^{-1}) of the external electric field. The error bars represent the standard errors of three independent observations.

In the case of set 1 peptides, the storage modulus (G') was low for **PFF** and **FFP** (42 and 59 Pa respectively) with γ_c at 10% Figure 4.5(g) and Figure 4.7(a)). Among the set 2 peptides, **pff** formed a stiffer gel (G'=80Pa and γ_c= 13%) while the G' of **ffp** reached 62Pa with γ_c of 10% (Figure 4.5(j) and Figure 4.7 (d)). In the case of set 3 peptides, **Fmoc-FFP** and **Fmoc-FPF** has a G' of 61 and 68Pa respectively. The γ_c for both the hydrogels was found to be 10%.

(Figure 4.7 (g, j)). The G' of the Fmoc- containing peptides is lower than the **pff** peptides. This may be due to steric interactions between bulky Fmoc-systems during self-assembly.[37]

Next, the visco-elastic properties of the hydrogels formed in the presence of EF are tested. In the case of set 1 peptides, the hydrogel formed by **FFP** in 150 and 300 Vcm^{-1} showed marginally lower G′ (53 Pa) while compared to the untreated sample. No difference was observed in terms of their γ_c (Figure 4.7(b and c)). The gel formed by **PFF** is inherently soft, and no remarkable difference was observed in the G' in the presence of EF (50 Pa) (Figure 4.5 (h and i)). However, the sample exposed to 300 Vcm^{-1} has a significantly reduced γ_c of 6% compared to the untreated sample. Among the set 2 peptides, application of field showed no effect on the **ffp** hydrogel (Figure 4.7 (e and f)). However, the rheology of EF-treated **pff** hydrogel shows a similar trend like the all L-analog where the γ_c has decreased to 10% (Figure 4.5(k and l)). Among the set 3 peptides, an opposite effect of the EF was observed in the case of **Fmoc-FFP** hydrogel. It showed an increased γ_c (18%) for the sample treated with 300 Vcm^{-1}. However, the storage modulus of the **Fmoc-FFP** hydrogel remains unchanged at 59 Pa (γ_c =10%), even at higher EF (Figure 4.7 (h, I and k,l)).

Further, we wanted to study the effect of hydrogel network size and substrate diffusivity on the observed difference in the catalytic efficiency of the EF treated and untreated hydrogels. The substrate diffusivity in a gel is determined by the structure of the gel, which in turn affects the functions and performances of the gel. The diffusion coefficient (D_g) value in the case of a macroporous gel is greater than that of a non-porous gel and consequently may be a more robust catalyst. The correlation of the substrate diffusivity with the structural parameters and characteristics of a polymeric hydrogel, e.g., volume fraction, is a promising tool to understand the extent of porosity.[343] In order to examine that, we performed a standard experiment to examine the release of anticancer drug, doxorubicin from the hydrogels with respect to time. Figure 4.8 shows the release of doxorubicin from the EF treated and untreated hydrogels at 0,1,3,5, and 48th hour of incubation. The hydrogels of all the samples formed in the presence and absence of external electric field, showed sustained release of the drug. The maximum drug concentration in the solution was recorded after 3h of incubation. Interestingly, pff hydrogel in particular, showed marginally less drug release (60%) compared to its all L-analogue (67%).

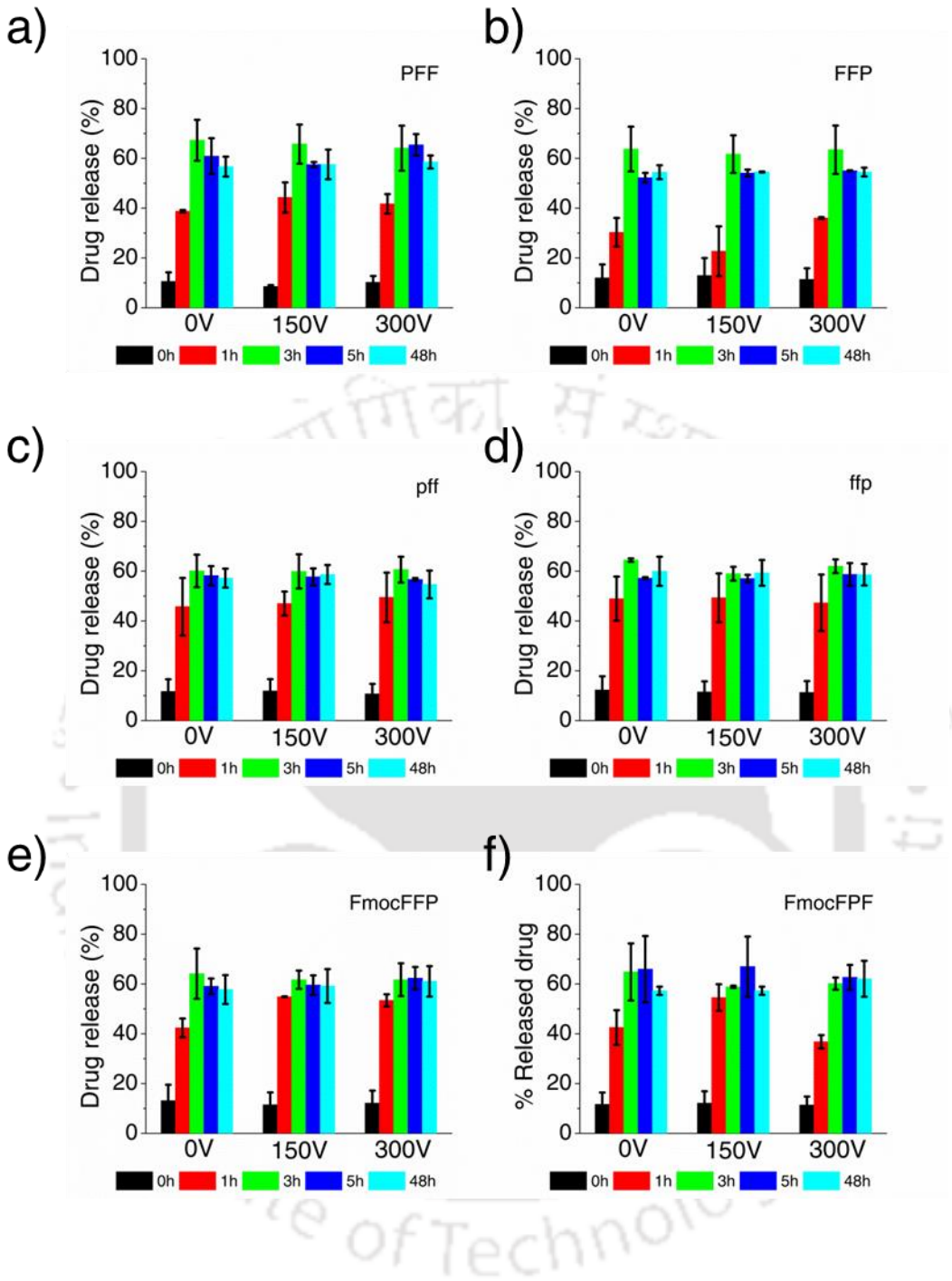

Figure 4.8.: Doxorubicin release assay: Doxorubicin release kinetics from EF treated and untreated gels a) PFF b) FFP c) pff d) ffp e) Fmoc-FFP and f) Fmoc-FPF as determined by monitoring the absorbance at 490 nm. The error bars represent the standard deviation of three independent observations.

This corroborates with the rheology findings that show higher storage modulus for pff gels. Overall, this experiment suggests that there is little to no difference in the substrate diffusivity among the EF treated and untreated samples and any difference observed in the catalytic

efficiency of the gel may be attributed to the 'confinement effect' in and around the catalytic residue.[344] The decrease in the doxorubicin concentration in the solution at 5th and 48th h may be attributed to photo degradation of the dye.[345,346]

4.4. DISCUSSION

4.4.1. Role of peptide sequence in catalytic hydrogel formation. All the gel-forming peptides contain predominant π-π stacking interactions either through the di-phenylalanine motif as in **PFF**, **FFP**, **ffp**, **pff** or due to the presence of a bulky aromatic Fmoc-group in the sequence. The powerful forces of π-π stacking in governing the self-assembly of sophisticated nanomaterials have been extensively reported.[173,174,31,32,347] Quadrupolar interaction mediates the self-assembly involving phenyl rings through parallel displaced and T-shaped configurations for maximum stability.[73] The lack of any ordered nanostructure for **FPp**, **FPF**, **FpF** further highlights the significance of quadrupolar interactions in the assembly of short peptides. Besides, the insertion of D-amino acids in the peptide sequence is a convenient approach to generate bioactive motifs.[67] In a recent study, Garcia et.al. studied eight possible Pro-Phe-Phe stereoisomers that formed hydrogels at physiological pH, by exploring divergent programming elements to direct supramolecular behaviour, based on the strategic use of heterochirality.[348] However, such was not the case with our designed peptides as none of the heterochiral peptides formed hydrogel in ambient conditions. This may be attributed to the effect of a single D-proline residue that promotes type II' turn.[67] The β-turn induced by proline residue may be hampering the gel formation.

4.4.2. Effect of the position of proline residue and stereochemistry on catalysis. Terminal proline containing peptides bearing an adjacent hydrophobic phenyl group showed superior catalytic activity.[331] In an efficient catalytic hydrogelator, the aromatic amino acids are more favorable in positions 2 and 3 to the N-terminal amino acid, while the proline is favored in position 1.[70] This could be because of its unique conformational properties allowing better packing of the short peptides. Such peptides are reported to have enhanced product yield.[340] In our case, a similar effect has been observed from the faster conversion rate in **PFF** hydrogel (> 90% conversion in 48h). However, the tripeptide has low *ee* (57 %),

suggesting a non-productive interaction of the hydrophobic side chain on streoselectivity. The **FFP** gel showed a moderate conversion rate but remarkably high *ee* (97%) and this is in agreement with already reported findings.[304] Having a D-proline in the terminal position is sufficient to achieve altered streoselectivity for **pff** and **ffp** peptide hydrogels.[331] The enantiomeric preference of the reaction was governed by the chirality of the terminal proline. The *ee* % of the product correlates to the moderate reaction rate of the hydrogels. **Fmoc-FFP** and **Fmoc-FPF** have a relatively low reaction rate (70% conversion in 94h). The hydrophobic region is indeed relevant for self-assembly and substrate solubilization, but the accessibility of the active site is the key factor for the observed differences in reaction rate and selectivity (74 and 71 *ee*% respectively).[304]

4.4.3. Effect of EF on the peptide hydrogels. External modulation can only be effective when a self-assembling system contains specific moieties whose physical and chemical properties can potentially be altered using an external stimulus. Theoretical studies suggest that the π- electrons responsible for directing self-assembly through the π- π stacking interactions, are prone to polarization in the presence of external EFs.[175] Application of adequate field strength should change their electrostatic and dispersive contributions to the non-covalent interactions. This may lead to the generation of field-induced anisotropy in the system.[175] Earlier, we have experimentally demonstrated the modulatory effect of external EF on the self-assembly of the aggregating peptides.[187, 193, 317] There are reports suggesting that methods such as dielectrophoresis exert EF stimulus on the nanostructure during self-assembly to influence the alignment of FF nanotubes.[349] Although the mechanism of electric field effects is not completely understood, it is believed that fields of specific frequency and intensity can excite certain vibrational modes of a macromolecule, which alters its conformation.[175] High-magnitude fields separate the polar end groups (COO^- and $NH3^+$) by a further average distance, and thus they stretch the backbone forming a conformational state with very close side chains and to experience additional favorable, the π-stacking interactions. The extent of such backbone stretch depends on the dipole strength and its position.

Nanostructures are made from periodic lattices of the peptide monomers.[175] We hypothesize that the application of an electric field across the peptide assembly would distort and rigidify its lattice, with direct effects on the elongation or contraction of the fibrillar dimensions and its

orientation. Any physical factor (e.g., change in temperature and pH) that significantly alters the probabilities of the peptide conformational states also distort the aggregate lattice that result in a change in assembly morphology. An external electric field of adequate strength is likely to offer one of the most sensitive ways to modulate and control the self-assembly process.

In an earlier published article, using high-resolution micro-Raman spectroscopy, our lab has tested the integrity of the diphenylalanine peptide assemblies formed in the presence of external electric field. [187] Similar characteristic Raman bands were observed in the field with EF treated and the untreated samples suggesting that there is no alteration in the chemical composition of the peptide. This was further verified using powder XRD of the samples. No spurious peaks were observed in the X-ray diffraction pattern of the electric field treated samples which confirms the integrity of diphenylalanine nanoassembly. Interestingly, however, the electric field treated samples differ in their lattice parameters.

In this study, we have investigated the effect of EF on the peptide hydrogels in terms of their structural, morphological, and rheological properties to further corroborate with the change in the catalytic efficiency. The CD and FTIR spectra of the field-treated samples, 300Vcm^{-1} in particular, suggest a gradual transition from their inherent structures in some of the tested samples. Since the π electrons are prone to polarization by external electric fields, we reason that the applied EF has successfully altered the electrostatic and dispersive contributions to the non-covalent interactions. The FESEM analysis reveals that the absence of external EF facilitated an organized network of intervening fibrils. However, the fibril morphology of the EF-treated hydrogels appeared rigid with less branching. This may be due to the alignment of the peptide dipoles under the influence of the EF, thus preventing random orientation and modulating the peptide in a single conformational state. This will alter the inter peptide hydrogen bonding during self-assembly. The effect of alternation in the hydrogen bonding in a gelating supramolecular assembly is manifested in gel strength and stability.[350] Our rheology experiments with all the uncapped gel-forming peptides (**FFP**, **PFF**, **ffp**, and **pff**) show that the EF application of adequate strength leads to a decrease in the G', compared to the control. The applied field effect is not prominent in modulating the molecular structure and morphology of the two Fmoc- containing peptides. This suggests that the influence of EF

depends on the size of the π-conjugated system, and the applied field may be inadequate to overcome the energy of the π-conjugated system.

The net dipole of the four molecules **FFP, PFF, ffp** and **pff** are different (Figure A3.10). Consequently, they may be modulated differently while forming the supramolecular assemblies and this may further affect the catalytic efficiency and enantioselectivity. Notably, in majority of the cases, the modulatory effect of the external electric field on the formation of local and supramolecular structures is limited. At times, the change in the structure as in the case of **FFP** or **ffp** (Figure 4.6) may not translate into a difference in the catalytic efficiency and selectivity as well.

4.3.8. Improved streoselectivity in EF-treated PFF and pff hydrogels. The catalytic mechanism for proline-based catalysts, proceed by forming an enamine intermediate between the catalyst and the ketone. A coherent mechanistic rationalization of the role of water in aldol reactions employing aromatic aldehydes shows that water suppresses the reaction rate and retard the formation of key intermediates in the cycle.[351] Therefore, based on our observations, we hypothesize that the external EF treated **PFF** and its stereochemical variant **pff** gel has undergone structural changes at the molecular level, resulting in a stabilizing hydrophobic interaction around the catalytic moiety. This may have resulted in a tailor-made catalytic site that could drastically improve the streoselectivity of the reaction. Our hypothesis is supported by earlier reports suggesting that positioning of hydrophobic functional groups can significantly stabilize transition states through hydrophobic interactions in water. Pelin et.al. have demonstrated the dependence of the peptide morphology on the stereoselective aldol reactions.[352] They have found that the folding pattern of the chiral peptides play determined the reactants' access to the active sites. Stepwise incorporation of more groups could lead to proline containing aldol catalysts with even greater activity.[331]

Among the two peptides (**PFF** and **pff**), there is observable difference in their streoselectivity. This may be explained on the basis of proline-based catalysis. Enamine is formed from the pyrrolidine nitrogen and the carbonyl donor. The iminium ion, created by attack of the enamine on the re-face of the aldehyde, is subsequently hydrolyzed to afford chiral β-hydroxyketone.[353] The enamine attacks the re-face of the aldehyde. The facial selectivity is dictated by minimizing steric interactions between the aldehyde substituent and the enamine

substituent. Therefore, attack of the enamine on the *si*-face of the aldehyde leads to the opposite and less stable transition state. Besides, the stereochemistry is also controlled by hydrogen transfer between the oxygen of the aldehyde and the carboxylate of proline residue, thus limiting the choice to one face, while enamine attacks the aldehyde.[354]

In case of the designed peptides containing D-amino acid (**pff** and **ffp**) the're-face' may be restricted by steric interactions between the phenylalanine's aromatic ring and the proline ring. The decreased rate of reaction in the case of **pff** (94h) while compared with **PFF** (48h) is in line with previous reports, suggesting that the yield of the product differ considerably with the proline structure.[355, 356] In the case of direct asymmetric aldol reaction between *p*-nitrobenzaldehyde (*p*NBA) and acetone, the D-Pro derivative drastically reduced the reaction yield.[322] List et. al have earlier reported that L-Pro shows increased reactivity of the enamine intermediate, suggesting that the enamine composed of L-Proline (or its derivatives) shows higher reactivity, compared to the D-Pro derivatives.[322]

4.5. CONCLUSIONS

This investigation on catalytic peptide hydrogels, focus on two experimental variables of chemical origin in the first phase. The effect of subtle change of amino acid position and their chirality on the gel-forming propensity of the peptides has been examined. The major driving forces for the observed gelation in six peptide sequences are hydrogen bonding and π–π interactions mediated by the FF motif or the attached Fmoc-group. We hypothesize that non-covalent interactions based on electrostatics can be modulated using external electric field. We have demonstrated that the **pff** and **PFF** peptide hydrogels formed in the presence of EF in particular, showed a remarkable 10 and 30 % increase in their respective *ee* estimates compared to the control. Structure-property relationship studies using CD and FTIR spectroscopy show a β to non-β conformational transition in 300 Vcm^{-1} treated samples. This is in corroboration with the observed morphology of the fibrils that shows reduced cross-link density and filament width in the field. The viscoelastic property of the gels, in general, exhibited decreased storage modulus in the presence of the EF. Doxorubicin release assay suggests that the diffusivity of the substrate has no correlation with the catalytic rate and streoselectivity in EF treated and untreated samples. Modulation of the external EF in directing

molecular assembly and its functional properties may open up new possibilities in using physical perturbants, and rational design of tunable, stimulus responsive peptide hydrogels using small peptides.

5.

Effect of Electric Field on Aggregation and Amyloid formation; Potential Non-invasive therapy for Alzheimer's Disease

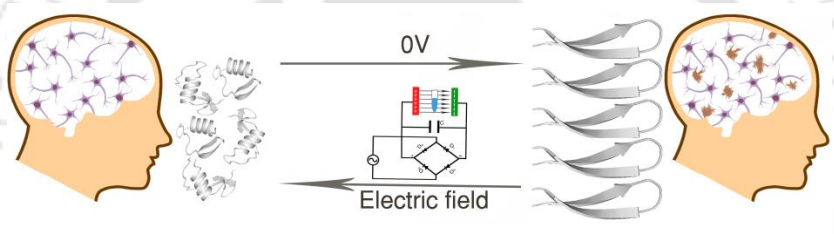

Aggregation of β-amyloid peptides is a key event in the formative stages of Alzheimer's disease. Promoting folding and inhibiting aggregation was reported as an effective strategy in reducing Aβ-elicited toxicity. In this chapter, we have experimentally investigated the influence of the external electric field (EF) and magnetic field (MF) of varying strengths on the in-vitro fibrillogenesis of hydrophobic core sequence $A\beta_{16-22}$ and its parent peptide $A\beta_{1-42}$. We have employed various biophysical methods such as ThT fluorescence, static light scattering, Dynamic Light Scattering (DLS), Circular Dichroism (CD) and Infrared spectroscopy to analyse the modulatory effect of EF. Further, Aβ elicited toxicity of EF treated samples were tested in two neuroblastoma cell lines (SH-SY5Y and IMR-32) and human embryonic kidney cell line (HEK293). Our results provide a scientific roadmap for future non-invasive, therapeutic solutions for the treatment of Alzheimer's disease.

5.1. INTRODUCTION

Alzheimer's disease is an age-related prototypical protein misfolding disease and a major unmet medical need, because of its prevalence, severity, cost, and lack of mechanism-based treatments. AD is the most common type of dementia and accounts for 80% of dementia-related cases reported annually.[357] Misfolding of β-amyloid proteins followed by their fibrillization and deposition as senile plaques in the grey matter of the brain is the hallmark of Alzheimer's disease. Such depositions lead to dysfunction and even death of neurons in specific regions of the brain that are important for memory and cognition. Recent discoveries have highlighted that the early oligomer intermediates rather than the matured fibrils are primarily responsible for severe neuro-degeneration.[358, 359] The lack of a clear understanding of the mechanism of disease progression is probably the main reason for non-availability of an effective therapeutic solution. However, an *in-vivo* conformational transition from αα (helical) to β conformation is identified as a key step in Aβ fibrillogenesis.[360, 361] Aβ results from the proteolysis of the amyloid precursor protein (APP). At the onset of the amyloidogenic pathway, β-secretase cleaves the APP between Met671 and Asp672. This is followed by the action of γ-secretase to produce $A\beta_{40}$ and $A\beta_{42}$, which subsequently aggregate to form oligomers or fibrils.[362] Efforts to design an effective clinical agent have been concentrated on three different strategies; design of inhibitors to block the expression of APP,[363] prevent the proteolytic cleavage of APP into Aβ and clear various Aβ fibrillar aggregates from the brain.[364, 365] To date, the most exciting report regarding the clearance of Aβ came from studies using active and passive Aβ immunotherapy. However, several problems have been associated with Aβ immunotherapy, including brain hemorrhage in the presence of congophilic angiopathy and even meningoencephalitis.[366] Another attractive therapeutic strategy for the AD is to develop a series of β-sheet breaker peptides based on the stereochemical structure of $A\beta_{1-42}$, which may destabilize the amyloidogenic Aβ conformer and thus precluding amyloid formation.[367, 368] However, the major disadvantage of using peptide-based drugs is their metabolic instability and poor permeability through the blood-brain barrier (BBB). Nonetheless, the development of 'invasive' or 'non-invasive therapeutic solutions that can overcome present drawbacks, at least in part, that can benefit AD patients has not been achieved so far. Analysis of peptide-based nanostructures indicates that side-chain aromatic π-π interactions are responsible for providing the energetic stability, order, and directionality to the

supra-molecular architecture.[369] Diphenylalanine, a fragment of $A\beta_{1-42}$ protein is the most extensively studied short peptide segment that can self-assemble into highly ordered nanotubes/microtubes, microcrystals, vertically aligned nanowires and nano-forests in different conditions.[32, 369] Interestingly, many truncated and shorter fragments of Aβ peptide such as KLVFFAE ($A\beta_{16-22}$) and KLVFF ($A\beta_{16-20}$) are also known to form fibrils in-vitro[370, 371] and have a crucial role in the fibrillization process of $A\beta_{1-42}$.[372, 373]The hydrophobic core of Aβ (LVFF, $A\beta_{17-20}$) has been proposed to be the key sequence for the β-sheet conformation and the diphenylalanine sequence ($A\beta_{19-20}$) is critical for fibrillization.[79, 374]

Protein misfolding occurs when it gets trapped in an off-pathway potential energy minimum that leads to a series of stable intermediates culminating in the formation of an amyloid aggregate.[375, 376] Last decade has witnessed an increase in the use of modified physiological conditions like temperature,[377] pH,[378, 379]or solvents[380] to perturb protein aggregation. Recently, microwave radiation has been reported to promote aggregation and amyloid fibril formation in bovine serum albumin in a time-dependent manner.[381] Leinenga et al. reported the use of repeated scanning ultrasound (SUS) for removing Aβ plaques from the brain of AD mice.[199] Such studies have accelerated the initiative of developing non-invasive and adjuvant therapeutic solutions for the AD. Several studies, investigating the effects of external electric[178-182, 185, 382, 383] and magnetic fields,[384] have shown irreversible structural changes in various proteins and peptides due to the peptide dipole alignment along the direction of the applied field. This results in the disruption of an inherent β-hairpin conformation, which is found to be the intermediate state for fibril formation of an amyloidogenic peptide. Modelling studies by Ojeda-May and Garcia predicted that a transition from a β-sheet into a helix-like conformation could be induced by a constant electric field.[181] They attributed this observation as a result of a global rearrangement of the dipole moments at the amide planes. Electric fields can induce rotational motion of molecules with a dipole moment, thus aligning the dipole in the direction of the field vector. Decade-long studies on the effect of the external electric field on biological molecules have led to two prominent mechanisms in molecule-field interactions. First, protein molecules with permanent or induced dipoles tend to align along the axis of the applied field. Second, due to the direct interaction of the molecular dipoles with the field, conformational transitions may occur and conformations with larger dipole moments gain more statistical weight from the external field than those with smaller moments. Porchke reported a

cooperative change in the bacteriorhodopsin structure, induced at a remarkably low field strength of 150 Vcm^{-1}.[385] Recently, Hill et al. demonstrated the alignment of FF tubes in the presence of a very strong magnetic field in the range of 10 – 15 T.[132] The alignment in response to an applied magnetic field was attributed to the effect of a magnetic torque associated with the diamagnetic anisotropy of the phenylalanine aromatic ring. In addition to this, the ordered arrangement of the peptide backbone also contributes to the net diamagnetic anisotropy of the nanotube.[386] We have earlier reported the modulation of chemical and structural properties of diphenylalanine peptide nano-assembly using an external electric and magnetic field .[387] Our study has demonstrated that the electric field can effectively arrest aggregation and self-assembly of diphenylalanine, the core aggregating segment of amyloidogenic sequence. This result prompted us to investigate the effect of an electric and magnetic field on Ac-KLVFFAE-NH_2 ($A\beta_{16-22}$) and $A\beta_{1-42}$ under similar conditions. This study primarily focuses on the potential use of an electric field based device as a non-invasive therapeutic option and a roadmap for a futuristic device.

5.2. EXPERIMENTAL SECTION

All chemicals used were of analytical grade. The $A\beta_{1-42}$ peptide was synthesized with the help of an automated peptide synthesizer (Protein Technologies, Tucson, AZ) using Fmoc chemistry. Ac-KLVFFAE-NH_2 ($A\beta_{16-22}$) peptide was synthesized manually using Fmoc chemistry in the laboratory. $A\beta_{1-40}$ and FITC-$A\beta_{1-42}$ were purchased from GL Biochem. (Shanghai) Ltd (Shanghai, China) and further verified with MALDI-TOF. The cerebrospinal fluid (CSF) samples were gifted by Guwahati Medical College and Hospital, Guwahati, India and were obtained as part of routine care from patients. Nonetheless, information on explaining the purpose of this study was specified at the time of sample collection adhering to the bioethics policy of the hospital.

5.2.1. Preparation of peptide monomers. Peptides were disaggregated using trifluoroacetic acid/1,1,1,3,3,3-hexafluoro-2-propanol (TFA/HFIP) by an already reported method. Briefly, 0.5 mg of $A\beta_{1-42}$ was dissolved in 1 mL of TFA to obtain a homogeneous solution free of aggregates. Aliquots of 30 µL were transferred equally to several 0.5 mL Eppendorf tubes. TFA was then evaporated using nitrogen gas. Any left-over TFA was further

removed by HFIP, followed by evaporation in a vacuum desiccator to obtain a film-like material. HFIP treatment was repeated twice. The peptide was dissolved in phosphate buffer (50 mM, pH 7.4) for all the experiments.

5.2.2. Pre-aggregation verification. The absence of any pre-aggregates in TFA/HFIP treated peptide stock solution of all the samples were verified by 90° static light scattering (λ_{Ex}:450 nm, slit width = 2.5 nm; λ_{Em}:450 nm, slit width = 2.5 nm) using a spectrofluorimeter (Jasco FP 8500).[388]

5.2.3. Electric Field setup. For the DC field setup, two parallel aluminium electrodes separated by a distance of 1 cm were anchored to a plate; which is then connected to a full-wave bridge rectifier. The voltage is regulated using a single phase variable autotransformer. The AC field setup is similar to DC field setup, but without a full-wave bridge rectifier.

5.2.4. Electric and Magnetic Field Experiments. Two different electric field set up generating field strength of 150, 300 Vcm^{-1} (DC) and 150, 300 Vcm^{-1}, $50Hz^{-1}$ were used for the experiments. In the magnetic field set up, the field strength was set at 0.8T for all the experiments. $A\beta_{16-22}$ (500 μM) was incubated in the field for 16 h, while $A\beta_{1-42}$ (100 μM) had an incubation time of 24 h. No external field is applied to the control experiment.

5.2.5. 90° Light Scattering Assay. The aggregation reaction was monitored by 90° light scattering at regular intervals of time. Both control and field exposed samples (600 μl) were placed directly in a fluorescence cuvette (Helma, Sigma Aldrich) with 1 cm path length and 90° scatter intensity in kilo counts/s was recorded (excitation λ= 450 nm, slit width = 2.5 nm; emission λ = 450 nm, slit width = 2.5 nm) using a Jasco FP 8500 spectrofluorometer.

5.2.6. ThT fluorescence assay. ThT dye was added to the peptide sample immediately after taking it out from the field to make a final concentration of 20 μM. Fluorescence measurements were recorded in a Horiba Florimax-4 spectrofluorimeter at 25 °C using quartz cuvette with 1 cm path length. The relative ThT fluorescence of the samples is measured. (λ_{Ex}:440 nm; slit width=2 nm and λ_{Em}:485 nm; slit=5 nm).

5.2.6.1. Experiments with pre-aggregated peptides. $A\beta_{1-42}$ (100 μM) in PBS (50 mM, pH 7.4) was allowed to aggregate in ambient conditions for 12 h. Subsequently, the samples were placed in the electric field. The control sample was not exposed to any field. The 0^{th} h in Figure

5.3b is the time when the samples are first placed in the field. Thereafter, the ThT fluorescence was recorded at regular time intervals.

5.2.6.2. Experiments with Human Cerebrospinal Fluid. Fresh human CSF was collected from healthy individuals (with no history of Alzheimer's disease) within the age group of 35-40 years. CSF from 6 subjects (three aliquots per subject for three experimental cases; 0, 150 and 300 Vcm^{-1}) were immediately frozen and kept at -80°C until further analysis. All three aliquots were analyzed after they were vortexed for 15 sec to prevent precipitation. ThT fluorescence of the native proteins present in the CSF was measured by adding 12 µL of 1 mM ThT to 600 µL of CSF to get a final concentration of 20 µM. The fluorescence intensity was recorded as mentioned earlier and was subtracted from all future experiments on CSF. Effect of electric field on aggregation of $A\beta_{1-42}$ (100 µM) in 600 µL CSF was achieved by adding 0.27 mg of $A\beta_{1-42}$ to the CSF directly and mixing to a homogenous solution. The samples were then incubated in the presence of the electric field of various strengths (both AC and DC).

5.2.6.3. Pre-seeded aggregation assays. $A\beta_{1-42}$ peptides were dissolved in PBS to reach a final concentration of 100 µM. To generate fibrils, the peptides were incubated at room temperature for 24 h. Seed solutions were made by subjecting the fibrils to shear. The reactions were initiated by adding 1% of the pre-aggregated seeds to 100 µM of peptide monomers or field treated samples and fibril growth was monitored by ThT fluorescence as described. The dead time between mixing the protein solution with the seeds and start of the measurements was usually 1 minute.

5.2.6.4. Cross-seeding experiments with $A\beta_{1-40}$ and $A\beta_{1-42}$. Cross-seeding experiments were performed adopting the earlier reported procedures.[52] Briefly, $A\beta_{1-40}$ fibril seeds were subjected to shear before adding 16% of the monomer-equivalent concentration to the EF treated $A\beta_{1-42}$ (100 µM) samples. The progress of aggregation was monitored using thioflavin T (20µM) at 0^{th}, 12^{th}, and 24^{th} h respectively. Fluorescence measurements were recorded in a Horiba Florimax-4 spectrofluorimeter at 25 °C using quartz cuvette with 1 cm path length. The relative ThT fluorescence of the samples is measured (λ_{Ex}:440 nm; slit width=2 nm and λ_{Em}:485 nm; slit=5 nm).

5.2.7. Dynamic light scattering (DLS) experiments. DLS experiments were performed on a Zetasizer Nano ZS (Malvern Instruments Ltd, UK) using a laser source with

λ= 633 nm and a detector at a scattering angle of θ=173 degrees. Sample containing 100 μM (100 μL) $Aβ_{1-42}$ (both EF treated and untreated) after 24 h of incubation were analyzed, and each measurement was consecutively repeated ten times. Zetasizer program was used for the analysis of average diameter and plotted the information as fractional distribution versus size.

5.2.8. Field Emission Transmission Electron Microscopy (FETEM) analysis. Samples (20 μL) were placed onto carbon-coated copper mesh grids immediately after taking out from the field after completion of their incubation period and were negatively stained using 2% (w/v) saturated uranyl acetate. After 30 seconds, excess stain was wicked away, and the grids were allowed to air dry. Images were captured with a JEM-2100F field emission transmission electron microscope (JOEL, Tokyo, Japan) at 200kV.

5.2.9. FTIR spectroscopic measurements. The field exposed samples of both $Aβ_{1-42}$ peptides were cast on a potassium bromide (KBr) pellet immediately after taking out from the field. FT-IR spectra were recorded on a Micro FTIR-200 (Jasco Co., Japan) equipped with an MCT detector at 4 cm^{-1} resolution between 1400 cm^{-1} to 1800 cm^{-1} (amide 1). The 16 scan data are collected, and the spectral evaluation was carried out by spectral manager software (Jasco Co., Tokyo, Japan).

5.2.10. Circular Dichroism measurements. Circular dichroism (CD) spectra were recorded on Jasco J-1500 spectropolarimeter in a 1 mm path length quartz cell with a slit width of 1 nm. Spectra were recorded for peptides immediately after taking out from the EF and data points were collected from 260 to 190 nm at room temperature. All peptides were dissolved in 10mM phosphate buffer to make a final concentration of 10 μM. The spectra are presented as mean residue ellipticity, $[θ]_{MRE}$. Mean residue ellipticity was calculated using the formula: $[θ]_{MRE} = (M_r * θmdeg)/(10 * l * c)$, where M_r is the mean residue weight, i.e., peptide molecular weight/number of residues, θ mdeg is the ellipticity in millidegrees, l is the length in centimeters, and c is the peptide concentration in $mgmL^{-1}$.

5.2.11. Cell viability assay. FBS (RM10432-Himedia), DMSO (61857105001730-Merck) and Whatman filter paper 42 (1442-125, GE Healthcare) were used for the study. Human Embryonic Kidney cells 293 (HEK293), human-derived neuroblastoma cells SH-SY5Y and human IMR-32 neuroblastoma cells were procured from National Center for Cell

Science (NCSS) Pune, India. All the cells are cultured in DMEM/F12 media containing 10% FBS under 5% CO_2. Cells were harvested from culture plates, and 10,000 cells were seeded per well in 96 well plates. Twelve hours later, cells were treated with 10 μM of the external electric field exposed $A\beta_{1-42}$ samples for 24 h. Cell viability was accessed by following a standard MTT assay protocol.[389] The absorbance of formed formazone crystals was measured at 570 nm using a microplate reader (Tecan, microplate reader, infinite M200; Austria). Fluorescence imaging of the cells was performed in a Cytell Cell Imaging System (code number 29-0567-49) after sequential addition of DAPI (4′,6-diamidino-2-phenylindole) for 10 mins followed by Propidium iodide staining for 20mins. Cell viability with seeded peptides was also performed with identical sequential steps using peptide solutions containing field treated and untreated seeds.

5.2.12. Cell internalization experiments. Assays were performed on SH-SY5Y, IMR32 and HEK293 cells cultured under standard conditions at 37°C in a humidified incubator with 5% CO_2. Cells were seeded at a density of 10,000 per well in a white-walled, clear-bottomed 6-well plate and cultured for 24 h in DMEM 10% FBS. The culture media were then replaced with pre-warmed phenol red-free DMEM without serum into which the fluorescently labelled peptide samples were diluted to a final concentration of 10 μM in media. The peptide samples were taken directly from an on-going aggregation reaction in the presence and absence of EF. Cells were then cultured in the presence of the FITC-$A\beta_{1-42}$ peptides for 24 h before fixing them with a 4% formaldehyde solution. Cellular uptake experiments were carried out with the FITC-$A\beta_{1-42}$ using a Leica SP5 confocal microscope (Leica Microsystems) after 24 h of incubation under standard conditions at 37 °C. FITC-$A\beta_{1-42}$ was excited by the 488 nm laser line, and the emission was recorded at 520 nm. The cells were washed 3 times with PBS prior to imaging to avoid background fluorescence from the excess peptides.

5.2.13. Trypsin activity. Trypsin solution was prepared by adding 25 μl of ice-cold Tris stock (0.4M, pH 7.8) and 75 μl of ice-cold MilliQ-water to 20 μg trypsin to get a final concentration of 0.2 μg μl^{-1}. The solution was then incubated in the presence of an external electric field of different strengths for 24 h. The control sample was not exposed to the field. The substrate protein BSA (1 mg) was treated with 8M urea for 30 mins to denature. The

concentration of urea was then lowered to ~1M by adding HCl (5 M) to get a final concentration of ~400μgμl^{-1}. After 24 h of incubation, the field treated and the control enzyme was incubated with denatured BSA for 4h at 37 °C in 1:20 (w/w) ratio. The reaction was stopped by lowering the pH to 4 by adding acetic acid to the solution. Sodium dodecyl sulfate-polyacrylamide gel electrophoresis (SDS-PAGE) was performed using 12% resolving gel.

5.2.14. Statistical analysis. Statistical analysis was performed using t-test in Microsoft Excel software. Error bars indicate standard deviation (s.d.). The exact sample numbers and *P*-values are clarified in the figure legends ($^{*}P \leq 0.05$; $^{**}P \leq 0.005$).

5.3. RESULTS AND DISCUSSION

Effect of electric and magnetic fields in modulating self-aggregating peptide units: We have developed two separate instrumental setups to test the effect of external electric and magnetic fields on the self-assembly of $A\beta_{16-22}$ and the clinically-relevant Aβ alloform parent peptide, $A\beta_{1-42}$. The circuit diagram of the setup used to generate the desired electric and magnetic fields are shown in Figure 4.3(a) and Figure. 5.1. In this work, we have experimentally analyzed the influence of external electric field (EF) and magnetic field (MF) on Aβ fibrillogenesis, and its possible use as a non-invasive therapeutic option for AD patients. To mimic and maximally align with clinical conditions, we have extended the study with human cerebrospinal fluid (CSF).

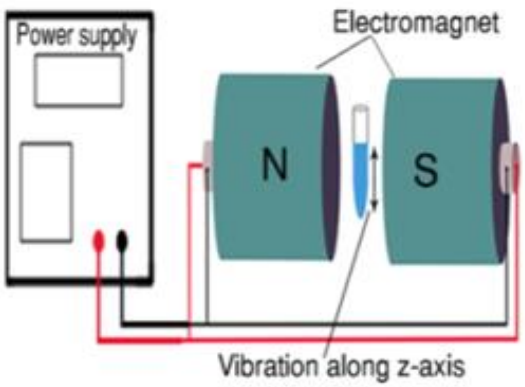

Figure 5.1. Experimental field setup of the magnetic field. The set-up can generate field up to 1T.

CSF is routinely checked for the presence of pathological biomarkers for nervous system disorders. $A\beta_{16-22}$ is among the shortest fibril-forming fragments and is thought to be the core β-sheet structure in the Alzheimer's β-amyloid. It has previously been shown to form fibrils with amyloid-like characteristics under specific conditions[371] and thus serves as a suitable model peptide to test the effect of an external field on the fibril formation. The time dependent evolution of nascent peptides to amyloid aggregates has been characterized as follows. The strength of the electric field is selected to systematically study the effect of moderate and relatively higher field strengths on aggregation. The propensity of aggregation of the two peptides is monitored by recording ThT fluorescence assay and static light scattering at regular intervals of time under ambient conditions at pH 7.4. Figure 5.2 shows aggregation kinetics of peptides at physiological pH. ThT fluorescence-based aggregation kinetics of both the peptides, $A\beta_{16-22}$, and $A\beta_{1-42}$, as a function of time, follows a sigmoidal curve; beginning with a short lag phase, followed by an exponential growth phase and then a plateau. Plateau signifies that nearly all the individual peptides have aggregated to form fibrils. Both the peptides are found to form ThT active species with emission maxima between 480 and 485 nm. Using this ThT data, the lag time for aggregation of both the peptides was estimated by sigmoidal fitting. The lag-time corresponds to the time point where half of the peptide monomers are transformed into fibrils.[390]

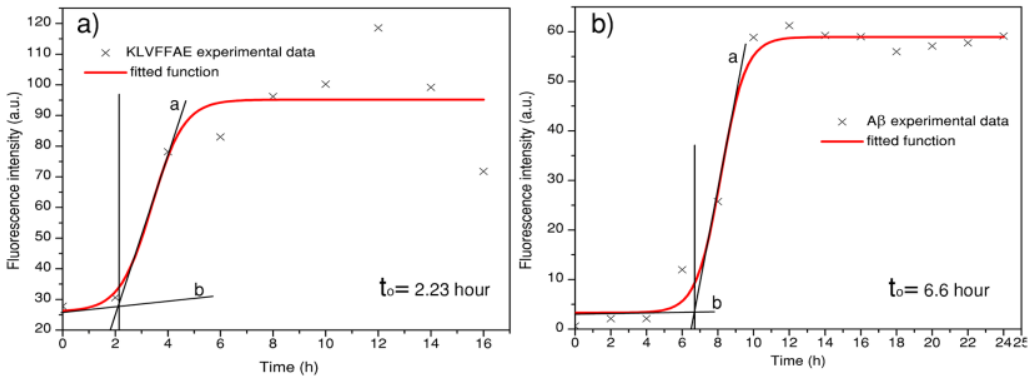

Figure 5.2. Kinetic evaluation of aggregation reaction. Aggregation kinetics of $A\beta_{16-22}$ (a) and $A\beta_{1-42}$ (b) peptides is determined using ThT fluorescence assay as a function of time at 500μM and 100μM concentrations respectively. Both the peptides follow a sigmoidal curve during the time course of aggregation with a lag phase followed by a steep exponential phase and a plateau. The t_o is a point where the two lines 'a' and 'intersect. It marks the end of the lag phase and start of exponential phase in the sigmoidal curve. All samples contain 10μM ThT, 50mM phosphate buffer, pH 7.4.

The effect of different external fields on the aggregation kinetics of $A\beta_{16-22}$ is tested by dissolving 500 μM of the peptide in phosphate buffer and allowed to aggregate in the presence of electric field. Both direct current and alternating current of field strengths 150 and 300 Vcm^{-1} were employed (Figure 5.3). In another setup, a 500 μM peptide solution is incubated in the presence of a magnetic field of 0.8 T. After 16 h of incubation under isolated conditions, samples exposed to EF show considerably reduced fluorescence intensity (approximately 35% reduction, Figure 5.3a,b). However, the efficacy of 0.8T magnetic field in perturbing the aggregation of $A\beta_{16-22}$ is approximately 27%, compared to the fluorescence intensity of the control (Figure 5.3c). Measurement of static light scattering under variable fields further confirm this observation.

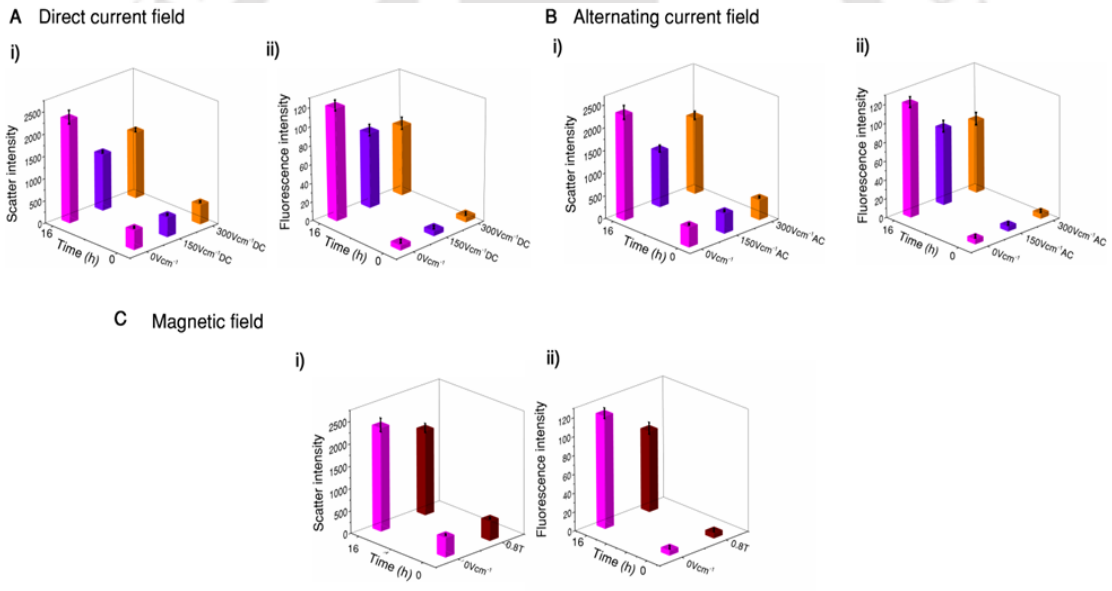

Figure 5.3. Electric and magnetic field induced effects on the aggregation of $A\beta_{16-22}$. Static light scattering and ThT fluorescence measures the extent of aggregation with different field strengths (both AC and DC field) as a function of time. Different colour codes are used for different external field strengths at the 0^{th} and 16^{th} h of incubation. A significantly reduced intensity has been observed for samples exposed to DC (a) and AC (b) fields suggesting a retarding effect on amyloid formation. However, the retarding effect of the magnetic field exposed samples (c) was comparatively less. Error bars are the mean and standard deviation of three independent experiments and all aggregation experiments were performed in PBS buffer at pH 7.4.

The aggregation profile of $A\beta_{1-42}$ is controlled by stochastic nucleation and is characteristically bipartite, with two distinct phases; a lag phase and a growth phase (log phase).[390] It has been reported that the rate of aggregation is determined by the addition or formation of these nucleation seeds. To test whether the application of external field results in inhibition or retardation of nucleation, we treated 100 μM of $A\beta_{1-42}$ with both AC and DC fields of 150Vcm^{-1} and 300 Vcm^{-1} for 24 h. The ThT fluorescence intensity measured after 24 h of incubation suggests that both AC and DC electric fields have a retarding effect on the aggregation kinetics of the peptide (Figure. 5.4a). In both the cases, ThT fluorescence intensity of 150 Vcm^{-1} shows relatively lesser fluorescence intensity compared to 300 Vcm^{-1}. Samples treated with 0.8T, however, did not show any reduction in ThT fluorescence and was similar to the control (Figure. 5.4d).

We further tested the effect of the external field on pre-formed aggregates, much like in the case of a matured disease condition. The objective of this study is to mimic an AD condition with mature Aβ fibrils already deposited in the inter-neuronal junctions of the brain. It was achieved by allowing 100 μM of $A\beta_{1-42}$ to aggregate at physiological conditions in PB for 12 h. The samples are then exposed to electric fields, both AC and DC. Effect of EF on the rate of aggregation was monitored by ThT fluorescence assay immediately after exposing to the field (0, 12 and 24 h of incubation). The results suggest that the applied field, in general, has substantially retarded the rate of aggregation, even after nucleation has occurred (Figure 5.4b). This confirms that field exposure not only retards the rate of aggregation but can also cause de-fibrillization of the amyloid fibril.

The process of aggregation *in vivo* occurs in a very complex environment containing high concentrations of different proteins, salts, and metabolites. Our investigations so far have been performed in a phosphate buffer system, at a pH of 7.4. In the following stage, we have extended the study with human cerebrospinal fluid to mimic and maximally align with the clinical and physiological conditions. Any biochemical change in the brain is reflected in the cerebrospinal fluid (CSF) as it is in direct contact with the brain's extracellular space. Since AD pathology is restricted to the brain, CSF has been evaluated for diagnostic biomarkers like tau protein, $A\beta_{1-42}$ etc..[391] Fresh CSF samples were collected from healthy patients, and the $A\beta_{1-42}$

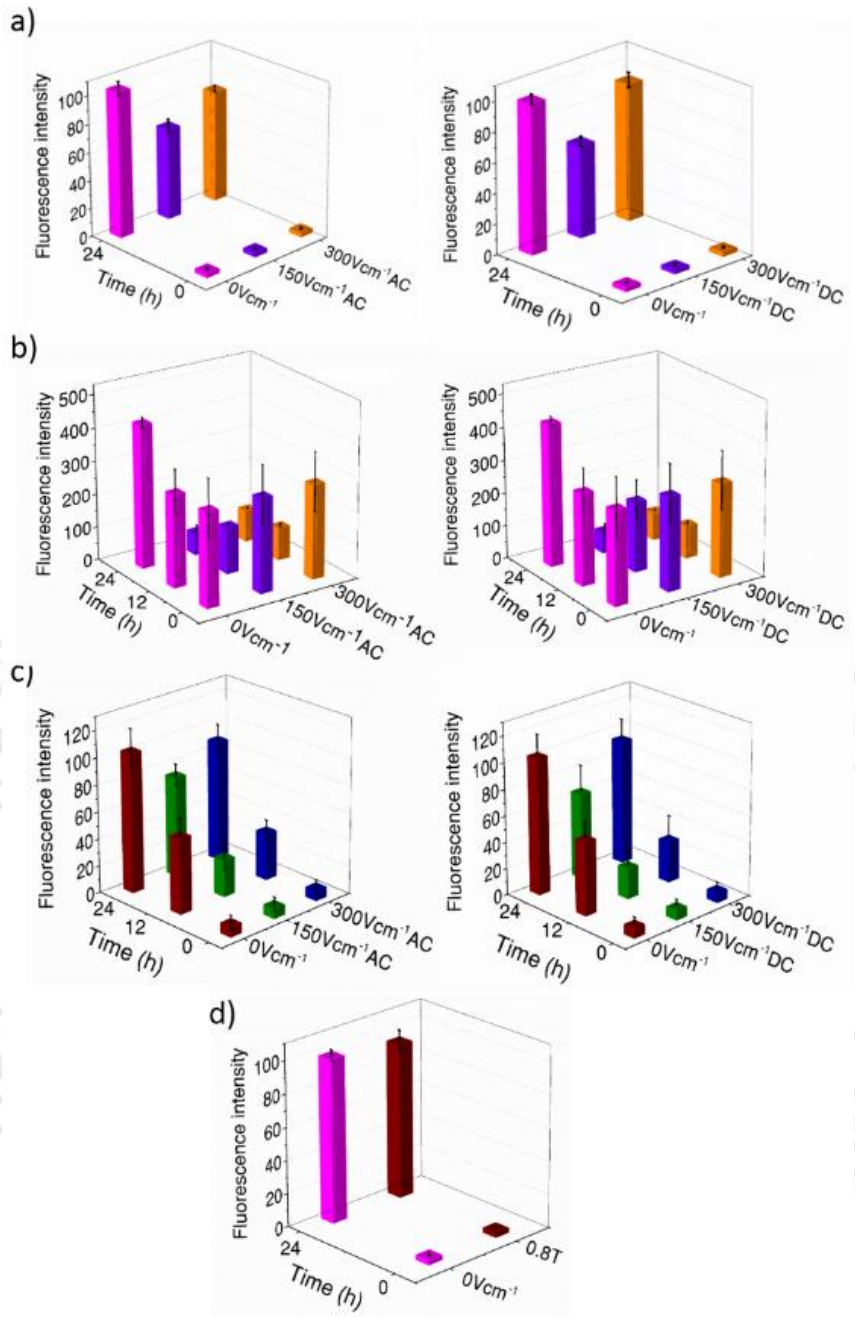

Figure 5.4. Effect of EF on $A\beta_{1-42}$ aggregation. a) Analysis of Aβ aggregation in the presence of different external fields (AC and DC) of varying strengths (150 and 300 Vcm^{-1}) measured by ThT fluorescence at different time points. Different colors correspond to the peptide in different external field strengths at 0th and 24th h of incubation. b) Effect of EF on pre-formed aggregates was studied under identical conditions, at reduced time intervals, 0, 12, and 24 h. c) Effect of EF on $A\beta_{1-42}$ aggregation in human cerebrospinal fluid (CSF). d) Effect of MF (0.8T) on $A\beta_{1-42}$ aggregation. Means of three independent experiments are reported; error bars indicate standard deviation.

peptide is added to get the desired 100 μM concentration. The samples are then subjected to electric fields for a period of 24 h (Figure 5.4c). Effect of electric field on peptide aggregation in CSF is monitored by recording ThT fluorescence (λ_{Ex}: 440 nm, λ_{Em}: 485 nm) of the samples at regular intervals of time. Samples exposed to the electric field, in general, have reduced ThT fluorescence intensity as compared to the control (0 Vcm^{-1}). Through this experiment, we wanted to verify whether field based therapy can be successfully employed under clinical conditions.

As we know, that the generation of $A\beta_{1-42}$ monomers is a physiologically relevant event, whereas their aggregation into larger oligomers and fibrils is pathogenic. You–Foong Mok et al. demonstrated the use of ultracentrifugation to separate amyloid fibrils and their oligomeric intermediates from monomeric subunits.[392] Here we have extended their protocol by measuring the absorbance of soluble Aβ monomers by using UV-Vis spectrometry. After 24 h of incubation, ultracentrifugation of the peptide solution was performed at 12000 g for 20 min. This result in pelleting of the large aggregates, thus, leaving only the soluble Aβ monomers suspended in the supernatant. The supernatant of external EF treated samples, however, has a higher absorbance at 280 nm suggesting a higher concentration of monomers compared to samples without external field (Figure 5.5). Sample exposed to 150 Vcm^{-1} in particular, appears to be more effective in retarding the aggregation of monomers, confirming the inferences of ThT assay and static light scattering experiments.

After 12 h of incubation in the field, peptide exposed to EF shows a gradual decline in the fluorescence intensity, and after 24 h, ThT fluorescence has reduced drastically compared to the control. Field-induced structural effects were predominant at lower field strengths after 12h, while the impact of higher fields was more pronounced after 24 h. Applied MF (0.8 T) however fails to make any significant change in $A\beta_{1-42}$ aggregation, and it is evident from the fluorescence intensity measurements, similar to that of the control experiment with no field applied.

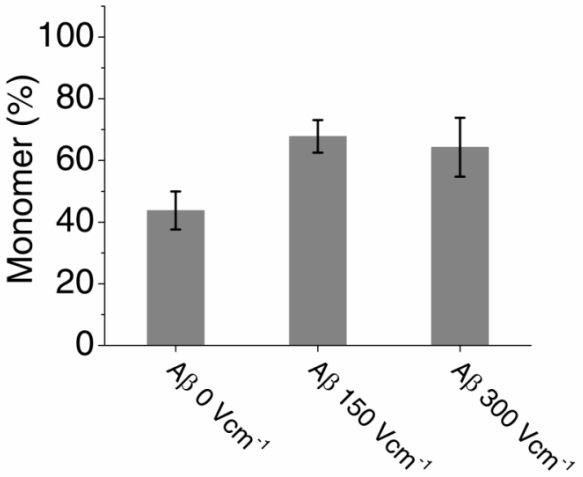

Figure 5.5. Estimation of monomer percentage at 280 nm (tyrosine estimation) by measuring the intensity of 100 µM $A\beta_{1-42}$ peptide in solution. Absorbance at 280 nm is measured with strength of external electric field as the only variable at 0^{th} and 24^{th} h of incubation. The higher intensity of the 0^{th} h sample (black) signifies large population of monomers. After 24 h, the supernatant obtained after ultracentrifugation of the control sample shows significant reduction in the monomer concentration, thus, suggesting formation of large aggregates with large molecular weight and sedimentation co-efficient corresponding to its size. Supernatant of both the field exposed samples, however, has noticeably higher absorbance than the control. This finding corroborates the retarding effect of the applied EF on the aggregation of $A\beta_{1-42,}$ observed in ThT and scattering assays.

5.3.1. Effect of the electric field in modulating secondary structure conformations. Earlier studies have identified that the conformational transition from α-helix to β-sheet is a critical step in Aβ fibrillogenesis. To understand the possible effects of field induction on secondary structure, Circular Dichroism (CD) and Fourier Transform Infrared Spectroscopic (FT-IR) technique were employed. We followed the conformational changes of the peptide samples as a function of applied external electric field. Our conformational studies are aimed at verifying the possible change in secondary structure upon exposure to the electric fields. In the CD experiments, the untreated sample (0 Vcm^{-1}) show a predominant negative ellipticity at wavelengths around 216 nm suggesting a conformation change to β-sheet structures; a pre-requisite for fibril formation. In contrast, the CD spectrum of the EF exposed samples (both 150 Vcm^{-1} and 300 Vcm^{-1}) shows a complete shift from β-sheet conformation and is dominated by a random coil-like shape with a negative peak at 195 nm.

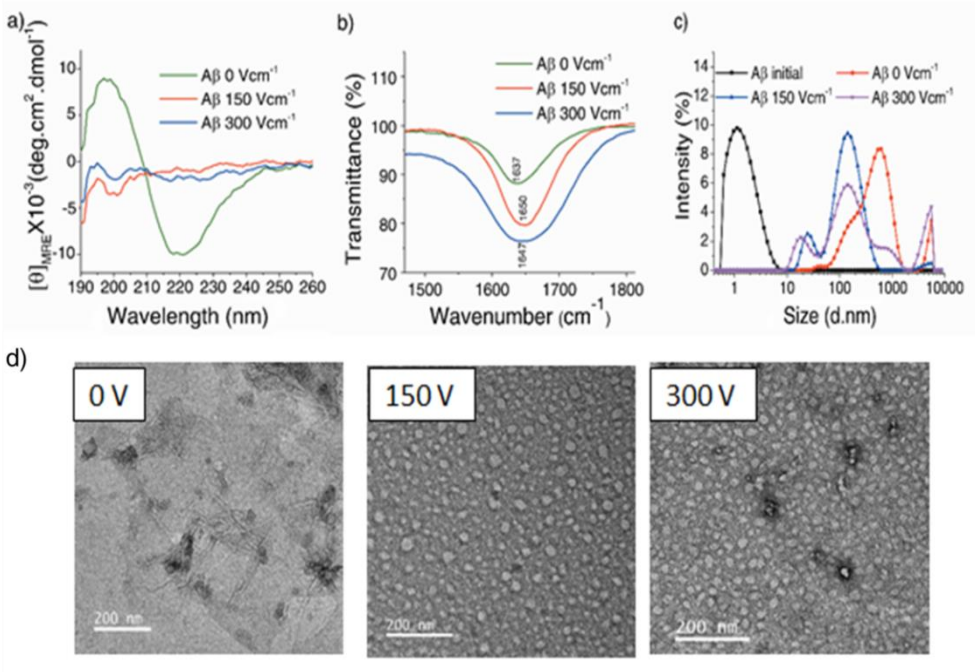

Figure 5.6. a) CD data describing secondary structure transitions of $A\beta 1_{-42}$ peptide from β to random conformations, in the presence of an external electric field, measured after 24 h of incubation. b) FT-IR, the amide I band (1600-1700 cm^{-1}) is associated with the C=O stretching vibration, indicating a periodic shift towards non-β conformation upon field exposure. CD and IR data suggest EF induced conformational modulation of secondary structures c) Changes in the hydrodynamic radius of $A\beta_{1-42}$ aggregates monitored by DLS. Samples containing 100 μM peptide was exposed to the external electric field of varying strengths, and the change in the size distribution of the aggregates formed was monitored over time at 0th (initial) and 24th h d) TEM of $A\beta_{1-42}$ after 24 h of incubation in ambient conditions and in the presence of the external electric field. The control sample has fibrils as predominant form, whereas, samples exposed to 150 Vcm^{-1} has homogenous spherical oligomer clusters and 300 Vcm^{-1} poly-disperse. Scale bars correspond to 200 nm.

This observation suggests a retarding effect of EF on conformational transition of $A\beta_{1-42}$ from random coil to β-sheet in solution (Figure 5.6a) and is similar to the findings of Kia et al..[393] In FT-IR, the amide I band (1600-1700 cm^{-1}) is associated with the C=O stretching vibration and is directly related to the peptide backbone conformation. In proteins, the mean frequency was found to be 1652 cm^{-1} for the amide I band of αα helix and 1637 cm^{-1} for the β strand.[394] A periodic shift from the mean frequency value corresponding to the β structures at 1637 cm^{-1} in the control experiment at 0 Vcm^{-1}, to 1650 cm^{-1} upon field exposure, very well support observations from circular dichroism experiments (Figure. 5.6b). This observation especially

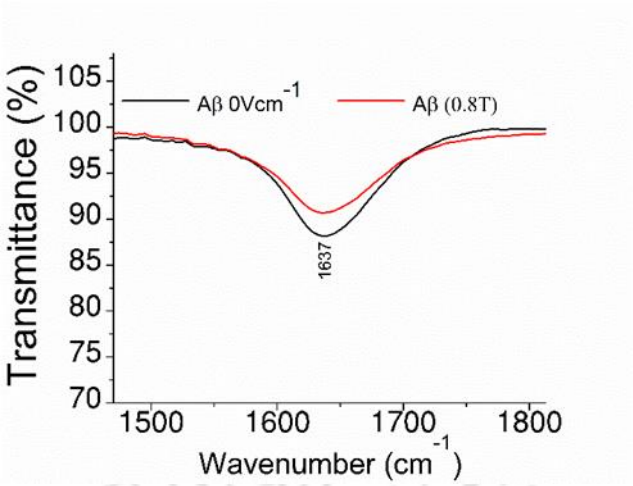

Figure 5.7. FT-IR analysis of effect of MF on Aβ. The amide I band (1600-1700 cm^{-1}) is associated with the C=O stretching vibration indicating a periodic shift towards non-β conformation upon field exposure. The peak at 1637cm^{-1} signifies the presence of a large population of β conformation structures.

has significance in light of earlier studies and our data in the control experiment at 0 Vcm^{-1}, suggesting β conformation for aggregates forming oligomer structures and mature fibrils. Samples exposed to the magnetic field (0.8T) however, have a predominant peak at 1637cm^{-1} similar to that of the control. This observation, as well as the ThT finding, suggests that the applied magnetic field strength is in-effective in modulating the secondary structure of the $Aβ_{1-42}$(Figure 5.7).

5.3.2. Size distribution of structures formed under the influence of EF.

Dynamic light scattering (DLS) of $Aβ_{1-42}$ (100 μM) was performed to get an insight into the size distribution of structures formed under the influence of field after 24 h incubation. Figure. 5.6c clearly shows that the electric field has a retarding effect on the aggregation of the peptide, with a significant shift in the peak position towards a smaller size with respect to the control. After 24 h incubation in the presence of the field, relatively smaller structures (most likely small oligomers) are observed, whereas, the structures are much larger, averaging 800 nm in the absence of a field (0 Vcm^{-1}). Samples exposed to 150 Vcm^{-1} have generated more of a mono-disperse population of structures with a major signal around 120 nm, while 300 Vcm^{-1} generated relatively poly-disperse population, with a small contribution even at the microscale (5-6 μm). The applied MF of 0.8T, in contrast, showed two peaks with a major population averaging 900 nm and a small population at 125 nm (Figure 5.8).

5.3.3. Morphological evolution of $A\beta_{1-42}$ in the presence of an external electric field. We examined the effect of 150 and 300 Vcm^{-1} DC electric field on the aggregation of $A\beta_{1-42}$ using Transmission Electron Microscope in 100 μM solution. Monomers of $A\beta_{1-42}$ were dissolved in phosphate buffer (pH 7.4) at room temperature 'in-field,' to get a 100 μM solution which was then incubated for 24 h followed by TEM imaging (Figure 5.6d). In the case of control at 0 Vcm^{-1}, thin fibrils with a diameter ranging from 10-15 nm were observed predominantly throughout the grid. Narrow, elongated thread-like structures suggest that the oligomers formed by the peptide monomers are on a pathway *en route* fibril formation as explained in the earlier reports by Ahmed et al. and Pachahara et al..[395,396]

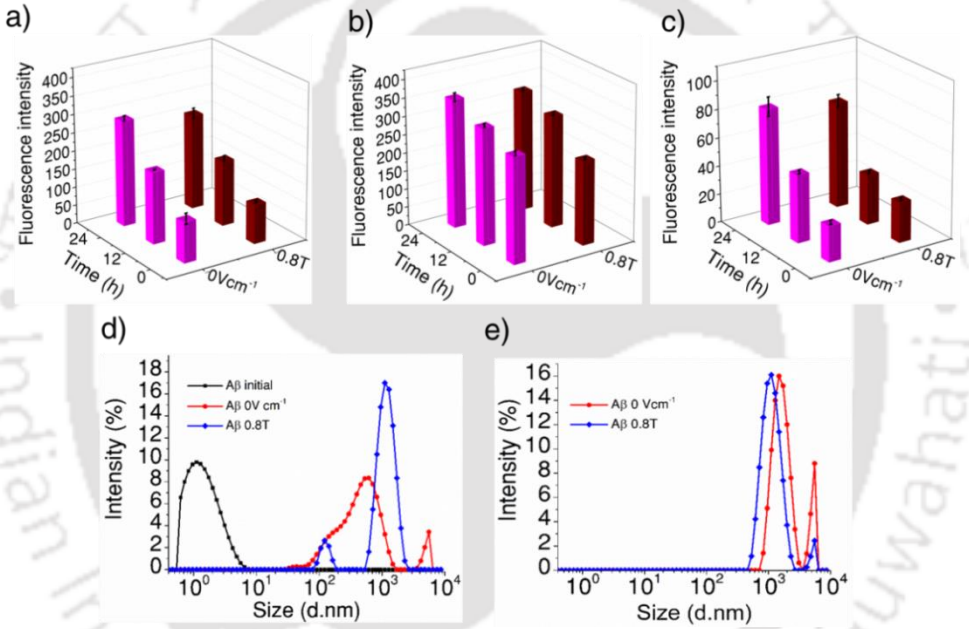

Figure 5.8: Self and cross seeding of Aβ fibrillization. . Aggregation profiles of the MF treated Aβ samples in the presence of 1% pre-aggregated seeds, measured by ThT fluorescence. a)Pre-aggregated $A\beta_{1-42}$ seeds were added and ThT fluorescence were measured in untreated and samples pre-treated for 24h at 0.8T. b) The resulting aggregates (from experiment described in figure 5.10d, after 24 h) were allowed to mature in the presence of 0.8T for another 24 h and ThT fluorescence was measured at regular intervals. c) Aggregation of 100 μM $A\beta_{1-42}$ monomers in the presence of 1% untreated and MF treated seeds to verify whether field treated samples can behave as seeds. Seeds from MF treated samples were added to $A\beta_{1-42}$ monomers and ThT fluorescence was measured. d) Changes in the hydrodynamic radius of $A\beta_{1-42}$ aggregates formed during secondary nucleation of the field treated samples monitored by DLS after 24 h of incubation without field. e) Changes in the hydrodynamic radius of $A\beta_{1-42}$ aggregates formed during secondary nucleation of the MF treated samples monitored by DLS.

The sample exposed to 150 Vcm^{-1} however, has well defined homogenous spheres as the dominant species. The average diameter of the oligomers is in the range between 20-35 nm, which is comparable to the reported dimensions of oligomers before they form toxic protofibrils. In support of our observation, clustering of oligomeric spheres with similar dimensions as intermediates characterized by TEM imaging have been reported by Ahmed et al., Pachahara et al. and Chimon et al., while attempting to characterize the self -assembly and transformation of Aβ peptides to neurotoxic fibrils.[395-397] Samples exposed to 300 Vcm^{-1} mostly contain spheres along with few short fibrillar structures that are morphologically different from that of the control.

All analytical experiments such as ThT assay, static and dynamic light scattering and monomer concentration estimation after ultracentrifugation points to the effect of the external electric field in modulating the aggregation kinetics of $Aβ_{1-42}$ monomers. The stability of the non-β-conformations, formed under the influence of an external electric field by Aβ peptide, holds the key in consolidating field-based treatment strategy. We have tested the stability of structures formed under 150 and 300 Vcm^{-1} by removing the applied field and recording the ThT fluorescence intensity at regular intervals of time for the next 24 h (Figure 5.9).

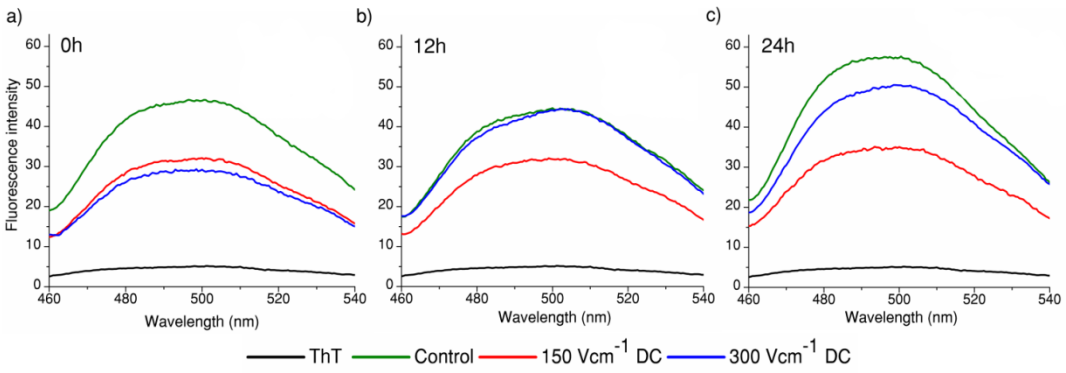

Figure 5.9. Stability of the field exposed $Aβ_{1-42}$ samples. Different color codes are used for different external field strengths at the 0^{th}, 12^{th} and 24^{th} hour after removing from the field. At 0^{th} hour after removing the field, electric field exposed samples, in general, show reduced ThT fluorescence confirming its retarding effect on the aggregation process. Samples exposed to 300 Vcm^{-1} show gradual increase in ThT fluorescence intensity and a 100% increase is observed after 24h when compared to 0^{th} hour. Samples in 150 Vcm^{-1}, however, has only a marginal increase in the ThT fluorescence intensity after 24h.

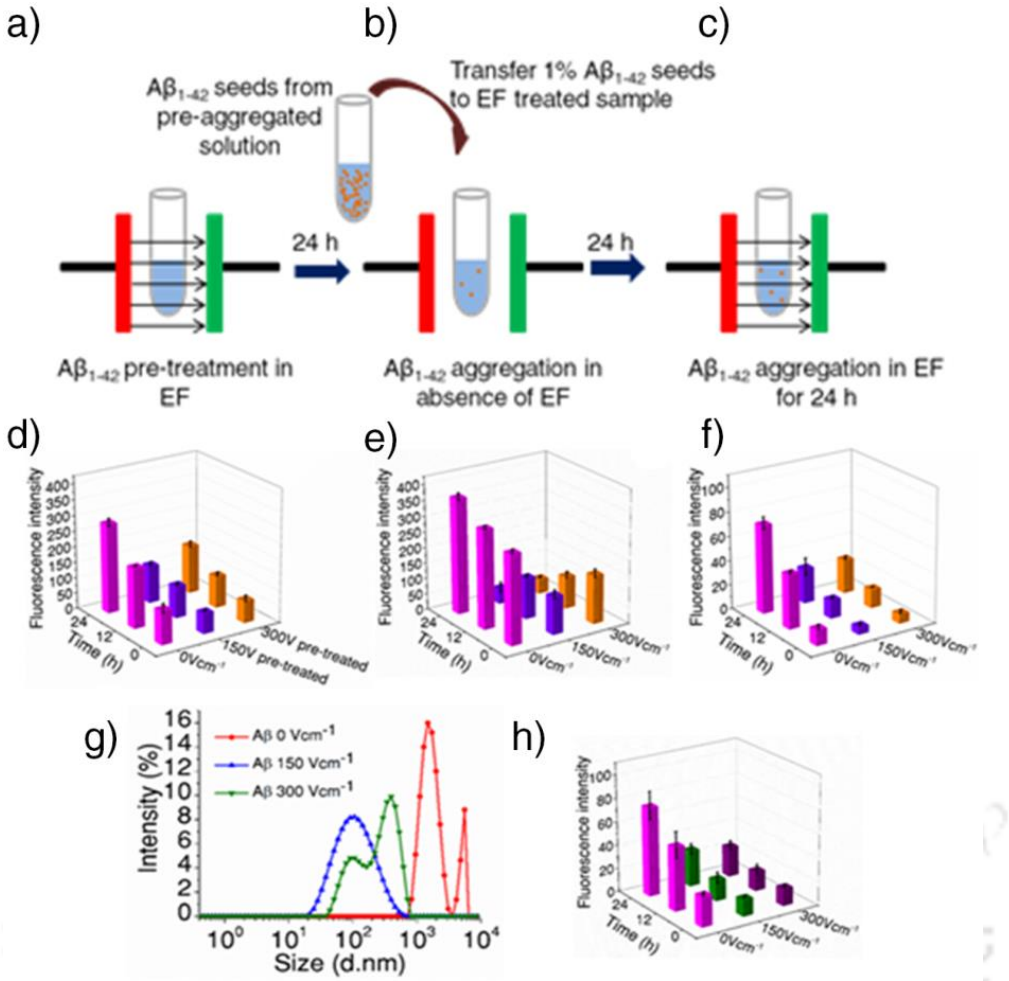

Figure 5.10. Self and cross-seeding of Aβ fibrillization. Aggregation profiles of the EF treated Aβ samples in the presence of 1% pre-aggregated seeds, measured by ThT fluorescence. Scheme showing experimental procedure: a) Pre-treatment of $A\beta_{1-42}$ in absence (0 Vcm^{-1}) and presence of EF (150 and 300Vcm^{-1}) for 24h. b) Addition of 1% pre-aggregated $A\beta_{1-42}$ seeds to the pre-treated sample (100 µM). The mixture was incubated for 24 h in absence of EF and ThT was measured at regular interval. c) After 24 h, EF is switched on and the samples were incubated in field for 24 h. Aggregation was monitored by ThT fluorescence assay. d) Pre-aggregated $A\beta_{1-42}$ seeds were added, and ThT fluorescence was measured at different time points in all the three test cases. e) The resulting aggregates (from the experiment described in Figure 5.4b, after 24 h) were allowed to mature in the presence of 0, 150 and 300 Vcm^{-1} for another 24 h and ThT fluorescence was measured at regular intervals. f) Aggregation of 100 µM $A\beta_{1-42}$ monomers in the presence of 1% EF untreated and EF treated seeds to verify whether field treated samples can behave as seeds. Seeds from EF treated samples were added to $A\beta_{1-42}$ monomers, and ThT fluorescence was measured. g) Changes in the hydrodynamic radius of $A\beta_{1-42}$ aggregates formed during secondary nucleation of the field treated samples monitored by DLS after 24 h of incubation without a field. h) Cross-seeding of Aβ fibrillization: Overall fibrillization was found to be retarded by cross-seeding with $A\beta_{1-40}$. However, fibrillization, in general, shows the same trend as observed in self-aggregation experiments. Means of three independent experiments are reported in d, e, f and h; error bars indicate standard deviation.

Sample exposed to 300 Vcm^{-1} shows a gradual increase in ThT fluorescence with time and in 24 h the fluorescence intensity has doubled. Samples under 150 Vcm^{-1}, however, are highly stable with a marginal increase in the fluorescence intensity throughout the 24 h time frame, set for comparative estimation.

5.3.4. Secondary nucleation on Aβ fibrillization modulated by electric field.

Secondary nucleation on the surface of an already existing aggregate that is formed with the same basic monomers may lead to autocatalytic amplification of a self-assembly process.[398] Therefore, it is necessary to validate the nature of the oligomer species formed under EF and MF. This was accomplished by adding 1% of $Aβ_{1-42}$ seeds from a pre-aggregated sample to 100 μM of samples treated with EF for 24 h (Figure 5.10a,b). A gradual increase in the ThT fluorescence was observed over time and after 24 h of incubation in the absence of a field. ThT fluorescence of the control has increased by 166% compared to the initial value, thus, suggesting the rapid formation of fibrils (Figure 5.10d, 0 Vcm^{-1}). In contrast, there is an 83% increase in ThT fluorescence for 150 Vcm^{-1} treated samples and a marginally higher 110% for 300 Vcm^{-1} from the initial value. This observation suggests that the EF treated species are modulated by the external EF into conformations that are different from the field-untreated $Aβ_{1-42}$ monomer. Such structures are not readily recruited by the existing aggregates for secondary nucleation. Next, we replaced the field treated mixture in the respective external fields to verify its effect on the formed aggregates (Figure 5.10c). Samples exposed to EF did not show any change in the ThT fluorescence intensity after 12 h of incubation in the field. However, after 24 h we observed 63-69% decrease in the fluorescence intensity suggesting de-fibrillization of the peptide (Figure 5.10e). In contrast, samples exposed to MF showed a gradual increase in the ThT, and after 24 h, the fluorescence intensity was comparable to the EF untreated control (Figure 5.8b).

We have extended our investigation to see if the seeds formed in the presence of electric field acts as nuclei for secondary nucleation in the presence of $Aβ_{1-42}$ monomer. 1% of both field treated and untreated $Aβ_{1-42}$ seeds were added to 100 μM of $Aβ_{1-42}$ monomers, and the rate of fibrillization was monitored by ThT fluorescence assay. We have observed an increase in the ThT fluorescence in all the three samples, but this growth is considerably less in EF treated samples compared to the EF untreated control (Figure 5.10f).

5.3.5. Size distribution of structures formed under the influence of EF and MF during secondary nucleation. Small structures formed under the influence of EF might be recruited by existing larger aggregation nuclei resulting in secondary nucleation. To verify the size of EF treated species, we performed DLS analysis after adding 1% of $A\beta_{1-42}$ seeds to the sample that initially contains 100 μM of field treated $A\beta_{1-42}$. Although the oligomers displayed sizes somewhat larger than those formed during primary nucleation as seen in Figure 5.6c; their size was considerably smaller than the control. Figure 5.10g shows that after 24 h of incubation outside the field, there is no appreciable increase in the size of the aggregates. A small peak is suggesting a population of $A\beta_{1-42}$ with a size range of ~30 nm as seen during primary nucleation is missing for 150 Vcm^{-1} treated sample and the newly generated species averages a size distribution of 100 nm. Samples treated with 300 Vcm^{-1} have a small shift in the peak position with a major peak around 600 nm. Considering that the control sample has a population in the microscale range, retarding effect of EF on aggregation kinetics of $A\beta_{1-42}$ even during secondary nucleation is noticeable. The particle size distribution in the case of the MF was comparable to the control sample suggesting the inability of the MF to modulate or retard secondary nucleation (Figure 5.8e).

5.3.6. Cross-seeding of EF and MF treated $A\beta_{1-42}$ with untreated $A\beta_{1-40}$ peptide. Given the high sequence similarity between $A\beta_{1-40}$ and $A\beta_{1-42}$, it is logical to assume that they cross-seed during the process of aggregation. Several reports suggest that pre-formed fibrils of $A\beta_{1-40}$ and $A\beta_{1-42}$ can promote each other's aggregation.[399, 400] We extended our investigation to see the effect of pre-formed seeds of $A\beta_{1-40}$ on the EF and MF treated $A\beta_{1-42}$ samples. Using ThT fluorescence assay we observed that both the EF treated $A\beta_{1-42}$ samples were not very receptive to seeded nucleation and the cross-seeding effect was less compared to the control (Figure 5.10h).However, seeding $A\beta_{1-42}$ with $A\beta_{1-40}$ seeds slows down the aggregation process; an observation shared by a few earlier reports with cross-seeding experiments.[400, 401]

5.3.7. Effect of EF on Aβ induced neurotoxicity. Aβ induced aggregation, and the resultant neurotoxicity is the hallmark of an AD. Using standard MTT (3-[4,5- dimethyl-thiazol-2yl],5-diphenyl tetrazolium bromide]) assay, we attempted to make a quantitative assessment of $A\beta_{1-42}$ induced toxicity by estimating the viability of two neuroblastoma cell lines

after 48 h of incubation, with EF exposed and non-exposed Aβ peptide. Cell viability estimation of neuroblastoma cells suggests moderate to high levels of toxicity in the case of SH-SY5Y and IMR-32 cells (65% and 55% viability respectively).

EF treated samples; however, has a much higher survival rate with estimates 15 to 18% higher in the case of SH-SY5Y and 23 to 27% for IMR-32 (Figure 5.11a, orange and blue). We repeated the experiment in a non-neuronal HEK-293 cell line as well, and in this case, the cell viability estimates show even a higher difference of 36 to 38% compared to the control (40%) (Figure 5.11a,olive). Combination of 4',6-diamidino-2-phenylindole (DAPI)-Propidium iodide fluorescent dye imaging show cell death due to oligomer elicit toxicity of HEK-293 cells after 48h of incubation with and without field exposed $A\beta_{1-42}$ (Figure 5.12). This observation is significant because EF is retarding the aggregation of Aβ peptide, thus, reducing the number of toxic oligomers and protofibrils in the solution.

It has been reported that secondary nucleation generates the majority of toxic $A\beta_{1-42}$ species.[402] Therefore, we have tested the cytotoxicity of the species collected from the inhibited reaction containing a mixture of field treated $A\beta_{1-42}$ species and monomer equivalent concentration of EF untreated $A\beta_{1-42}$ seeds to mimic secondary nucleation conditions. The EF treated samples, in general, show higher cell viability in all the studied cell lines as compared to the control, thus, suggesting the generation of non-toxic species (Figure 11b). We have observed the cell viability of 57-63% and 54-57% in the case of EF treated samples in SHY-5Y and IMR-32 neuroblastoma cell lines respectively. In contrast, the EF untreated samples appeared more toxic to the cells, and the cell viability was found to be between 33%-37%. The results with HEK-293 also fall in the same range, where 50-55% of cells are viable in the field treated samples as compared to 36% in the case of the control. This supports the earlier finding by Gal Bitan et al. suggesting that the neurotoxicity by $A\beta_{1-42}$ may differ significantly even within the amyloid aggregate population of relatively smaller molecular weights.[403]

5.3.8. Cellular uptake of EF treated fluorescent labelled $A\beta_{1-42}$. The "intraneuronal Aβ hypothesis" indicates that accumulation of Aβ inside neurons plays an important role in the pathogenesis of Alzheimer's disease.[404] Having understood that the EF treated $A\beta_{1-42}$ species are less toxic compared to the EF untreated ones, it is important to correlate between inhibitions of cell toxicity by the field treated samples and its internalization

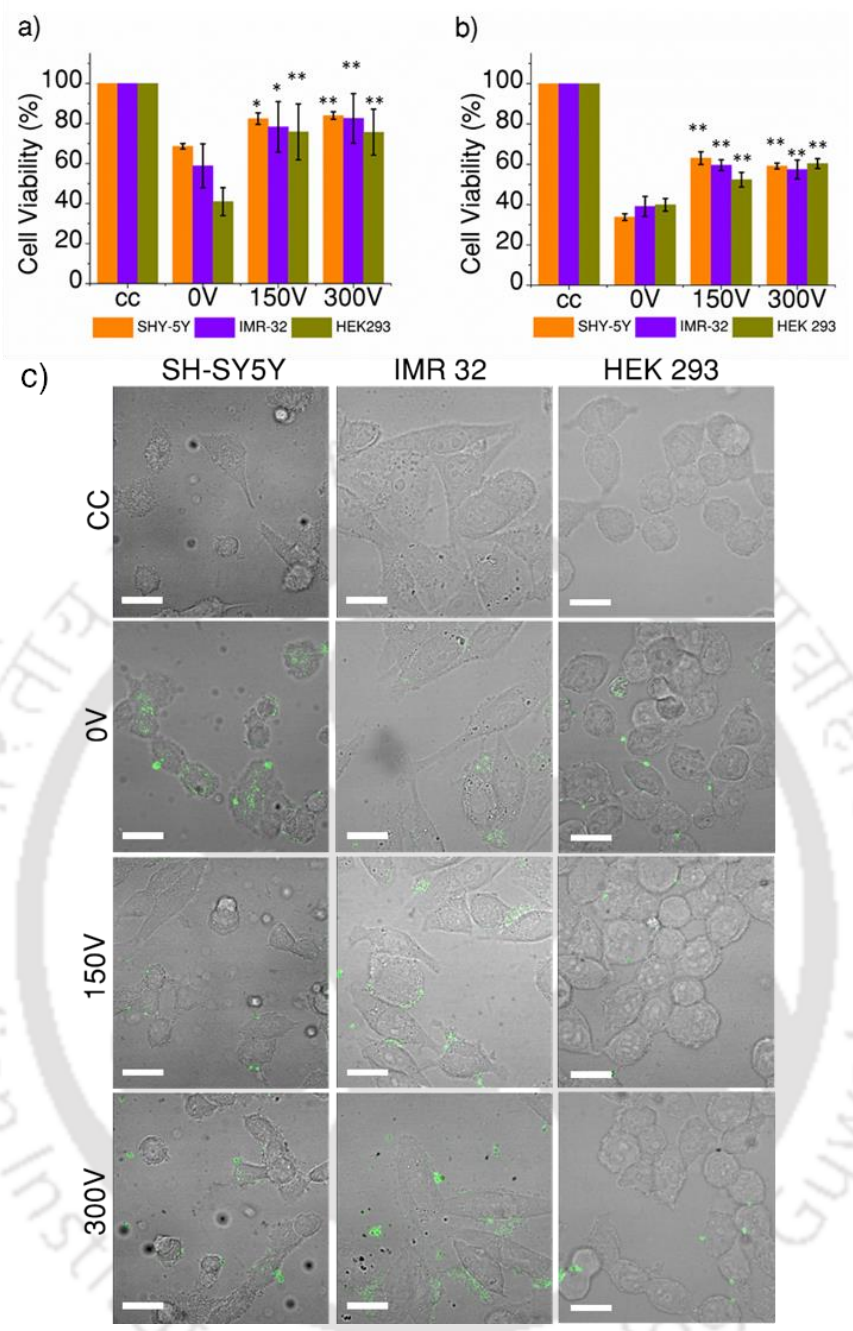

Figure 5.11. Assessment of EF treated Aβ $_{1-42}$ illicit cellular toxicity and its correlation with cellular uptake. a) Differentiated cells were treated with 10 µM of both untreated (0Vcm^{-1}) and external EF treated (150 and 300Vcm^{-1}) $A\beta_{1-42}$ peptide solution for 48h and the toxicity was estimated using the MTT assay. b) Cytotoxicity assessment of the aggregates collected from the inhibited mixture after secondary nucleation. Different color codes correspond to different cell lines. Histograms showing cell viability after peptide treatment (mean ± error, n=3). The t-test revealed the statistical significance between control (0V) and EF treated samples { * ($p < 0.05$), ** ($p < 0.005$)} c) Uptake of EF treated FITC- $A\beta_{1-42}$ (green) by SH-SY5Y, IMR32 and HEK293 cells after 24 h of incubation at 10 µM peptide concentration. All scale bars correspond to 20µm.

in the cell. To characterize the uptake and internalization of the EF treated peptides under the conditions used in our study, we added aliquots of fluorescein isothiocyanate labelled $A\beta_{1-42}$ (FITC $A\beta_{1-42}$) to cultures of SHY-5Y, IMR-32, and HEK 293 cells to give a final peptide concentration of 10 μM in the cellular medium. Using confocal microscopy, we observed that the cells did not internalize any detectable quantities of EF treated FITC-$A\beta_{1-42}$ species after 24 h incubation. Fluorescence was detected around the cell membrane or in the intercellular space. (Figure 5.11c and Appendix FigureA10-12) On the other hand, we observed intracellular fluorescence in the case of EF untreated samples suggesting internalization of the peptide. A possible explanation for the uptake of EF-untreated AB could be that the interaction of $A\beta_{1-42}$ aggregates with cell membranes is dependent on their size and surface hydrophobicity.[405, 406] This suggests that exposure of hydrophobic surfaces in $A\beta_{1-42}$ aggregates with solvent is critical for their cell membrane interactions.[406-408] However, EF-treated $A\beta_{1-42}$ do not form such aggregates, and therefore, their cellular uptake is limited. Very less fluorescence signal was observed in human embryonic kidney (HEK293) cells (Figure 5.11c) incubated with an untreated peptide. These observations, consistent with previously published findings,[408] suggest cellular specificity in the uptake of FITC-$A\beta_{1-42}$.

5.3.9. Effect of electric field on functions of normal proteins. The goal of this study was to experimentally verify the possibility of electric field elicited toxicity by analyzing the effect of the external electric field on other native proteins. The interaction of another β-sheet containing protein; trypsin, with electric fields of varying strengths was investigated after 24 h incubation. Trypsin is a commonly available serine protease in the body and cleaves protein next to lysine and arginine residues. The proximity with His-57 makes the serine residue more reactive, which exhibits enhanced reactivity because of H-bonding to a negative aspartate residue Asp-102, resulting in a charge relay system.[409] Any change in the secondary structure of trypsin affects the catalytic triad and thus its functionality. Trypsin is incubated in the presence of external electric field strength of 150 and 300 Vcm^{-1} for 24 h followed by verification of its activity against bovine serum albumin (BSA) protein (50 mg mL^{-1}). Figure 5.12 shows BSA bands on SDS-PAGE after staining with Coomassie brilliant blue. The addition of trypsin (control) resulted in several fragments (L1and L2 of Figure 5.12). The field- exposed and non-exposed trypsin were compared, and the bands formed by the field

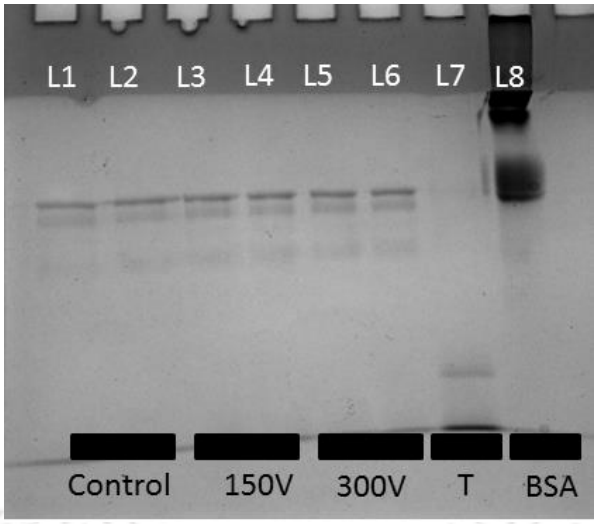

Figure 5.12. SDS-PAGE of BSA fragments after treatment with trypsin. L1 and L2 show SDS-PAGE patterns of digestion of BSA by trypsin not exposed to the field (control). L3 and L4 show digestion by trypsin exposed to 150 Vcm^{-1} (DC) for 24h and L5 and L6 show band position of BSA fragments after treatment with trypsin exposed to 300 Vcm^{-1} (DC) for 24h. No noticeable difference in the band position of the BSA fragments among the three different experimental conditions is observed confirming the functional stability of trypsin in the presence of an external field.L7 and L8 show band position of standard trypsin and undigested BSA alone.

exposed trypsin (L3 and L4 for 150 Vcm^{-1} and L5 and L6 for 300 Vcm^{-1}) show no noticeable difference in the band position of BSA fragments, suggesting a negligible effect on overall function of the trypsin molecule upon exposure to the applied field.

5.3.10. Mechanistic insights for 'molecule-field' interactions. The possibility of using electric and magnetic fields as the principal or supplementary therapeutic options have been examined in this study. The critical step in amyloid formation involves $A\beta_{42}$ sequence undergoing a conformational transition from α-helix to β-sheet, which in turn exposes hydrophobic residues thus promoting the formation of protofibrils and plaques around neuronal cells. We hypothesize that in the presence of electric field of adequate strength, the alignment of the dipole moment of each fibril results in the increase of the total dipole moment and marks the first step of the destabilization of fibril formation. This is followed by the alignment of the dipole moment that leads to the separation between the participating entities. This disrupting mechanism is based on a simple argument that conformational modification of

the Aβ fibril is directly correlated to the reorientation and the increased intensity of the total dipole moment. More precisely, conformations with larger dipole moments gain more in statistical weight because of interactions with the field than the states with the lower moments. When the dipole moment reaches a critical value, rupture between the two intertwined proto-filaments is promoted. In literature, it is well established that any change and the rearrangement of the orientation of the dipole moment plays a crucial role in the Aβ destabilization process.[185-187] In fact, the dipole moment influences the protein-protein or peptide-peptide interactions and represents a good descriptor of mechanical stability of a supramolecular fibril assembly.[185]

Using ThT fluorescence and static right angle light scattering, we have demonstrated that electric field retards aggregation of both $A\beta_{16-22}$ and its parent amyloid forming $A\beta_{1-42}$ peptide segments. Spectroscopic analysis with CD and FT-IR suggests that samples exposed to EF have a higher percentage of non-β conformation compared to the EF untreated control samples. Results from dynamic light scattering experiments show the presence of small structures in case of the EF treated samples that were absent in the EF untreated one. Transmission electron microscopic analysis also indicates retardation in fibril formation, with clearly differentiated fibrils observed at 0 Vcm^{-1} and spherical oligomers at 150 Vcm^{-1} respectively. Samples exposed to 300 Vcm^{-1} contain a small population of fibrils that are morphologically different from those formed in the EF untreated sample. This further confirms that electric field influences secondary structure formation of amyloid-forming peptide segments, promoting non-β conformation than β; a pre-requisite for fibril formation. ThT assays suggest that the non-β structures formed as a result of EF exposure are stable enough, even after the field has been removed. This result is further corroborated by the observations from Aβ induced toxicity studies on neuronal and embryonic cell lines.

Although the mechanism of electric field effects is not completely understood, it is believed that fields of specific frequency and intensity can excite certain vibrational modes of a macromolecule, which alters its conformation.[410] This might be the reason for 150 Vcm^{-1} showing relatively more effective in retarding the aggregation kinetics of both the model peptide $A\beta_{16-22}$ and $A\beta_{1-42}$. Mapping the conformational transition of Aβ peptide, Tomaselli et al. have shown that α to β conformational transition is reversible.[361] Field-induced cooperative

change in structure was originally suggested by Porschke, while analyzing the electro-optical data from bacteriorhodopsin, induced at very low field strength of 150 Vcm^{-1}.[385] MD simulation experiments using OPLS force-field by Andrij Baumketner predicts field induced transition to α-helical state,[183] while MD simulation with CHARMM force-field by Toschi et al. predicted α to β conformational transition.[411] Both these studies suggest that the applied external EF acts on the inherent dipole of the two helices of the $A\beta_{1-42}$ peptide strand in the direction parallel to the EF thus, causing a strain, which in turn increases the frequency of sterically uncommon backbone angles. The interaction between the dipole moment and the electric field determines the orientation of the peptide in space and imposes an oscillatory motion. Astrakas et al. by using Stochastic modelling and MD simulation demonstrated the destabilization of β-hairpin was forming chignolin's structure by EF.[412] They have related the destabilization of chignolin to the orientational anisotropy of the mechanical resistance of the molecule due to its network of parallel inter-strand hydrogen bonds. This finding concludes that the electric field can not only disrupt but also enhance hydrogen bond formation.

5.5. CONCLUSIONS

Theoretical studies on the possible effects of electric field on protein aggregation broadly suggest two mechanisms for molecule-field interactions. First is the alignment of macromolecules with permanent or induced dipoles along the axis of the applied field leading to preferential orientation in the external field. Second is the conformational transition that may occur due to the direct interaction of the molecular dipoles with the field. This mechanism is based on a simple argument that conformations with larger dipole moments gain more in statistical weight from interactions with the field than do the states with the lower moments. The expected result is a shift of population, driven by the field, towards the states with the largest moments resulting in β to non-β conformational transition. In a theoretical study, Baumketner reported that electric field induces folding into α-helical state driven by a combination of enthalpic and entropic contributions.[183] Our experiments on pre-formed aggregates clearly show a shift from β to non-β conformation. Our laboratory studied the impact of electric and magnetic field-mediated perturbation in the self-assembly of diphenylalanine superstructures.[387] Since FF is the core recognition motif of $A\beta_{16-22}$ and Aβ, the modulatory effect of electric field on the structure of FF nanotubes reported, has significance

in light of the present study. Bekard and Dunstan in a recent study with BSA and Lysozyme noted that the conformational change observed is more pronounced at low field strengths compared to higher fields;[179] an observation we also share, when we compare between 150 Vcm^{-1} with 300 Vcm^{-1}. The potential health implications of such a study may be far-reaching, which demands future work in this direction. However, the pilot study to verify any potential field induced functional disorders on trypsin as a model protein was very encouraging. Trypsin functions were largely unaffected, and our findings agree with the observation by Baumketner,[183] suggesting that low strength electric field can be used to inhibit aggregation of short peptides without affecting the native structure and therefore, the function of other proteins. The observation that longer peptides experience 'folding' at low field strengths, and the age-old wisdom in protein folding theory that peptides need to be in the folding funnel to prevent aggregation, provides the philosophical background for developing a field induced therapy, well within the safety levels of disease management.

Our experiments with pre-formed fibrils also resulted in β to non-β conformational transition. ThT experiments to analyze the rate of aggregation and the nature of the EF treated species in the presence of pre-aggregated seeds showed a significant reduction in the aggregation rate during secondary nucleation. DLS study of these species indicates generation of much smaller structures as compared to the control. These new species are found to have lesser toxicity against two neuroblastoma and one normal cell line as compared to the EF untreated sample. Using FITC-$A\beta_{1-42}$, we were able to correlate between reduced cell toxicity and cell internalization. Samples treated with EF were on the periphery without much internalization while in EF untreated samples internalization was observed. This is especially relevant from a therapeutic perspective because the formation of fibrillar aggregates must have been already completed for AD patients. In an earlier study, Sen and Dasgupta have shown that oscillation induced by application of AC field, can aid the disintegration of pre-formed Human Serum Albumin (HSA) fibrils.[192] Since the AD is characterized by amyloid deposits composed of Aβ peptides and neurofibrillary tangles composed of tau proteins, their differential levels are used to investigate the clinical signs of the AD. We have repeated the experiment in human CSF, to maximally align with the clinical conditions and mimic an *in vivo* environment. Overall results are concordant, suggesting the effect of electric field on fibril formation and its potential use as a future therapeutic option.

On the other hand, the magnetic field in the range of 0.8 T, has little ability to induce a conformational switch. This observation supports a previous study by Hill et al.,[132] suggesting the requirement of a very high field in the range of 10 – 15 T, to induce a conformational switch in the case of FF nano-assembly. A magnetic field based therapy may be difficult to implement and hence, have minimum therapeutic value as per our findings.

Inhibition of the formation of toxic forms of Aβ is recognized as one of the possible therapeutic options. The most important result from our studies (especially after DLS and ultracentrifugation experiments) is that an electric field can alter the kinetics of amyloid formation, shifting the equilibrium from higher order oligomers and amyloid fibrils to lower order ones. Chemical agents and short peptides are employed to inhibit fibril formation by binding with small oligomeric structures.[413] Shifting of equilibrium to lower order oligomers, thus precluding the formation of large oligomers or fibrils with a non-invasive option like electric field, hence, have a decisive advantage of preparing the system to be more amenable to invasive treatments by modifying the assembly pathway. This study may provide the much needed scientific background in the design and development of such a futuristic device.

6.

Conclusions and Future Directions

6.1. CONCLUSIONS

Developing an effective way to direct the self-assembly of peptides opens a new frontier in the research and engineering of novel materials with unique properties. Furthermore, the ability to modulate peptide self-assembly using an external stimulus offers ways for developing non-invasive therapies for various protein misfolding diseases. This thesis explored and unveiled various physical and chemical modulators during peptide self-assembly with implications ranging from developing functional materials to pave the way for developing non-invasive therapy against Alzheimer's disease.

This thesis consists of three working chapters. Chapters 1 and 2 provide a background to the previous and current research progresses on peptide self-assembly and its modulation. Chapter 3 elucidates a minimalistic design strategy for functional and structural mimicry of the active site of the lytic polysaccharide monooxygenase. Results showed that the incorporation of D-histidine at the C terminal of the peptide sequence promoted the binding of Cu (II) ion to the imidazole nitrogen through a 3N coordination that results in distorted square-planner geometry, similar to that observed in LPMO active site. The Cu-HPh complex at pH 7 showed enhanced catalytic activity against a standard benzyl alcohol oxidation reaction.

In Chapter 4, we investigated the effect of three independent variables that can modulate the function of a self-assembling peptide. The first two variables, amino acid position and its stereochemistry, were examined for their specific roles in the epitaxial growth and hydrogelation properties of a series of catalytic tripeptides. Subsequently, the influence of the third variable, external electric field was also being tested to verify its catalytic efficiency for the asymmetric C-C bond-forming aldol reaction. We observed that the aromatic π-π interactions direct the self-assembly of the designed peptides, and the catalytic characteristics of the hydrogels are governed by the position and chirality of the proline residue. The electric field treated **pff** and **PFF** gels, in particular, showed 16 and 30% higher stereoselectivity compared to the control. Structure-property analysis using CD and FTIR indicates electric field-induced β to non-β conformational transition in the peptide secondary structure, which corroborates with the reduced cross-link density and fibril width. The frequency sweep rheology of the gels suggests a decrease in the storage modulus with increased field strength. Overall, the results

indicate that the electric field of adequate strength could modulate the physical characteristics of the hydrogel, which is manifested in the observed difference in enantioselectivity.

In Chapter 5, we have extended our study to test the effect of electric and magnetic fields of varying strengths on the aggregation propensity of $A\beta_{1-42}$. We have experimentally demonstrated that EF has a stabilizing effect on the secondary structure, initiating a conformational switch of $A\beta_{1-42}$ from β to non-β conformation. Morphological analysis revealed that the EF exposure retarded the fibrillation of the peptide even during secondary nucleation. Aβ-elicited toxicity of EF-treated samples in two neuroblastoma cell lines (SH-SY5Y and IMR-32) and human embryonic kidney cell line (HEK293) were found to be 15–38% less toxic than the EF untreated ones due to reduced cellular uptake. These results prompted us to propose an EF-based, futuristic non-invasive therapeutic device for Alzheimer's disease.

The possibility of using electric and magnetic fields as the principal or supplementary therapeutic options have been examined in this study. The critical step in amyloid formation involves $A\beta_{42}$ sequence undergoing a conformational transition from α-helix to β-sheet, which in turn exposes hydrophobic residues thus promoting the formation of protofibrils and plaques around neuronal cells. We hypothesize that in the presence of electric field of adequate strength, the alignment of the dipole moment of each fibril results in the increase of the total dipole moment and marks the first step of the destabilization of fibril formation. This is followed by the alignment of the dipole moment that leads to the separation between the participating entities. This disrupting mechanism is based on a simple argument that conformational modification of the Aβ fibril is directly correlated to the reorientation of the total dipole moment. More precisely, conformations with larger dipole moments gain more in statistical weight because of interactions with the field than the states with the lower moments. When the dipole moment reaches a critical value, rupture between the two intertwined proto-filaments is promoted. In literature, it is well established that any change and the rearrangement of the orientation of the dipole moment plays a crucial role in the Aβ destabilization process.[185-187] In fact, the dipole moment influences the protein-protein or peptide-peptide interactions and represents a good descriptor for mechanical stability of a supramolecular assembly.[185]

6.2. FUTURE DIRECTIONS

The work put forth in this thesis opens up the following opportunities to explore:

- Conceptual emergence of biomimetic peptide design platform to be translated to other industrially relevant enzymes.

- Development of electric field as an efficient, non-invasive modulator of peptide self-assembly for applications ranging from functional nano-materials to therapeutics.

- *in-vivo* studies: Progress in the field of non-invasive therapeutic strategies and their advantages are evidenced by the growing number of translational reports. It will be interesting to investigate the efficacy of EF on AD animal models, thus, paving a way for clinical trials.

REFERENCES

1. Janiak, C. (2000) A critical account on π–π stacking in metal complexes with aromatic nitrogen-containing ligands, *Journal of the Chemical Society, Dalton Transactions*, 3885-3896.
2. Whitesides, G. M., and Grzybowski, B. (2002) Self-assembly at all scales, *Science 295*, 2418-2421.
3. Hartl, F. U. (2017) Protein misfolding diseases, *Annual review of biochemistry 86*, 21-26.
4. Prakash Sharma, P., Rathi, B., and Rodrigues, J. (2015) Self-assembled peptide nanoarchitectures: Applications and future aspects, *Current topics in medicinal chemistry 15*, 1268-1289.
5. Fischer, E., and Fourneau, E. (1906) Ueber einige derivate des glykocolls. In *Untersuchungen über Aminosäuren, Polypeptide und Proteïne (1899–1906)* pp 279-289, Springer.
6. Merrifield, R. B. (1963) Solid phase peptide synthesis. I. The synthesis of a tetrapeptide, *Journal of the American Chemical Society 85*, 2149-2154.
7. Grzelczak, M., Vermant, J., Furst, E. M., and Liz-Marzán, L. M. (2010) Directed self-assembly of nanoparticles, *ACS nano 4*, 3591-3605.
8. Chockalingam, K., Blenner, M., and Banta, S. (2007) Design and application of stimulus-responsive peptide systems, *Protein Engineering, Design & Selection 20*, 155-161.
9. Challener, C. A. (2017) *Chiral drugs*, Routledge.
10. Nichols, E., Szoeke, C. E., Vollset, S. E., Abbasi, N., Abd-Allah, F., Abdela, J., Aichour, M. T. E., Akinyemi, R. O., Alahdab, F., and Asgedom, S. W. (2019) Global, regional, and national burden of Alzheimer's disease and other dementias, 1990–2016: a systematic analysis for the Global Burden of Disease Study 2016, *The Lancet Neurology 18*, 88-106.
11. Casey, D. A., Antimisiaris, D., and O'Brien, J. (2010) Drugs for Alzheimer's disease: are they effective?, *Pharmacy and Therapeutics 35*, 208.
12. Weiner, H. L., and Frenkel, D. (2006) Immunology and immunotherapy of Alzheimer's disease, *Nature Reviews Immunology 6*, 404-416.
13. Boncheva, M., and Whitesides, G. M. (2005) Making things by self-assembly, *MRS bulletin 30*, 736-742.
14. Hsieh, M.-C., Lynn, D. G., and Grover, M. A. (2017) Kinetic model for two-step nucleation of peptide assembly, *The Journal of Physical Chemistry B 121*, 7401-7411.
15. Hursthouse, M. B., Huth, L. S., and Threlfall, T. L. (2009) Why do organic compounds crystallise well or badly or ever so slowly? Why is crystallisation nevertheless such a good purification technique?, *Organic Process Research & Development 13*, 1231-1240.
16. Chi, X., Guerin, A. J., Haycock, R. A., Hunter, C. A., and Sarson, L. D. (1995) The thermodynamics of self-assembly, *Journal of the Chemical Society, Chemical Communications*, 2563-2565.
17. Wang, J., Liu, K., Xing, R., and Yan, X. (2016) Peptide self-assembly: thermodynamics and kinetics, *Chemical Society Reviews 45*, 5589-5604.
18. Whitesides, G. M., Mathias, J. P., and Seto, C. T. (1991) Molecular self-assembly and nanochemistry: a chemical strategy for the synthesis of nanostructures, *Science 254*, 1312-1319.
19. McLaughlin, C. K., Hamblin, G. D., and Sleiman, H. F. (2011) Supramolecular DNA assembly, *Chemical Society Reviews 40*, 5647-5656.
20. Surewicz, W. K., Mantsch, H. H., and Chapman, D. (1993) Determination of protein secondary structure by Fourier transform infrared spectroscopy: a critical assessment, *Biochemistry 32*, 389-394.
21. Zhang, S. (2017) Discovery and design of self-assembling peptides, *Interface Focus 7*, 20170028.

22. Briggs, B. D., and Knecht, M. R. (2012) Nanotechnology meets biology: peptide-based methods for the fabrication of functional materials, *The journal of physical chemistry letters 3*, 405-418.
23. Ekiz, M. S., Cinar, G., Khalily, M. A., and Guler, M. O. (2016) Self-assembled peptide nanostructures for functional materials, *Nanotechnology 27*, 402002.
24. Czyzewski, A. M., and Barron, A. E. (2008) Protein and peptide biomimicry: Gold-mining inspiration from nature's ingenuity, *AIChE journal 54*, 2-8.
25. Smith, K. H., Tejeda-Montes, E., Poch, M., and Mata, A. (2011) Integrating top-down and self-assembly in the fabrication of peptide and protein-based biomedical materials, *Chemical Society Reviews 40*, 4563-4577.
26. Fleming, S., and Ulijn, R. V. (2014) Design of nanostructures based on aromatic peptide amphiphiles, *Chemical Society Reviews 43*, 8150-8177.
27. Gazit, E. (2007) Self assembly of short aromatic peptides into amyloid fibrils and related nanostructures, *Prion 1*, 32-35.
28. Chen, T., Li, M., and Liu, J. (2018) π–π stacking interaction: a nondestructive and facile means in material engineering for bioapplications, *Crystal Growth & Design 18*, 2765-2783.
29. Martinez, C. R., and Iverson, B. L. (2012) Rethinking the term “pi-stacking”, *Chemical Science 3*, 2191-2201.
30. Zhu, P., Yan, X., Su, Y., Yang, Y., and Li, J. (2010) Solvent-Induced Structural Transition of Self-Assembled Dipeptide: From Organogels to Microcrystals, *Chemistry–A European Journal 16*, 3176-3183.
31. Gazit, E. (2002) A possible role for π-stacking in the self-assembly of amyloid fibrils, *The FASEB Journal 16*, 77-83.
32. Reches, M., and Gazit, E. (2003) Casting metal nanowires within discrete self-assembled peptide nanotubes, *Science 300*, 625-627.
33. Reches, M., and Gazit, E. (2005) Self-assembly of peptide nanotubes and amyloid-like structures by charged-termini-capped diphenylalanine peptide analogues, *Israel journal of chemistry 45*, 363-371.
34. Yan, X., Zhu, P., and Li, J. (2010) Self-assembly and application of diphenylalanine-based nanostructures, *Chemical Society Reviews 39*, 1877-1890.
35. Singh, V., Snigdha, K., Singh, C., Sinha, N., and Thakur, A. K. (2015) Understanding the self-assembly of Fmoc–phenylalanine to hydrogel formation, *Soft Matter 11*, 5353-5364.
36. Jayawarna, V., Ali, M., Jowitt, T. A., Miller, A. F., Saiani, A., Gough, J. E., and Ulijn, R. V. (2006) Nanostructured hydrogels for three-dimensional cell culture through self-assembly of fluorenylmethoxycarbonyl–dipeptides, *Advanced Materials 18*, 611-614.
37. Orbach, R., Mironi-Harpaz, I., Adler-Abramovich, L., Mossou, E., Mitchell, E. P., Forsyth, V. T., Gazit, E., and Seliktar, D. (2012) The rheological and structural properties of Fmoc-peptide-based hydrogels: the effect of aromatic molecular architecture on self-assembly and physical characteristics, *Langmuir 28*, 2015-2022.
38. McCloskey, A. P., Draper, E. R., Gilmore, B. F., and Laverty, G. (2017) Ultrashort self-assembling Fmoc-peptide gelators for anti-infective biomaterial applications, *Journal of Peptide Science 23*, 131-140.
39. Wang, Y., Zhang, Z., Xu, L., Li, X., and Chen, H. (2013) Hydrogels of halogenated Fmoc-short peptides for potential application in tissue engineering, *Colloids and Surfaces B: Biointerfaces 104*, 163-168.
40. Yu, Z., Xu, Q., Dong, C., Lee, S. S., Gao, L., Li, Y., D'Ortenzio, M., and Wu, J. (2015) Self-assembling peptide nanofibrous hydrogel as a versatile drug delivery platform, *Current pharmaceutical design 21*, 4342-4354.
41. Huang, Z., Guan, S., Wang, Y., Shi, G., Cao, L., Gao, Y., Dong, Z., Xu, J., Luo, Q., and Liu, J. (2013) Self-assembly of amphiphilic peptides into bio-functionalized nanotubes: a novel hydrolase model, *Journal of Materials Chemistry B 1*, 2297-2304.

42. Soto, C. (2003) Unfolding the role of protein misfolding in neurodegenerative diseases, *Nature Reviews Neuroscience 4*, 49-60.
43. Agorogiannis, E., Agorogiannis, G., Papadimitriou, A., and Hadjigeorgiou, G. (2004) Protein misfolding in neurodegenerative diseases, *Neuropathology and applied neurobiology 30*, 215-224.
44. Naiki, H., and Gejyo, F. (1999) [20] Kinetic analysis of amyloid fibril formation, *Methods in enzymology 309*, 305-318.
45. Arosio, P., Knowles, T. P., and Linse, S. (2015) On the lag phase in amyloid fibril formation, *Physical Chemistry Chemical Physics 17*, 7606-7618.
46. Maïza, A., Chantepie, S., Vera, C., Fifre, A., Huynh, M. B., Stettler, O., Ouidja, M. O., and Papy-Garcia, D. (2018) The role of heparan sulfates in protein aggregation and their potential impact on neurodegeneration, *FEBS letters 592*, 3806-3818.
47. Eisenberg, D., and Jucker, M. (2012) The amyloid state of proteins in human diseases, *Cell 148*, 1188-1203.
48. Ke, P. C., Sani, M.-A., Ding, F., Kakinen, A., Javed, I., Separovic, F., Davis, T. P., and Mezzenga, R. (2017) Implications of peptide assemblies in amyloid diseases, *Chemical Society Reviews 46*, 6492-6531.
49. Abe, K., Kobayashi, N., Sode, K., and Ikebukuro, K. (2007) Peptide ligand screening of α-synuclein aggregation modulators by in silico panning, *Bmc Bioinformatics 8*, 1-7.
50. Villar-Piqué, A., Lopes da Fonseca, T., and Outeiro, T. F. (2016) Structure, function and toxicity of alpha-synuclein: the Bermuda triangle in synucleinopathies, *Journal of neurochemistry 139*, 240-255.
51. Knowles, T. P., Vendruscolo, M., and Dobson, C. M. (2014) The amyloid state and its association with protein misfolding diseases, *Nature reviews Molecular cell biology 15*, 384-396.
52. Mason, T. O., and Buell, A. K. (2019) The kinetics, thermodynamics and mechanisms of short aromatic peptide self-assembly, *Biological and Bio-inspired Nanomaterials*, 61-112.
53. Grzybowski, B. A., Fitzner, K., Paczesny, J., and Granick, S. (2017) From dynamic self-assembly to networked chemical systems, *Chemical Society Reviews 46*, 5647-5678.
54. Bowerman, C. J., and Nilsson, B. L. (2010) A reductive trigger for peptide self-assembly and hydrogelation, *Journal of the American Chemical Society 132*, 9526-9527.
55. Zhang, S., and Altman, M. (1999) Peptide self-assembly in functional polymer science and engineering, *Reactive and Functional Polymers 41*, 91-102.
56. Wang, X., Li, Y., He, X., Chen, S., and Zhang, J. Z. (2014) Effect of strong electric field on the conformational integrity of insulin, *The Journal of Physical Chemistry A 118*, 8942-8952.
57. Löwik, D. W., Leunissen, E., van den Heuvel, M., Hansen, M., and van Hest, J. C. (2010) Stimulus responsive peptide based materials, *Chemical Society Reviews 39*, 3394-3412.
58. Mattia, E., and Otto, S. (2015) Supramolecular systems chemistry, *Nature nanotechnology 10*, 111-119.
59. Zhao, X., and Zhang, S. (2007) Designer self-assembling peptide materials, *Macromolecular bioscience 7*, 13-22.
60. Marshall, K. E., Morris, K. L., Charlton, D., O'Reilly, N., Lewis, L., Walden, H., and Serpell, L. C. (2011) Hydrophobic, aromatic, and electrostatic interactions play a central role in amyloid fibril formation and stability, *Biochemistry 50*, 2061-2071.
61. Bowerman, C. J., and Nilsson, B. L. (2012) Review self-assembly of amphipathic β-sheet peptides: insights and applications, *Peptide Science 98*, 169-184.
62. Tartaglia, G. G., Pawar, A. P., Campioni, S., Dobson, C. M., Chiti, F., and Vendruscolo, M. (2008) Prediction of aggregation-prone regions in structured proteins, *Journal of molecular biology 380*, 425-436.

63. Xiong, H., Buckwalter, B. L., Shieh, H.-M., and Hecht, M. H. (1995) Periodicity of polar and nonpolar amino acids is the major determinant of secondary structure in self-assembling oligomeric peptides, *Proceedings of the National Academy of Sciences 92*, 6349-6353.
64. Ryan, D. M., Doran, T. M., Anderson, S. B., and Nilsson, B. L. (2011) Effect of C-terminal modification on the self-assembly and hydrogelation of fluorinated Fmoc-Phe derivatives, *Langmuir 27*, 4029-4039.
65. Das Mahapatra, R., Dey, J., and Weiss, R. G. (2017) L-Carnosine-derived Fmoc-tripeptides forming pH-sensitive and proteolytically stable supramolecular hydrogels, *Langmuir 33*, 12989-12999.
66. Yanlian, Y., Ulung, K., Xiumei, W., Horii, A., Yokoi, H., and Shuguang, Z. (2009) Designer self-assembling peptide nanomaterials, *Nano Today 4*, 193-210.
67. Melchionna, M., E Styan, K., and Marchesan, S. (2016) The unexpected advantages of using D-amino acids for peptide self-assembly into nanostructured hydrogels for medicine, *Current topics in medicinal chemistry 16*, 2009-2018.
68. Garcia, A. M., Iglesias, D., Parisi, E., Styan, K. E., Waddington, L. J., Deganutti, C., De Zorzi, R., Grassi, M., Melchionna, M., and Vargiu, A. V. (2018) Chirality effects on peptide self-assembly unraveled from molecules to materials, *Chem 4*, 1862-1876.
69. Bera, S., Xue, B., Rehak, P., Jacoby, G., Ji, W., Shimon, L. J., Beck, R., Král, P., Cao, Y., and Gazit, E. (2020) Self-assembly of aromatic amino acid enantiomers into supramolecular materials of high rigidity, *ACS nano 14*, 1694-1706.
70. Frederix, P. W., Scott, G. G., Abul-Haija, Y. M., Kalafatovic, D., Pappas, C. G., Javid, N., Hunt, N. T., Ulijn, R. V., and Tuttle, T. (2015) Exploring the sequence space for (tri-) peptide self-assembly to design and discover new hydrogels, *Nature chemistry 7*, 30.
71. Struthers, M. D., Cheng, R. P., and Imperiali, B. (1996) Design of a monomeric 23-residue polypeptide with defined tertiary structure, *Science 271*, 342-345.
72. Ghadiri, M. R., Granja, J. R., Milligan, R. A., McRee, D. E., and Khazanovich, N. (1993) Self-assembling organic nanotubes based on a cyclic peptide architecture, *Nature 366*, 324-327.
73. Sasidharan, S., Hazam, P. K., and Ramakrishnan, V. (2017) Symmetry-directed self-organization in peptide nanoassemblies through aromatic π–π interactions, *The Journal of Physical Chemistry B 121*, 404-411.
74. Hazam, P. K., Jerath, G., Chaudhary, N., and Ramakrishnan, V. (2018) Peptido-mimetic approach in the design of syndiotactic antimicrobial peptides, *International Journal of Peptide Research and Therapeutics 24*, 299-307.
75. Hazam, P. K., Singh, A., Chaudhary, N., and Ramakrishnan, V. (2019) Bactericidal potency and extended serum life of stereo-chemically engineered peptides against Mycobacterium, *International Journal of Peptide Research and Therapeutics 25*, 465-472.
76. Jerath, G., Goyal, R., Trivedi, V., Santhoshkumar, T., and Ramakrishnan, V. (2019) Syndiotactic peptides for targeted delivery, *Acta biomaterialia 87*, 130-139.
77. Hazam, P. K., Goyal, R., and Ramakrishnan, V. (2019) Peptide based antimicrobials: Design strategies and therapeutic potential, *Progress in biophysics and molecular biology 142*, 10-22.
78. Hazam, P. K., Jerath, G., Kumar, A., Chaudhary, N., and Ramakrishnan, V. (2017) Effect of tacticity-derived topological constraints in bactericidal peptides, *Biochimica et Biophysica Acta (BBA)-Biomembranes 1859*, 1388-1395.
79. Castelletto, V., Cheng, G., and Hamley, I. W. (2011) Amyloid peptides incorporating a core sequence from the amyloid beta peptide and gamma amino acids: relating bioactivity to self-assembly, *Chemical Communications 47*, 12470-12472.
80. Marchesan, S., Easton, C. D., Kushkaki, F., Waddington, L., and Hartley, P. G. (2012) Tripeptide self-assembled hydrogels: unexpected twists of chirality, *Chemical Communications 48*, 2195-2197.

81. Marchesan, S., Waddington, L., Easton, C. D., Winkler, D. A., Goodall, L., Forsythe, J., and Hartley, P. G. (2012) Unzipping the role of chirality in nanoscale self-assembly of tripeptide hydrogels, *Nanoscale 4*, 6752-6760.
82. Narayanaswamy, R., and Torchilin, V. P. (2019) Hydrogels and their applications in targeted drug delivery, *Molecules 24*, 603.
83. Dalmau, M., Lim, S., and Wang, S.-W. (2009) Design of a pH-dependent molecular switch in a caged protein platform, *Nano Letters 9*, 160-166.
84. Tang, J. D., Mura, C., and Lampe, K. J. (2019) Stimuli-responsive, pentapeptide, nanofiber hydrogel for tissue engineering, *Journal of the American Chemical Society 141*, 4886-4899.
85. Wong, S., Shim, M. S., and Kwon, Y. J. (2014) Synthetically designed peptide-based biomaterials with stimuli-responsive and membrane-active properties for biomedical applications, *Journal of Materials Chemistry B 2*, 595-615.
86. Zimenkov, Y., Dublin, S. N., Ni, R., Tu, R. S., Breedveld, V., Apkarian, R. P., and Conticello, V. P. (2006) Rational design of a reversible pH-responsive switch for peptide self-assembly, *Journal of the American Chemical Society 128*, 6770-6771.
87. Paternostre, M., and Artzner, F. (2017) pH responsive peptide self-assemblies: a mechanism as old as viruses, *Biophysical journal 112*, 359a-360a.
88. Aggeli, A., Bell, M., Carrick, L. M., Fishwick, C. W., Harding, R., Mawer, P. J., Radford, S. E., Strong, A. E., and Boden, N. (2003) pH as a trigger of peptide β-sheet self-assembly and reversible switching between nematic and isotropic phases, *Journal of the American Chemical Society 125*, 9619-9628.
89. Cote, Y., Fu, I. W., Dobson, E. T., Goldberger, J. E., Nguyen, H. D., and Shen, J. K. (2014) Mechanism of the pH-controlled self-assembly of nanofibers from peptide amphiphiles, *The Journal of Physical Chemistry C 118*, 16272-16278.
90. Zou, R., Wang, Q., Wu, J., Wu, J., Schmuck, C., and Tian, H. (2015) Peptide self-assembly triggered by metal ions, *Chemical Society Reviews 44*, 5200-5219.
91. Tainer, J. A., Roberts, V. A., and Getzoff, E. D. (1991) Metal-binding sites in proteins, *Current Opinion in Biotechnology 2*, 582-591.
92. Hutchinson, E. G., and Thornton, J. M. (1994) A revised set of potentials for β-turn formation in proteins, *Protein Science 3*, 2207-2216.
93. Imperiali, B., Moats, R., Fisher, S., and Prins, T. (1992) A conformational study of peptides with the general structure Ac-L-Xaa-Pro-D-Xaa-L-Xaa-NH2: spectroscopic evidence for a peptide with significant. beta.-turn character in water and in dimethyl sulfoxide, *Journal of the American Chemical Society 114*, 3182-3188.
94. Dyson, H. J., Rance, M., Houghten, R. A., Lerner, R. A., and Wright, P. E. (1988) Folding of immunogenic peptide fragments of proteins in water solution: I. Sequence requirements for the formation of a reverse turn, *Journal of molecular biology 201*, 161-200.
95. Cheng, R. P., Fisher, S. L., and Imperiali, B. (1996) Metallopeptide design: tuning the metal cation affinities with unnatural amino acids and peptide secondary structure, *Journal of the American Chemical Society 118*, 11349-11356.
96. Waldron, K. J., Rutherford, J. C., Ford, D., and Robinson, N. J. (2009) Metalloproteins and metal sensing, *Nature 460*, 823-830.
97. Thomson, A. J., and Gray, H. B. (1998) Bio-inorganic chemistry, *Current opinion in chemical biology 2*, 155-158.
98. Berthon, G. (1995) Critical evaluation of the stability constants of metal complexes of amino acids with polar side chains (Technical Report), *Pure and applied chemistry 67*, 1117-1240.
99. Lee, B.-C., and Zuckermann, R. N. (2010) Templated display of biomolecules and inorganic nanoparticles by metal ion-induced peptide nanofibers, *Chemical communications 46*, 1634-1636.

100. Salgado, E. N., Radford, R. J., and Tezcan, F. A. (2010) Metal-directed protein self-assembly, *Accounts of chemical research 43*, 661-672.
101. Mascini, M., Gaggiotti, S., Della Pelle, F., Di Natale, C., Qakala, S., Iwuoha, E., Pittia, P., and Compagnone, D. (2018) Peptide modified ZnO nanoparticles as gas sensors array for volatile organic compounds (VOCs), *Frontiers in chemistry 6*, 105.
102. Gooding, J. J., Hibbert, D. B., and Yang, W. (2001) Electrochemical metal ion sensors. Exploiting amino acids and peptides as recognition elements, *Sensors 1*, 75-90.
103. Wallin, C., Jarvet, J., Biverstål, H., Wärmländer, S., Danielsson, J., Gräslund, A., and Abelein, A. (2020) Metal ion coordination delays amyloid-β peptide self-assembly by forming an aggregation–inert complex: Mechanistic insights into Aβ self-assembly by metal ions, *Journal of Biological Chemistry 295*, 7224-7234.
104. Di Natale, C., De Benedictis, I., De Benedictis, A., and Marasco, D. (2020) Metal–Peptide Complexes as Promising Antibiotics to Fight Emerging Drug Resistance: New Perspectives in Tuberculosis, *Antibiotics 9*, 337.
105. Wang, W., Anderson, C. F., Wang, Z., Wu, W., Cui, H., and Liu, C.-J. (2017) Peptide-templated noble metal catalysts: syntheses and applications, *Chemical science 8*, 3310-3324.
106. Reiersen, H., Clarke, A. R., and Rees, A. R. (1998) Short elastin-like peptides exhibit the same temperature-induced structural transitions as elastin polymers: implications for protein engineering, *Journal of molecular biology 283*, 255-264.
107. Chen, C., Wang, Z., and Li, Z. (2011) Thermoresponsive polypeptides from pegylated poly-L-glutamates, *Biomacromolecules 12*, 2859-2863.
108. Komori, H., and Inai, Y. (2007) Control of peptide helix sense by temperature tuning of noncovalent chiral domino effect, *The Journal of organic chemistry 72*, 4012-4022.
109. Wang, C., Stewart, R. J., and KopeČek, J. (1999) Hybrid hydrogels assembled from synthetic polymers and coiled-coil protein domains, *Nature 397*, 417-420.
110. Kim, W., Thévenot, J., Ibarboure, E., Lecommandoux, S., and Chaikof, E. L. (2010) Self-assembly of thermally responsive amphiphilic diblock copolypeptides into spherical micellar nanoparticles, *Angewandte Chemie 122*, 4353-4356.
111. Huang, R., Wang, Y., Qi, W., Su, R., and He, Z. (2014) Temperature-induced reversible self-assembly of diphenylalanine peptide and the structural transition from organogel to crystalline nanowires, *Nanoscale research letters 9*, 1-9.
112. Yu, L., and Ding, J. (2008) Injectable hydrogels as unique biomedical materials, *Chemical Society Reviews 37*, 1473-1481.
113. Nguyen, M. K., and Lee, D. S. (2010) Injectable biodegradable hydrogels, *Macromolecular bioscience 10*, 563-579.
114. Pal, A., Shrivastava, S., and Dey, J. (2009) Salt, pH and thermoresponsive supramolecular hydrogel of N-(4-n-tetradecyloxybenzoyl)-l-carnosine, *Chemical communications*, 6997-6999.
115. Pochan, D. J., Schneider, J. P., Kretsinger, J., Ozbas, B., Rajagopal, K., and Haines, L. (2003) Thermally reversible hydrogels via intramolecular folding and consequent self-assembly of a de novo designed peptide, *Journal of the American Chemical Society 125*, 11802-11803.
116. Ryu, J., and Park, C. B. (2008) High-temperature self-assembly of peptides into vertically well-aligned nanowires by aniline vapor, *Advanced Materials 20*, 3754-3758.
117. Pappas, C. G., Mutasa, T., Frederix, P. W., Fleming, S., Bai, S., Debnath, S., Kelly, S. M., Gachagan, A., and Ulijn, R. V. (2015) Transient supramolecular reconfiguration of peptide nanostructures using ultrasound, *Materials Horizons 2*, 198-202.
118. Ye, F., Chen, S., Tang, G., and Wang, X. (2014) Sonication induced morphological transformation between 3D gel network and globular structure in a two-component gelation system, *Colloids and Surfaces A: Physicochemical and Engineering Aspects 452*, 165-172.
119. Hirst, A. R., Smith, D. K., Feiters, M. C., Geurts, H. P., and Wright, A. C. (2003) Two-component dendritic gels: easily tunable materials, *Journal of the American Chemical Society 125*, 9010-9011.

120. Pappas, C. G., Frederix, P. W., Mutasa, T., Fleming, S., Abul-Haija, Y. M., Kelly, S. M., Gachagan, A., Kalafatovic, D., Trevino, J., and Ulijn, R. V. (2015) Alignment of nanostructured tripeptide gels by directional ultrasonication, *Chemical communications 51*, 8465-8468.
121. Nomura, H., Matsuoka, T., and Koda, S. (2004) Ultrasonically induced birefringence in polymer solutions, *Pure and applied chemistry 76*, 97-104.
122. Tsuda, A., Nagamine, Y., Watanabe, R., Nagatani, Y., Ishii, N., and Aida, T. (2010) Spectroscopic visualization of sound-induced liquid vibrations using a supramolecular nanofibre, *Nature chemistry 2*, 977-983.
123. Naota, T., and Koori, H. (2005) Molecules that assemble by sound: an application to the instant gelation of stable organic fluids, *Journal of the American Chemical Society 127*, 9324-9325.
124. Wang, C., Zhang, D., and Zhu, D. (2005) A low-molecular-mass gelator with an electroactive tetrathiafulvalene group: tuning the gel formation by charge-transfer interaction and oxidation, *Journal of the American Chemical Society 127*, 16372-16373.
125. Hung, A. M., and Stupp, S. I. (2009) Understanding factors affecting alignment of self-assembling nanofibers patterned by sonication-assisted solution embossing, *Langmuir 25*, 7084-7089.
126. Paulusse, J. M., and Sijbesma, R. P. (2006) Molecule-based rheology switching, *Angewandte Chemie International Edition 45*, 2334-2337.
127. Bardelang, D., Camerel, F., Margeson, J. C., Leek, D. M., Schmutz, M., Zaman, M. B., Yu, K., Soldatov, D. V., Ziessel, R., and Ratcliffe, C. I. (2008) Unusual sculpting of dipeptide particles by ultrasound induces gelation, *Journal of the American Chemical Society 130*, 3313-3315.
128. Geng, H., Ye, L., Zhang, A.-y., Shao, Z., and Feng, Z.-g. (2017) Ultrasound-induced gelation of fluorenyl-9-methoxycarbonyl-l-lysine (fluorenyl-9-methoxycarbonyl)-OH and its dipeptide derivatives showing very low minimum gelation concentrations, *Journal of colloid and interface science 490*, 665-676.
129. Potenza, L., Ubaldi, L., De Sanctis, R., De Bellis, R., Cucchiarini, L., and Dachà, M. (2004) Effects of a static magnetic field on cell growth and gene expression in Escherichia coli, *Mutation Research/Genetic Toxicology and Environmental Mutagenesis 561*, 53-62.
130. Lacy-hulbert, A., Metcalfe, J. C., and Hesketh, R. (1998) Biological responses to electromagnetic fields 1, *The FASEB Journal 12*, 395-420.
131. Kwon, S., Kim, B. J., Lim, H.-K., Kang, K., Yoo, S. H., Gong, J., Yoon, E., Lee, J., Choi, I. S., and Kim, H. (2015) Magnetotactic molecular architectures from self-assembly of β-peptide foldamers, *Nature communications 6*, 1-7.
132. A. Hill, R., Sedman, V. L., Allen, S., Williams, P., Paoli, M., Adler-Abramovich, L., Gazit, E., Eaves, L., and Tendler, S. J. (2007) Alignment of aromatic peptide tubes in strong magnetic fields, *Advanced Materials 19*, 4474-4479.
133. Housaindokht, M. R., and Moosavi, F. (2018) Magnetic field effect on the structural properties of a peptide model: Molecular dynamics simulation study, *Journal of Molecular Structure 1161*, 393-402.
134. Yang, H., Mu, L., Zhang, L., Wang, Z., Sheng, S., Song, Y., Xiu, P., Wang, J., Shi, G., and Hu, J. (2020) Unexpectedly super strong paramagnetism of aromatic peptides due to cations of divalent metals, *arXiv preprint arXiv:2011.12797*.
135. Löwik, D. W., Shklyarevskiy, I. O., Ruizendaal, L., Christianen, P. C., Maan, J. C., and van Hest, J. C. (2007) A highly ordered material from magnetically aligned peptide amphiphile nanofiber assemblies, *Advanced materials 19*, 1191-1195.
136. Pauling, L. (1936) The diamagnetic anisotropy of aromatic molecules, *The Journal of Chemical Physics 4*, 673-677.
137. London, F. (1937) Supraconductivity in Aromatic Compounds, *The Journal of Chemical Physics 5*, 837-838.

138. Babu, S. S., Praveen, V. K., and Ajayaghosh, A. (2014) Functional π-gelators and their applications, *Chemical reviews 114*, 1973-2129.
139. Popova, G., Bobrov, M., and Vantsyan, M. (2008) Light-sensitive polyaminoacids as bio-inspired molecular materials, *Journal of Photochemistry and Photobiology A: Chemistry 196*, 246-253.
140. Chen, C.-S., Xu, X.-D., Li, S.-Y., Zhuo, R.-X., and Zhang, X.-Z. (2013) Photo-switched self-assembly of a gemini α-helical peptide into supramolecular architectures, *Nanoscale 5*, 6270-6274.
141. Huang, Y., Qiu, Z., Xu, Y., Shi, J., Lin, H., and Zhang, Y. (2011) Supramolecular hydrogels based on short peptides linked with conformational switch, *Organic & biomolecular chemistry 9*, 2149-2155.
142. Haines, L. A., Rajagopal, K., Ozbas, B., Salick, D. A., Pochan, D. J., and Schneider, J. P. (2005) Light-activated hydrogel formation via the triggered folding and self-assembly of a designed peptide, *Journal of the American Chemical Society 127*, 17025-17029.
143. Son, G., Lee, B. I., Chung, Y. J., and Park, C. B. (2018) Light-triggered dissociation of self-assembled β-amyloid aggregates into small, nontoxic fragments by ruthenium (II) complex, *Acta biomaterialia 67*, 147-155.
144. Ma, H., Fei, J., Li, Q., and Li, J. (2015) Photo-induced Reversible Structural Transition of Cationic Diphenylalanine Peptide Self-Assembly, *Small 11*, 1787-1791.
145. Roth-Konforti, M. E., Comune, M., Halperin-Sternfeld, M., Grigoriants, I., Shabat, D., and Adler-Abramovich, L. (2018) UV Light–Responsive Peptide-Based Supramolecular Hydrogel for Controlled Drug Delivery, *Macromolecular rapid communications 39*, 1800588.
146. Alfimov, M. V., Fedorova, O. A., and Gromov, S. P. (2003) Photoswitchable molecular receptors, *Journal of Photochemistry and Photobiology A: Chemistry 158*, 183-198.
147. Draper, E. R., and Adams, D. J. (2016) Photoresponsive gelators, *Chemical Communications 52*, 8196-8206.
148. Hettiarachchi, C. A., Melton, L. D., Gerrard, J. A., and Loveday, S. M. (2012) Formation of β-lactoglobulin nanofibrils by microwave heating gives a peptide composition different from conventional heating, *Biomacromolecules 13*, 2868-2880.
149. Kawasaki, T., Yamaguchi, Y., Ueda, T., Ishikawa, Y., Yaji, T., Ohta, T., Tsukiyama, K., Idehara, T., Saiki, M., and Tani, M. (2020) Irradiation effect of a submillimeter wave from 420 GHz gyrotron on amyloid peptides in vitro, *Biomedical optics express 11*, 5341-5351.
150. Zhang, S., and Rich, A. (1997) Direct conversion of an oligopeptide from a β-sheet to an α-helix: a model for amyloid formation, *Proceedings of the National Academy of Sciences 94*, 23-28.
151. Altman, M., Lee, P., Rich, A., and Zhang, S. (2000) Conformational behavior of ionic self-complementary peptides, *Protein Science 9*, 1095-1105.
152. Kammerer, R. A., Kostrewa, D., Zurdo, J., Detken, A., García-Echeverría, C., Green, J. D., Müller, S. A., Meier, B. H., Winkler, F. K., and Dobson, C. M. (2004) Exploring amyloid formation by a de novo design, *Proceedings of the National Academy of Sciences 101*, 4435-4440.
153. Ciani, B., Hutchinson, E. G., Sessions, R. B., and Woolfson, D. N. (2002) A designed system for assessing how sequence affects α to β conformational transitions in proteins, *Journal of Biological Chemistry 277*, 10150-10155.
154. Kostal, J., Mulchandani, A., Gropp, K. E., and Chen, W. (2003) A temperature responsive biopolymer for mercury remediation, *Environmental science & technology 37*, 4457-4462.
155. Prabhukumar, G., Matsumoto, M., Mulchandani, A., and Chen, W. (2004) Cadmium removal from contaminated soil by tunable biopolymers, *Environmental science & technology 38*, 3148-3152.
156. Garcia, A., Kurbasic, M., Kralj, S., Melchionna, M., and Marchesan, S. (2017) A biocatalytic and thermoreversible hydrogel from a histidine-containing tripeptide, *Chemical Communications 53*, 8110-8113.

157. Muraoka, T., Koh, C. Y., Cui, H., and Stupp, S. I. (2009) Light-triggered bioactivity in three dimensions, *Angewandte Chemie 121*, 6060-6063.
158. Negri, G. E., and Deming, T. J. (2016) Triggered copolypeptide hydrogel degradation using photolabile lysine protecting groups, *ACS Macro Letters 5*, 1253-1256.
159. Ke, D., Zhan, C., Li, X., Wang, X., Zeng, Y., and Yao, J. (2009) Ultrasound-induced modulations of tetrapeptide hierarchical 1-D self-assembly and underlying molecular structures via sonocrystallization, *Journal of colloid and interface science 337*, 54-60.
160. Afrasiabi, R., and Kraatz, H. B. (2013) Sonication-Induced Coiled Fibrous Architectures of Boc-L-Phe-L-Lys (Z)-OMe, *Chemistry–A European Journal 19*, 1769-1777.
161. Maity, S., Sarkar, S., Jana, P., Maity, S. K., Bera, S., Mahalingam, V., and Haldar, D. (2012) Sonication-responsive organogelation of a tripodal peptide and optical properties of embedded Tm 3+ nanoclusters, *Soft Matter 8*, 7960-7966.
162. Sazaki, G., Yoshida, E., Komatsu, H., Nakada, T., Miyashita, S., and Watanabe, K. (1997) Effects of a magnetic field on the nucleation and growth of protein crystals, *Journal of crystal growth 173*, 231-234.
163. Wallace, M., Cardoso, A. Z., Frith, W. J., Iggo, J. A., and Adams, D. J. (2014) Magnetically aligned supramolecular hydrogels, *Chemistry–A European Journal 20*, 16484-16487.
164. Kelly, C. M., Northey, T., Ryan, K., Brooks, B. R., Kholkin, A. L., Rodriguez, B. J., and Buchete, N.-V. (2015) Conformational dynamics and aggregation behavior of piezoelectric diphenylalanine peptides in an external electric field, *Biophysical chemistry 196*, 16-24.
165. Martin, L. J., Akhavan, B., and Bilek, M. M. (2018) Electric fields control the orientation of peptides irreversibly immobilized on radical-functionalized surfaces, *Nature communications 9*, 1-11.
166. Han, T. H., Kim, J., Park, J. S., Park, C. B., Ihee, H., and Kim, S. O. (2007) Liquid crystalline peptide nanowires, *Advanced Materials 19*, 3924-3927.
167. Velichko, Y. S., Mantei, J. R., Bitton, R., Carvajal, D., Shull, K. R., and Stupp, S. I. (2012) Electric Field Controlled Self-Assembly of Hierarchically Ordered Membranes, *Advanced functional materials 22*, 369-377.
168. Jenkins, K., Kelly, S., Nguyen, V., Wu, Y., and Yang, R. (2018) Piezoelectric diphenylalanine peptide for greatly improved flexible nanogenerators, *Nano Energy 51*, 317-323.
169. Servoli, E., Maniglio, D., Motta, A., and Migliaresi, C. (2008) Folding and assembly of fibroin driven by an AC electric field: effects on film properties, *Macromolecular bioscience 8*, 827-835.
170. Morotomi-Yano, K., Akiyama, H., and Yano, K.-i. (2014) Different involvement of extracellular calcium in two modes of cell death induced by nanosecond pulsed electric fields, *Archives of biochemistry and biophysics 555*, 47-54.
171. Ge, J., Neofytou, E., Cahill III, T. J., Beygui, R. E., and Zare, R. N. (2012) Drug release from electric-field-responsive nanoparticles, *ACS nano 6*, 227-233.
172. Zu, Y., Huang, S., Liao, W.-C., Lu, Y., and Wang, S. (2014) Gold nanoparticles enhanced electroporation for mammalian cell transfection, *Journal of biomedical nanotechnology 10*, 982-992.
173. Claessens, C. G., and Stoddart, J. F. (1997) π–π Interactions in self-assembly, *Journal of Physical Organic Chemistry 10*, 254-272.
174. Tang, C., Smith, A. M., Collins, R. F., Ulijn, R. V., and Saiani, A. (2009) Fmoc-diphenylalanine self-assembly mechanism induces apparent p K a shifts, *Langmuir 25*, 9447-9453.
175. Youn, I. S., Cho, W. J., and Kim, K. S. (2016) Effects of an electric field on interaction of aromatic systems, *Journal of Computational Chemistry 37*, 971-975.
176. Tan, H. L., Shamsudeen, H., and So'aib, M. S. (2018) Effects of Electric Filed on β-sheet Propensity Self-Assembled Amphiphile Peptides, *Materials Today: Proceedings 5*, S143-S148.

177. Yu, J., Wang, Q., and Zhang, X. (2014) Effects of external force fields on peptide self-assembly and biomimetic silica synthesis, *Applied surface science 311*, 799-807.
178. Lugli, F., Toschi, F., Biscarini, F., and Zerbetto, F. (2010) Electric field effects on short fibrils of Aβ amyloid peptides, *Journal of Chemical Theory and Computation 6*, 3516-3526.
179. Bekard, I., and Dunstan, D. E. (2014) Electric field induced changes in protein conformation, *Soft Matter 10*, 431-437.
180. Singh, A., Munshi, S., and Raghavan, V. (2013) Effect of external electric field stress on gliadin protein conformation, *Proteomes 1*, 25-39.
181. Ojeda-May, P., and Garcia, M. E. (2010) Electric field-driven disruption of a native β-sheet protein conformation and generation of a helix-structure, *Biophysical journal 99*, 595-599.
182. Lu, Y., Shi, X.-F., Salsbury Jr, F. R., and Derreumaux, P. (2017) Small static electric field strength promotes aggregation-prone structures in amyloid-β (29-42), *The Journal of chemical physics 146*, 145101.
183. Baumketner, A. (2014) Electric field as a disaggregating agent for amyloid fibrils, *The Journal of Physical Chemistry B 118*, 14578-14589.
184. Muscat, S., Stojceski, F., and Danani, A. (2020) Elucidating the Effect of Static Electric Field on Amyloid Beta 1–42 Supramolecular Assembly, *Journal of Molecular Graphics and Modelling 96*, 107535.
185. Lu, Y., Shi, X.-F., Salsbury Jr, F. R., and Derreumaux, P. (2018) Influence of electric field on the amyloid-β (29-42) peptides embedded in a membrane bilayer, *The Journal of chemical physics 148*, 045105.
186. Jiang, Z., You, L., Dou, W., Sun, T., and Xu, P. (2019) Effects of an electric field on the conformational transition of the protein: A molecular dynamics simulation study, *Polymers 11*, 282.
187. Pandey, G., Saikia, J., Sasidharan, S., Joshi, D. C., Thota, S., Nemade, H. B., Chaudhary, N., and Ramakrishnan, V. (2017) Modulation of peptide based nano-assemblies with electric and magnetic fields, *Scientific reports 7*, 1-9.
188. Nguyen, V., Zhu, R., Jenkins, K., and Yang, R. (2016) Self-assembly of diphenylalanine peptide with controlled polarization for power generation, *Nature communications 7*, 1-6.
189. Nguyen, V., Jenkins, K., and Yang, R. (2015) Epitaxial growth of vertically aligned piezoelectric diphenylalanine peptide microrods with uniform polarization, *Nano Energy 17*, 323-329.
190. Song, Y., Wu, R., Wang, Y., Liu, L., and Dong, M. (2020) Structural conversion of human islet amyloid polypeptide aggregates under an electric field, *Chemical Communications 56*, 11497-11500.
191. Worley, C. G., Linton, R. W., and Samulski, E. T. (1995) Electric-Field-Enhanced Self-Assembly of. alpha.-helical polypeptides, *Langmuir 11*, 3805-3810.
192. Sen, S., Chakraborty, M., Goley, S., Dasgupta, S., and DasGupta, S. (2017) Fibrillar disruption by AC electric field induced oscillation: A case study with human serum albumin, *Biophysical chemistry 226*, 23-33.
193. Pandey, G., Morla, S., Nemade, H. B., Kumar, S., and Ramakrishnan, V. (2019) Modulation of aggregation with an electric field; scientific roadmap for a potential non-invasive therapy against tauopathies, *RSC advances 9*, 4744-4750.
194. De, D., Pawar, N., and Gupta, A. N. (2021) Electric field-driven conformational changes in the elastin protein, *Physical Chemistry Chemical Physics*.
195. Zibly, Z., Averbuch, S., and Deogaonker, M. (2020) Emerging Technologies and Indications of Neuromodulation and Increasing Role of Non Invasive Neuromodulation, *Neurology India 68*, 316.
196. Nicodemus, N. E., Becerra, S., Kuhn, T. P., Packham, H. R., Duncan, J., Mahdavi, K., Iovine, J., Kesari, S., Pereles, S., and Whitney, M. (2019) Focused transcranial ultrasound for treatment

of neurodegenerative dementia, *Alzheimer's & Dementia: Translational Research & Clinical Interventions 5*, 374-381.
197. Rezai, A. R., Ranjan, M., D'Haese, P.-F., Haut, M. W., Carpenter, J., Najib, U., Mehta, R. I., Chazen, J. L., Zibly, Z., and Yates, J. R. (2020) Noninvasive hippocampal blood− brain barrier opening in Alzheimer's disease with focused ultrasound, *Proceedings of the National Academy of Sciences 117*, 9180-9182.
198. D'Haese, P.-F., Ranjan, M., Song, A., Haut, M. W., Carpenter, J., Dieb, G., Najib, U., Wang, P., Mehta, R. I., and Chazen, J. L. (2020) β-Amyloid Plaque Reduction in the Hippocampus After Focused Ultrasound-Induced Blood–Brain Barrier Opening in Alzheimer's Disease, *Frontiers in Human Neuroscience 14*, 422.
199. Leinenga, G., and Götz, J. (2015) Scanning ultrasound removes amyloid-β and restores memory in an Alzheimer's disease mouse model, *Science translational medicine 7*, 278ra233-278ra233.
200. Meng, Y., Hynynen, K., and Lipsman, N. (2020) Applications of focused ultrasound in the brain: From thermoablation to drug delivery, *Nature Reviews Neurology*, 1-16.
201. Deisseroth, K. (2011) Optogenetics, *Nature methods 8*, 26-29.
202. Ismail, R., Hansen, A. K., Parbo, P., Brændgaard, H., Gottrup, H., Brooks, D. J., and Borghammer, P. (2018) The effect of 40-Hz light therapy on amyloid load in patients with prodromal and clinical Alzheimer's disease, *International Journal of Alzheimer's Disease 2018*.
203. Lee, J. S., Lee, B. I., and Park, C. B. (2015) Photo-induced inhibition of Alzheimer's β-amyloid aggregation in vitro by rose bengal, *Biomaterials 38*, 43-49.
204. George, M. S., Lisanby, S. H., and Sackeim, H. A. (1999) Transcranial magnetic stimulation: applications in neuropsychiatry, *Archives of general psychiatry 56*, 300-311.
205. Maldonado-Moreles, A., Cordova-Fraga, T., Bonilla-Jaime, H., Lopez-Camacho, P. Y., and Basurto-Islas, G. (2021) Low frequency vortex magnetic field reduces amyloid β aggregation, increase cell viability and protect from amyloid β toxicity, *Electromagnetic Biology and Medicine 40*, 191-200.
206. Kwon, J., Choi, J. S., Lee, J., Na, J., Sung, J., Lee, H.-J., Lee, H.-s., Lim, Y.-b., and Choi, H.-J. (2020) Disaggregation of Amyloid-β Plaques by a Local Electric Field Generated by a Vertical Nanowire Electrode Array, *ACS Applied Materials & Interfaces*.
207. Zheng, Y., Wang, Q., Yang, X., Nie, W., Zou, L., Liu, X., and Wang, K. (2018) Aptamer as a tool for investigating the effects of electric field on Aβ40 monomer and aggregates using single-molecule force spectroscopy, *Analytical chemistry 91*, 1954-1961.
208. Budi, A., Legge, F. S., Treutlein, H., and Yarovsky, I. (2005) Electric field effects on insulin chain-B conformation, *The Journal of Physical Chemistry B 109*, 22641-22648.
209. Toschi, F., Lugli, F., Biscarini, F., and Zerbetto, F. (2009) Effects of electric field stress on a β-amyloid peptide, *The Journal of Physical Chemistry B 113*, 369-376.
210. Goldberger, M. L., and Watson, K. M. (2004) *Collision theory*, Courier Corporation.
211. Boudart, M. (1995) Turnover rates in heterogeneous catalysis, *Chemical reviews 95*, 661-666.
212. Schüth, F., Ward, M. D., and Buriak, J. M. (2018) Common pitfalls of catalysis manuscripts submitted to chemistry of materials, ACS Publications.
213. Corma, A., and Garcia, H. (2008) Crossing the borders between homogeneous and heterogeneous catalysis: developing recoverable and reusable catalytic systems, *Topics in Catalysis 48*, 8-31.
214. Haibach, M. C., Kundu, S., Brookhart, M., and Goldman, A. S. (2012) Alkane metathesis by tandem alkane-dehydrogenation–olefin-metathesis catalysis and related chemistry, *Accounts of chemical research 45*, 947-958.
215. Tiltscher, H., Wolf, H., and Schelchshorn, J. (1981) A mild and effective method for the reactivation or maintenance of the activity of heterogeneous catalysts, *Angewandte Chemie International Edition in English 20*, 892-894.

216. Muhler, M. (1997) JM Thomas and WJ Thomas: Principles and Practice of Heterogeneous Catalysis, VCH, Weinheim, 1997, ISBN 3-527-29239-X, Preis: 88,–DM, Wiley Online Library.
217. Campbell, I. M. (1988) *Catalysis at surfaces*, Springer Science & Business Media.
218. Joubert, J., Delbecq, F., Sautet, P., Le Roux, E., Taoufik, M., Thieuleux, C., Blanc, F., Copéret, C., Thivolle-Cazat, J., and Basset, J.-M. (2006) Molecular understanding of alumina supported single-site catalysts by a combination of experiment and theory, *Journal of the American Chemical Society 128*, 9157-9169.
219. Mlynarski, J., and Paradowska, J. (2008) Catalytic asymmetric aldol reactions in aqueous media, *Chemical Society Reviews 37*, 1502-1511.
220. McMorn, P., and Hutchings, G. J. (2004) Heterogeneous enantioselective catalysts: strategies for the immobilisation of homogeneous catalysts, *Chemical Society Reviews 33*, 108-122.
221. Liu, M., Zhang, L., and Wang, T. (2015) Supramolecular chirality in self-assembled systems, *Chemical reviews 115*, 7304-7397.
222. Chapman, J., Ismail, A. E., and Dinu, C. Z. (2018) Industrial applications of enzymes: Recent advances, techniques, and outlooks, *Catalysts 8*, 238.
223. Kuah, E., Toh, S., Yee, J., Ma, Q., and Gao, Z. (2016) Enzyme mimics: advances and applications, *Chemistry–A European Journal 22*, 8404-8430.
224. Labádi, I., Benkő, M., Markó, K., and Szilágyi, I. (2009) Mimicking a Superoxide Dismutase (SOD) Enzyme by copper (II) and zinc (II)-complexes, *Reaction Kinetics and Catalysis Letters 96*, 327-333.
225. Makam, P., and Gazit, E. (2018) Minimalistic peptide supramolecular co-assembly: expanding the conformational space for nanotechnology, *Chemical Society Reviews 47*, 3406-3420.
226. Cleij, M. C., Drenth, W., and Nolte, R. J. (1991) Mechanism of enantioselective ester cleavage by histidine containing dipeptides at a micellar interface, *The Journal of Organic Chemistry 56*, 3883-3891.
227. Zaramella, D., Scrimin, P., and Prins, L. J. (2012) Self-assembly of a catalytic multivalent peptide–nanoparticle complex, *Journal of the American Chemical Society 134*, 8396-8399.
228. Das, G., Sakai, N., and Matile, S. (2002) Toward catalytic rigid-rod β-barrels: A hexamer with multiple histidines, *Chirality 14*, 18-24.
229. Singh, N., Tena-Solsona, M., Miravet, J. F., and Escuder, B. (2015) Towards Supramolecular Catalysis with Small Self-assembled Peptides, *Israel Journal of Chemistry 55*, 711-723.
230. Díaz, D. D., Kühbeck, D., and Koopmans, R. J. (2011) Stimuli-responsive gels as reaction vessels and reusable catalysts, *Chemical Society Reviews 40*, 427-448.
231. Guler, M. O., and Stupp, S. I. (2007) A self-assembled nanofiber catalyst for ester hydrolysis, *Journal of the American Chemical Society 129*, 12082-12083.
232. Rodriguez-Llansola, F., Escuder, B., and Miravet, J. F. (2009) Switchable perfomance of an L-proline-derived basic catalyst controlled by supramolecular gelation, *Journal of the American Chemical Society 131*, 11478-11484.
233. Rodríguez-Llansola, F., Miravet, J. F., and Escuder, B. (2009) A supramolecular hydrogel as a reusable heterogeneous catalyst for the direct aldol reaction, *Chemical communications*, 7303-7305.
234. Rodríguez-Llansola, F., Miravet, J. F., and Escuder, B. (2010) Supramolecular Catalysis with Extended Aggregates and Gels: Inversion of Stereoselectivity Caused by Self-Assembly, *Chemistry–A European Journal 16*, 8480-8486.
235. Vallee, B. L., and Williams, R. (1968) Metalloenzymes: the entatic nature of their active sites, *Proceedings of the National Academy of Sciences of the United States of America 59*, 498.
236. DeGrado, W. F., Summa, C. M., Pavone, V., Nastri, F., and Lombardi, A. (1999) De novo design and structural characterization of proteins and metalloproteins, *Annual review of biochemistry 68*, 779-819.

237. Greenfield, S. J., Agarkov, A., and Gilbertson, S. R. (2003) High asymmetric induction with β-turn-derived palladium phosphine complexes, *Organic letters 5*, 3069-3072.
238. Breit, B., and Laungani, A. C. (2003) Copper-catalyzed enantioselective conjugate addition of dialkylzinc reagents to enones with new peptidyl phosphane ligands, *Tetrahedron: Asymmetry 14*, 3823-3826.
239. Degrado, S. J., Mizutani, H., and Hoveyda, A. H. (2001) Modular peptide-based phosphine ligands in asymmetric catalysis: efficient and enantioselective Cu-catalyzed conjugate additions to five-, six-, and seven-membered cyclic enones, *Journal of the American Chemical Society 123*, 755-756.
240. Josephsohn, N. S., Kuntz, K. W., Snapper, M. L., and Hoveyda, A. H. (2001) Mechanism of enantioselective Ti-catalyzed Strecker reaction: peptide-based metal complexes as bifunctional catalysts, *Journal of the American Chemical Society 123*, 11594-11599.
241. Schwizer, F., Okamoto, Y., Heinisch, T., Gu, Y., Pellizzoni, M. M., Lebrun, V., Reuter, R., Köhler, V., Lewis, J. C., and Ward, T. R. (2018) Artificial metalloenzymes: reaction scope and optimization strategies, *Chemical reviews 118*, 142-231.
242. Mori, A., Abet, H., and Inoue, S. (1995) Amino-Acids, peptides and their derivatives: Powerful chiral ligands for metal-catalyzed asymmetric syntheses, *Applied organometallic chemistry 9*, 189-197.
243. Davis, H. J., and Ward, T. R. (2019) Artificial metalloenzymes: Challenges and opportunities, *ACS central science 5*, 1120-1136.
244. Sasaki, T., and Kaiser, E. T. (1989) Helichrome: synthesis and enzymic activity of a designed hemeprotein, *Journal of the American Chemical Society 111*, 380-381.
245. Sluka, J. P., Horvath, S. J., Bruist, M. F., Simon, M. I., and Dervan, P. B. (1987) Synthesis of a sequence-specific DNA-cleaving peptide, *Science 238*, 1129-1132.
246. Mack, D. P., Iverson, B. L., and Dervan, P. B. (1988) Design and chemical synthesis of a sequence-specific DNA-cleaving protein, *Journal of the American Chemical Society 110*, 7572-7574.
247. Sambasivan, R., and Ball, Z. T. (2010) Metallopeptides for asymmetric dirhodium catalysis, *Journal of the American Chemical Society 132*, 9289-9291.
248. Sambasivan, R., and Ball, Z. T. (2012) Screening rhodium metallopeptide libraries "on bead": asymmetric cyclopropanation and a solution to the enantiomer problem, *Angewandte Chemie International Edition 51*, 8568-8572.
249. Sambasivan, R., and Ball, Z. T. (2013) Studies of Asymmetric Styrene Cyclopropanation with a Rhodium (II) Metallopeptide Catalyst Developed with a High-Throughput Screen, *Chirality 25*, 493-497.
250. Artner, L. M., Merkel, L., Bohlke, N., Beceren-Braun, F., Weise, C., Dernedde, J., Budisa, N., and Hackenberger, C. P. (2012) Site-selective modification of proteins for the synthesis of structurally defined multivalent scaffolds, *Chemical Communications 48*, 522-524.
251. Gilbertson, S. R., and Pawlick, R. V. (1996) Synthesis of Thiophosphoryl Derivatives of Proline: Building Blocks for Phosphanyl-Substituted Peptides with β-Turns, *Angewandte Chemie International Edition in English 35*, 902-904.
252. Agarkov, A., Greenfield, S. J., Ohishi, T., Collibee, S. E., and Gilbertson, S. R. (2004) Catalysis with phosphine-containing amino acids in various "turn" motifs, *The Journal of organic chemistry 69*, 8077-8085.
253. Zastrow, M. L., Peacock, A. F., Stuckey, J. A., and Pecoraro, V. L. (2012) Hydrolytic catalysis and structural stabilization in a designed metalloprotein, *Nature chemistry 4*, 118-123.
254. Dürrenberger, M., and Ward, T. R. (2014) Recent achievments in the design and engineering of artificial metalloenzymes, *Current opinion in chemical biology 19*, 99-106.
255. Park, G. Y., Lee, J. Y., Himes, R. A., Thomas, G. S., Blackburn, N. J., and Karlin, K. D. (2014) Copper–peptide complex structure and reactivity when found in conserved his-xaa-his sequences, *Journal of the American Chemical Society 136*, 12532-12535.

256. Krupa, K., Korabik, M., and Kowalik-Jankowska, T. (2019) Coordination properties of Cu (II) ions towards the peptides based on the His-Xaa-His motif from Fusobacterium nucleatum P1 protein, *Journal of inorganic biochemistry 201*, 110819.
257. Árus, D., Nagy, N. V., Dancs, Á., Jancsó, A., Berkecz, R., and Gajda, T. (2013) A minimalist chemical model of matrix metalloproteinases—Can small peptides mimic the more rigid metal binding sites of proteins?, *Journal of inorganic biochemistry 126*, 61-69.
258. Kopera, E., Krezel, A., Protas, A. M., Belczyk, A., Bonna, A., Wysłouch-Cieszyńska, A., Poznański, J., and Bal, W. (2010) Sequence-specific Ni (II)-dependent peptide bond hydrolysis for protein engineering: reaction conditions and molecular mechanism, *Inorganic chemistry 49*, 6636-6645.
259. Jancsó, A., Paksi, Z., Jakab, N., Gyurcsik, B., Rockenbauer, A., and Gajda, T. (2005) Solution chemical properties and catecholase-like activity of the copper (II)–Ac-His-His-Gly-His-OH system, a relevant functional model for copper containing oxidases, *Dalton Transactions*, 3187-3194.
260. Árus, D., Jancsó, A., Szunyogh, D., Matyuska, F., Nagy, N. V., Hoffmann, E., Körtvélyesi, T., and Gajda, T. (2012) On the possible roles of N-terminal His-rich domains of Cu, Zn SODs of some Gram-negative bacteria, *Journal of inorganic biochemistry 106*, 10-18.
261. Jakab, N. I., Jancsó, A., Gajda, T., Gyurcsik, B., and Rockenbauer, A. (2008) Copper (II), nickel (II) and zinc (II) complexes of N-acetyl-His-Pro-His-His-NH2: Equilibria, solution structure and enzyme mimicking, *Journal of inorganic biochemistry 102*, 1438-1448.
262. Timári, S., Cerea, R., and Várnagy, K. (2011) Characterization of CuZnSOD model complexes from a redox point of view: Redox properties of copper (II) complexes of imidazole containing ligands, *Journal of inorganic biochemistry 105*, 1009-1017.
263. Prigge, S. T., Kolhekar, A. S., Eipper, B. A., Mains, R. E., and Amzel, L. M. (1997) Amidation of bioactive peptides: the structure of peptidylglycine α-hydroxylating monooxygenase, *Science 278*, 1300-1305.
264. Prigge, S. T., Mains, R., Eipper, B., and Amzel, L. (2000) New insights into copper monooxygenases and peptide amidation: structure, mechanism and function, *Cellular and Molecular Life Sciences CMLS 57*, 1236-1259.
265. Gleason, J. E., Galaleldeen, A., Peterson, R. L., Taylor, A. B., Holloway, S. P., Waninger-Saroni, J., Cormack, B. P., Cabelli, D. E., Hart, P. J., and Culotta, V. C. (2014) Candida albicans SOD5 represents the prototype of an unprecedented class of Cu-only superoxide dismutases required for pathogen defense, *Proceedings of the National Academy of Sciences 111*, 5866-5871.
266. Hesse, L., Beher, D., Masters, C. L., and Multhaup, G. (1994) The βA4 amyloid precursor protein binding to copper, *FEBS letters 349*, 109-116.
267. Peacock, A. F., Hemmingsen, L., and Pecoraro, V. L. (2008) Using diastereopeptides to control metal ion coordination in proteins, *Proceedings of the National Academy of Sciences 105*, 16566-16571.
268. Ciano, L., Davies, G. J., Tolman, W. B., and Walton, P. H. (2018) Bracing copper for the catalytic oxidation of C–H bonds, *Nature Catalysis 1*, 571-577.
269. Arora, R., Bharval, P., Sarswati, S., Sen, T. Z., and Yennamalli, R. M. (2019) Structural dynamics of lytic polysaccharide monoxygenases reveals a highly flexible substrate binding region, *Journal of Molecular Graphics and Modelling 88*, 1-10.
270. Horn, S. J., Vaaje-Kolstad, G., Westereng, B., and Eijsink, V. (2012) Novel enzymes for the degradation of cellulose, *Biotechnology for biofuels 5*, 45.
271. Span, E. A., and Marletta, M. A. (2015) The framework of polysaccharide monooxygenase structure and chemistry, *Current opinion in structural biology 35*, 93-99.
272. Walton, P. H., and Davies, G. J. (2016) On the catalytic mechanisms of lytic polysaccharide monooxygenases, *Current opinion in chemical biology 31*, 195-207.

273. Kjaergaard, C. H., Qayyum, M. F., Wong, S. D., Xu, F., Hemsworth, G. R., Walton, D. J., Young, N. A., Davies, G. J., Walton, P. H., and Johansen, K. S. (2014) Spectroscopic and computational insight into the activation of O2 by the mononuclear Cu center in polysaccharide monooxygenases, *Proceedings of the National Academy of Sciences 111*, 8797-8802.
274. Vaaje-Kolstad, G., Forsberg, Z., Loose, J. S., Bissaro, B., and Eijsink, V. G. (2017) Structural diversity of lytic polysaccharide monooxygenases, *Current opinion in structural biology 44*, 67-76.
275. Equbal, A., Madhu, P. K., Meier, B. H., Nielsen, N. C., Ernst, M., and Agarwal, V. (2017) Parameter independent low-power heteronuclear decoupling for fast magic-angle spinning solid-state NMR, *The Journal of chemical physics 146*, 084202.
276. Hanwell, M. D., Curtis, D. E., Lonie, D. C., Vandermeersch, T., Zurek, E., and Hutchison, G. R. (2012) Avogadro: an advanced semantic chemical editor, visualization, and analysis platform, *Journal of cheminformatics 4*, 1-17.
277. Frisch, M., Trucks, G., Schlegel, H., Scuseria, G., Robb, M., Cheeseman, J., Scalmani, G., Barone, V., Petersson, G., and Nakatsuji, H. (2016) Gaussian 16, Gaussian, Inc. Wallingford, CT.
278. Kozłowski, H., Bal, W., Dyba, M., and Kowalik-Jankowska, T. (1999) Specific structure–stability relations in metallopeptides, *Coordination Chemistry Reviews 184*, 319-346.
279. Cai, D., and Klinman, J. P. (1994) Copper amine oxidase: heterologous expression, purification, and characterization of an active enzyme in Saccharomyces cerevisiae, *Biochemistry 33*, 7647-7653.
280. Garajova, S., Mathieu, Y., Beccia, M. R., Bennati-Granier, C., Biaso, F., Fanuel, M., Ropartz, D., Guigliarelli, B., Record, E., and Rogniaux, H. (2016) Single-domain flavoenzymes trigger lytic polysaccharide monooxygenases for oxidative degradation of cellulose, *Scientific reports 6*, 1-9.
281. Gonzalez, P., Vileno, B., Bossak, K., El Khoury, Y., Hellwig, P., Bal, W., Hureau, C., and Faller, P. (2017) Cu (II) binding to the peptide Ala-His-His, a chimera of the canonical Cu (II)-binding motifs Xxx-His and Xxx-Zzz-His, *Inorganic chemistry 56*, 14870-14879.
282. Fawcett, T. G., Bernarducci, E. E., Krogh-Jespersen, K., and Schugar, H. J. (1980) Charge-transfer absorptions of copper (II)-imidazole and copper (II)-imidazolate chromophores, *Journal of the American Chemical Society 102*, 2598-2604.
283. Zoroddu, M. A., Medici, S., and Peana, M. (2009) Copper and nickel binding in multi-histidinic peptide fragments, *Journal of inorganic biochemistry 103*, 1214-1220.
284. Momotani, Y., Arie, R., and Takagi, T. (1981) Novel transient circular dichroic spectra with a trough near 230 nm observed in the denaturation processes of lectins by sodium dodecyl sulfate, *Biochimica et Biophysica Acta (BBA)-Protein Structure 668*, 193-196.
285. Iyer, A., Roeters, S. J., Kogan, V., Woutersen, S., Claessens, M. M. E., and Subramaniam, V. (2017) C-terminal truncated α-synuclein fibrils contain strongly twisted β-sheets, *Journal of the American Chemical Society 139*, 15392-15400.
286. Kivelson, D., and Neiman, R. (1961) ESR studies on the bonding in copper complexes, *The Journal of Chemical Physics 35*, 149-155.
287. Getz, D., and Silver, B. L. (1974) ESR of Cu2+ (H2O) 6. I. The oxygen-17 superhyperfine tensors in 63Cu2+ doped zinc Tutton's salt at 20° K, *The Journal of Chemical Physics 61*, 630-637.
288. Stanila, A., Marcu, A., Rusu, D., Rusu, M., and David, L. (2007) Spectroscopic studies of some copper (II) complexes with amino acids, *Journal of Molecular Structure 834*, 364-368.
289. Smulevich, G., Mauro, J. M., Fishel, L. A., English, A. M., Kraut, J., and Spiro, T. G. (1988) Heme pocket interactions in cytochrome c peroxidase studied by site-directed mutagenesis and resonance Raman spectroscopy, *Biochemistry 27*, 5477-5485.
290. Escobar, S., Velasco-Lozano, S., Lu, C.-H., Lin, Y.-F., Mesa, M., Bernal, C., and López-Gallego, F. (2017) Understanding the functional properties of bio-inorganic nanoflowers as

biocatalysts by deciphering the metal-binding sites of enzymes, *Journal of Materials Chemistry B 5*, 4478-4486.
291. Gulseren, G., Khalily, M. A., Tekinay, A. B., and Guler, M. O. (2016) Catalytic supramolecular self-assembled peptide nanostructures for ester hydrolysis, *Journal of Materials Chemistry B 4*, 4605-4611.
292. Kaplan, J., and DeGrado, W. (2004) De novo design of catalytic proteins, *Proceedings of the National Academy of Sciences 101*, 11566-11570.
293. Mahalakshmi, R., and Balaram, P. (2007) The use of D-amino acids in peptide design, *D-Amino Acids: A New Frontier in Amino Acid and Protein Research—Practical Methods and Protocols*, 415-430.
294. Hasegawa, K., Ono, T.-a., and Noguchi, T. (2002) Ab initio density functional theory calculations and vibrational analysis of zinc-bound 4-methylimidazole as a model of a histidine ligand in metalloenzymes, *The Journal of Physical Chemistry A 106*, 3377-3390.
295. Marti, E. M., Methivier, C., Dubot, P., and Pradier, C. (2003) Adsorption of (S)-histidine on Cu (110) and oxygen-covered Cu (110), a combined Fourier transform reflection absorption infrared spectroscopy and force field calculation study, *The Journal of Physical Chemistry B 107*, 10785-10792.
296. Tishmack, P. A., Bashford, D., Harms, E., and Van Etten, R. L. (1997) Use of 1H NMR Spectroscopy and Computer Simulations To Analyze Histidine p K a Changes in a Protein Tyrosine Phosphatase: Experimental and Theoretical Determination of Electrostatic Properties in a Small Protein, *Biochemistry 36*, 11984-11994.
297. Muthuramalingam, S., Maheshwaran, D., Velusamy, M., and Mayilmurugan, R. (2019) Regioselective oxidative carbon-oxygen bond cleavage catalysed by copper (II) complexes: A relevant model study for lytic polysaccharides monooxygenases activity, *Journal of Catalysis 372*, 352-361.
298. Duncan, K. L., and Ulijn, R. V. (2015) Short peptides in minimalistic biocatalyst design, *Biocatalysis 1*, 67-81.
299. Li, S., and Hong, M. (2011) Protonation, tautomerization, and rotameric structure of histidine: a comprehensive study by magic-angle-spinning solid-state NMR, *Journal of the American Chemical Society 133*, 1534-1544.
300. Platzer, G., Okon, M., and McIntosh, L. P. (2014) pH-dependent random coil 1 H, 13 C, and 15 N chemical shifts of the ionizable amino acids: a guide for protein pK a measurements, *Journal of biomolecular NMR 60*, 109-129.
301. McCann, S. D., and Stahl, S. S. (2015) Copper-catalyzed aerobic oxidations of organic molecules: pathways for two-electron oxidation with a four-electron oxidant and a one-electron redox-active catalyst, *Accounts of chemical research 48*, 1756-1766.
302. Hawkins, K., Patterson, A. K., Clarke, P. A., and Smith, D. K. (2020) Catalytic Gels for a Prebiotically Relevant Asymmetric Aldol Reaction in Water: From Organocatalyst Design to Hydrogel Discovery and Back Again, *Journal of the American Chemical Society 142*, 4379-4389.
303. Singh, N., Kumar, M., Miravet, J. F., Ulijn, R. V., and Escuder, B. (2017) Peptide-based molecular hydrogels as supramolecular protein mimics, *Chemistry–A European Journal 23*, 981-993.
304. Zhang, C., Xue, X., Luo, Q., Li, Y., Yang, K., Zhuang, X., Jiang, Y., Zhang, J., Liu, J., and Zou, G. (2014) Self-assembled peptide nanofibers designed as biological enzymes for catalyzing ester hydrolysis, *Acs Nano 8*, 11715-11723.
305. Kang, M., Zhang, P., Cui, H., and Loverde, S. M. (2016) π–π stacking mediated chirality in functional supramolecular filaments, *Macromolecules 49*, 994-1001.
306. Tao, K., Levin, A., Adler-Abramovich, L., and Gazit, E. (2016) Fmoc-modified amino acids and short peptides: simple bio-inspired building blocks for the fabrication of functional materials, *Chemical Society Reviews 45*, 3935-3953.

307. Dadhwal, S., Fairhall, J. M., Hook, S., and Gamble, A. B. (2020) Tetrafluoroaryl azide as an N-terminal capping group for click-to-dissolve diphenylalanine hydrogels, *RSC Advances 10*, 9234-9244.
308. Smith, A. M., Williams, R. J., Tang, C., Coppo, P., Collins, R. F., Turner, M. L., Saiani, A., and Ulijn, R. V. (2008) Fmoc-diphenylalanine self assembles to a hydrogel via a novel architecture based on π–π interlocked β-sheets, *Advanced materials 20*, 37-41.
309. Orbach, R., Adler-Abramovich, L., Zigerson, S., Mironi-Harpaz, I., Seliktar, D., and Gazit, E. (2009) Self-assembled Fmoc-peptides as a platform for the formation of nanostructures and hydrogels, *Biomacromolecules 10*, 2646-2651.
310. Du, X., Zhou, J., Shi, J., and Xu, B. (2015) Supramolecular hydrogelators and hydrogels: from soft matter to molecular biomaterials, *Chemical reviews 115*, 13165-13307.
311. Dasgupta, A., Mondal, J. H., and Das, D. (2013) Peptide hydrogels, *Rsc Advances 3*, 9117-9149.
312. Löwik, D. W., Leunissen, E., van den Heuvel, M., Hansen, M. B., and van Hest, J. C. (2010) Stimulus responsive peptide based materials, *Chemical Society Reviews 39*, 3394-3412.
313. Lawrence, R. L., Olagunju, M. O., Liu, Y., Mahalingam, K., Slocik, J. M., Naik, R. R., Frenkel, A. I., and Knecht, M. R. (2021) Remote controlled optical manipulation of bimetallic nanoparticle catalysts using peptides, *Catalysis Science & Technology 11*, 2386-2395.
314. Dreher, M. R., Simnick, A. J., Fischer, K., Smith, R. J., Patel, A., Schmidt, M., and Chilkoti, A. (2008) Temperature triggered self-assembly of polypeptides into multivalent spherical micelles, *Journal of the American Chemical Society 130*, 687-694.
315. Ni, R., Liu, J., and Chau, Y. (2018) Ultrasound-facilitated assembly and disassembly of a pH-sensitive self-assembly peptide, *RSC advances 8*, 29482-29487.
316. Gazit, E. (2007) Self-assembled peptide nanostructures: the design of molecular building blocks and their technological utilization, *Chemical Society Reviews 36*, 1263-1269.
317. Saikia, J., Pandey, G., Sasidharan, S., Antony, F., Nemade, H. B., Kumar, S., Chaudhary, N., and Ramakrishnan, V. (2019) Electric Field Disruption of Amyloid Aggregation: Potential Noninvasive Therapy for Alzheimer's Disease, *ACS chemical neuroscience 10*, 2250-2262.
318. Berdugo, C., Miravet, J. F., and Escuder, B. (2013) Substrate selective catalytic molecular hydrogels: the role of the hydrophobic effect, *Chemical communications 49*, 10608-10610.
319. Machajewski, T. D., and Wong, C. H. (2000) The catalytic asymmetric aldol reaction, *Angewandte Chemie International Edition 39*, 1352-1375.
320. Mukaiyama, T. (2004) Explorations into new reaction chemistry, *Angewandte Chemie International Edition 43*, 5590-5614.
321. Lindström, U. M. (2002) Stereoselective organic reactions in water, *Chemical Reviews 102*, 2751-2772.
322. List, B., Lerner, R. A., and Barbas, C. F. (2000) Proline-catalyzed direct asymmetric aldol reactions, *Journal of the American Chemical Society 122*, 2395-2396.
323. Panday, S. K. (2011) Advances in the chemistry of proline and its derivatives: an excellent amino acid with versatile applications in asymmetric synthesis, *Tetrahedron: Asymmetry 22*, 1817-1847.
324. Notz, W., and List, B. (2000) Catalytic asymmetric synthesis of anti-1, 2-diols, *Journal of the American Chemical Society 122*, 7386-7387.
325. Fuentes-Caparrós, A. M., Canales-Galarza, Z., Barrow, M., Dietrich, B., Läuger, J. r., Nemeth, M., Draper, E. R., and Adams, D. J. (2021) Mechanical Characterization of Multilayered Hydrogels: A Rheological Study for 3D-Printed Systems, *Biomacromolecules 22*, 1625-1638.
326. Datta, D., Kumar, V., Kumar, S., Nagaraj, R., and Chaudhary, N. (2019) Limpid hydrogels from β-turn motif-connected tandem repeats of Aβ 16–22, *Soft matter 15*, 4827-4835.

327. Tian, Y., Bromberg, L., Lin, S., Hatton, T. A., and Tam, K. C. (2007) Complexation and release of doxorubicin from its complexes with pluronic P85-b-poly (acrylic acid) block copolymers, *Journal of Controlled Release 121*, 137-145.
328. Mase, N., and Barbas III, C. F. (2010) In water, on water, and by water: mimicking nature's aldolases with organocatalysis and water, *Organic & biomolecular chemistry 8*, 4043-4050.
329. Lu, A., Moatsou, D., Longbottom, D. A., and O'Reilly, R. K. (2013) Tuning the catalytic activity of L-proline functionalized hydrophobic nanogel particles in water, *Chemical Science 4*, 965-969.
330. Kleinschmidt, D., Fernandes, M. S., Mork, M., Meyer, A. A., Krischel, J., Anakhov, M. V., Gumerov, R. A., Potemkin, I. I., Rueping, M., and Pich, A. (2020) Enhanced catalyst performance through compartmentalization exemplified by colloidal L-proline modified microgel catalysts, *Journal of colloid and interface science 559*, 76-87.
331. Zhao, Q., Lam, Y.-h., Kheirabadi, M., Xu, C., Houk, K., and Schafmeister, C. E. (2012) Hydrophobic substituent effects on proline catalysis of aldol reactions in water, *The Journal of organic chemistry 77*, 4784-4792.
332. Rodríguez-Llansola, F., Escuder, B., and Miravet, J. F. (2009) Remarkable increase in basicity associated with supramolecular gelation, *Organic & Biomolecular Chemistry 7*, 3091-3094.
333. Bellotto, O., Kralj, S., De Zorzi, R., Geremia, S., and Marchesan, S. (2020) Supramolecular hydrogels from unprotected dipeptides: a comparative study on stereoisomers and structural isomers, *Soft Matter 16*, 10151-10157.
334. Tena-Solsona, M., Nanda, J., Díaz-Oltra, S., Chotera, A., Ashkenasy, G., and Escuder, B. (2016) Emergent Catalytic Behavior of Self-Assembled Low Molecular Weight Peptide-Based Aggregates and Hydrogels, *Chemistry–A European Journal 22*, 6687-6694.
335. Copeland, G. T., Jarvo, E. R., and Miller, S. J. (1998) Minimal acylase-like peptides. Conformational control of absolute stereospecificity, *The Journal of Organic Chemistry 63*, 6784-6785.
336. Fichman, G., and Gazit, E. (2014) Self-assembly of short peptides to form hydrogels: Design of building blocks, physical properties and technological applications, *Acta biomaterialia 10*, 1671-1682.
337. Tymoczko, J. L., Berg, J. M., and Stryer, L. (2011) *Biochemistry: a short course*, Macmillan.
338. Mase, N., Nakai, Y., Ohara, N., Yoda, H., Takabe, K., Tanaka, F., and Barbas, C. F. (2006) Organocatalytic direct asymmetric aldol reactions in water, *Journal of the American Chemical Society 128*, 734-735.
339. Sakthivel, K., Notz, W., Bui, T., and Barbas, C. F. (2001) Amino acid catalyzed direct asymmetric aldol reactions: a bioorganic approach to catalytic asymmetric carbon− carbon bond-forming reactions, *Journal of the American Chemical Society 123*, 5260-5267.
340. Kofoed, J., Nielsen, J., and Reymond, J.-L. (2003) Discovery of new peptide-based catalysts for the direct asymmetric aldol reaction, *Bioorganic & medicinal chemistry letters 13*, 2445-2447.
341. Xie, Y., Wang, Y., Qi, W., Huang, R., Su, R., and He, Z. (2017) Reconfigurable Chiral Self-Assembly of Peptides through Control of Terminal Charges, *Small 13*, 1700999.
342. Tao, K., Wang, J., Zhou, P., Wang, C., Xu, H., Zhao, X., and Lu, J. R. (2011) Self-assembly of short Aβ (16− 22) peptides: Effect of terminal capping and the role of electrostatic interaction, *Langmuir 27*, 2723-2730.
343. Tokuyama, H., Nakahata, Y., and Ban, T. (2020) Diffusion coefficient of solute in heterogeneous and macroporous hydrogels and its correlation with the effective crosslinking density, *Journal of Membrane Science 595*, 117533.
344. Mouarrawis, V., Plessius, R., van der Vlugt, J. I., and Reek, J. N. (2018) Confinement effects in catalysis using well-defined materials and cages, *Frontiers in chemistry 6*, 623.

345. Bandak, S., Ramu, A., Barenholz, Y., and Gabizon, A. (1999) Reduced UV-induced degradation of doxorubicin encapsulated in polyethyleneglycol-coated liposomes, *Pharmaceutical research 16*, 841-846.
346. Wood, M., Irwin, W., and Scott, D. (1990) Photodegradation of doxorubicin, daunorubicin and epirubicin measured by high-performance liquid chromatography, *Journal of clinical pharmacy and therapeutics 15*, 291-300.
347. Reches, M., and Gazit, E. (2004) Formation of closed-cage nanostructures by self-assembly of aromatic dipeptides, *Nano letters 4*, 581-585.
348. Garcia, A. M., Melchionna, M., Bellotto, O., Kralj, S., Semeraro, S., Parisi, E., Iglesias, D., D'Andrea, P., De Zorzi, R., and Vargiu, A. V. (2021) Nanoscale Assembly of Functional Peptides with Divergent Programming Elements, *ACS nano 15*, 3015-3025.
349. Castillo, J., Tanzi, S., Dimaki, M., and Svendsen, W. (2008) Manipulation of self-assembly amyloid peptide nanotubes by dielectrophoresis, *Electrophoresis 29*, 5026-5032.
350. Arslan, E., Garip, I. C., Gulseren, G., Tekinay, A. B., and Guler, M. O. (2014) Bioactive supramolecular peptide nanofibers for regenerative medicine, *Advanced healthcare materials 3*, 1357-1376.
351. Zotova, N., Franzke, A., Armstrong, A., and Blackmond, D. G. (2007) Clarification of the role of water in proline-mediated aldol reactions, *Journal of the American Chemical Society 129*, 15100-15101.
352. Pelin, J. N., Gerbelli, B. B., Soares, B. M., Aguilar, A. M., and Alves, W. A. (2019) Amyloidogenic model peptides as catalysts for stereoselective aldol reactions, *Catalysis Science & Technology 9*, 4304-4313.
353. List, B. (2001) Asymmetric aminocatalysis, *Synlett 2001*, 1675-1686.
354. Notz, W., Tanaka, F., and Barbas, C. F. (2004) Enamine-based organocatalysis with proline and diamines: the development of direct catalytic asymmetric aldol, Mannich, Michael, and Diels− Alder reactions, *Accounts of chemical research 37*, 580-591.
355. Mandalapu, D. (2015) L-proline and d-proline (chiral amino acid catalysts), *Synlett 26*, 707-708.
356. Conde, E., Bello, D., de Cózar, A., Sánchez, M., Vázquez, M. A., and Cossío, F. P. (2012) Densely substituted unnatural L-and D-prolines as catalysts for highly enantioselective stereodivergent (3+ 2) cycloadditions and aldol reactions, *Chemical Science 3*, 1486-1491.
357. Maurer, K., Volk, S., and Gerbaldo, H. (1997) Auguste D and Alzheimer's disease, *The Lancet 349*, 1546-1549.
358. Benilova, I., Karran, E., and De Strooper, B. (2012) The toxic Aβ oligomer and Alzheimer's disease: an emperor in need of clothes, *Nature neuroscience 15*, 349.
359. Nguyen, P., and Derreumaux, P. (2013) Understanding amyloid fibril nucleation and Aβ oligomer/drug interactions from computer simulations, *Accounts of chemical research 47*, 603-611.
360. Sarroukh, R., Cerf, E., Derclaye, S., Dufrêne, Y. F., Goormaghtigh, E., Ruysschaert, J.-M., and Raussens, V. (2011) Transformation of amyloid β (1–40) oligomers into fibrils is characterized by a major change in secondary structure, *Cellular and molecular life sciences 68*, 1429-1438.
361. Tomaselli, S., Esposito, V., Vangone, P., van Nuland, N. A., Bonvin, A. M., Guerrini, R., Tancredi, T., Temussi, P. A., and Picone, D. (2006) The α-to-β conformational transition of Alzheimer's Aβ-(1–42) peptide in aqueous media is reversible: a step by step conformational analysis suggests the location of β conformation seeding, *ChemBioChem 7*, 257-267.
362. Gervais, F. G., Xu, D., Robertson, G. S., Vaillancourt, J. P., Zhu, Y., Huang, J., LeBlanc, A., Smith, D., Rigby, M., and Shearman, M. S. (1999) Involvement of caspases in proteolytic cleavage of Alzheimer's amyloid-β precursor protein and amyloidogenic Aβ peptide formation, *Cell 97*, 395-406.

363. Halima, S. B., Mishra, S., Raja, K. M. P., Willem, M., Baici, A., Simons, K., Brüstle, O., Koch, P., Haass, C., and Caflisch, A. (2016) Specific inhibition of β-secretase processing of the Alzheimer disease amyloid precursor protein, *Cell reports 14*, 2127-2141.
364. Doig, A. J., del Castillo-Frias, M. P., Berthoumieu, O., Tarus, B., Nasica-Labouze, J., Sterpone, F., Nguyen, P. H., Hooper, N. M., Faller, P., and Derreumaux, P. (2017) Why is research on amyloid-β failing to give new drugs for Alzheimer's disease?, ACS Publications.
365. Yiannopoulou, K. G., and Papageorgiou, S. G. (2013) Current and future treatments for Alzheimer's disease, *Therapeutic advances in neurological disorders 6*, 19-33.
366. Orgogozo, J.-M., Gilman, S., Dartigues, J.-F., Laurent, B., Puel, M., Kirby, L., Jouanny, P., Dubois, B., Eisner, L., and Flitman, S. (2003) Subacute meningoencephalitis in a subset of patients with AD after Aβ42 immunization, *Neurology 61*, 46-54.
367. Beck, M. W., Oh, S. B., Kerr, R. A., Lee, H. J., Kim, S. H., Kim, S., Jang, M., Ruotolo, B. T., Lee, J.-Y., and Lim, M. H. (2015) A rationally designed small molecule for identifying an in vivo link between metal–amyloid-β complexes and the pathogenesis of Alzheimer's disease, *Chemical science 6*, 1879-1886.
368. Soto, C., Sigurdsson, E. M., Morelli, L., Kumar, R. A., Castaño, E. M., and Frangione, B. (1998) β-sheet breaker peptides inhibit fibrillogenesis in a rat brain model of amyloidosis: implications for Alzheimer's therapy, *Nature medicine 4*, 822-826.
369. Gazit, E. (2002) A possible role for π-stacking in the self-assembly of amyloid fibrils, *The FASEB Journal 16*, 77-83.
370. Tjernberg, L. O., Näslund, J., Lindqvist, F., Johansson, J., Karlström, A. R., Thyberg, J., Terenius, L., and Nordstedt, C. (1996) Arrest of-amyloid fibril formation by a pentapeptide ligand, *Journal of Biological Chemistry 271*, 8545-8548.
371. Wagoner, V. A., Cheon, M., Chang, I., and Hall, C. K. (2014) Impact of sequence on the molecular assembly of short amyloid peptides, *Proteins: Structure, Function, and Bioinformatics 82*, 1469-1483.
372. Li, H., Luo, Y., Derreumaux, P., and Wei, G. (2011) Carbon nanotube inhibits the formation of β-sheet-rich oligomers of the Alzheimer's amyloid-β (16-22) peptide, *Biophysical journal 101*, 2267-2276.
373. Maji, S. K., Loo, R. R. O., Inayathullah, M., Spring, S. M., Vollers, S. S., Condron, M. M., Bitan, G., Loo, J. A., and Teplow, D. B. (2009) Amino acid position-specific contributions to amyloid β-protein oligomerization, *Journal of Biological Chemistry*, jbc. M109. 038133.
374. Lakshmanan, A., Cheong, D. W., Accardo, A., Di Fabrizio, E., Riekel, C., and Hauser, C. A. (2013) Aliphatic peptides show similar self-assembly to amyloid core sequences, challenging the importance of aromatic interactions in amyloidosis, *Proceedings of the National Academy of Sciences 110*, 519-524.
375. Michaels, T. C., Šarić, A., Habchi, J., Chia, S., Meisl, G., Vendruscolo, M., Dobson, C. M., and Knowles, T. P. (2018) Chemical kinetics for bridging molecular mechanisms and macroscopic measurements of amyloid fibril formation, *Annual review of physical chemistry 69*, 273-298.
376. Todorova, N., Bentvelzen, A., English, N. J., and Yarovsky, I. (2016) Electromagnetic-field effects on structure and dynamics of amyloidogenic peptides, *The Journal of Chemical Physics 144*, 085101.
377. Gursky, O., and Aleshkov, S. (2000) Temperature-dependent β-sheet formation in β-amyloid Aβ1–40 peptide in water: uncoupling β-structure folding from aggregation, *Biochimica et Biophysica Acta (BBA)-Protein Structure and Molecular Enzymology 1476*, 93-102.
378. Fraser, P. E., Nguyen, J. T., Surewicz, W. K., and Kirschner, D. A. (1991) pH-dependent structural transitions of Alzheimer amyloid peptides, *Biophysical journal 60*, 1190-1201.
379. Xu, W., Zhang, C., Derreumaux, P., Gräslund, A., Morozova-Roche, L., and Mu, Y. (2011) Intrinsic determinants of Aβ12–24 pH-dependent self-assembly revealed by combined computational and experimental studies, *PLoS One 6*, e24329.

380. Shen, C.-L., and Murphy, R. M. (1995) Solvent effects on self-assembly of beta-amyloid peptide, *Biophysical journal 69*, 640-651.
381. de Pomerai, D. I., Smith, B., Dawe, A., North, K., Smith, T., Archer, D. B., Duce, I. R., Jones, D., and Candido, E. P. M. (2003) Microwave radiation can alter protein conformation without bulk heating, *FEBS letters 543*, 93-97.
382. Nasica-Labouze, J., Nguyen, P. H., Sterpone, F., Berthoumieu, O., Buchete, N.-V., Cote, S., De Simone, A., Doig, A. J., Faller, P., and Garcia, A. (2015) Amyloid β protein and Alzheimer's disease: When computer simulations complement experimental studies, *Chemical reviews 115*, 3518-3563.
383. Zheng, Z., Jing, B., Sorci, M., Belfort, G., and Zhu, Y. (2015) Accelerated insulin aggregation under alternating current electric fields: Relevance to amyloid kinetics, *Biomicrofluidics 9*, 044123.
384. Wakayama, N. I. (2003) Effects of a strong magnetic field on protein crystal growth, *Crystal Growth & Design 3*, 17-24.
385. Porschke, D. (1996) Electrostatics and electrodynamics of bacteriorhodopsin, *Biophysical journal 71*, 3381-3391.
386. Worcester, D. (1978) Structural origins of diamagnetic anisotropy in proteins, *Proceedings of the National Academy of Sciences 75*, 5475-5477.
387. Pandey, G., Saikia, J., Sasidharan, S., Joshi, D. C., Thota, S., Nemade, H. B., Chaudhary, N., and Ramakrishnan, V. (2017) Modulation of peptide based nano-assemblies with electric and magnetic fields, *Scientific Reports 7*, 2726.
388. Kunitani, M., Wolfe, S., Rana, S., Apicella, C., Levi, V., and Dollinger, G. (1997) Classical light scattering quantitation of protein aggregates: off-line spectroscopy versus HPLC detection1, *Journal of pharmaceutical and biomedical analysis 16*, 573-586.
389. Denizot, F., and Lang, R. (1986) Rapid colorimetric assay for cell growth and survival: modifications to the tetrazolium dye procedure giving improved sensitivity and reliability, *Journal of immunological methods 89*, 271-277.
390. Cohen, S. I., Linse, S., Luheshi, L. M., Hellstrand, E., White, D. A., Rajah, L., Otzen, D. E., Vendruscolo, M., Dobson, C. M., and Knowles, T. P. (2013) Proliferation of amyloid-β42 aggregates occurs through a secondary nucleation mechanism, *Proceedings of the National Academy of Sciences 110*, 9758-9763.
391. Anoop, A., Singh, P. K., Jacob, R. S., and Maji, S. K. (2010) CSF biomarkers for Alzheimer's disease diagnosis, *International journal of Alzheimer's disease 2010*.
392. Mok, Y. F., and Howlett, G. J. (2006) Sedimentation velocity analysis of amyloid oligomers and fibrils, *Methods in enzymology 413*, 199-217.
393. Kai, T., Zhang, L., Wang, X., Jing, A., Zhao, B., Yu, X., Zheng, J., and Zhou, F. (2015) Tabersonine inhibits amyloid fibril formation and cytotoxicity of Aβ (1–42), *ACS chemical neuroscience 6*, 879-888.
394. Haris, P. I., and Chapman, D. (1995) The conformational analysis of peptides using Fourier transform IR spectroscopy, *Biopolymers: Original Research on Biomolecules 37*, 251-263.
395. Ahmed, M., Davis, J., Aucoin, D., Sato, T., Ahuja, S., Aimoto, S., Elliott, J. I., Van Nostrand, W. E., and Smith, S. O. (2010) Structural conversion of neurotoxic amyloid-β 1–42 oligomers to fibrils, *Nature structural & molecular biology 17*, 561.
396. Pachahara, S. K., Adicherla, H., and Nagaraj, R. (2015) Self-Assembly of Aβ40, Aβ42 and Aβ43 peptides in aqueous mixtures of fluorinated alcohols, *PloS one 10*, e0136567.
397. Chimon, S., Shaibat, M. A., Jones, C. R., Calero, D. C., Aizezi, B., and Ishii, Y. (2007) Evidence of fibril-like β-sheet structures in a neurotoxic amyloid intermediate of Alzheimer's β-amyloid, *Nature Structural and Molecular Biology 14*, 1157.
398. Cohen, S. I., Cukalevski, R., Michaels, T. C., Šarić, A., Törnquist, M., Vendruscolo, M., Dobson, C. M., Buell, A. K., Knowles, T. P., and Linse, S. (2018) Distinct thermodynamic

signatures of oligomer generation in the aggregation of the amyloid-β peptide, *Nature chemistry 10*, 523.
399. Jan, A., Gokce, O., Luthi-Carter, R., and Lashuel, H. A. (2008) The ratio of monomeric to aggregated forms of Aβ40 and Aβ42 is an important determinant of Aβ aggregation, fibrillogenesis, and toxicity, *Journal of Biological Chemistry*.
400. Tran, J., Chang, D., Hsu, F., Wang, H., and Guo, Z. (2017) Cross-seeding between Aβ40 and Aβ42 in Alzheimer's disease, *FEBS letters 591*, 177-185.
401. Pauwels, K., Williams, T. L., Morris, K. L., Jonckheere, W., Vandersteen, A., Kelly, G., Schymkowitz, J., Rousseau, F., Pastore, A., and Serpell, L. C. (2012) Structural basis for increased toxicity of pathological aβ42: aβ40 ratios in Alzheimer disease, *Journal of biological chemistry 287*, 5650-5660.
402. Linse, S. (2017) Monomer-dependent secondary nucleation in amyloid formation, *Biophysical reviews 9*, 329-338.
403. Bitan, G., Kirkitadze, M. D., Lomakin, A., Vollers, S. S., Benedek, G. B., and Teplow, D. B. (2003) Amyloid β-protein (Aβ) assembly: Aβ40 and Aβ42 oligomerize through distinct pathways, *Proceedings of the National Academy of Sciences 100*, 330-335.
404. Wirths, O., Multhaup, G., and Bayer, T. A. (2004) A modified β-amyloid hypothesis: intraneuronal accumulation of the β-amyloid peptide–the first step of a fatal cascade, *Journal of neurochemistry 91*, 513-520.
405. Campioni, S., Mannini, B., Zampagni, M., Pensalfini, A., Parrini, C., Evangelisti, E., Relini, A., Stefani, M., Dobson, C. M., and Cecchi, C. (2010) A causative link between the structure of aberrant protein oligomers and their toxicity, *Nature chemical biology 6*, 140.
406. Kremer, J. J., Pallitto, M. M., Sklansky, D. J., and Murphy, R. M. (2000) Correlation of β-amyloid aggregate size and hydrophobicity with decreased bilayer fluidity of model membranes, *Biochemistry 39*, 10309-10318.
407. Esbjörner, E. K., Chan, F., Rees, E., Erdelyi, M., Luheshi, L. M., Bertoncini, C. W., Kaminski, C. F., Dobson, C. M., and Schierle, G. S. K. (2014) Direct observations of amyloid β self-assembly in live cells provide insights into differences in the kinetics of Aβ (1–40) and Aβ (1–42) aggregation, *Chemistry & biology 21*, 732-742.
408. Knauer, M. F., Soreghan, B., Burdick, D., Kosmoski, J., and Glabe, C. G. (1992) Intracellular accumulation and resistance to degradation of the Alzheimer amyloid A4/beta protein, *Proceedings of the National Academy of Sciences 89*, 7437-7441.
409. Huang, H., and Zhao, M. (2008) Changes of trypsin in activity and secondary structure induced by complex with trypsin inhibitors and tea polyphenol, *European Food Research and Technology 227*, 361-365.
410. Cooper, M. S. (1995) Membrane potential perturbations induced in tissue cells by pulsed electric fields, *Bioelectromagnetics 16*, 255-262.
411. Toschi, F., Lugli, F., Biscarini, F., and Zerbetto, F. (2008) Effects of electric field stress on a β-amyloid peptide, *The Journal of Physical Chemistry B 113*, 369-376.
412. Astrakas, L., Gousias, C., and Tzaphlidou, M. (2011) Electric field effects on chignolin conformation, *Journal of Applied Physics 109*, 094702.
413. Barucker, C., Bittner, H. J., Chang, P. K.-Y., Cameron, S., Hancock, M. A., Liebsch, F., Hossain, S., Harmeier, A., Shaw, H., and Charron, F. M. (2015) Aβ42-oligomer Interacting Peptide (AIP) neutralizes toxic amyloid-β42 species and protects synaptic structure and function, *Scientific reports 5*, 15410.

Appendix #1

Table A1.1: Various amino acid abbreviation systems. All the L-amino acids are represented in upper case and D-amino acids are represented in lower case one letter abbreviations.

Amino acid name	Three letter abbreviations	One letter abbreviations for L-amino acids	One letter abbreviations for D-amino acids
Alanine	Ala	A	a
Arginine	Arg	R	r
Asparagine	Asn	N	n
Aspartic acid	Asp	D	d
Cysteine	Cys	C	c
Glutamine	Gln	Q	q
Glutamic acid	Glu	E	e
Glycine	Gly	G	g
Histidine	His	H	h
Isoleucine	Ile	I	i
Leucine	Leu	L	l
Lysine	Lys	K	k
Methionine	Met	M	m
Phenylalanine	Phe	F	f
Proline	Pro	P	p
Pyrrolysine	Pyl	O	o
Serine	Ser	S	s
Selenocysteine	Sec	U	u
Threonine	Thr	T	t
Tryptophan	Trp	W	w
Tyrosine	Tyr	Y	y
Valine	Val	V	v

Appendix #2

1. Characterization of the designed peptide

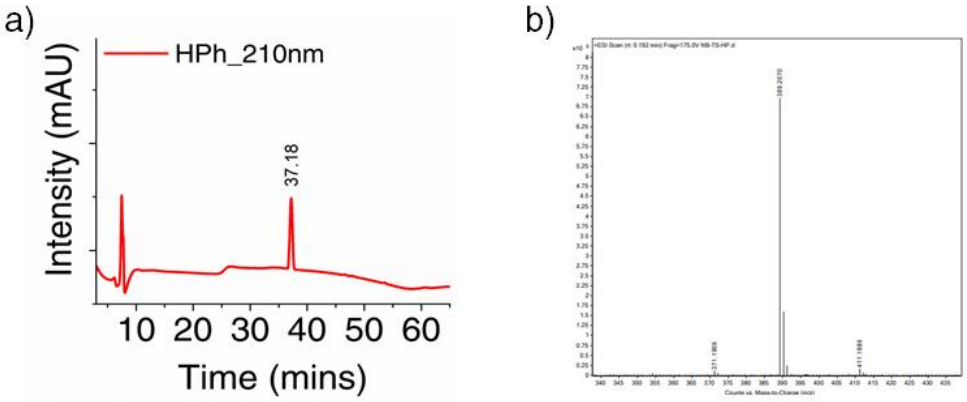

Figure A2.1: Characterization of the HPh peptide a) Reverse-phase HPLC spectrum b) HRMS spectrum showing the observed mass equal to the calculated mass (389.41Da).

2. ^{13}C NMR peak assignment of the peptide

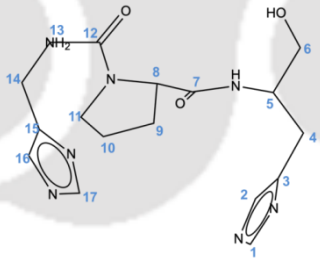

Figure A2.2: ^{13}C NMR peak assignment of the nascent HPh peptide using general electronegativity trend of chemical shifts and ChemBioDraw predictions of ^{13}C NMR spectrum.

Table: A2.1: ^{13}C Chemical Shifts (in ppm) of nascent HPh peptide.

Atom label	Experimental	Predicted (ChemBioDraw)
C10	25.2	24.1
C4	25.2	28.3
C9	29.4	29.5
C14	29.4	32.5

Atom label	Experimental	Predicted (ChemBioDraw)
C11	48.1	49.5
C13	51.5	51.2
C5	51.5	57.8
C6	61.1	64.6
C8	116.2	68.5
C2	117.8	117.9
C16	118.9	117.9
C15	126.2	131.3
C3	130.0	132.7
C1	134.8	136.2
C17	162.4	136.2
C7	167.2	170.7
C12	174.1	173.3

3. The ESI-MS spectrum of the HPh-Cu complex

Calculated mass of HPh-NH_2-Cu: 467.31Da, **Observed mass:** 467.95 Da

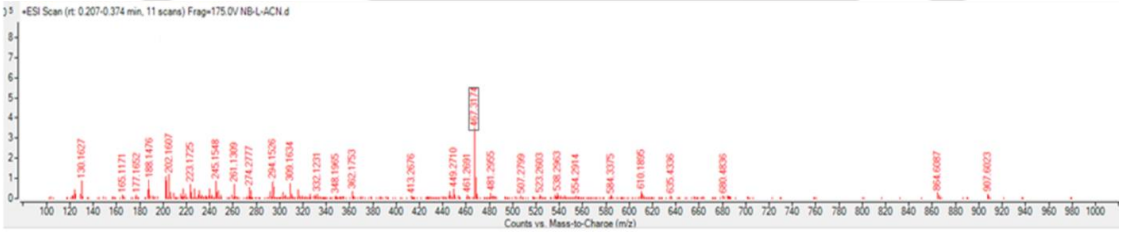

Figure A2.3: ESI-MS spectrum of HPh-NH_2-Cu Complex formed at pH 7.

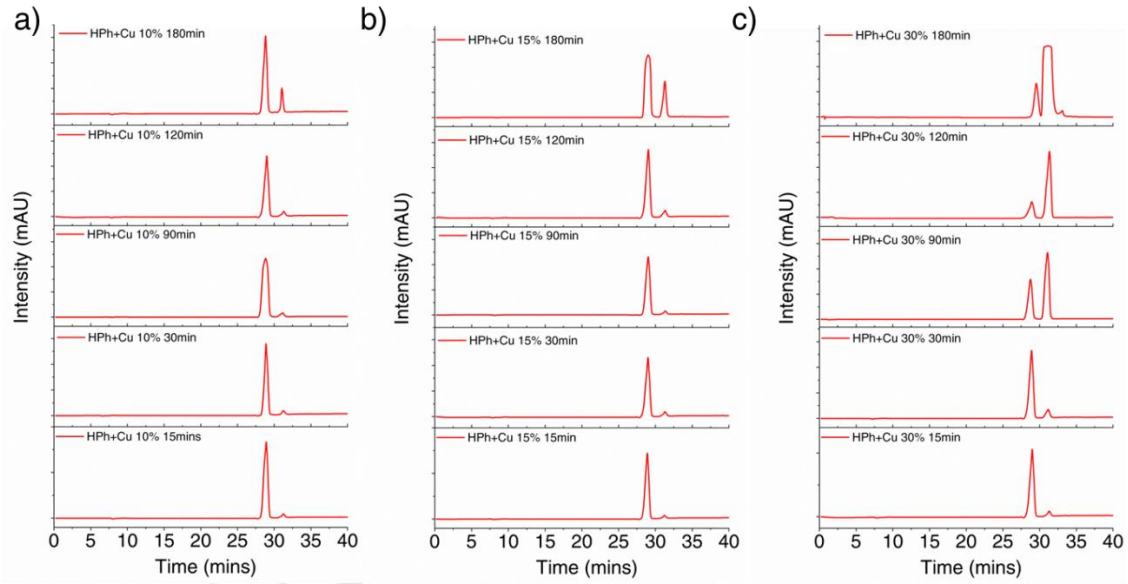

Figure A2.3: HPLC chromatograms showing the oxidation of benzyl alcohol to benzaldehyde in presence of a) 10 mol% b) 15mol% and c) 30mol% Cu-HPh catalyst in 3h. Reactions were performed at 40 ^{o}C and aliquot of 20µL was collected at regular time interval. HPLC spectrum was recorded at 283nm**.**

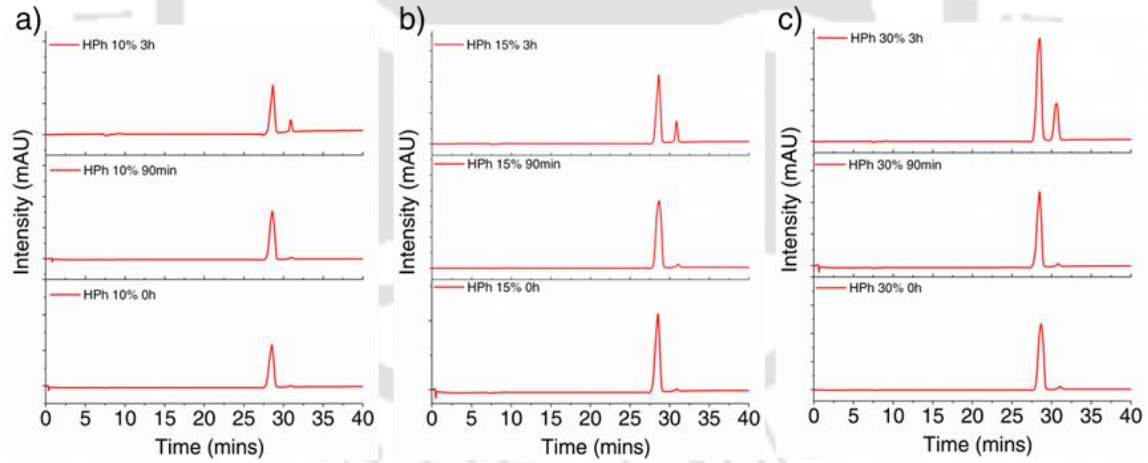

Figure A2.4: HPLC chromatograms showing the oxidation of benzyl alcohol to benzaldehyde in presence of a) 10 mol% b) 15mol% and c) 30mol% HPh peptide in 3h. Reactions were performed at 40^{o}C and aliquot of 20µL was collected at regular time interval. HPLC spectrum was recorded at 283nm.

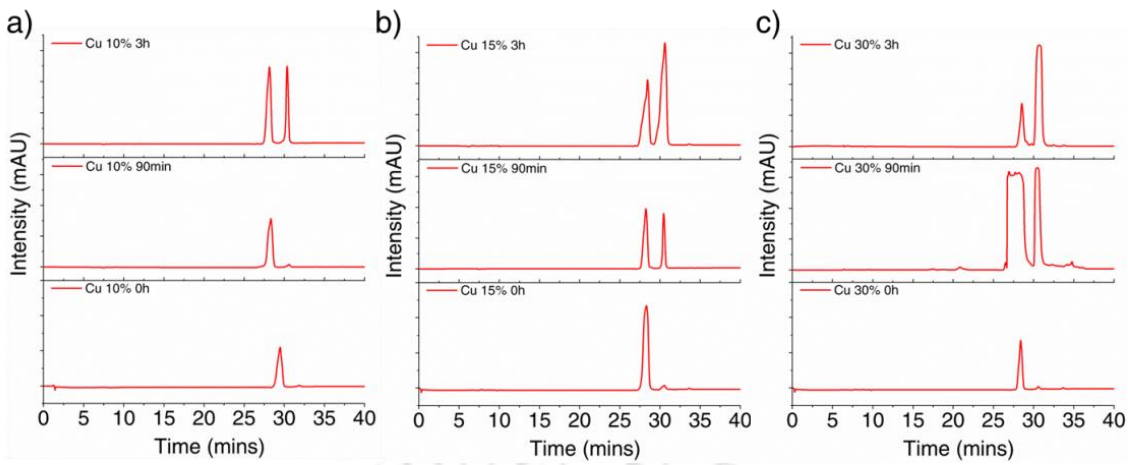

Figure A2.5: HPLC chromatograms showing the oxidation of benzyl alcohol to benzaldehyde in presence of a) 10 mol% b) 15mol% and c) 30mol% of Cu(II) in 3h. Reactions were performed at 40 ^{o}C and aliquot of 20µL was collected at regular time interval. HPLC spectrum was recorded at 283nm.

Appendix #3

Table A3.1: Characterization of the HPh peptide a) Reverse-phase HPLC spectrum b) MALDI-TOF spectra showing the observed mass and its comparison with the calculated mass.

Reverse phase HPLC chromatogram at 254nm	Observed Mass(MALDI-TOF)
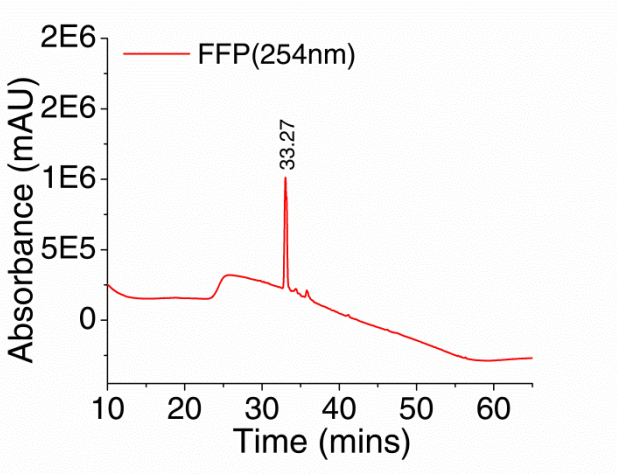	**Calculated mass: 409.56Da** 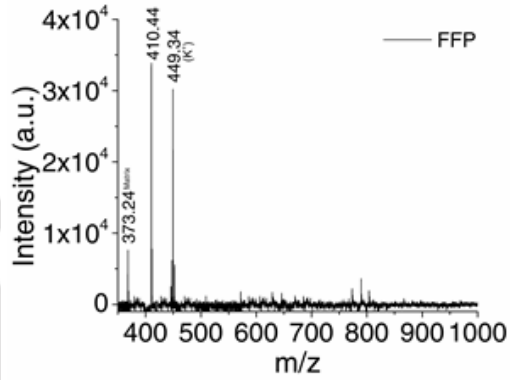
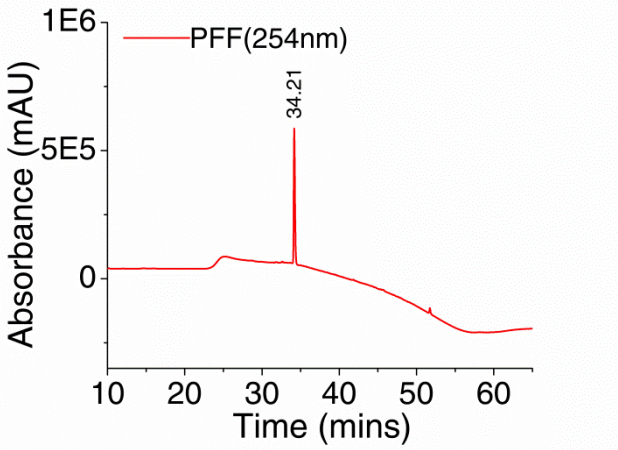	**Calculated mass: 409.56Da** 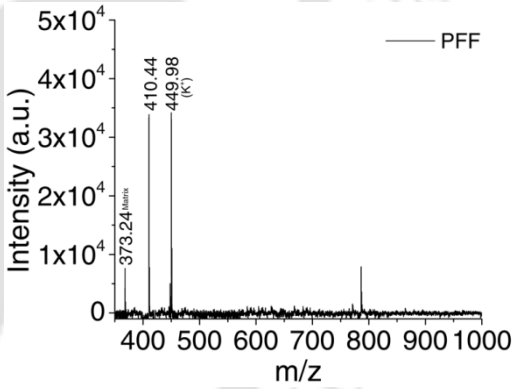
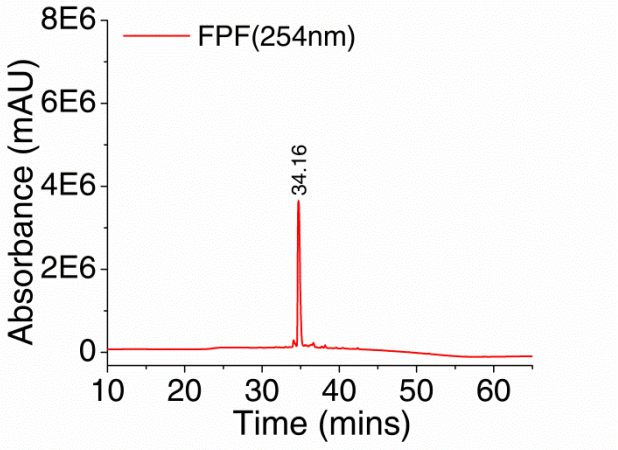	**Calculated mass: 409.56Da** 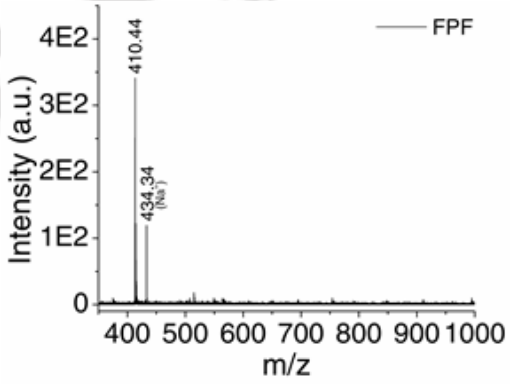

Reverse phase HPLC chromatogram at 254nm

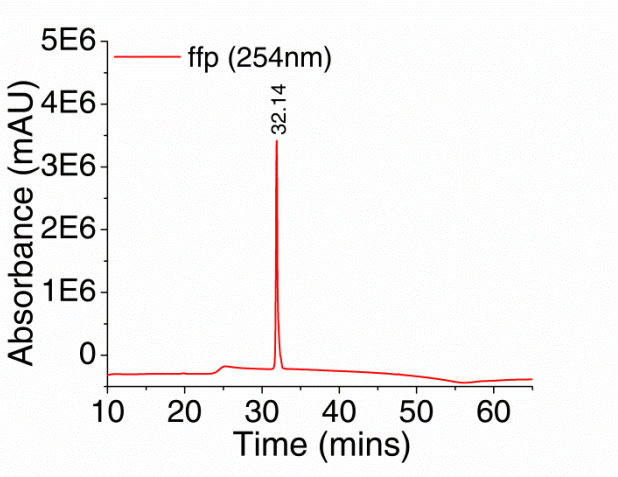

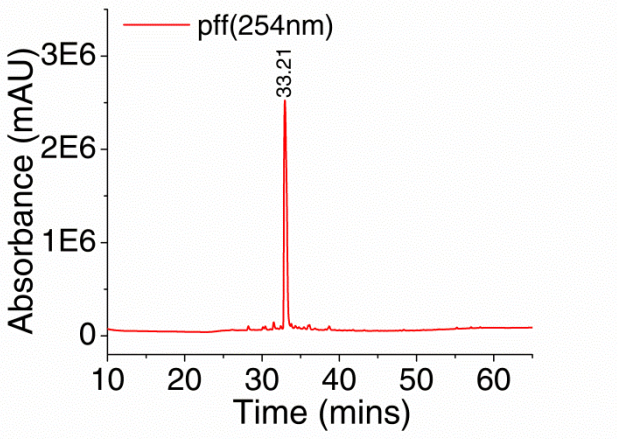

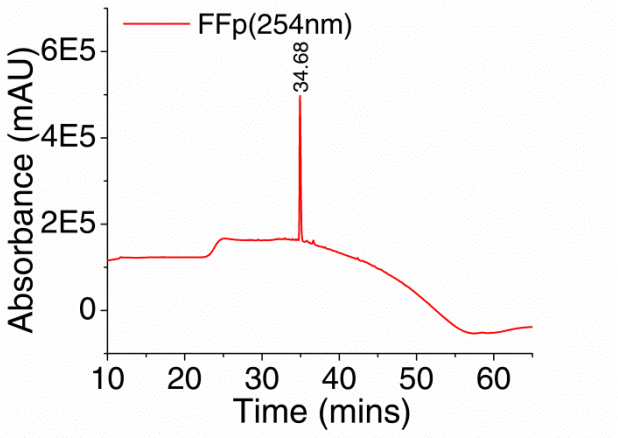

Observed Mass(MALDI-TOF)

Calculated mass: 409.56Da

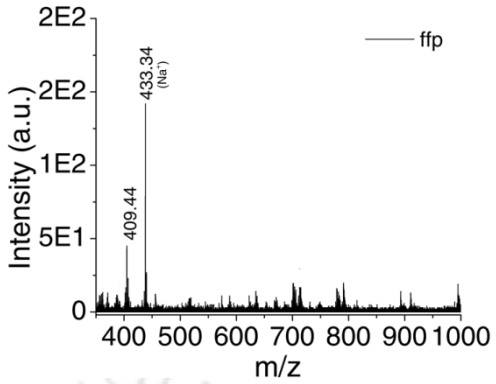

Calculated mass: 409.56Da

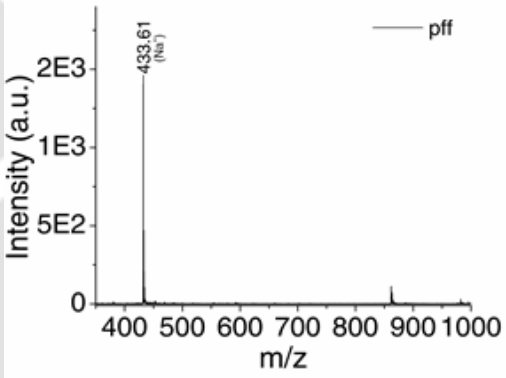

Calculated mass: 409.56Da

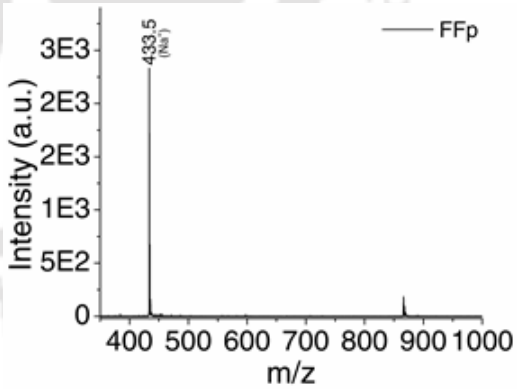

Reverse phase HPLC chromatogram at 254nm

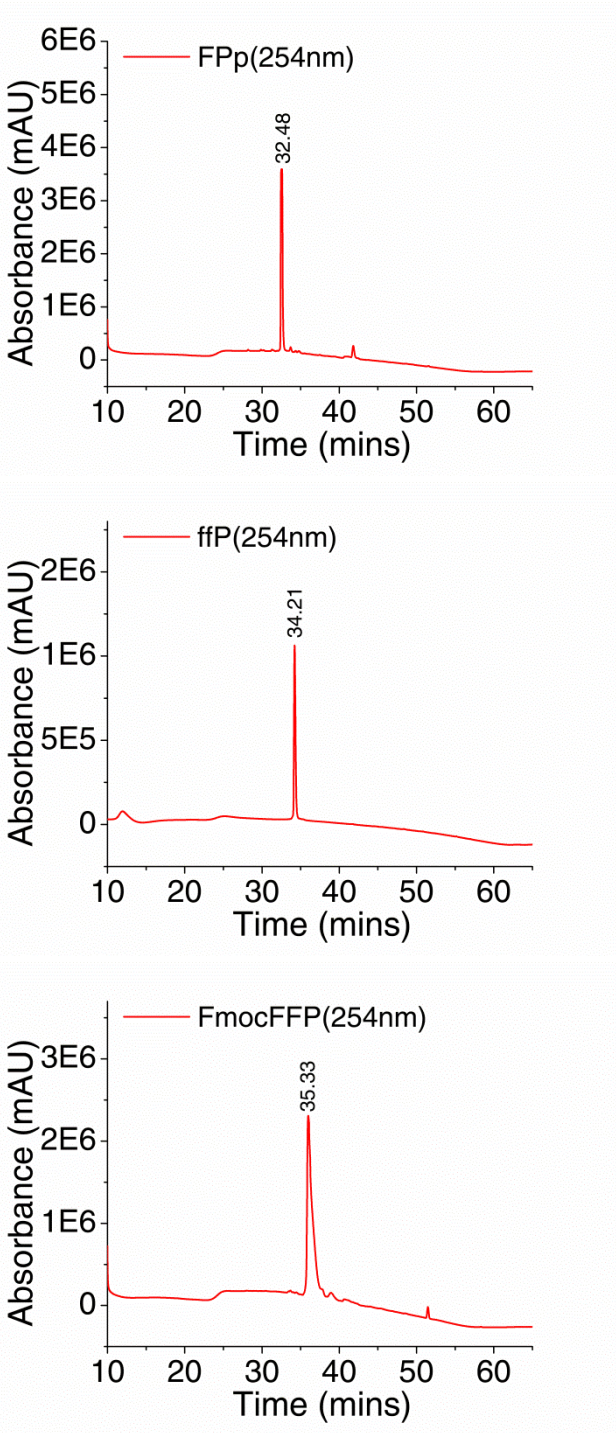

Observed Mass(MALDI-TOF)

Calculated mass: 359.40Da

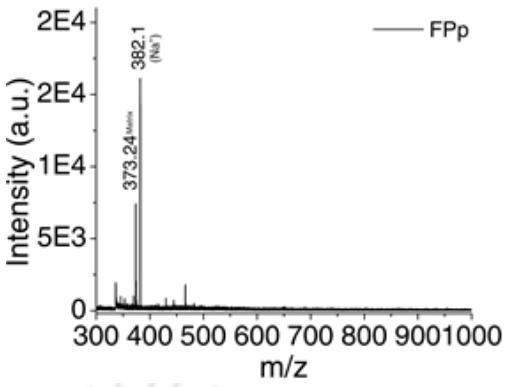

Calculated mass: 409.56Da

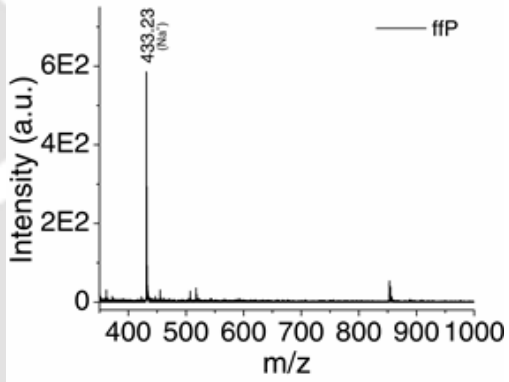

Calculated mass: 632.16Da

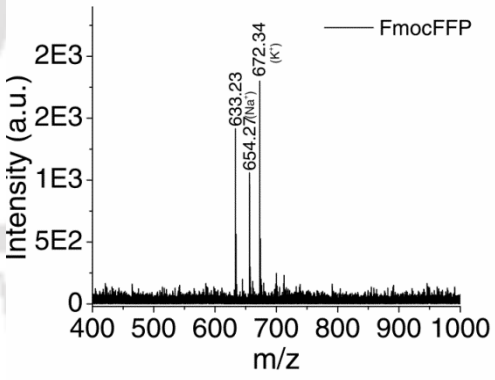

Reverse phase HPLC chromatogram at 254nm

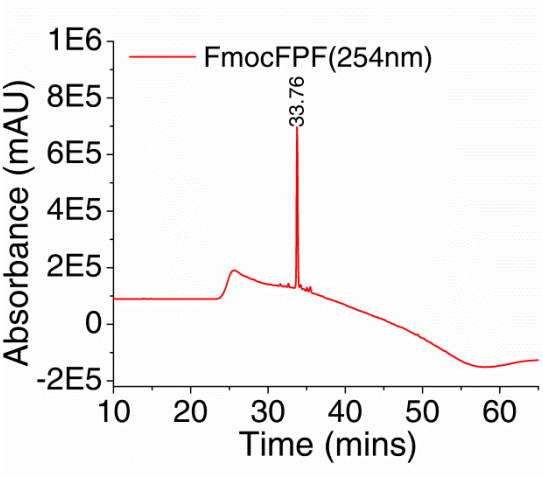

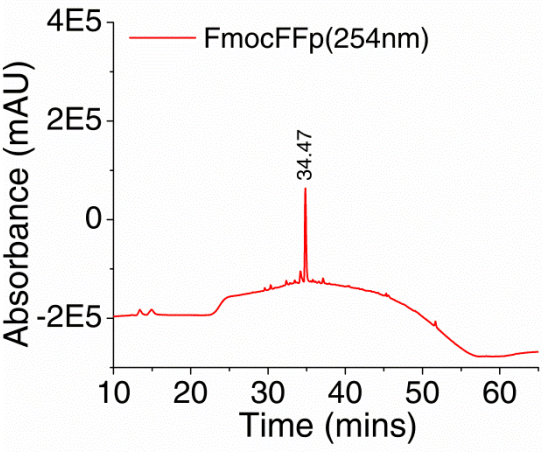

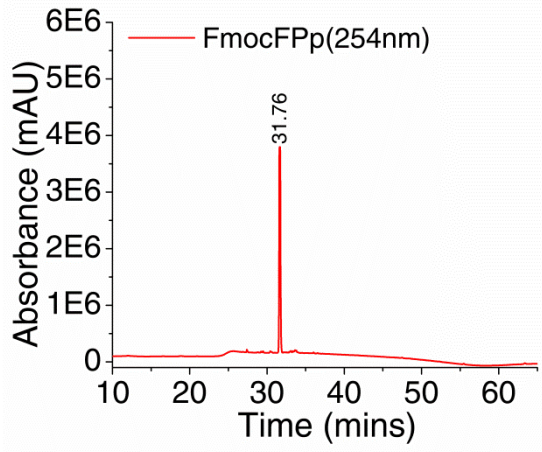

Observed Mass(MALDI-TOF)

Calculated mass: 632.16Da

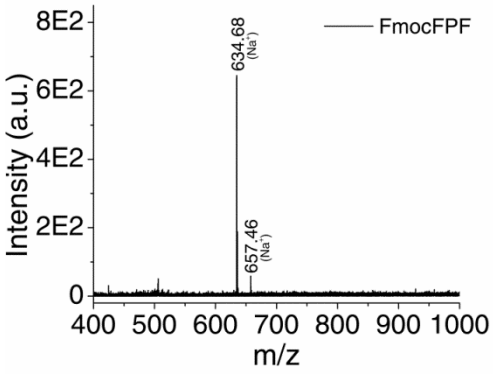

Calculated mass: 632.16Da

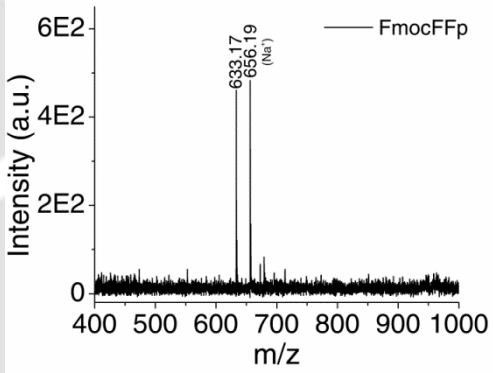

Calculated mass: 582.10Da

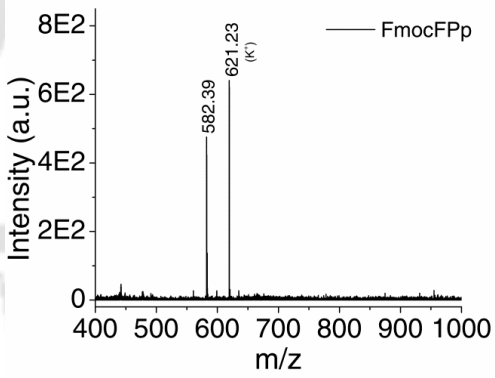

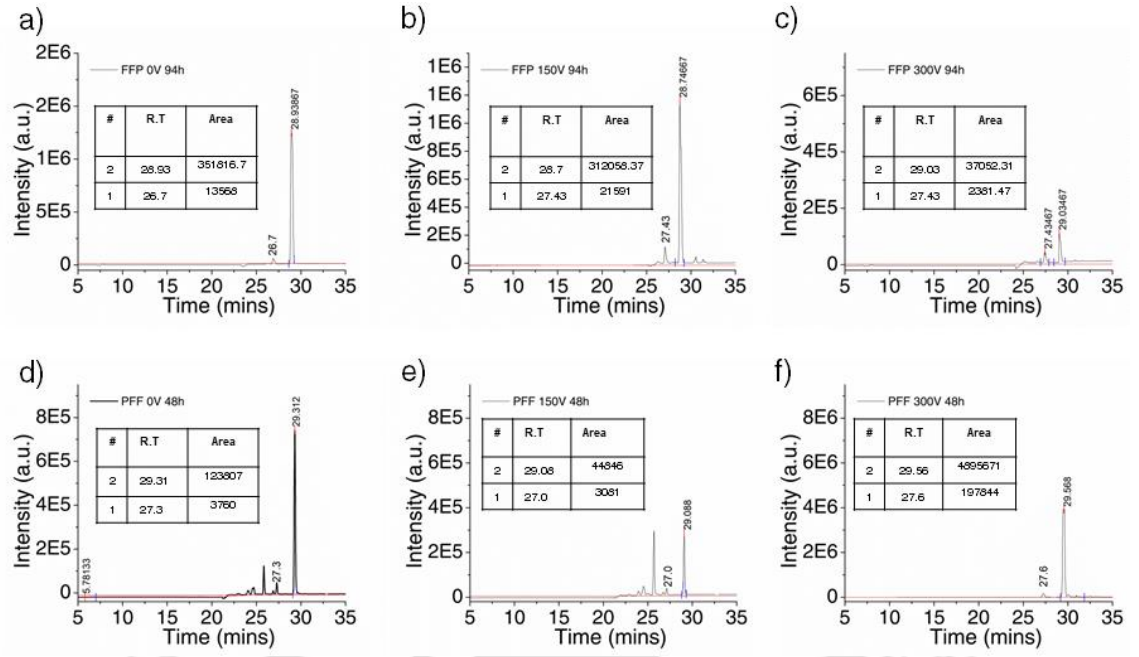

Figure A3.1: HPLC chromatogram of reaction products obtained from reaction between cyclohexanone and 4-nitrobenzyldehyde. Catalyst: **FFP** and **PFF**, Catalyst load: 30 mol%, reaction time: 94 h, 48h for **PFF**, reaction temperature: 27 °C.

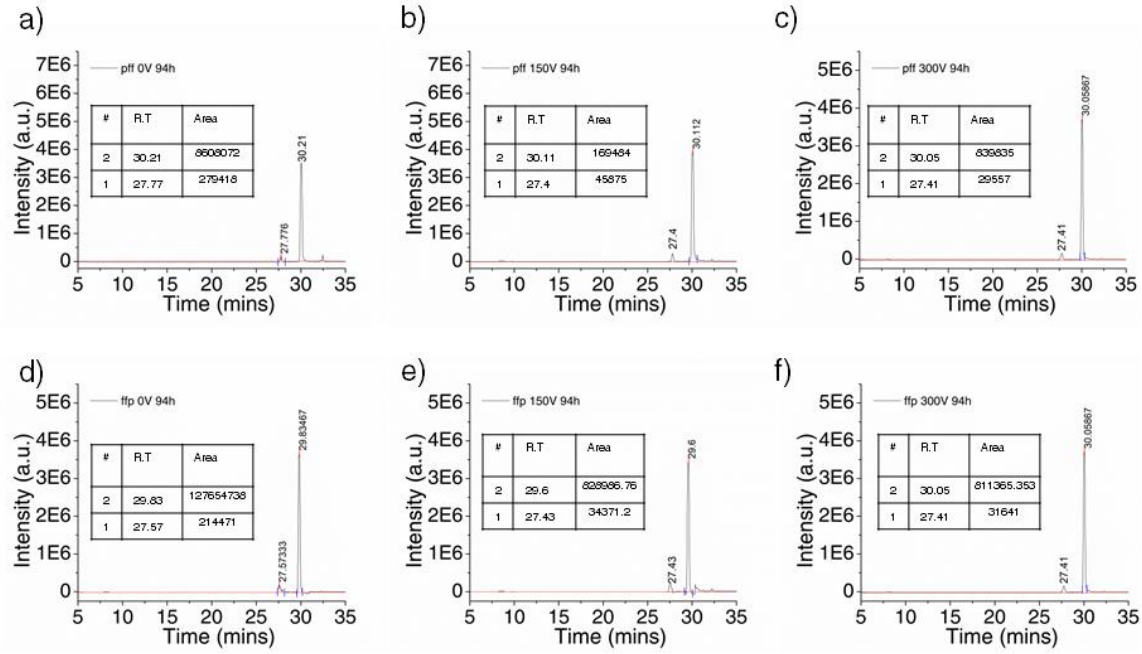

Figure A3.2: HPLC chromatogram of reaction products obtained from reaction between cyclohexanone and 4-nitrobenzyldehyde. Catalyst: **ffp** and **pff**, Catalyst load: 30 mol%, reaction time: 94 h, reaction temperature: 27 °C.

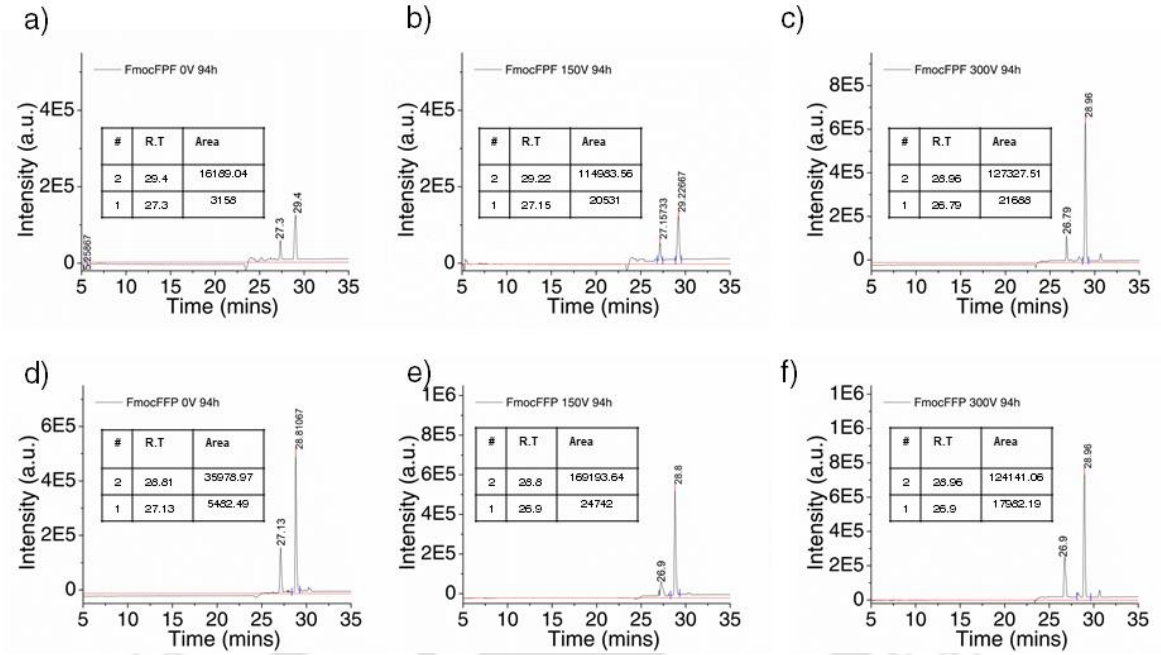

Figure A3.3: HPLC chromatogram of reaction products obtained from reaction between cyclohexanone and 4-nitrobenzyldehyde. Catalyst: **FmocFFP** and **FmocFPF**, Catalyst load: 30 mol%, reaction time: 94 h, reaction temperature: 27 °C.

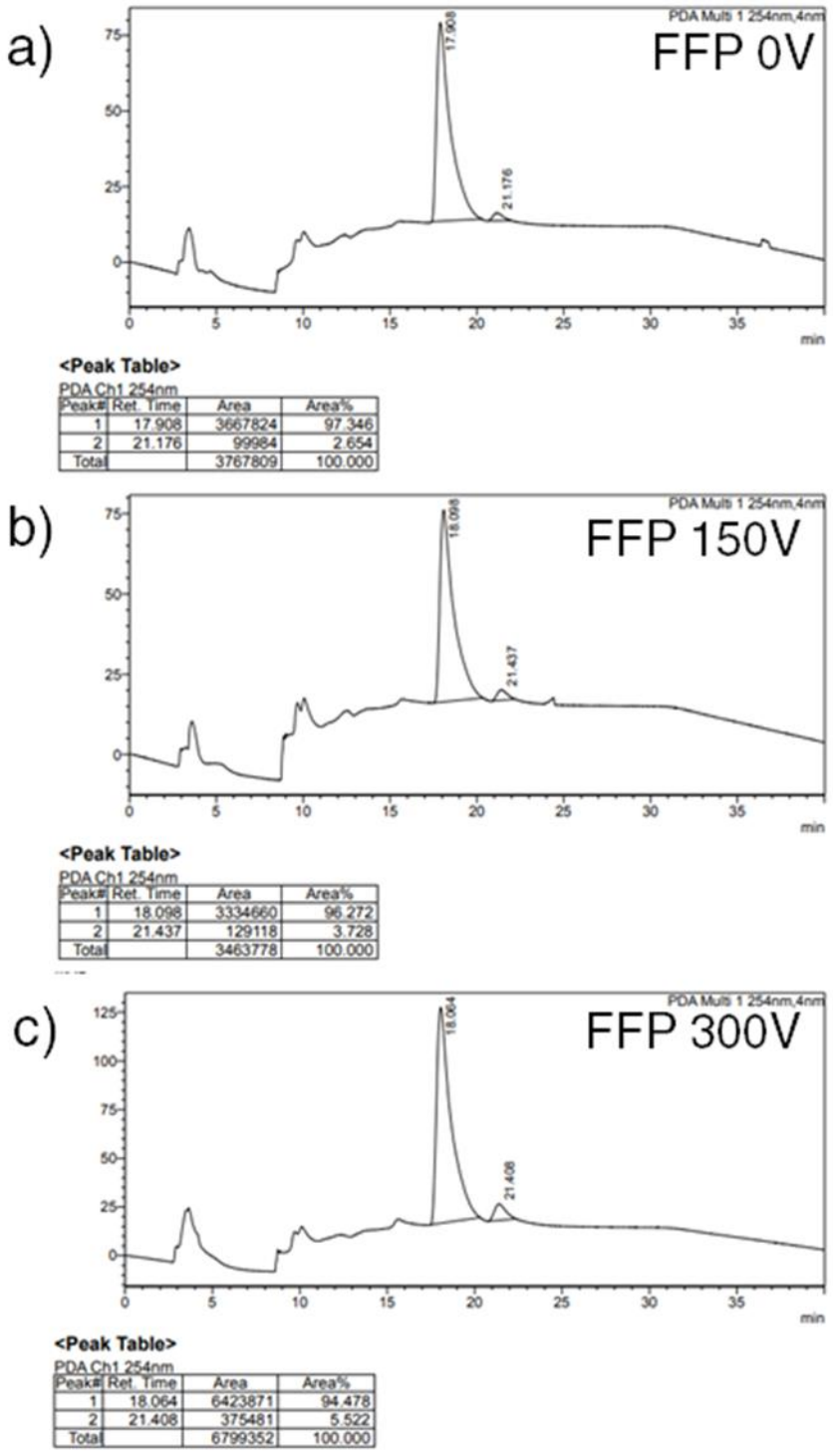

Figure A3.4: Typical chiral chromatogram for the aldol products catalyzed by FFP hydrogel formed in different EF strength. Labeled peaks correspond to *sin* aldol and *anti*-aldol. Integral ratio between the minor and the major diastereomers was used to determine the diastereomeric ratio.

a)

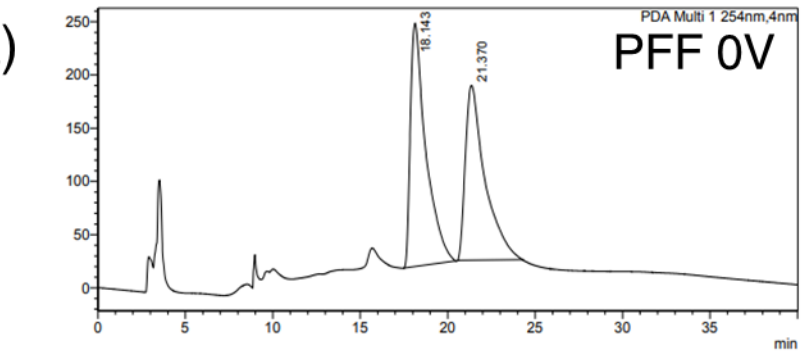

<Peak Table>
PDA Ch1 254nm

Peak#	Ret. Time	Area	Area%
1	18.143	14060658	52.312
2	21.370	12817720	47.688
Total		26878378	100.000

b)

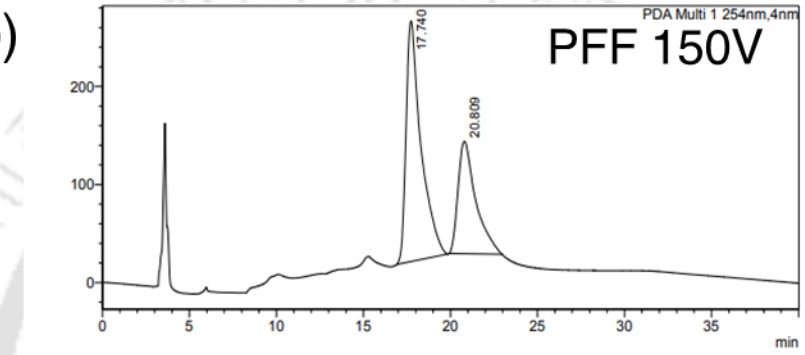

<Peak Table>
PDA Ch1 254nm

Peak#	Ret. Time	Area	Area%
1	17.740	14604138	64.195
2	20.809	8145352	35.805
Total		22749490	100.000

c)

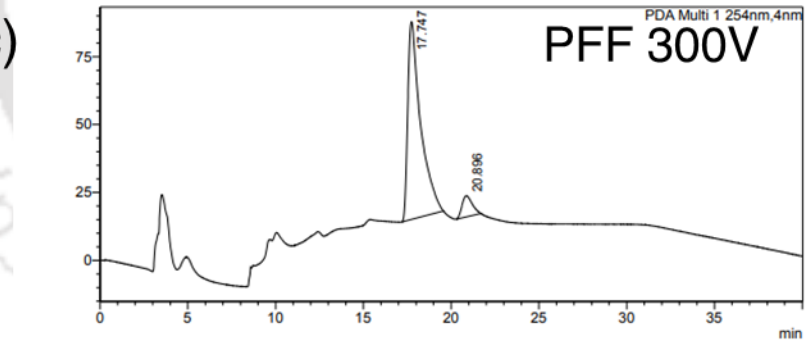

<Peak Table>
PDA Ch1 254nm

Peak#	Ret. Time	Area	Area%
1	17.747	3704293	92.226
2	20.896	312250	7.774
Total		4016543	100.000

Figure A3.5: Typical chiral chromatogram for the aldol products catalyzed by PFF hydrogel formed in different EF strength. Labeled peaks correspond to *sin* aldol and *anti*-aldol. Integral ratio between the minor and the major diastereomers was used to determine the diastereomeric ratio.

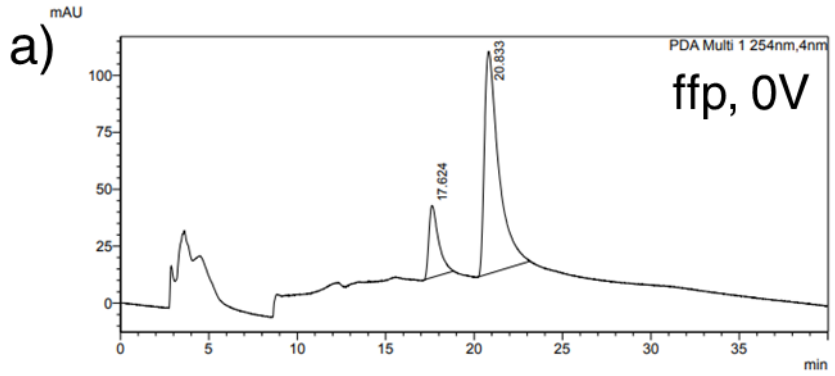

<Peak Table>
PDA Ch1 254nm

Peak#	Ret. Time	Area	Area%
1	17.624	1208709	17.971
2	20.833	5517345	82.029
Total		6726053	100.000

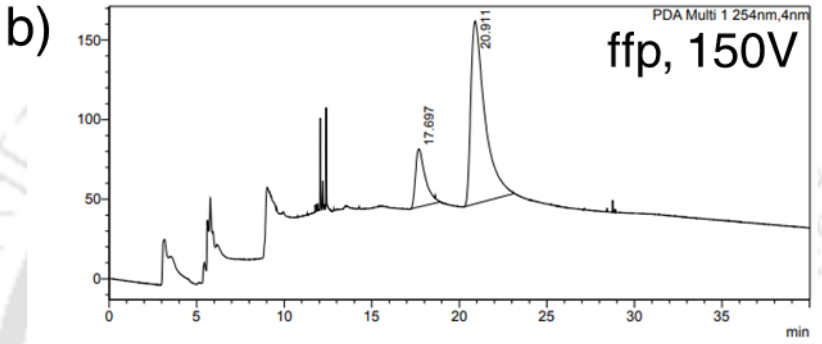

<Peak Table>
PDA Ch1 254nm

Peak#	Ret. Time	Area	Area%
1	17.697	1408901	17.895
2	20.911	6464419	82.105
Total		7873321	100.000

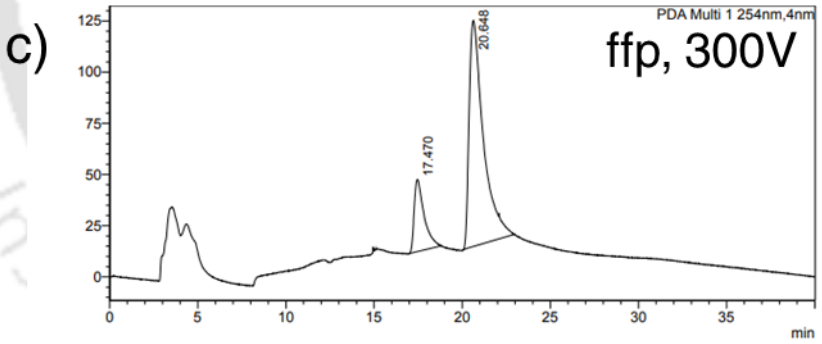

<Peak Table>
PDA Ch1 254nm

Peak#	Ret. Time	Area	Area%
1	17.470	1388468	18.297
2	20.648	6200238	81.703
Total		7588706	100.000

Figure A3.6: Typical chiral chromatogram for the aldol products catalyzed by ffp hydrogel formed in different EF strength. Labeled peaks correspond to *sin* aldol and *anti*-aldol. Integral ratio between the minor and the major diastereomers was used to determine the diastereomeric ratio.

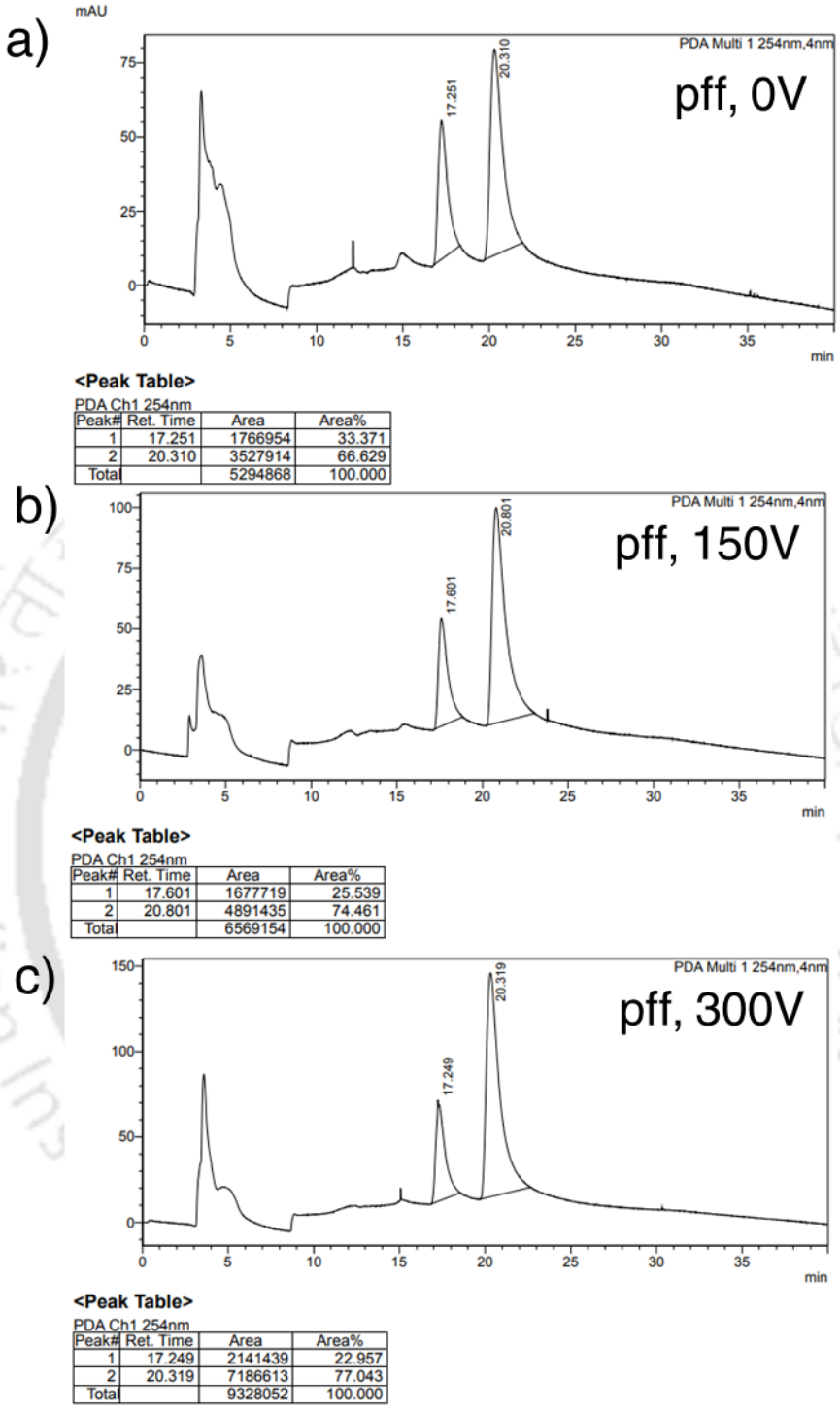

Figure A3.7: Typical chiral chromatogram for the aldol products catalyzed by pff hydrogel formed in different EF strength. Labeled peaks correspond to *sin* aldol and *anti*-aldol. Integral ratio between the minor and the major diastereomers was used to determine the diastereomeric ratio.

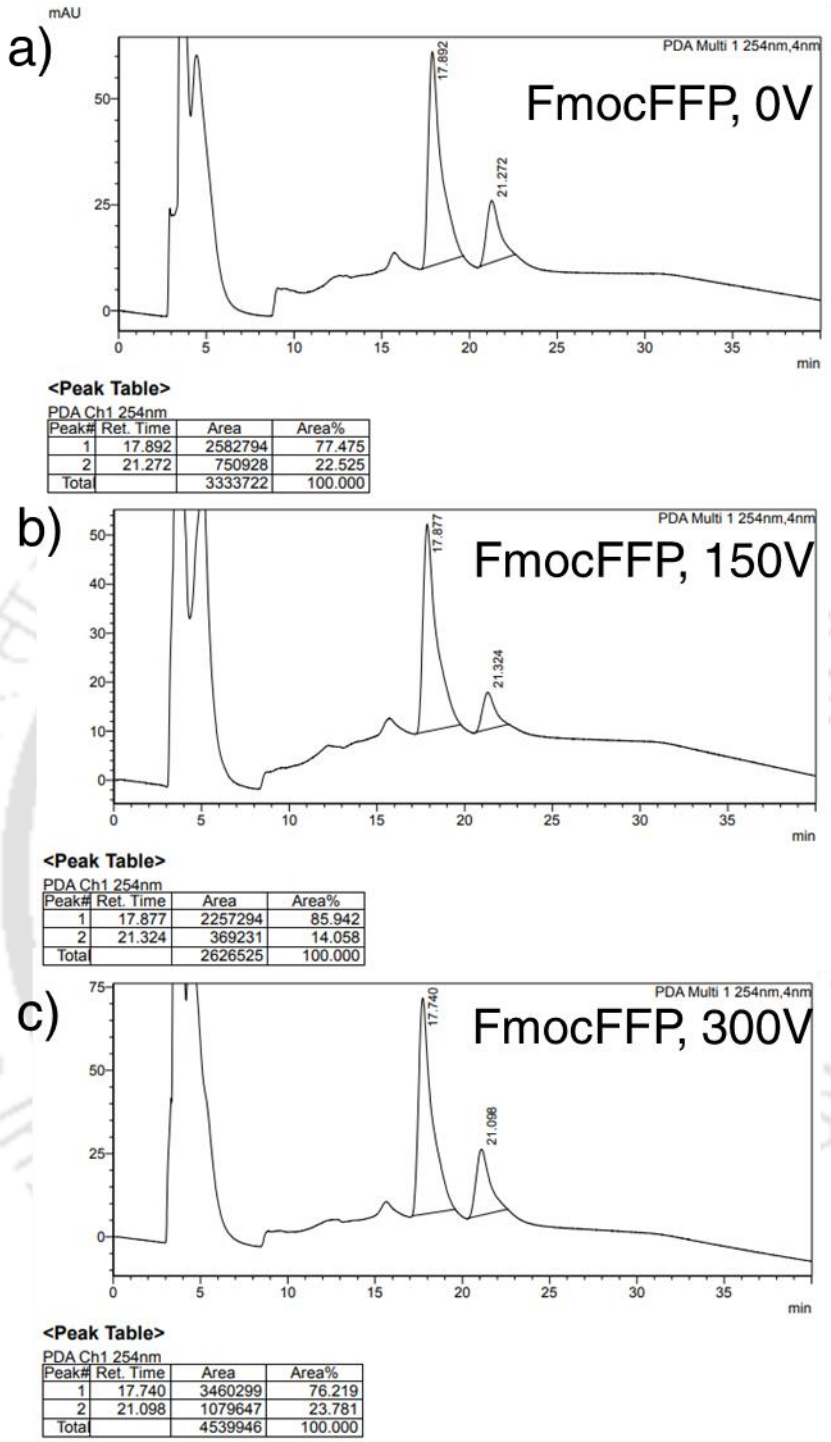

Figure A3.8: Typical chiral chromatogram for the aldol products catalyzed by Fmoc-FFP hydrogel formed in different EF strength. Labeled peaks correspond to *sin* aldol and *anti*-aldol. Integral ratio between the minor and the major diastereomers was used to determine the diastereomeric ratio.

a)

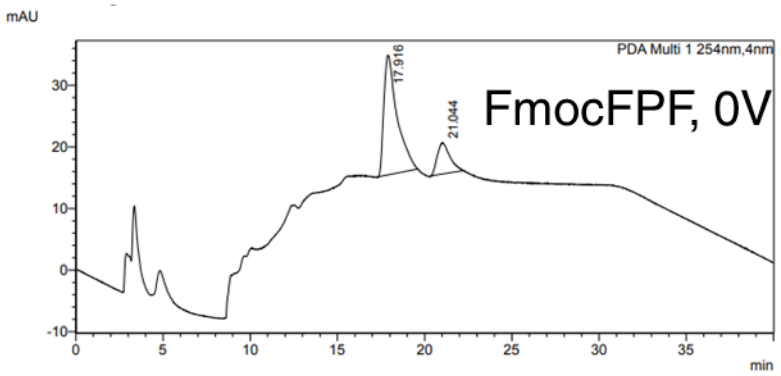

<Peak Table>
PDA Ch1 254nm

Peak#	Ret. Time	Area	Area%
1	17.916	1029019	80.147
2	21.044	254900	19.853
Total		1283919	100.000

b)

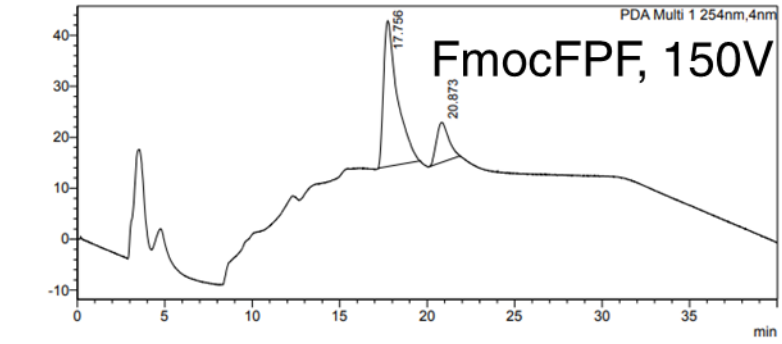

<Peak Table>
PDA Ch1 254nm

Peak#	Ret. Time	Area	Area%
1	17.756	1568310	80.594
2	20.873	377631	19.406
Total		1945941	100.000

c)

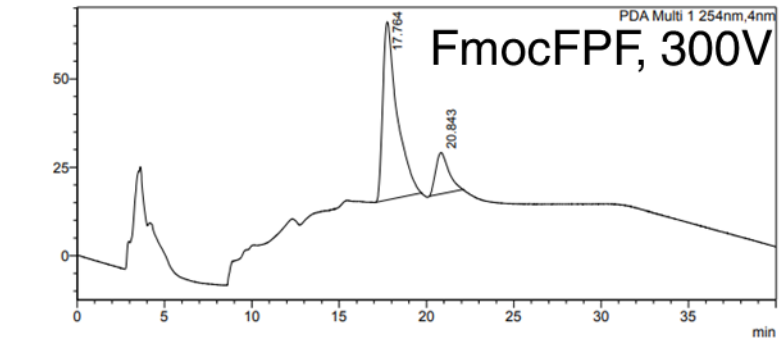

<Peak Table>
PDA Ch1 254nm

Peak#	Ret. Time	Area	Area%
1	17.764	2883606	82.606
2	20.843	607183	17.394
Total		3490789	100.000

Figure A3.9: Typical chiral chromatogram for the aldol products catalyzed by Fmoc-FPF hydrogel formed in different EF strength. Labeled peaks correspond to *sin* aldol and *anti*-aldol. Integral ratio between the minor and the major diastereomers was used to determine the diastereomeric ratio.

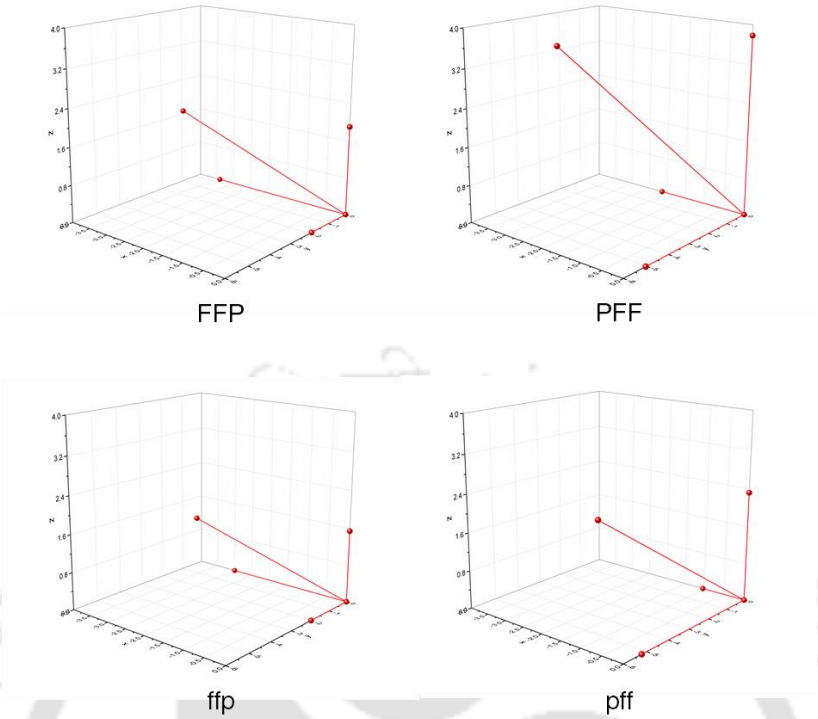

Figure A3.10: Dipole moment of the designed peptides in water. To study the dipole moment of the peptides in water, Molecular Dynamics (MD) simulations were performed with a GROMOS96 force field (54a7 parameter set) using GROMACS 5.0.4 package. Changes were made in the residue topology of the simulation tool, to incorporate the structural parameters of the D-amino acids. Each peptide was placed in a dodecahedron box with a spacing of 1.0 Å from the box edge. The system was solvated using the flexible SPC/E water model. The solvated system was neutralised to zero. Energy minimisation was carried out using the steepest descent until a tolerance of 1000 KJ mol^{-1} nm^{-1} was reached. Periodic boundary conditions were deployed in all the systems. The dipole moment of the peptides was calculated using gmx dipole for the energy minimised frame. < M_i >, i for X, Y and Z axis, is the net vector in each frame. Dipole moments were calculated as the square root of the sum of the squares of <M_i>.

Appendix #4

1. Characterization of the synthesized peptide

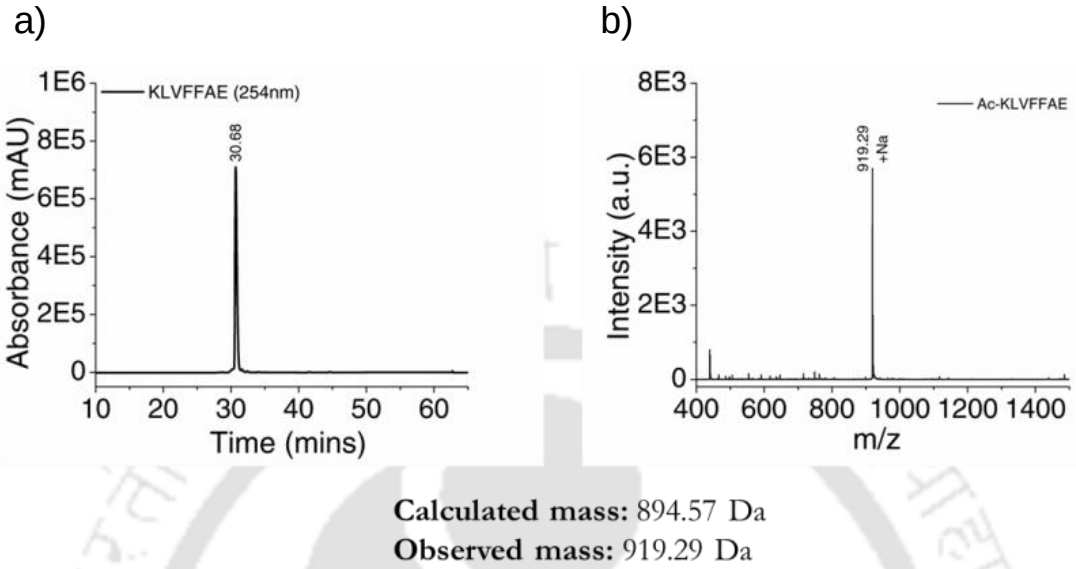

FigureA4.1: a) HPLC chromatogram of Ac-KLVFFAE b) MALDI-TOF spectrum of Ac-KLVFFAE

2. **Confocal images showing internalization of EF treated and untreated FITC-Aβ$_{1-42}$**

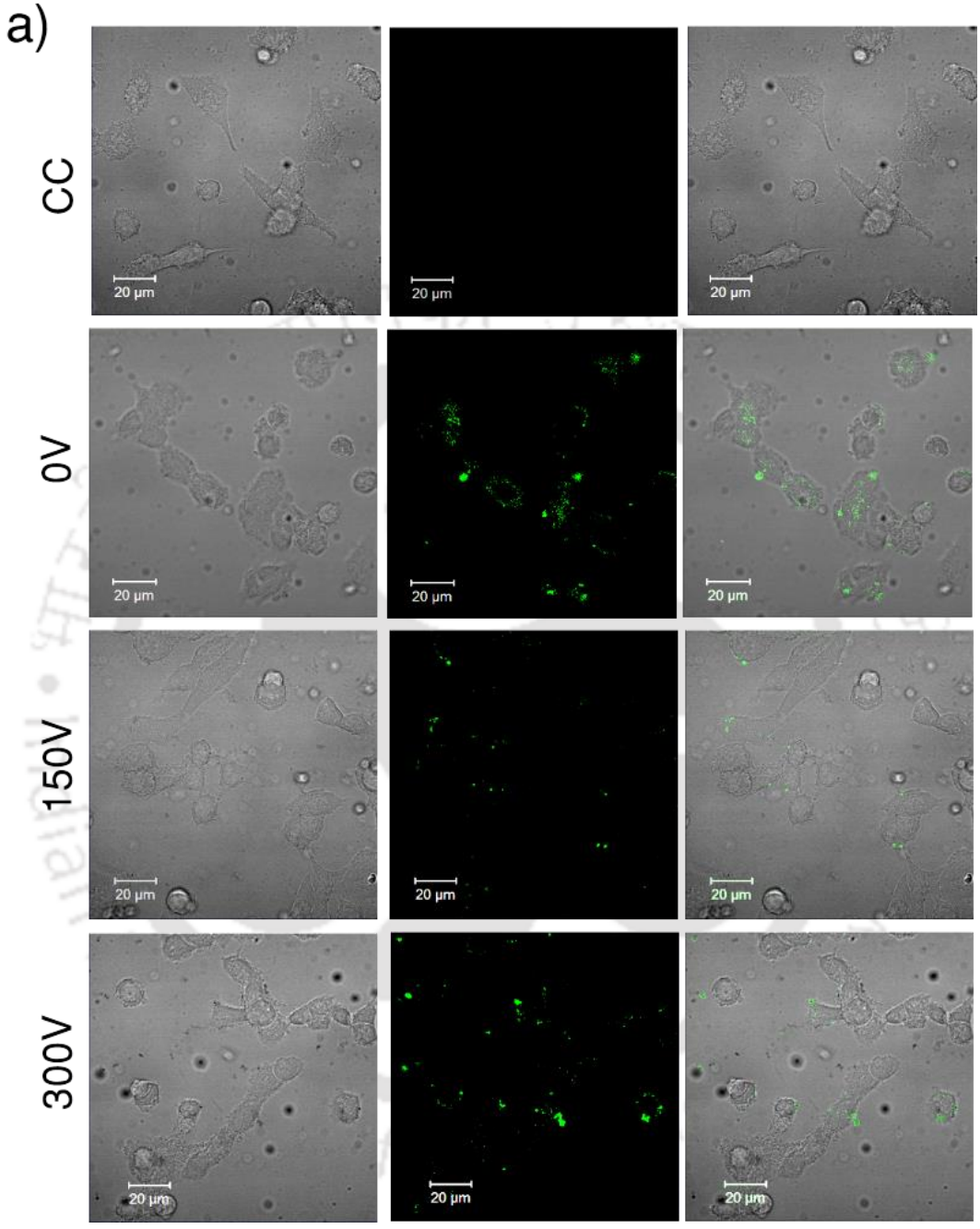

Figure A4.2: Confocal images showing internalization of EF treated and untreated FITC-Aβ$_{1-42}$ by SHSY5Y human neuroblastoma cells.

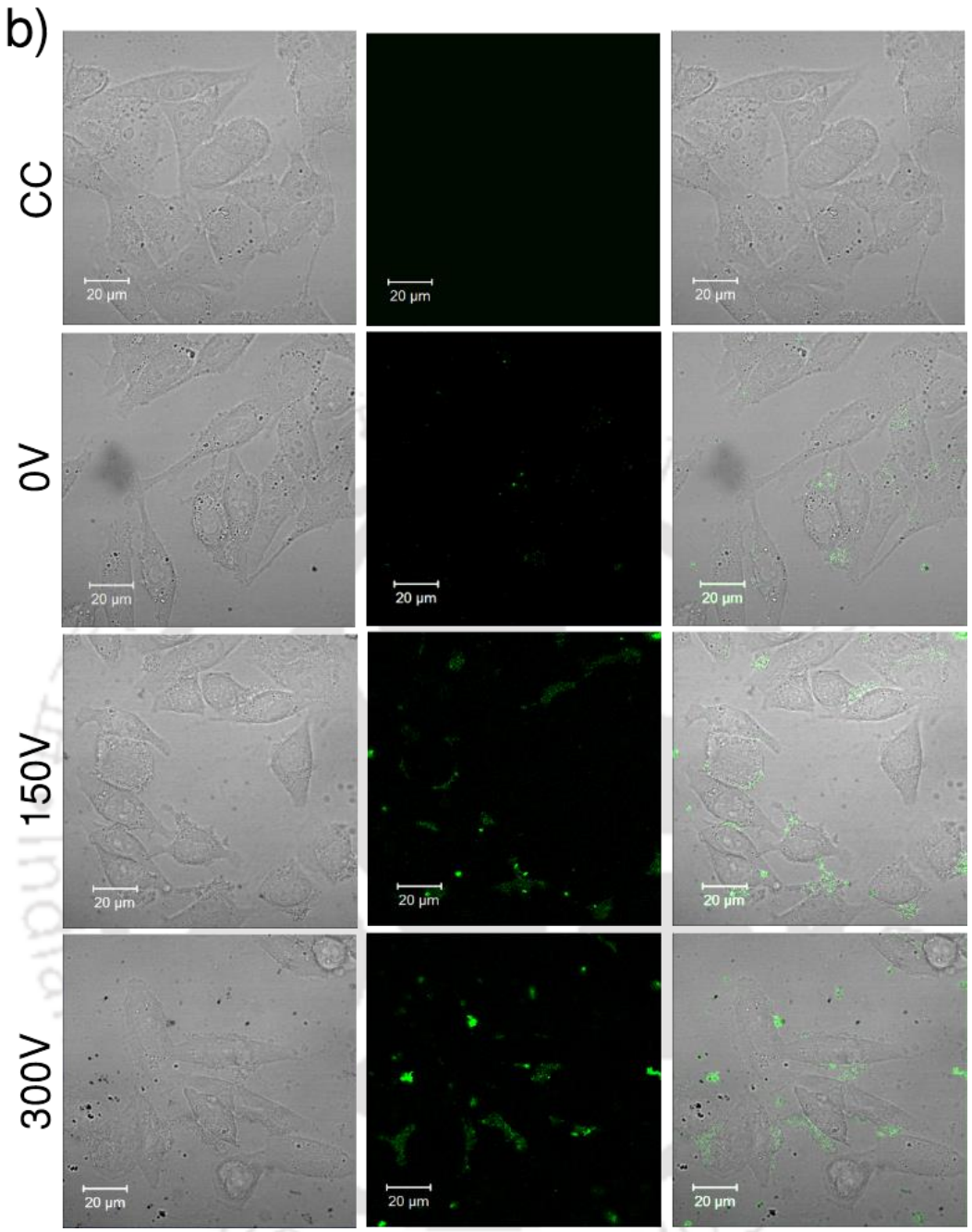

Figure A4.3: Confocal images showing internalization of EF treated and untreated FITC-Aβ_{1-42} by IMR-32 human neuroblastoma cells.

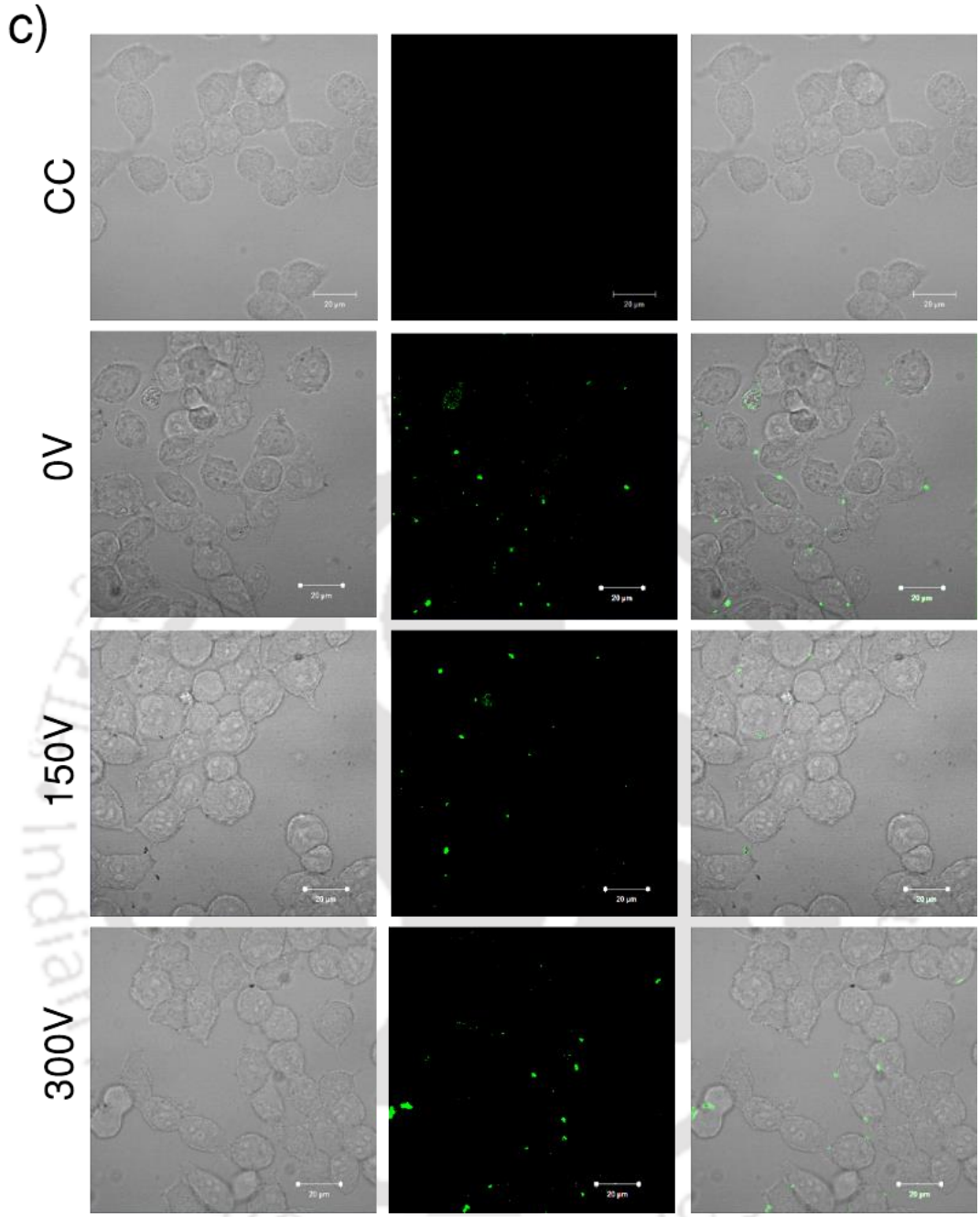

Figure A4.4: Confocal images showing internalization of EF treated and untreated FITC-Aβ_{1-42} by HEK293 cells.

LIST OF PUBLICATIONS

Patents

International Patent

1. A device for non-invasive treatment of neurodegenerative diseases. Patent No. WO/2019/012556. **Present Status:** Published

Publications

1. **Jahnu Saikia**, K. Dharmalingam, R. Anandalakshmi, Amay S. Redkar, Venu Bhat, and Vibin Ramakrishnan. "Electric Field Modulated Peptide based Hydrogel Nanocatalyst." ***Soft Matter*** (2021). doi: 10.1039/D1SM00724F

2. **Jahnu Saikia**, Gaurav Pandey, Sajitha Sasidharan, Ferrin Antony, Harshal B. Nemade, Sachin Kumar, Nitin Chaudhary, and Vibin Ramakrishnan*. Electric Field Disrupts Amyloid Aggregation; Potential Non-invasive Therapy for Alzheimer's Disease. ***ACS Chemical Neuroscience,*** (2019), doi:10.1021/acschemneuro.8b00490.

3. Praksah Kishore Hazam, Akhil, R., Gaurav Jerath, **Jahnu Saikia** and Vibin Ramakrishnan. Topological effects on the designability and bactericidal potency of antimicrobial peptides. ***Biophysical Chemistry,*** (2019), doi.org/10.1016/j.bpc.2019.02.005.

4. Gaurav Pandey, **Jahnu Saikia**, Sajitha Sasidharan, Deep C. Joshi, Subhash Thota, Harshal B.Nemade, Nitin Chaudhary, and Vibin Ramakrishnan*. Modulation of Peptide Based NanoAssemblies with Electric and Magnetic Fields. ***Scientific Reports,*** (2017). doi:10.1038/s41598-017-02609-z.

5. **Jahnu Saikia**, Lokeswara Rao Potnuru, Vipin Agarwal, Venugopal T. Bhat*, Vibin Ramakrishnan* Minimalist *de-novo* design of an artificial enzyme. (*under review*)

6. **Jahnu Saikia** and Vibin Ramakrishnan. Stimulus responsive peptide nano-assemblies (*under preparation*)

Conferences

1. **Jahnu Saikia** and Vibin Ramakrishnan, "Effect of electric field on the aggregation of β-amyloid peptide', 63rd Biophysical Society annual meeting in Baltimore, Maryland, USA, 1st to 6th March.